AN EXPERIMENTAL AND THEORETICAL STUDY OF THE FLOW PHENOMENA WITHIN A VORTEX SINK RATE SENSOR

FINAL TECHNICAL REPORT

By

G.L. Goglia

and

D.K. Patel

Page Intentionally Left Blank

ABSTRACT

AN EXPERIMENTAL AND THEORETICAL STUDY OF
THE FLOW PHENOMENA WITHIN A
VORTEX SINK RATE SENSOR

by

Dr. G. L. Goglia (Principal Investigator)
Professor & Chairman
Mechanical Engineering
Old Dominion University

and

Dr. D. K. Patel
Research Associate
Old Dominion University

June 1974

The objective of this investigation was to obtain a de-
tailed description of the flow field within a vortex sink
rate sensor and to observe the influence of viscous effects
on its performance.

The sensor basically consists of a vortex chamber and a
sink tube. The vortex chamber consists of two circular co-
axial disks held apart, at their periphery, by a porous
coupling. One circular disk has an opening to permit the
mounting of the sink tube, in such a manner that the vortex
chamber as well as the sink tube have a common axis of
rotation.

Air was supplied radially to the sensor through its
porous coupling as the sensor was rotated at various speeds.
Particular emphasis was directed toward an understanding of
the flow field in the sink tube region. Thus velocity measure-
ments at various stations along the length of the sink tube
as well as along a given radius at any designated station
were taken.

A computer program was developed, for obtaining the numerical solution of the Navier-Stokes equations, assuming laminar flow, having generally prescribed inlet conditions and axisymmetric boundary conditions. Computational results for various viscous flows and assorted boundary conditions have been obtained.

For a specific mass flow rate and the geometry of the vortex chamber, it was found that the flow in the vortex chamber was only affected, locally (i.e., only near the sink region), by the size of the sink tube diameter. However, within the sink tube, all three velocity components were found to be higher for the smaller sink tube diameters. As the speed of rotation of the sensor was increased, the tangential velocities within the vortex chamber, as well as in the sink tube increased almost in proportion to the speed of rotation.

The only noticeable effect on the flow pattern, due to the variation of the vortex chamber spacing, was found to be at the entrance section of the sink tube. For a given mass flow, the radial and tangential velocities in the vortex chamber increased with an increase in the chamber diameter. The same effect was also observed in the entrance region of the sink tube.

A change in the flow rate had an appreciable effect within the sensor and particularly near the sink tube entrance. As the flow rate was increased, both the tangential velocity and tangential vorticity increased rapidly. At the higher flow rates, vortices were produced at the corner of the entrance section of the sink tube and thus the flow became unstable.

The theoretical predictions were found to be in reasonable agreement with the experimental results.

ACKNOWLEDGEMENTS

TABLE OF CONTENTS

Page

LIST OF FIGURES

*refers to figures for vortex chamber, and ** for sink tube

x

LIST OF SYMBOLS

a	dimensionless grid size, ΔR, ΔZ
A, B	constants
h	spacing between two vortex chamber plates, ft.
H	dimensionless spacing between two vortex chamber plates, h/r_o
i	subscript correspond to R-axis
j	subscript correspond to Z-axis
K	counter index for number of iteration for time step
K_o	constant for velocity calculation
ℓ	the total axial length from outer vortex chamber plate to sink tube exit, ft.
L	dimensionless total axial length of sink tube, ℓ/r_o
m	number of mesh (grid) points along axial direction between two vortex chamber plates
mm	number of grid points along the axial length from vortex chamber outer plate to sink tube exit
n	number of grid points along the radial direction in the vortex chamber
(n)	counter index for number of iteration
nn	number of grid points along the radial direction in the sink tube
N_{Re-u}	radial Reynolds number, $Q_o/(2\pi h\nu)$
$N_{Re-\theta}$	tangential Reynolds number, $\omega r_o^2/\nu$
N_{Ro}	Rossby number, $Q_o/(2\pi\omega r_o^3)$
p	static pressure, $lb/ft.^2$
$\hat{p}$	dimensionless static pressure, $p/(\rho\omega^2 r_o^2)$

r_1	the distance between the center of the hot wire probe wire and the probe longitudinal rotating axis, ft.
r	radial coordinate, ft.
r_0	vortex chamber outside radius, ft.
r_i	sink tube radius, ft.
Δr	grid size along radial direction, ft.
ΔR	dimensionless grid size along radial direction, $\Delta r / r_0$
R	dimensionless radius
R_i	dimensionless sink tube radius, r_i / r_0
S	slenderness ratio, h / r_i
S_1, S_2	vertical travel of the hot wire probe support axis from the sink tube axis, ft.
t	time, sec.
T	dimensionless time, $t \cdot \omega$
ΔT	dimensionless time step for iteration
u	radial velocity, ft./sec.
u_0	inlet radial velocity in vortex chamber, $Q_0 / (2\pi h r_0)$, ft./sec.
U	dimensionless radial velocity, $u / (\omega r_0)$
v	tangential velocity, ft./sec.
v_0	tangential velocity at vortex chamber entrance, ωr_0, ft./sec.
V	dimensionless tangential velocity, $v / (\omega r_0)$
V^*	resultant velocity, ft./sec.
V_H	velocity measured when hot wire is horizontal
V_V	velocity measured when hot wire is vertical
w	axial velocity, ft./sec.
W	dimensionless axial velocity, $w / (\omega r_0)$

z	axial coordinate, ft.
Z	Dimensionless axial length, z/r_0
z_1, z_2	distance of pin bearing from sink tube entrance, ft.
Δz	grid size along axial direction, ft.
ΔZ	dimensionless grid size along axial direction, $\Delta z/r_0$
α	longitudinal flow angle, degrees
α_1, α_2	angles made by the resultant velocity with the plane perpendicular to the hot wire, degrees
$\bar{\Gamma}$	circulation, $v \cdot r$, ft.^{2}/sec.
Γ	dimensionless circulation, $\bar{\Gamma}/(\omega r_0^2)$
ϵ	tolerance
$\bar{\eta}$	tangential vorticity, $(\partial u/\partial z) - (\partial w/\partial r)$, radians/sec.
η	dimensionless tangential vorticity, $\bar{\eta}/\omega$
θ	longitudinal angle in the horizontal plane made by hot wire probe axis with probe support axis, degrees
λ_ω	relaxation parameter
Λ	parameter used for dummy ψ, Γ or η
$\Lambda^*, \psi^*, \Gamma^*, \eta^*$	temporary dependent variables
μ	dynamic viscosity, lb. sec/ft.^{2}
ν	kinematic viscosity, ft.^{2}/sec.
ρ	fluid density, lb./ft.^{3}
ϕ	longitudinal angle in the vertical plane made by hot wire probe axis with probe support axis, degrees
$\bar{\psi}$	stream function, ft.^{3}/sec.
ψ	dimensionless stream function, $\bar{\psi}/(\omega r_0^3)$
ω	angular velocity of apparatus, radians/sec.
Ω	electrical resistance, ohms

I. INTRODUCTION

An interest in vortex flows has existed for many decades. The beauty and vigor of the whirling and swirling motions in water and air has fascinated man from his earliest days. Vortices may have been what inspired the Mediterranean artists and craftsmen, well over 3000 years ago to create their spiral ornamentations. Today, man describes vortex motions as the sinews and muscles of fluid motion and the scientists through research efforts attempt to harness the energy contained therein. Researchers are attempting to utilize vortex flows in many energy conversion schemes such as in aeroplanes and other lifting bodies. As the state of the art of vortex flow develops many new applications are brought into focus. In recent years, vortex flows within confined chambers have become of considerable interest. This interest arose as a direct consequence of attempting to learn more about the flow phenomena relevant to the gaseous core of a nuclear rocket [28], electric power generation using magneto-hydrodynamic effects [12], and pure fluidic devices such as the vortex amplifier and the fluidic gyroscope [15].

A search of the literature readily reveals that there have been many contributions made to the study of vortex flows through investigations pertaining to meteorology, the Ranque-Hilsh tube, the cyclone separator, wing theory, compressors, fluidics and others. To adequately discuss here the voluminous literature on vortex flows would serve little purpose, thus, a condensation of the important contributions

1

is presented.

Vogelpohl [61] was the first investigator to attempt an analysis of a confined vortex. He obtained an analytic solution for the tangential velocity under the restrictive assumptions that the radial velocity was completely independent of the axial coordinates and that the axial velocity was zero. These assumptions precluded the increase of the radial mass flow within the boundary layers due to the action of the pressure defect. Thus, his solution was not an accurate representation of the vortex flow between two flat plates.

In the case of coaxial disks flow, by assuming the axial velocity to be radius independent, Kármán [25] obtained a set of ordinary differential equations that described the steady state viscous flow above an infinitely large rotating disk. A numerical solution to these equations was presented by Cochran [9]. Bödewadt [4] solved the problem of a uniformly rotating fluid over an infinite stationary wall.

Batchelor [3] generalized the Kármán's method to include the case of two rotating disks and discussed, semi-quanti-tatively, the nature of the steady flow between the two disks. Additional comments on this problem have been presented by Stewartson [57]. He also studied the boundary layer on a semi-infinite cylinder which was either rotating about its axis in a fluid otherwise at rest or was stationary with a rotating fluid inside it [59]. He also investigated the shear layer at the boundary of a finite circular cylinder for a

fluid rotating uniformly about its axis in the same reference.

Matsch and Rice [36, 37, and 38] studied the inward flow between rotating disks, which corresponded to the multiple-disk turbine. Their analyses and results were for the potential flow between the disks as well as for creeping flow between the disks accounting for the centrifugal effects. These analyses considered both partial and full admission of the fluid at the outer periphery. The asymptotic flow was shown to depend only on the fluid flow rate and the radial Reynolds number (N_{Re-u}), while independent of the tangential velocity.

By employing the numerical method developed by Hall [20], Stewartson and Hall [58] obtained a solution for a viscous incompressible flow within the inner core of a nuclear reactor.

Theoretical investigations of unstable flows of the second kind were reported by Ludwieg [33] and Jones [24]. Axisymmetric and spiral disturbances were considered. Ludwieg presented stability criteria for the core flow of Hall [19] and predicted instability for small disturbances if the pitch angle of the helical streamlines became too steep and thus the Rossby number too small.

Rosenzweig, Lewellen and Ross [52] also analyzed the two plate problem. They limited their analysis to the case where the tangential velocity was much greater than the radial velocity and the separation distance between the plates was greater than the radius of the plates.

Viscous effects in vortex motions driven by an inward

radial convection of an angular momentum were examined in
more detail by Lewellen [30]. Exact and some nearly exact
solutions of the Navier-Stokes equations, applicable to this
case, were also obtained. These solutions were found by a
general expansion of the equations of motion for a large
swirl (i.e. for a small Rossby number) and by linearizing
the equations for perturbations about known flows for a weak
swirl (i.e., a large Rossby number). He discussed the axial
variations of flow. The results for large Rossby numbers
indicated that as the circulation decayed with increasing
axial distance, the axial velocity in an annulus about the
axis actually increased faster than on the axis itself. This
caused a reduced axial pressure gradient along the axis. The
results for small Rossby numbers indicated that the axial
pressure gradient could be reversed to produce a reverse
flow. It was found that in the flows dominated by rotation,
the fluid motion was forced to be two dimensional except for
a thin shear region where all necessary adjustments imposed
by the boundary conditions were satisfied by the flow.

Granger [18] studied the steady three dimensional
vortex flow for a specified vorticity distribution along the
axis of rotation within a vortex chamber whose disks were
an appreciable distance apart.

Kidd and Farris [29] obtained rather interesting results
from a flow produced by the interaction of a potential vortex
with a stationary surface. In the analysis they transformed
the full Navier-Stokes equations by a similarity technique

and then numerically integrated resulting ordinary differential equations. Very close to the surface, the radial velocity was found to be directed towards the axis and therefore the flow was able to redistribute itself. Such problems were of interest in the study of tornadoes and hurricanes. Recently, they have become of interest especially in the design of nuclear reactors.

Donaldson and Sullivan [13] made an extensive study of the class of solutions $u = u(r)$, $v = v(r)$, $w = z\bar{w}(r)$ for laminar incompressible flow conditions. The solutions by Burgers [5] and Rott [53], in which $u = -ar$, $v = v(r)$ and $w = 2az$, $(a = constant)$, were included in this class. Donaldson and Sullivan began their work as a consequence of an interest on "canned" vortex flows, where fluid imparted with a swirl entered a cylindrical container through its side and discharged axially.

Yih [65] obtained a closed form solution of the Euler's equations for an axisymmetric flow of a swirling and non-swirling flow discharging into a point sink. He, however, made no provision for boundary layer development.

Ostrach and Loper [41] analyzed the vortex motion between two closely spaced disks. The vortex was assumed to be driven by the tangential injection of the fluid at the periphery of the configuration and was discharged at its center. The momentum integral solution of this problem showed the strong dependence of the boundary layer thickness as well as the radial velocity on the imposed radial mass flow. The

results indicated that the boundary layer blockage effects could be reduced by increasing the imposed radial mass flow. It should be noted that they considered the case where the relative tangential velocity at the periphery of the configuration had a finite magnitude. Thus the results are not applicable to the vortex rate sensor, where indeed the relative tangential velocity at the periphery of the configuration is zero.

Fiebig [15] studied the response of the radial flow to harmonic oscillations of the sensor. The approach used was to approximate the transport flow by a family of "parabolic" profiles which satisfied the equation of continuity but not the momentum equation.

Egli, Kizilos and Reilly [14] analyzed the radial flow boundary layer on a circular flat disk. In their investigation, the drain was approximated by a line sink and the radial potential flow was assumed to be unaffected by the boundary layers.

Sarpkaya [54] studied the radial flow between two coaxial disks. He computed the boundary layer development by two methods. Similarity solutions of the equations were obtained by employing an integral momentum technique through utilization of an approximation suggested by Thwaits [60]. The result showed that the boundary layer thickness decreased linearly to zero from the periphery to the center of the disks.

A theoretical and experimental investigation of the gain and the frequency response in a vortex sink rate sensor was

conducted by Ostdiek [40]. He reported that the dynamic characteristics of the viscous flow within a rate sensor operating in the fully developed range were significantly more favorable than those for the inviscid fluid within the sensor.

Richards [48] applied the numerical techniques of the implicit alternating direction (ADI) method, as well as of the explicit iteration method to study the characteristics of the flow in a vortex rate sensor in which fluid discharged into a point sink. He compared his numerical results with the experimental results obtained by Hellbaum [22] and found that the agreement was good for values of $r \geq 0.2\ r_o$.

Roache and Muller [51] developed a numerical procedure for finding solutions to both incompressible and compressible laminar separated flows, using time dependent finite difference equations. They used the conservation forms of the governing equations and used the upwind difference technique for the advection (inertial) terms in both the compressible and incompressible flows.

Macagno and Hung [34] studied the annular laminar captive eddy in a conduit expansion. The numerical procedure used was restricted to an expansion ratio of 2:1 and was limited to radial Reynolds numbers (N_{Re-u}) up to 200. A correlation of experimental results with their numerical results was also included.

Pao [42, 43] considered two cases of the rotary disk-cylinder combinations and numerically computed the flow

pattern of a viscous incompressible fluid confined within the cylindrical chamber. He found that for a tangential Reynolds number $N_{Re-\theta} = (\omega r_o^2/\nu)$ in excess of 8, nonlinearities appeared in the flow. He also observed that as the tangential Reynolds number $(N_{Re-\theta})$ was increased beyond 400, convergence by the numerical iteration technique for steady state conditions became extremely slow.

Pearson [44] described a method for obtaining an exact numerical solution for the flow between two infinite rotating disks. He also described a computational method for solving the time-dependent two-dimensional viscous flow problems [45].

In addition to the numerical and analytical investigations of vortex flows, a number of experimental investigations are reported in the literature. Experimental studies of confined vortex flows can be broadly classified into two subcategories. The first is concerned mainly with high swirl flows. Because of its practical importance, such as in the case of hydraulic cyclones, magnetohydrodynamic vortex power generators (nuclear reaction chambers), dust cleaners, etc., high swirl flows received a great deal of attention.

One of the earlier experiments, was a visual experiment by Savino and Keshock [55]. It was conducted in an attempt to suspend fine particles of various sizes in a vortex of air inside a right circular cylinder, which had a length-to-diameter ratio of approximately one. This study revealed the presence of some axial motion, as particles appeared to always cluster at the corner of the cylindrical surface and

the exit end wall. This observation suggested that an appreciable radial in-flow existed at the end-wall boundary layer. They concluded that the amount of swirl (ratio of tangential to radial velocities) imparted to the fluid, as it was injected into the chamber, alone determined that fraction of the total mass flow which was forced inwardly within the end wall boundary layers. When the swirl was low (less than 0.5), the radial inflow had sufficient inward momentum to penetrate the centrifugal field. The inflow existed at all axial and radial positions away from the walls. When the swirl was high (greater than 10), the radial inflow was diverted axially and if the flow was confined within two walls, all the fluid left the chamber by way of the boundary regions adjacent to the end walls. This latter conclusion was consistent with the result of Lewellen [30].

Kelsall [26] made measurements of the radial, tangential and axial velocity components inside a hydrocyclone separator. His experiments revealed the existence of large secondary motions with most of the mass movement occurring close to the walls where the centrifugal force was least.

Williamson and McCune [64], and Donaldson [13] conducted experiments in short cylinders $(0.130 \leq (L/D) \leq 0.281)$. In both references, the radial distribution of the tangential velocity was calculated through axial traverses of the total pressure.

Ragsdale [46] took pitot tube measurements within a vortex chamber $(L/D = 0.5)$ at two radial stations and several

axial stations. He concluded that the motion was essentially tangential with very little variation of magnitude in the axial direction.

Kendall [27] experimented with a vortex that was generated by a rotating porous cylinder which imparted a swirl to the fluid supplied to it through the porous wall. A flattened pitot tube was used to traverse the boundary layers. In the measurements of both total pressure and local fluid direction, the radial velocity was assumed zero at distances far removed from the wall.

The second subcategory of experimental studies of confined vortex flows is mainly concerned with the low swirl flows. One such flow is the flow in a vortex rate sensor as reported in references [10, 22, 40].

Hellbaum [22] conducted experimental work in a vortex rate sensor and obtained characteristic flow angles for different tangential Reynolds numbers, radial Reynolds numbers and plate-spacings. By the smoke trace technique, he studied the effects of the geometrical parameters on the characteristics of flow angle in the vortex chamber of the sensor. He selected $r = 0.2\ r_0$ as the smallest radius for which the flow angle α was not appreciably affected by the sink proximity. By determining $\alpha_{0.2}$ (flow angle α at $0.2\ r_0$), he plotted graphs of $\tan \alpha_{0.2}$ versus tangential Reynolds number ($h^2\omega/\nu$), with (r_0/h) and radial Reynolds number ($Q_0/h\nu$) as dimensionless parameters. Hellbaum showed an increase in $\tan \alpha_{0.2}$ for a decrease in flow rate.

The paper by DeSantis and Rakowsky [10, 11] reported the experimental velocity profiles and boundary layer characteristics in a steady state weak vortex flow produced by the combination of an axisymmetric sink flow and a vortex flow between two coaxial circular plates of very small aspect ratio ($h/r_0 \leq 0.03$).

In the experimental studies of Sarpkaya [54], using air as the fluid, it was observed that the output of the pickoff signal was linear for small values of 'ω' and that linearity increased with increasing flow rates. He further observed that rotations in counterclockwise as well as clockwise directions about the axis of symmetry gave identical differential pressure signals.

Rakowsky and Schmidlin [47], with water as the working fluid, studied the flow in the vortex chamber by photographing the dye traces of the streamlines and then reducing the resulting data. Angular momentum efficiency (ratio of angular momentum at any r to that at $r = r_0$) of the midplane of the vortex chamber was plotted as a function of radius. These results were then compared with the results predicted by a momentum integral method with an assumed parabolic momentum profile and the unknown matching parameter was determined.

In addition to the effect that the coupler diameter had on the pickoffs, Burke and Roffman [7] studied the performance of two different pickoffs (one axially slotted and one circumferentially slotted). They observed that for couplers of smaller diameters the pressure output decreased.

With an angular rate sensor, Burke [6] observed the effect of the coupler height and pickoff on the sensitivity (defined as signal output unit rate of rotation). He reported that for a given rate of rotation, the sensitivity (which now is a measure of differential pressure) decreased rapidly as the angle between the axis of spin and the axis of symmetry increased. The maximum sensitivity occurred when the two axes coincided. The sensitivity was also found to increase with increased spacing between the couplers. He also discussed the time dependent phenomena such as the noise frequency in the output of the pickoff, the transport time and the threshold (ratio of Δp of signal to Δp of noise). These phenomena are of importance in the practical use of sensors when the response time is of importance.

Arimilli [2], Gala [17] and Lu [32] each undertook an experimental investigation of a vortex sink rate sensor. Their studies, however, were confined only to the sink tube. The apparatus they used had vortex chamber diameters of 5 and 10 inches, while the sink tube diameters ranged from 1/4 to 1 inch. The objective of their studies was to observe experimentally the effect of the flow rate, change of rotation, and change of configuration on the tangential velocity within the sink tube.

Several investigators have undertaken studies, experimentally as well as theoretically, within the vortex chamber only. Rakowsky and Schmidlin [47] have considered the entire vortex sink rate sensor as their system. However, they assumed the fluid to be inviscid and therefore were able to use the

Euler equations and easily find the numerical solutions. None of the previous investigators, however, have considered a viscous fluid. No direct measurements of the velocities in the sink tube have been made before. Thus in the present investigation a viscous fluid is assumed and the velocities within the sink tube are directly measured. In addition to this experimental investigation, a complete numerical analysis of the flow pattern in the entire sensor is undertaken.

The vortex sink rate sensor presently under consideration, consists basically of an ideal sink flow between two coaxial plates having a single outlet. The entrance flow to the device is radial and the sensor design permits an angular rotation about its geometric axis. This arrangement results in the creation of a vortex flow within the sensor.

The sensor is essentially a fluidic device which, in addition to being inexpensive to manufacture, has all the desired characteristics for use as a guidance control instrument. Its simplicity, high reliability and long life are assets not to be overlooked. The present exploration of space has also created the need for a guidance control instrument. that would essentially be unaffected by severe environmental conditions such as high temperature, shock, vibration and nuclear radiation. The sensor can indeed serve this need as a fluidic gyroscope. The fluid vortex amplifier also shows promise for future application to liquid propellant rocket engine control systems. The advances in the art of fluidics within the past few years, and the successful application of fluid amplifiers has made the sensing and amplification of a

signal possible by merely varying the rotation of the sensor.

As the sink tube is considered the most likely location for any signal detection element, the study of the flow pattern within the sink tube is given particular attention here. A signal detection element senses changes as a consequence of fluctuations at its location. The signal could be a relatively weak one and therefore could need to be amplified for transmission to the controlling device. Thus it is important to strategically locate the signal detection element at the location where maximum amplification occurs.

This present investigation was therefore undertaken with the primary objectives being to investigate the steady state flow conditions, and to develop an understanding of the flow pattern within the sensor.

Chapter II describes the formulation of the governing equations. Chapter III presents the numerical analysis used for solution of the flow field. Chapter IV and V are devoted to the numerical results. The experimental investigation and results are discussed in Chapter VI. Experimental results are compared with numerical results in Chapter VII and the conclusions are given in Chapter VIII.

II. BASIC FORMULATION

2.1 Governing Equations

The vortex sink rate sensor considered for this investigation is shown in Figs. (2.1) and (2.2). The sensor, basically, consists of a vortex chamber and a sink tube. The vortex chamber consists of two circular co-axial disks held apart, at their periphery, by a porous coupling. One circular disk has an opening to permit the mounting of the sink tube in such a manner that the vortex chamber as well as the sink tube have a common axis of rotation. Air flow was supplied radially to the vortex chamber through the porous coupling. The objective behind this investigation was to determine the flow pattern within the vortex sink rate sensor.

The axisymmetric flow through the sensor suggested the selection of the cylindrical coordinate system, as shown in Fig. (2.3), to establish the governing equations for the flow. The radial, tangential and axial coordinates are respectively represented by r, θ and z while u, v and w denote the respective velocity components. In the analysis that follows, the top plate of the vortex chamber is considered to be located at $z = 0$ and the axis of symmetry is located at $r = 0$.

The Navier-Stokes equations for a viscous incompressible fluid with constant properties may be expressed in cylindrical coordinates as
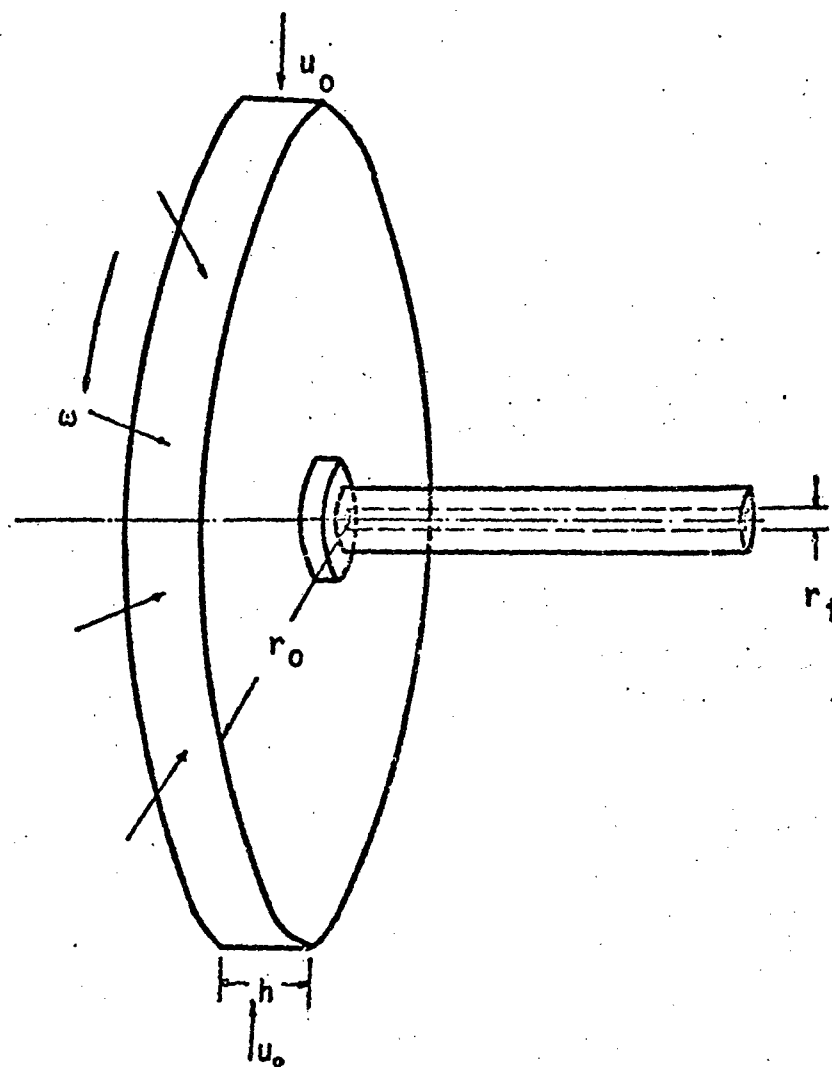
Figure 2.1   The Vortex Sink Rate Sensor
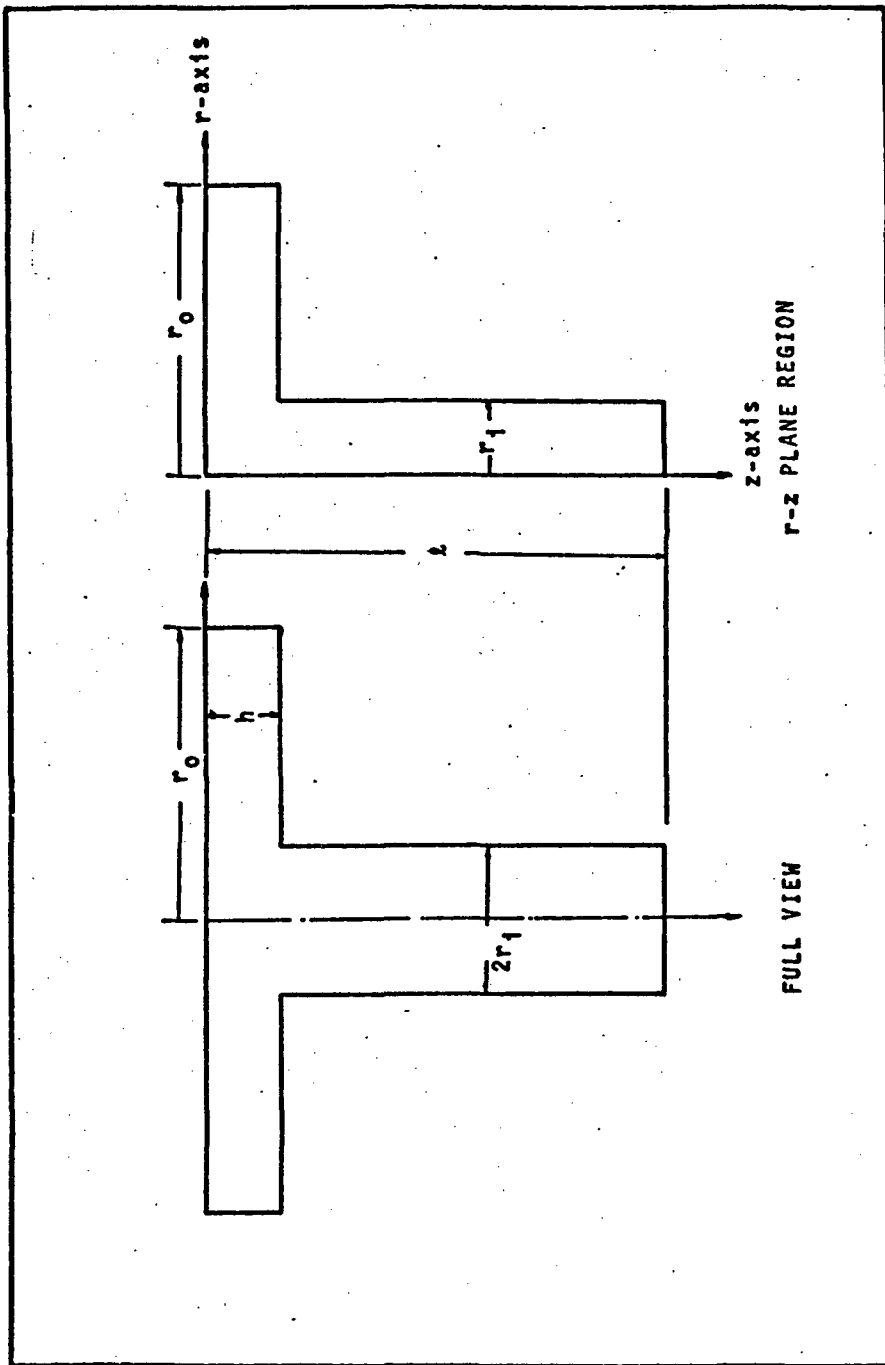
Figure 2.2   Sectional View of the Vortex Sink Rate Sensor
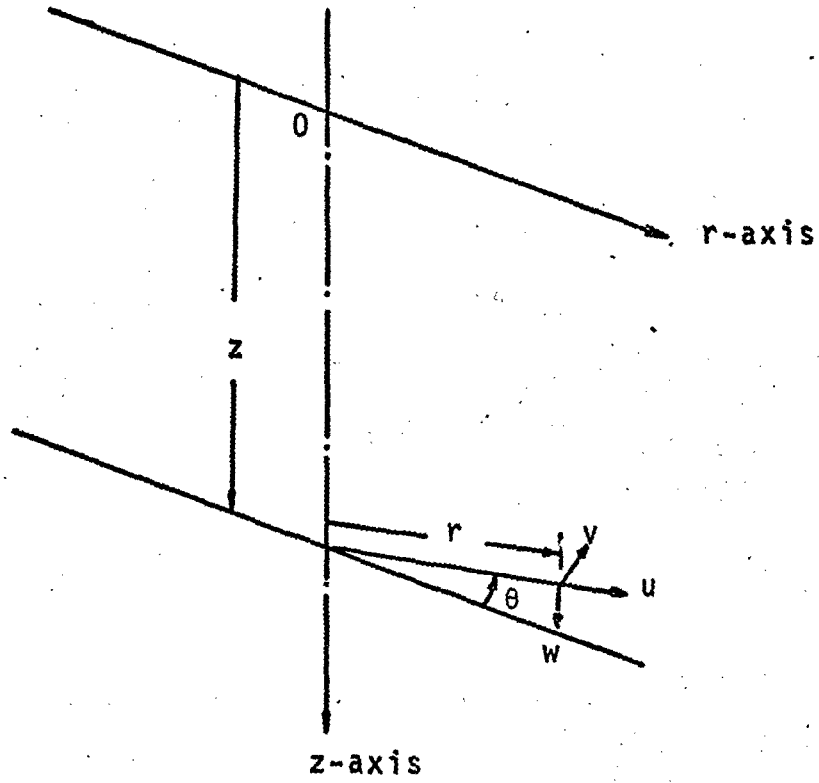
Figure 2.3   Coordinate System for Axially-Symmetric Flows

$$\rho\left[\frac{\partial u}{\partial t} + u\frac{\partial u}{\partial r} + \frac{v}{r}\frac{\partial u}{\partial \theta} - \frac{v^2}{r} + w\frac{\partial u}{\partial z}\right] = F_r - \frac{\partial p}{\partial r}$$

$$+ \mu\left[\frac{\partial^2 u}{\partial r^2} + \frac{1}{r}\frac{\partial u}{\partial r} - \frac{u}{r^2} + \frac{1}{r^2}\frac{\partial^2 u}{\partial \theta^2} - \frac{2}{r^2}\frac{\partial v}{\partial \theta} + \frac{\partial^2 u}{\partial z^2}\right] \quad , \quad (2\text{-}1)$$

$$\rho\left[\frac{\partial v}{\partial t} + u\frac{\partial v}{\partial r} + \frac{v}{r}\frac{\partial v}{\partial \theta} + \frac{uv}{r} + w\frac{\partial v}{\partial z}\right] = F_\theta - \frac{1}{r}\frac{\partial p}{\partial \theta}$$

$$+ \mu\left[\frac{\partial^2 v}{\partial r^2} + \frac{1}{r}\frac{\partial v}{\partial r} - \frac{v}{r^2} + \frac{1}{r^2}\frac{\partial^2 v}{\partial \theta^2} + \frac{2}{r^2}\frac{\partial u}{\partial \theta} + \frac{\partial^2 v}{\partial z^2}\right] \quad , \quad (2\text{-}2)$$

$$\rho\left[\frac{\partial w}{\partial t} + u\frac{\partial w}{\partial r} + \frac{v}{r}\frac{\partial v}{\partial \theta} + w\frac{\partial w}{\partial z}\right] = F_z - \frac{\partial p}{\partial z}$$

$$+ \mu\left[\frac{\partial^2 w}{\partial r^2} + \frac{1}{r}\frac{\partial w}{\partial r} + \frac{1}{r^2}\frac{\partial^2 w}{\partial \theta^2} + \frac{\partial^2 w}{\partial z^2}\right] \quad , \quad (2\text{-}3)$$

and the continuity equation is given by

$$\frac{\partial u}{\partial r} + \frac{u}{r} + \frac{1}{r}\frac{\partial v}{\partial \theta} + \frac{\partial w}{\partial z} = 0 \quad . \quad (2\text{-}4)$$

Essentially, two methods are employed in obtaining numerical solutions of the governing equations. In the first method, a steady state approach is used to find the solution of the flow field for low Reynolds numbers. At higher Reynolds numbers the steady state equations become unstable and are not applicable. Thus, a transient approach is adapted in obtaining the solutions for flow at higher Reynolds numbers.

2.1.1 Steady State Approach

Steady flow conditions are assumed throughout the sensor, and since the air velocities are small, the flow is assumed to be incompressible. The temperature of the air entering the sensor is considered constant and is taken to be the same as the environmental temperature. Throughout the sensor, laminar flow is assumed and the influence of body forces is neglected. Axial symmetry is also assumed and therefore the $\frac{\partial}{\partial \theta}(\ )$ term is set equal to zero.

Under these assumptions, Equations (2-1), (2-2), (2-3) and (2-4) reduce to

$$u\frac{\partial u}{\partial r} + w\frac{\partial u}{\partial z} - \frac{v^2}{r} = -\frac{1}{\rho}\frac{\partial p}{\partial r} + \nu\left[\frac{\partial^2 u}{\partial r^2} + \frac{1}{r}\frac{\partial u}{\partial r} - \frac{u}{r^2} + \frac{\partial^2 u}{\partial z^2}\right], \quad (2\text{-}5)$$

$$u\frac{\partial v}{\partial r} + w\frac{\partial v}{\partial z} + \frac{uv}{r} = \nu\left[\frac{\partial^2 v}{\partial r^2} + \frac{1}{r}\frac{\partial v}{\partial r} - \frac{v}{r^2} + \frac{\partial^2 v}{\partial z^2}\right], \quad (2\text{-}6)$$

$$u\frac{\partial w}{\partial r} + w\frac{\partial w}{\partial z} = -\frac{1}{\rho}\frac{\partial p}{\partial z} + \nu\left[\frac{\partial^2 w}{\partial r^2} + \frac{1}{r}\frac{\partial w}{\partial r} + \frac{\partial^2 w}{\partial z^2}\right], \quad (2\text{-}7)$$

$$\frac{\partial u}{\partial r} + \frac{u}{r} + \frac{\partial w}{\partial z} = 0 \quad . \quad (2\text{-}8)$$

Equations (2-5), (2-6) and (2-7) are then, respectively the radial, tangential and axial momentum equations for the flow in the sensor. The continuity equation, Equation (2-8), is eliminated by introduction of the stream function, $\bar{\psi}$, such that

$$u = \frac{1}{r}\frac{\partial\bar{\psi}}{\partial z} \quad\quad (2\text{-}9a)$$

and

$$w = -\frac{1}{r}\frac{\partial\bar{\psi}}{\partial r} \quad . \quad (2\text{-}9b)$$

Thus the velocity components u and w can be expressed in terms of $\bar{\psi}$.

The tangential vorticity is defined by

$$\bar{\eta} = \frac{\partial u}{\partial z} - \frac{\partial w}{\partial r} \quad . \tag{2-10}$$

A combination of Equations (2-9) and (2-10) results in

$$\bar{\eta} = \frac{1}{r} \frac{\partial^2 \bar{\psi}}{\partial r^2} - \frac{1}{r^2} \frac{\partial \bar{\psi}}{\partial r} + \frac{1}{r} \frac{\partial^2 \bar{\psi}}{\partial z^2} \quad . \tag{2-11}$$

Since vorticity and circulation are related, it seems desirable to express Equation (2-6) in terms of circulation. Equation (2-6) is first multiplied by r and then rearranged to give

$$u \frac{\partial}{\partial r}(rv) + w \frac{\partial}{\partial z}(rv) = \nu \left[r \frac{\partial}{\partial r}(\frac{\partial v}{\partial r} + \frac{v}{r}) + \frac{\partial^2}{\partial z^2}(rv) \right]. \tag{2-12}$$

Upon cross differentiation of Equations (2-5) and (2-7), followed by taking their difference, the pressure term is eliminated and the result is expressed as

$$u \frac{\partial \bar{\eta}}{\partial r} + w \frac{\partial \bar{\eta}}{\partial z} - \frac{u\bar{\eta}}{r} - \frac{2v}{r} \frac{\partial v}{\partial z} = \nu \left[\frac{\partial^2 \bar{\eta}}{\partial r^2} + \frac{1}{r} \frac{\partial \bar{\eta}}{\partial r} - \frac{\bar{\eta}}{r^2} + \frac{\partial^2 \bar{\eta}}{\partial z^2} \right]. \tag{2-13}$$

By employing the definition of circulation, $\bar{\Gamma} = v \cdot r$, Equations (2-12) and (2-13) are transformed to give

$$u \frac{\partial \bar{\Gamma}}{\partial r} + w \frac{\partial \bar{\Gamma}}{\partial z} = \nu \left[\frac{\partial^2 \bar{\Gamma}}{\partial r^2} - \frac{1}{r} \frac{\partial \bar{\Gamma}}{\partial r} + \frac{\partial^2 \bar{\Gamma}}{\partial z^2} \right] \quad , \tag{2-14}$$

$$u \frac{\partial \bar{\eta}}{\partial r} + w \frac{\partial \bar{\eta}}{\partial z} - \frac{u\bar{\eta}}{r} - \frac{2\bar{\Gamma}}{r^3} \frac{\partial \bar{\Gamma}}{\partial z} = \nu \left[\frac{\partial^2 \bar{\eta}}{\partial r^2} + \frac{1}{r} \frac{\partial \bar{\eta}}{\partial r} - \frac{\bar{\eta}}{r^2} + \frac{\partial^2 \bar{\eta}}{\partial z^2} \right]. \tag{2-15}$$

Equations (2-11), (2-14) and (2-15) now constitute the governing equations for flow through the sensor under steady state conditions.

2.1.2 Transient Approach

In a manner similar to that described above, the transient form of the governing equations are found to be

$$\frac{1}{r}\frac{\partial^2 \bar{\psi}}{\partial r^2} - \frac{1}{r^2}\frac{\partial \bar{\psi}}{\partial r} + \frac{1}{r}\frac{\partial^2 \bar{\psi}}{\partial z^2} = \eta \quad , \tag{2-16}$$

$$\frac{\partial \bar{\Gamma}}{\partial t} + u\frac{\partial \bar{\Gamma}}{\partial r} + w\frac{\partial \bar{\Gamma}}{\partial z} = \nu\left[\frac{\partial^2 \bar{\Gamma}}{\partial r^2} - \frac{1}{r}\frac{\partial \bar{\Gamma}}{\partial r} + \frac{\partial^2 \bar{\Gamma}}{\partial z^2}\right] \quad , \tag{2-17}$$

$$\frac{\partial \bar{\eta}}{\partial t} + u\frac{\partial \bar{\eta}}{\partial r} + w\frac{\partial \bar{\eta}}{\partial z} - \frac{u\bar{\eta}}{r} - \frac{2\bar{\Gamma}}{r^3}\frac{\partial \bar{\Gamma}}{\partial z} = \nu\left[\frac{\partial^2 \bar{\eta}}{\partial r^2} + \frac{1}{r}\frac{\partial \bar{\eta}}{\partial r}\right.$$

$$\left. - \frac{\bar{\eta}}{r^2} + \frac{\partial^2 \bar{\eta}}{\partial z^2}\right] \quad . \tag{2-18}$$

These equations, with appropriate initial and boundary conditions, are used to find solutions in the transient approach.

2.2 Initial and Boundary Conditions

Initial conditions are necessary for Equations (2-17) and (2-18). Upon considering the inertia of the fluid, the simple and physically realistic assumption for the initial condition is found to be that of a solid body rotation of the fluid. Thus the radial and axial velocities are assumed to be zero, and initial fluid shear stress is therefore neglected. Consequently, at t = 0

$$\bar{\Gamma}(r,z) = \omega r^2, \tag{2-19a}$$

$$\bar{\eta}(r,z) = 0 \quad . \tag{2-19b}$$

The boundary conditions valid for both the transient and steady state equations are the same, and are shown in Fig. (2.4).

Since the flow is symmetric with respect to the z-axis, it is only necessary to specify boundary conditions for half of the sensor. With the origin chosen as the center of the top plate of the vortex chamber the boundary conditions can be written as

(i) Sink tube and vortex chamber axis, $r = 0$, $0 \leq z \leq \ell$

$$\bar{\psi}(0,z) = \bar{\Gamma}(0,z) = \bar{\eta}(0,z) = u(0,z) = v(0,z) = 0, \tag{2.20a}$$

$$w(0,z) = - \left. \frac{\partial^2 \bar{\psi}}{\partial r^2} \right|_{r=0} . \tag{2-20b}$$

(ii) Top plate of vortex chamber, $z = 0$, $0 \leq r \leq r_0$

$$\bar{\psi}(r,0) = u(r,0) = w(r,0) = 0 \quad , \tag{2-21a}$$

$$v(r,0) = \omega r \, , \tag{2-21b}$$

$$\bar{\Gamma}(r,0) = \omega r^2, \tag{2-21c}$$

$$\bar{\eta}(r,0) = \frac{1}{r} \left. \frac{\partial^2 \bar{\psi}}{\partial z^2} \right|_{z=0} . \tag{2-21d}$$

(iii) Entrance to vortex chamber, $r = r_0$, $0 < z < h$

$$\bar{\psi}(r_0,z) = \frac{Q_0}{2\pi} \cdot \frac{z}{h} \, , \tag{2-22a}$$

$$u(r_0,z) = u_0 = \frac{Q_0}{2\pi h r_0} \, , \tag{2-22b}$$

$$v(r_0,z) = \omega r_0 \quad . \tag{2-22c}$$

$\bar{\psi} = 0$, $u = 0$, $v = r\omega$, $w = 0$, $\bar{\Gamma} = r^2\omega$

$\bar{n} = \frac{1}{r}\frac{\partial^2\bar{\psi}}{\partial z^2}\bigg|_{z=0}$

R-axis

$\bar{\psi} = \frac{Q_0}{2\pi}\frac{z}{h}$, $u = u_0 = \frac{Q_0}{2\pi r_0 h}$

$v = r_0\omega$, $w = 0$, $\bar{\Gamma} = r_0^2\omega$, $\bar{n} = 0$

$(r = r_0, z = h)$

$\bar{\psi} = \frac{Q_0}{2\pi}$

$u = 0$, $v = r\omega$,

$\bar{\Gamma} = r^2\omega$, $\bar{n} = \frac{1}{r}\frac{\partial^2\bar{\psi}}{\partial z^2}$, $w = 0$

$(r = r_1, z = h)$

$\bar{\psi} = \frac{Q_0}{2\pi}$, $u = 0$, $v = r_1\omega$

$w = 0$, $\bar{\Gamma} = r_1^2\omega$, $\bar{n} = \frac{1}{r_1}\frac{\partial^2\bar{\psi}}{\partial r^2}\bigg|_{r=r_1}$

$(r = r_1, z = \ell)$

$\frac{\partial\bar{\psi}}{\partial z} = 0$, $\frac{\partial\bar{n}}{\partial z} = 0$, $\frac{\partial\bar{\Gamma}}{\partial z} = 0$

$u = 0$, $\frac{\partial w}{\partial z} = 0$, $\frac{\partial v}{\partial z} = 0$

Z-axis

$\bar{\psi} = 0$, $u \neq 0$, $v = 0$

$w = -\frac{\partial^2\bar{\psi}}{\partial r^2}\bigg|_{r=0}$

$\bar{\Gamma} = 0$, $\bar{n} = 0$
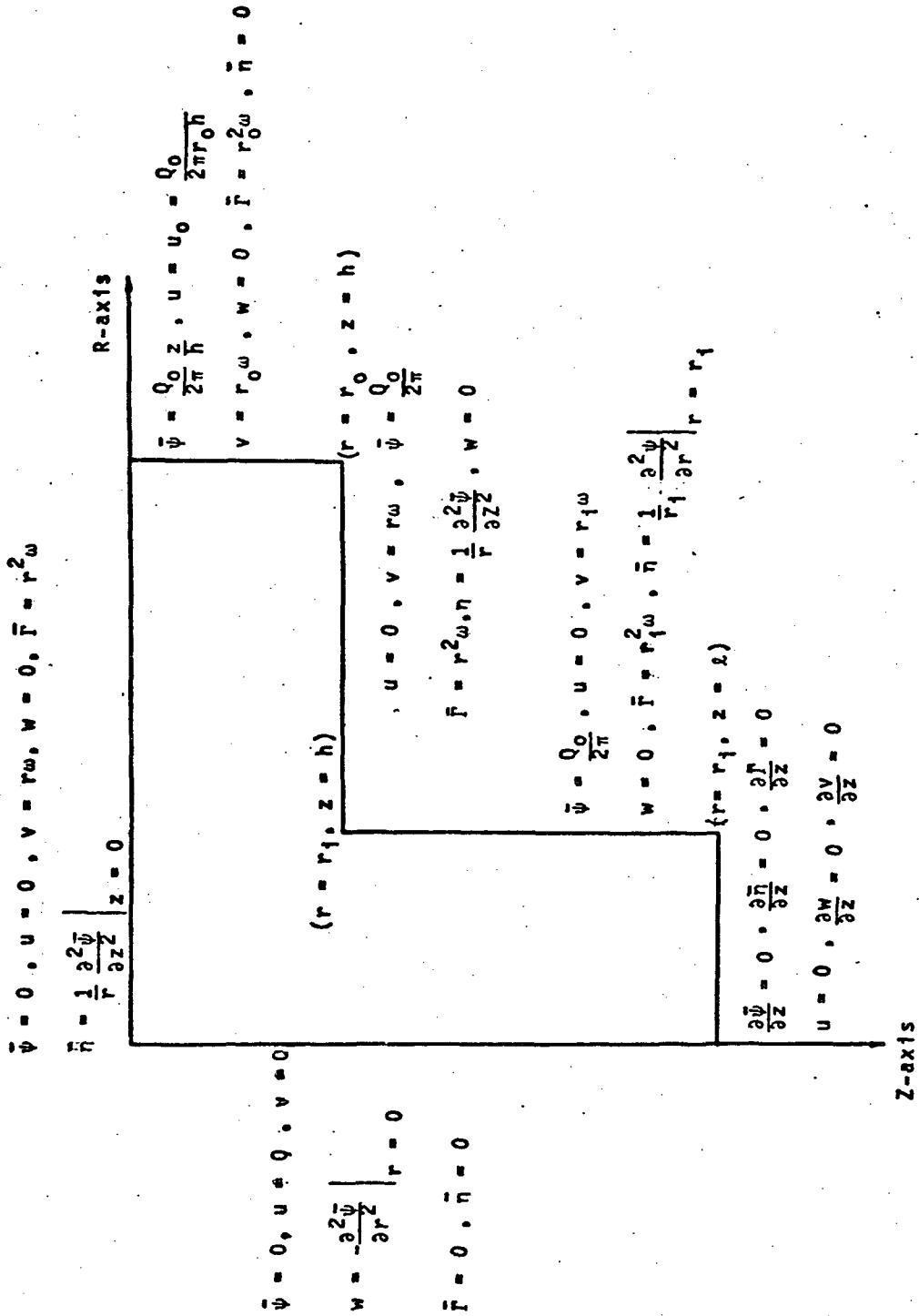
Figure 2.4   Boundary Conditions in Vortex Sink Rate Sensor

$$\bar{\Gamma}(r_0,z) = \omega r_0^2 \quad , \tag{2-22d}$$

$$w(r_0,z) = \bar{n}(r_0,z) = 0 \quad . \tag{2-22e}$$

(iv) Bottom plate of vortex chamber, $z = h$, $r_i \leq r \leq r_0$

$$\bar{\psi}(r,h) = \frac{Q_0}{2\pi} \quad , \tag{2-23a}$$

$$u(r,h) = w(r,h) = 0 \quad , \tag{2-23b}$$

$$v(r,h) = \omega r \quad , \tag{2-23c}$$

$$\bar{\Gamma}(r,h) = \omega r^2 \quad , \tag{2-23d}$$

$$\bar{n}(r,h) = \frac{1}{r} \left. \frac{\partial^2 \bar{\psi}}{\partial z^2} \right|_{z=h} \tag{2-23e}$$

(v) Sink tube wall, $r = r_i$, $h \leq z \leq \ell$

$$\bar{\psi}(r_i,z) = \frac{Q_0}{2\pi} \quad , \tag{2-24a}$$

$$u(r_i,z) = w(r_i,z) = 0 \quad , \tag{2-24b}$$

$$v(r_i,z) = \omega r_i \tag{2-24c}$$

$$\bar{\Gamma}(r_i,z) = \omega r_i^2 \quad , \tag{2-24d}$$

$$\bar{n}(r_i,z) = \frac{1}{r} \left. \frac{\partial^2 \bar{\psi}}{\partial r^2} \right|_{r=r_i} \quad . \tag{2-24e}$$

(vi) Sink tube exit, $z = \ell$, $0 \leq r \leq r_i$

$$\frac{\partial \bar{\psi}}{\partial z}(r,\ell) = \frac{\partial \bar{\Gamma}}{\partial z}(r,\ell) = \frac{\partial \bar{n}}{\partial z}(r,\ell) = 0 \tag{2-25a}$$

$$\frac{\partial v}{\partial z}(r,\ell) = \frac{\partial w}{\partial z}(r,\ell) = u(r,\ell) = 0 \tag{2-25b}$$

The justification of the above boundary conditions is given in Appendix A.

2.3 Nondimensional Form of the Governing Equations

The system of governing equations are made dimensionless by introducing the following nondimensional quantities.

Independent Variables,

$$R = \frac{r}{r_0} \; , \quad Z = \frac{z}{r_0}, \quad H = \frac{h}{r_0}, \quad R_i = \frac{r_i}{r_0}, \quad L = \frac{\ell}{r_0}, \quad T = t\omega. \quad (2\text{-}26)$$

Dependent Variables,

$$U = \frac{u}{\omega r_0} \; , \qquad \qquad \psi = \frac{\tilde{\psi}}{\omega r_0^{\,3}} \; ,$$

$$V = \frac{v}{\omega r_0} \; , \qquad \qquad \Gamma = \frac{\bar{\Gamma}}{\omega r_0^{\,2}} \; ,$$

$$W = \frac{w}{\omega r_0} \; , \qquad \qquad \eta = \bar{\eta}/\omega \; , \qquad \qquad (2\text{-}27)$$

$$N_{Re\text{-}\theta} = \frac{\omega r_0^{\,2}}{\nu} \; , \qquad \qquad N_{Ro} = \frac{Q_0}{2\pi\omega r_0^{\,3}} \; .$$

$$N_{Re\text{-}u} = \frac{Q_0}{2\pi h\nu} \; ,$$

Upon introducing Equations (2-26) and (2-27) into Equations (2-11), (2-14) and (2-15), the nondimensional form of the steady state equations are found to be

$$\frac{1}{R}\frac{\partial^2\psi}{\partial R^2} - \frac{1}{R^2}\frac{\partial\psi}{\partial R} + \frac{1}{R}\frac{\partial^2\psi}{\partial Z^2} = 0 \; , \qquad \qquad (2\text{-}28)$$

$$U\frac{\partial \Gamma}{\partial R} + W\frac{\partial \Gamma}{\partial Z} = \frac{1}{N_{Re-\theta}} \left[\frac{\partial^2 \Gamma}{\partial R^2} - \frac{1}{R}\frac{\partial \Gamma}{\partial R} + \frac{\partial^2 \Gamma}{\partial Z^2} \right] , \qquad (2\text{-}29)$$

$$U\frac{\partial \eta}{\partial R} + W\frac{\partial \eta}{\partial Z} - \frac{U\eta}{R} - \frac{2\Gamma}{R^3}\frac{\partial \Gamma}{\partial Z} = \frac{1}{N_{Re-\theta}} \left[\frac{\partial^2 \eta}{\partial R^2} + \frac{1}{R}\frac{\partial \eta}{\partial R} \right.$$

$$\left. - \frac{\eta}{R^2} + \frac{\partial^2 \eta}{\partial Z^2} \right] . \qquad (2\text{-}30)$$

Similarly Equations (2-16), (2-17) and (2-18) are transformed to give the dimensionless form of the transient equations as

$$\frac{1}{R}\frac{\partial^2 \psi}{\partial R^2} - \frac{1}{R^2}\frac{\partial \psi}{\partial R} + \frac{1}{R}\frac{\partial^2 \psi}{\partial Z^2} = \eta , \qquad (2\text{-}31)$$

$$\frac{\partial \Gamma}{\partial T} + U\frac{\partial \Gamma}{\partial R} + W\frac{\partial \Gamma}{\partial Z} = \frac{1}{N_{Re-\theta}} \left[\frac{\partial^2 \Gamma}{\partial R^2} - \frac{1}{R}\frac{\partial \Gamma}{\partial R} + \frac{\partial^2 \Gamma}{\partial Z^2} \right] , \qquad (2\text{-}32)$$

$$\frac{\partial \eta}{\partial T} + U\frac{\partial \eta}{\partial R} + W\frac{\partial \eta}{\partial Z} - \frac{U\eta}{R} - \frac{2\Gamma}{R^3}\frac{\partial \Gamma}{\partial Z} = \frac{1}{N_{Re-\theta}} \times$$

$$\left[\frac{\partial^2 \eta}{\partial R^2} + \frac{1}{R}\frac{\partial \eta}{\partial R} - \frac{\eta}{R^2} + \frac{\partial^2 \eta}{\partial Z^2} \right] . \qquad (2\text{-}33)$$

The dimensionless initial conditions for the transient equations are

for T = 0

$$\Gamma(R,Z) = R^2 , \qquad (2\text{-}34a)$$

$$\eta(R,Z) = 0 . \qquad (2\text{-}34b)$$

The dimensionless boundary conditions are shown in Fig. (2.5) and are written as

R-axis

$\psi = N_{Ro} \times \dfrac{Z}{H}$, $U = N_{Ro}/H$, $V = 1$

$W = 0$, $\Gamma = 1$, $\eta = 0$

$(R = 1, Z = H)$

$n = \dfrac{1}{R}\dfrac{\partial^2\psi}{\partial Z^2}\Big|_{Z=0}$

$\psi = 0$, $U = 0$, $V = R$, $W = 0$, $\Gamma = R^2$

$(R = R_1, Z = H)$

$\psi = N_{Ro}$, $U = 0$, $V = R$, $W = 0$

$\Gamma = R^2$, $n = \dfrac{1}{R}\dfrac{\partial^2\psi}{\partial Z^2}\Big|_{Z=h}$

$\psi = N_{Ro}$, $U = 0$, $V = R_1$, $W = 0$

$\Gamma = R_1^2$, $n = \dfrac{1}{R}\dfrac{\partial^2\psi}{\partial R^2}\Big|_{R1}$

$(R=R_1, Z=L)$

$\dfrac{\partial\Gamma}{\partial Z} = 0$, $\dfrac{\partial\eta}{\partial Z} = 0$

$U = 0$, $\dfrac{\partial W}{\partial Z} = 0$

$\dfrac{\partial\psi}{\partial Z} = 0$

$U = 0$

Z-axis

$\psi = 0$, $U = 0$, $V = 0$

$W = -\dfrac{\partial^2\psi}{\partial R^2}\Big|_{R=0}$

$\Gamma = 0$, $\eta = 0$
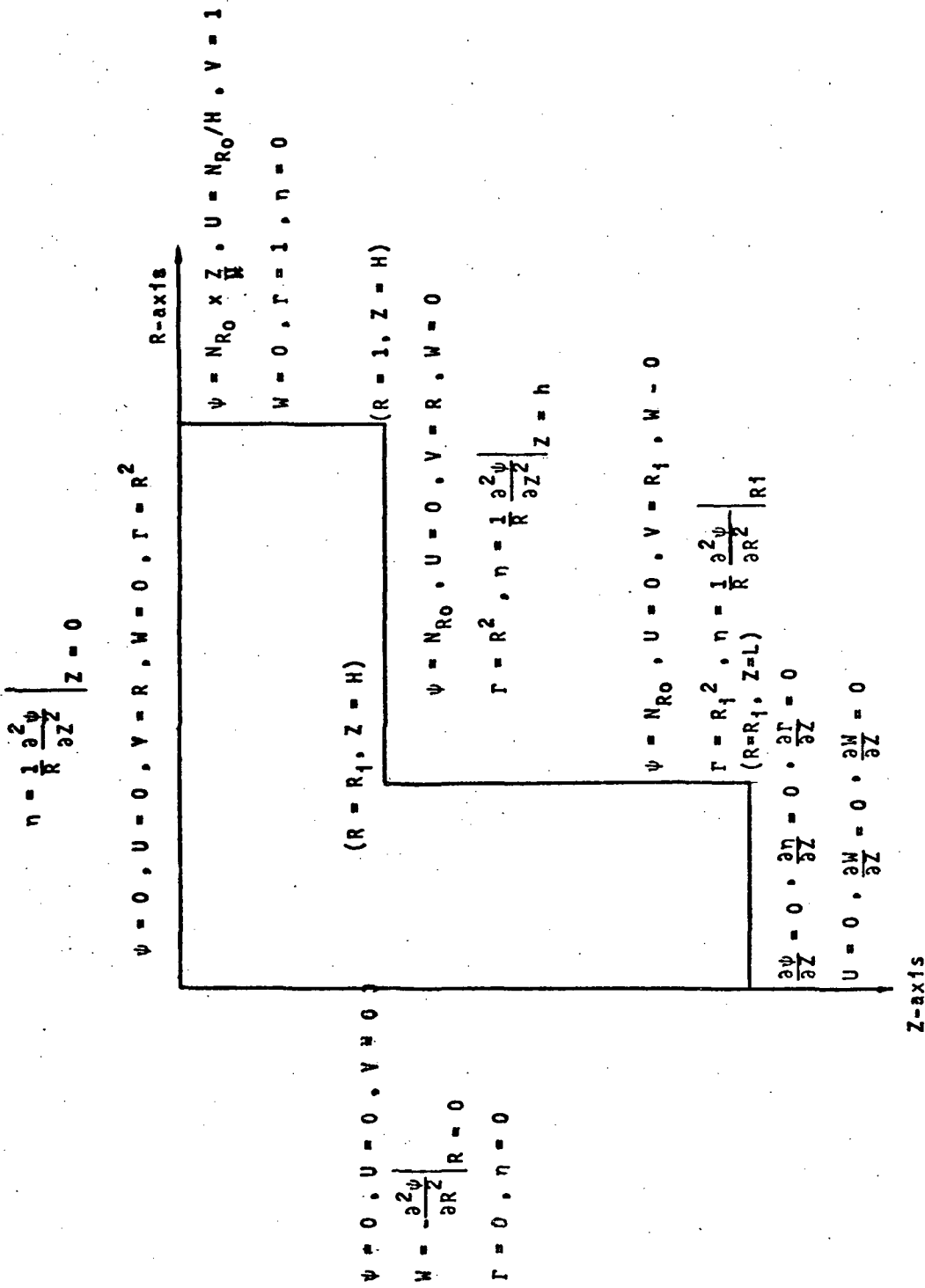
Figure 2.5   Dimensionless Boundary Conditions

(i) Sink tube and vortex chamber axis, $R = 0$, $0 \leq Z \leq L$

$$U(0,Z) = V(0,Z) = \Gamma(0,Z) = \eta(0,Z) = \psi(0,Z) = 0, \quad (2\text{-}35a)$$

$$W(0,Z) = -\left.\frac{\partial^2 \psi}{\partial R^2}\right|_{R=0} . \quad (2\text{-}35b)$$

(ii) Top plate of vortex chamber, $Z = 0$, $0 \leq R \leq 1$

$$U(R,0) = W(R,0) = \psi(R,0) = 0 , \quad (2\text{-}36a)$$

$$V(R,0) = R , \quad (2\text{-}36b)$$

$$\Gamma(R,0) = R^2, \quad (2\text{-}36c)$$

$$\eta(R,0) = \frac{1}{R} \left.\frac{\partial^2 \psi}{\partial Z^2}\right|_{Z=0} . \quad (2\text{-}36d)$$

(iii) Entrance to vortex chamber, $R = 1$, $0 < Z < H$

$$U(1,Z) = \frac{Q_o}{2\pi r_o^2 \omega h} = \frac{N_{Ro}}{H}, \quad (2\text{-}37a)$$

$$W(1,Z) = \eta(1,Z) = 0 , \quad (2\text{-}37b)$$

$$V(1,Z) = \Gamma(1,Z) = 1 , \quad (2\text{-}37c)$$

$$\psi(1,Z) = \frac{Q_o}{2\pi r_o^3 \omega} \cdot \frac{z}{h} = N_{Ro} \cdot \frac{Z}{H} . \quad (2\text{-}37d)$$

(iv) Bottom plate of vortex chamber, $Z = H$, $R_i \leq R \leq 1$

$$U(R,H) = W(R,H) = 0, \quad (2\text{-}38a)$$

$$\psi(R,H) = N_{Ro} , \quad (2\text{-}38b)$$

$$V(R,H) = R . \quad (2\text{-}38c)$$

$$\Gamma(R,H) = R^2 \tag{2-38d}$$

$$\eta(R,H) = \frac{1}{R} \left. \frac{\partial^2 \psi}{\partial Z^2} \right|_{Z = H} . \tag{2-38e}$$

(v) Sink tube wall, $R = R_{\dagger}$, $H \leq Z \leq L$

$$U(R_{\dagger},Z) = W(R_{\dagger},Z) = 0, \tag{2-39a}$$

$$\psi(R_{\dagger},Z) = N_{Ro} , \tag{2-39b}$$

$$V(R_{\dagger},Z) = R_{\dagger} , \tag{2-39c}$$

$$\Gamma(R_{\dagger},Z) = R^2_{\dagger} , \tag{2-39d}$$

$$\eta(R_{\dagger},Z) = \frac{1}{R_{\dagger}} \left. \frac{\partial^2 \psi}{\partial R^2} \right|_{R = R_{\dagger}} . \tag{2-39e}$$

(vi) Sink tube exit, $Z = L$, $0 \leq R \leq R_{\dagger}$

$$\frac{\partial \psi}{\partial Z}(R,L) = \frac{\partial \Gamma}{\partial Z}(R,L) = \frac{\partial \eta}{\partial Z}(R,L) = 0 , \tag{2-40a}$$

$$\frac{\partial V}{\partial Z}(R,L) = \frac{\partial W}{\partial Z}(R,L) = U(R,L) = 0 . \tag{2-40b}$$

These initial and boundary conditions are utilized in the numerical analysis of this investigation.

The systems of nondimensional governing equations, along with appropriate initial and boundary conditions, are then solved to obtain the stream function, circulation and the tangential vorticity in the vortex sink rate sensor.

III. FORMULATIONS FOR
NUMERICAL ANALYSIS

As mentioned in the introduction, it is necessary to approximate the governing equations by a finite difference scheme, so that calculations remain stable for all Reynolds numbers. A similar approach for viscous flows has been used by other investigators [8, 16, 45], and is discussed in the introduction. In references [48, 49] the finite difference technique was used to solve the non-linear equations for the flow within a vortex chamber. Both the implicit alternative direction (ADI) method and explicit finite difference methods were used in reference [48]. The agreement in results was found to be within one percent for the stream function and one and half percent for the radial velocity variation. The computer running time for the explicit method, however, was noted to be two orders of magnitude less than that for the ADI method. Consequently, for this study, the explicit method was selected to determine the flow pattern in the vortex sensor.

For stability purposes the central difference method is most suitable [34, 42, 45], and therefore it was used in the numerical analysis for this problem. The central differences are obtained by using a Taylor series expansion for each term in the differential equation.

As mentioned in Section (2.1), steady state and transient procedures were adopted for computational purposes. In the steady state approach, when the viscous equations are expressed

in a finite difference form, an iterative numerical scheme
is employed to obtain an approximate solution. In this
approach the procedure begins with an assumption of some
approximate flow pattern for a very low Reynolds number. The
numerical iteration technique is then used and continued,
until the finite difference equations are satisfied. This
ultimately leads to an acceptable flow pattern, for that
Reynolds number. This flow pattern then becomes the input
data at a slightly higher Reynolds number, and the procedure
is continued, until convergence is reached.

At the higher Reynolds numbers, these equations become un-
stable and thus a transient approach, rather than the steady
state approach, is used. In this approach a technique of
expressing the differential equations in a succession of
discrete steps is employed. As an initial input for
calculations at the higher Reynolds numbers, a known flow
pattern from the steady state approach is used. The iteration
is then continued until the results approach steady state
conditions. For subsequent higher Reynolds numbers the last
results are used as the input data and the procedure is con-
tinued.

3.1 Steady State Problem

By employing the central space difference technique,
Equations (2-28), (2-29) and (2-30) can be written in the
finite difference form as

$$\psi^*_{i,j} = \frac{1}{4} (\psi_{i+1,j} + \psi_{i-1,j} + \psi_{i,j+1} + \psi_{i,j-1})$$

$$- \frac{a}{8R} (2R^2 a\, n_{i,j} + \psi_{i+1,j} - \psi_{i-1,j}) \ , \qquad (3\text{-}1)$$

$$\Gamma^*_{i,j} = \frac{1}{4} (\Gamma_{i+1,j} + \Gamma_{i-1,j} + \Gamma_{i,j+1} + \Gamma_{i,j-1})$$

$$- \frac{N_{Re-\theta}}{16R} (\psi_{i,j+1} - \psi_{i,j-1} + \frac{2a}{N_{Re-\theta}}) (\Gamma_{i+1,j}$$

$$- \Gamma_{i-1,j}) - (\psi_{i+1,j} - \psi_{i-1,j}) (\Gamma_{i,j+1} - \Gamma_{i,j-1}) \ ,$$
$$(3\text{-}2)$$

$$n^*_{i,j} = \left[\frac{1}{4} (n_{i+1,j} + n_{i-1,j} + n_{i,j+1} + n_{i,j-1}) \right.$$

$$- \frac{N_{Re-\theta}}{16} \left\{ (\psi_{i,j+1} - \psi_{i,j-1} - \frac{2a}{N_{Re-\theta}}) (n_{i+1,j} \right.$$

$$\left. - n_{i-1,j}) - (\psi_{i+1,j} - \psi_{i-1,j}) (n_{i,j+1} - n_{i,j-1}) \right\}$$

$$\left. - \frac{4a}{R^2} \Gamma_{i,j} (\Gamma_{i,j+1} - \Gamma_{i,j-1}) \right] \Bigg/$$

$$\left[1 + \frac{a^2}{4R^2} + \frac{aN_{Re-\theta}}{8R^2} (\psi_{i,j-1} - \psi_{i,j+1}) \right] \ . \quad (3\text{-}3)$$

This procedure is employed to calculate the temporary values of ψ^*, Γ^* and n^*. In the above equations i and j denote the space point in R and Z direction respectively. For a given value of i and j, the space coordinates are represented by R = $(i-1)a$ and Z = $(j-1)a$, where a is the size of the grid spacing. The explanation of these difference equations is

given in Appendix B.

In the above equations, the non-superscripted dependent variables are assumed to have the superscript (n) whereas the asterisk is used to denote a temporary value such as $\Lambda^*_{i,j}$ respresenting the new iterate $\Lambda^{(n+1)}_{i,j}$ at that point. This new iterate is obtained from the temporary values and the preceding (old) iterate $\Lambda^{(n)}_{i,j}$ by the relaxation procedure as given by

$$\Lambda^{(n+1)}_{i,j} = (1 - \omega_\lambda) \Lambda^{(n)}_{i,j} + \omega_\lambda \Lambda^*_{i,j} \quad , \tag{3-4}$$

where $0 \leq \omega_\lambda \leq 1$.

3.2 Transient Problem

In the procedure used to solve the initial boundary value problem, governed by Equations (2-31), (2-32) and (2-33), the derivatives are approximated by finite differences in a manner similar to that used in the steady state problem. In this case, however, the central time difference as well as the central space difference techniques are used and result in the following equations.

$$\psi^{k+1}_{i,j} = \frac{1}{4} (\psi^k_{i+1,j} + \psi^k_{i-1,j} + \psi^k_{i,j+1} + \psi^k_{i,j-1})$$

$$- \frac{a}{8R} (2R^2 a\, n^k_{i,j} + \psi^k_{i+1,j} - \psi^k_{i-1,j}) \quad , \tag{3-5}$$

$$\Gamma_{i,j}^{k+1} = \left[\Gamma_{i,j}^{k-1} + \frac{\Delta T}{2a^2 R} \left\{ (\psi_{i+1,j}^k - \psi_{i-1,j}^k) \times \right. \right.$$

$$(\Gamma_{i,j+1}^k - \Gamma_{i,j-1}^k) - (\psi_{i,j+1}^k - \psi_{i,j-1}^k) \times$$

$$(\Gamma_{i+1,j}^k - \Gamma_{i-1,j}^k) + \frac{4R}{N_{Re-\theta}} (\Gamma_{i+1,j}^k + \Gamma_{i-1,j}^k$$

$$+ \Gamma_{i,j+1}^k + \Gamma_{i,j-1}^k - 2\Gamma_{i,j}^{k-1}) - \frac{2a}{N_{Re-\theta}} (\Gamma_{i+1,j}^k$$

$$\left. \left. - \Gamma_{i-1,j}^k) \right\} \right] \bigg/ \left[1 + \frac{4\Delta T}{a^2 N_{Re-\theta}} \right] , \qquad (3-6)$$

$$n_{i,j}^{k+1} = \left[n_{i,j}^{k-1} + \frac{\Delta T}{2Ra^2} \left\{ (\psi_{i+1,j}^k - \psi_{i-1,j}^k) (n_{i,j+1}^k \right. \right.$$

$$-n_{i,j-1}^k) - (\psi_{i,j+1}^k - \psi_{i,j-1}^k) (n_{i+1,j}^k - n_{i-1,j}^k)$$

$$+ \frac{2a}{R} n_{i,j}^k (\psi_{i,j+1}^k - \psi_{i,j-1}^k - \frac{2a}{N_{Re-\theta}}) + \frac{4a}{R^2} \Gamma_{i,j}^k \times$$

$$(\Gamma_{i,j+1}^k - \Gamma_{i,j-1}^k) + \frac{2a}{N_{Re-\theta}} (n_{i+1,j}^k - n_{i-1,j}^k)$$

$$+ \frac{4R}{N_{Re-\theta}} (n_{i+1,j}^k + n_{i-1,j}^k + n_{i,j+1}^k + n_{i,j-1}^k$$

$$\left. \left. - 2n_{i,j}^{k-1}) \right\} \right] \bigg/ \left[1 + \frac{4\Delta T}{N_{Re-\theta} a^2} \right] \qquad (3-7)$$

In the above equations, the subscripts i and j designate
the space point in the R and Z directions respectively, where-
as the superscript k denotes the time point. For given
values of i, j, k, the space and time coordinates are re-
presented by R = (i-1)a, Z = (i-1)a and T = KΔT, where a is
the size of the grid spacings and ΔT is the size of the time
step.

The method for obtaining these equations are similar
to that adapted by Fromm [16], Pao [42], and Macagno and
Hung [34]. The explanation of these equations is given in
Appendix B.

This procedure mandated considering numerical stability
in the selection of the time step size. The most stringent
restriction on the time step size, for the cases considered,
is suggested in reference [21], and is given by

$$\Delta T \leq \left[\frac{2}{N_{Re-\theta} \, (\Delta Z)^2} + (\frac{1}{1 + \frac{R}{2}} + \frac{1}{1 - R}) \, \frac{1}{N_{Re-\theta} \, (\Delta R)^2} \right.$$

$$\left. - \frac{\bar{U}}{\Delta R} - \frac{\bar{W}}{\Delta Z} \right]^{-1} \qquad . \tag{3-8}$$

In this equation, $\bar{U}$ and $\bar{W}$ are the average velocities for
the grid point under consideration. For the sake of con-
venience, ΔT, in most of the calculation, is taken to be
$(\Delta R/4\bar{U})$ in the present formulation.

3.3 Finite Difference Forms of the Boundary Conditions

The only boundary conditions that have to be expressed

in the finite difference form are those that involve a derivative. They, in turn, are the expressions for the tangential vorticities on the solid surfaces as well as for the axial velocity along the geometrical axis.

The tangential vorticities are calculated by use of the Taylor series expansion. By using B as a point on the plate or wall and A at one mesh distance away, the Taylor series expansion is expressed as

$$\psi_A = \psi_B + a\frac{\partial \psi}{\partial Z}\bigg|_B + \frac{a^2}{2}\frac{\partial^2 \psi}{\partial Z^2}\bigg|_B + O(a^3) \quad , \tag{3-9}$$

for vortex chamber plates. Upon neglecting the terms of order a^3 or higher order and by using the plate boundary conditions,

$$W = 0, \ U = 0, \ \frac{\partial \psi}{\partial Z} = 0 \ , \ \frac{\partial \psi}{\partial R} = 0 \ ,$$

the series expansion is reduced to

$$\frac{\partial^2 \psi}{\partial Z^2}\bigg|_B = \frac{2}{a^2}(\psi_A - \psi_B) \quad . \tag{3-10}$$

The expressions below for vorticities are found at $J = 1$ or $Z = 0$, and at $J = m$ or $Z = H$, by using Equation (3-10) in Equations (2-36d) and (2-38e).

$$\eta_{i,1} = \frac{1}{Ra^2}(\psi_{i,2} - \psi_{i,1}) \quad \text{for } 0 \le R \le 1 \tag{3-11}$$

$$\eta_{i,m} = \frac{2}{Ra^2}(\psi_{i,m-1} - \psi_{i,m}) \quad \text{for } R_i \le R \le 1. \tag{3-12}$$

A similar procedure is used for the sink tube wall boundary conditions and from Equation (2-35e) the vorticity is obtained

at i = nn or R = R$_i$ and is given by

$$\eta_{nn,j} = \frac{2}{R_i a^2} (\psi_{nn-1,j} - \psi_{i,m}) \quad \text{for } H \le Z \le L. \quad (3\text{-}13)$$

The tangential vorticities can also be obtained by employing the MAC method [62] where a phantom boundary point is used. The MAC method produces the same results as given above.

An alternate method for computing vorticities is the one suggested by Hung [23] which has the advantage of requiring only information at an adjacent point. Consistent with the above notations, the expressions for vorticities are found to be

$$\eta_B = \frac{3}{Ra^2} (\psi_A - \psi_B) - \frac{\eta_A}{2} .$$

Thus, the vorticity, at J = 1 or

$$\eta_{i,1} = \frac{3}{Ra^2} (\psi_{i,2} - \psi_{i,1}) - \frac{\eta_{i,2}}{2} , \quad \text{for } 0 \le R \le 1, \quad (3\text{-}14)$$

and at J = m or Z = H, as

$$\eta_{i,m} = \frac{3}{Ra^2} (\psi_{i,m-1} - \psi_{i,m}) - \frac{\eta_{i,m-1}}{2}, \quad \text{for } R_i < R \le 1. \quad (3\text{-}15)$$

Similarly along the sink tube wall, one finds at i = nn or R = R$_i$.

$$\eta_{nn,j} = \frac{3}{R_i a^2} (\psi_{nn-1,j} - \psi_{nn,j}) - \frac{\eta_{nn-1,j}}{2} , \quad H < Z \le L. \quad (3\text{-}16)$$

The boundary condition for the tangential vorticity at the corner junction of the sink tube and the vortex chamber is

determined by use of a method suggested by Roache [50]. He calculated the boundary conditions for the tangential vorticity at the corner by using both the upstream and downstream neighboring points for given values of stream function and vorticity. Thus the boundary condition can be represented by

at $i = nn$, $j = m$ or $R = R_f$, $Z = H$

$$\eta_{nn,m} = \frac{1}{2R_f a^2} (\psi_{nn-1,m} + \psi_{nn,m-1} - 2\psi_{nn,m}) , \qquad (3-17)$$

or

$$\eta_{nn,m} = \frac{3}{2R_f a^2} (\psi_{nn-1,m} + \psi_{nn,m-1} - 2\psi_{nn,m})$$

$$- \frac{1}{4} (\eta_{nn-1,m} + \eta_{nn,m-1}). \qquad (3-18)$$

The axial velocity boundary condition along the geometrical axis is given by

at $R = 0$

$$W(0,Z) = \lim_{R \to 0} \left(-\frac{1}{R} \frac{\partial \psi}{\partial R} \right)$$

$$= -\frac{\partial^2 \psi}{\partial R^2} \bigg|_{R = 0} \quad \text{for } 0 \le Z \le L.$$

By use of the forward difference technique, this can be written as ,

at $i = 1$ or $R = 0$,

$$W_{1,j} = \frac{1}{6a^2} (15\psi_{1,j} - 16\psi_{2,j} + \psi_{3,j}) , \qquad (3-19)$$

or

$$W_{1,j} = -\frac{1}{5a^2}(-\psi_{4,j} + 2\psi_{3,j} + 11\psi_{2,j} - 12\psi_{1,j}), \qquad (3\text{-}20)$$

where $0 \leq Z \leq L$.

In the sink tube at the downstream section, the dependent variables are assumed to be constant and parallel to the tube axis. Thus at the sink tube exit, the boundary conditions can be determined through use of a parabolic extrapolation. The relationship for boundary conditions employed here was developed by Hung [23]. Consequently, for this case (where $0 \leq R \leq R_t$) the boundary conditions can be written as at $j = mm$ or $Z = L$,

$$\psi_{i,mm} = \psi_{i,mm-4} - 2\psi_{i,mm-3} + 2\psi_{i,mm-1} . \qquad (3\text{-}21)$$

$$\Gamma_{i,mm} = \Gamma_{i,mm-4} - 2\Gamma_{i,mm-3} + 2\Gamma_{i,mm-1} , \qquad (3\text{-}22)$$

$$\eta_{i,mm} = \eta_{i,mm-4} - 2\eta_{i,mm-3} + 2\eta_{i,mm-1} , \qquad (3\text{-}23)$$

$$W_{i,mm} = W_{i,mm-4} - 2W_{i,mm-3} + 2W_{i,mm-1} . \qquad (3\text{-}24)$$

3.4 Iteration Technique

In the iteration procedure for this region, sweeps of the interior mesh points are made, in turn, for each of the dependent variables, ψ, Γ and η. This procedure is continued until

$$\left| \frac{\Lambda_{i,j}^{(n+1)} - \Lambda_{i,j}^{(n)}}{\max \Lambda_{i,j}^{(n+1)}} \right| \leq \varepsilon , \qquad (3\text{-}25)$$

where ε is the required tolerance.

To accomplish the sweeps as mentioned above, it becomes essential to adapt the following sequence of steps, which are also illustrated in Fig. (3.1).

1) Assign the initial values for ψ, Γ and η as
   $\psi = 0$, $\Gamma = R^2$, $\eta = 0$.

2) Assign the boundary conditions for ψ.

3) Solve the stream function Equation (3-1) by the relaxation method.

4) Solve the circulation Equation (3-2) by the relaxation method.

5) Calculate the boundary conditions for η.

6) Solve the tangential vorticity Equation (3-3) by the relaxation method.

7) Repeat procedure commencing with Step 3 through Step 6 until required tolerance is reached.

The sequence of numerical procedures described above is basically the same as that proposed by Pao [42], with the exception of the use of the relaxation technique. This technique is sufficiently discussed in Section (3.1).

Having obtained the solutions to the difference equations for ψ, Γ and η, the velocity components are calculated from the relations

```
                    ┌─────────────────────┐
                    │     READ DATA       /
                    └─────────────────────┘
                              │
                    ┌─────────────────────┐
                    │ INITIALIZE THE      │
                    │ VALUE ψ=0,η=0,      │
                    │      Γ=R²           │
                    └─────────────────────┘
                              │
          ┌───────────────────────────────────────┐
          │    GIVE BOUNDARY CONDITIONS OF ψ       │
          └───────────────────────────────────────┘
                              │
            ┌───────────────────────────────────┐
            │ SOLVE FOR ψ USING RELAXATION      │
            │ METHOD WITH 10 TO 40 ITERATIONS   │
            └───────────────────────────────────┘
                              │
            ┌───────────────────────────────────┐
            │   SOLVE FOR Γ USING RELAXATION    │
            │             METHOD                │
            └───────────────────────────────────┘
                              │
            ┌───────────────────────────────────┐
            │   CALCULATE B.C. OF η USING ψ      │
            └───────────────────────────────────┘
                              │
          ┌───────────────────────────────────────┐
          │  SOLVE FOR η USING RELAXATION METHOD   │
          └───────────────────────────────────────┘
                              │
```

$$\frac{|\Lambda_{old} - \Lambda_{new}|}{|Max\ \Lambda_{New}|} < \epsilon\ \ ?$$

NO

YES

```
                         ┌─────────┐
                         │   END   │
                         └─────────┘
```
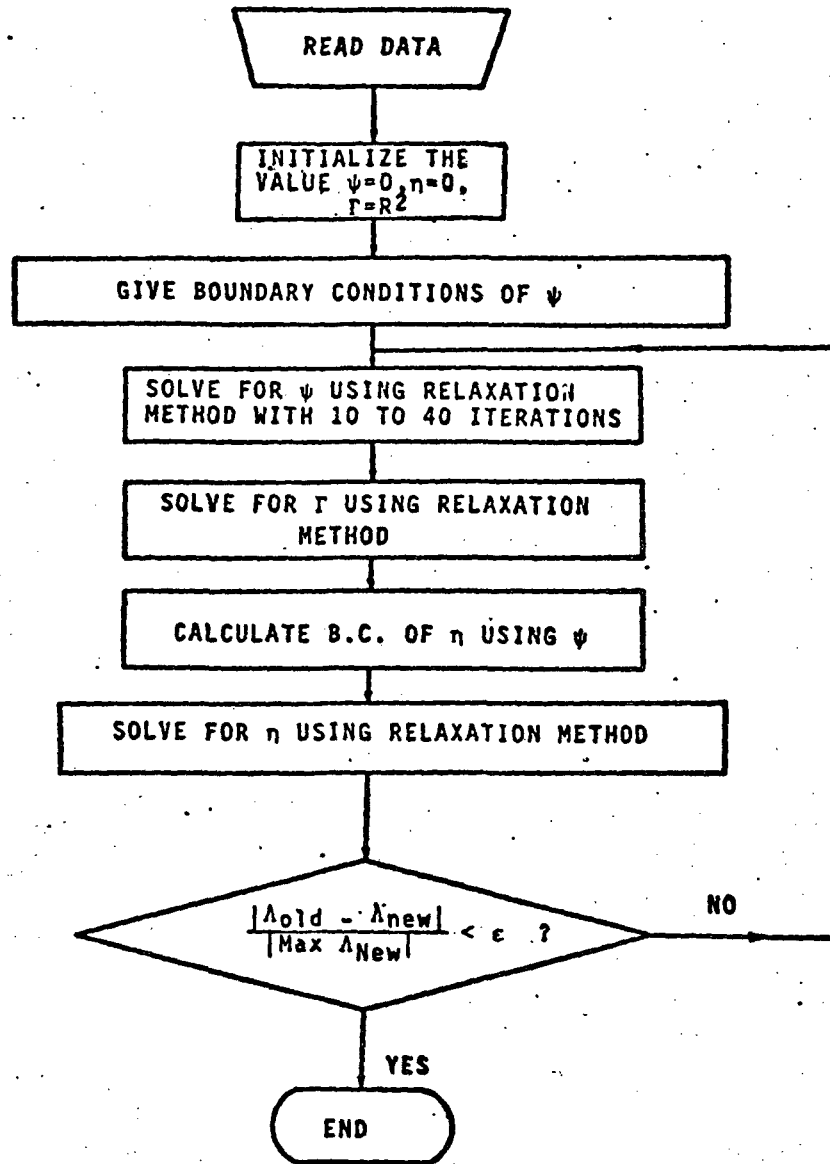
Figure 3.1   Simplified Computer Flow Diagram

$$U = \frac{1}{R} \frac{\partial \psi}{\partial Z} \quad , \tag{3-26a}$$

$$W = \frac{1}{R} \frac{\partial \psi}{\partial R} \quad , \tag{3-26b}$$

and

$$V = \frac{\Gamma}{R} \quad . \tag{3-26c}$$

These are then expressed in the difference form as

$$U_{i,j} = \frac{1}{2aR} \left(\psi_{i,j+1} - \psi_{i,j-1} \right) \quad . \tag{3-27}$$

$$W_{i,j} = - \frac{1}{2aR} \left(\psi_{i+1,j} - \psi_{i-1,j} \right) \quad . \tag{3-28}$$

and

$$V_{i,j} = \frac{\Gamma_{i,j}}{R} \quad . \tag{3-29}$$

where $R = (i-1)a$.

Through use of the numerical technique of Chapter III, numerical results are obtained. These results are discussed in Chapter IV and V.

IV. RESULTS OF THE NUMERICAL ANALYSIS

4.1 Stream Function

The symmetry of the sensor permits one to assign a value of zero to the streamline corresponding to its geometrical axis. On the top plate of the vortex chamber, the stream function is arbitrarily assigned the value of zero. Since N_{Ro} is the value of the stream function along $Z = H$ and $R = R_i$, it is taken to be the value on the bottom plate of the vortex chamber. At the entrance to the vortex chamber (i.e., at $R = 1$), the flow is assumed to be uniform and therefore the stream function is directly proportional to Z, and along the sink tube wall it is assigned the value N_{Ro}. On the downstream section of the sink tube, the streamlines are assumed to be parallel to the geometrical axis. With this information as input data, Equation (3-1) is solved numerically by following the procedure described in Section (3.4). The pattern of the streamlines in the sensor is shown in Fig. (4.1) and (4.2) for two different sets of values of the radial and tangential Reynolds numbers.

The variation of the stream function within the vortex chamber, in moving from the periphery to its center, is shown in Figs. (4.3) and (4.4). From Fig. (4.3), it is evident that the streamlines in the region $0 \leq Z \leq H$ contract in a manner similar to a vena contracta. This contraction is a different consequence of the boundary layer at the entrance to the region. The plots in Fig. (4.3) further reveal that the streamlines in the region $0.3 < R < 0.9$ are approximately .

45

AXIAL LENGTH, $Z = z/r_0$

RADIUS, $R = r/r_0$

$\psi = -0.0002$
-0.0004
-0.0006
-0.0008
-0.0010
-0.0012
-0.0014

AXIAL LENGTH, $Z = z/r_0$

RADIUS, $R = r/r_0$
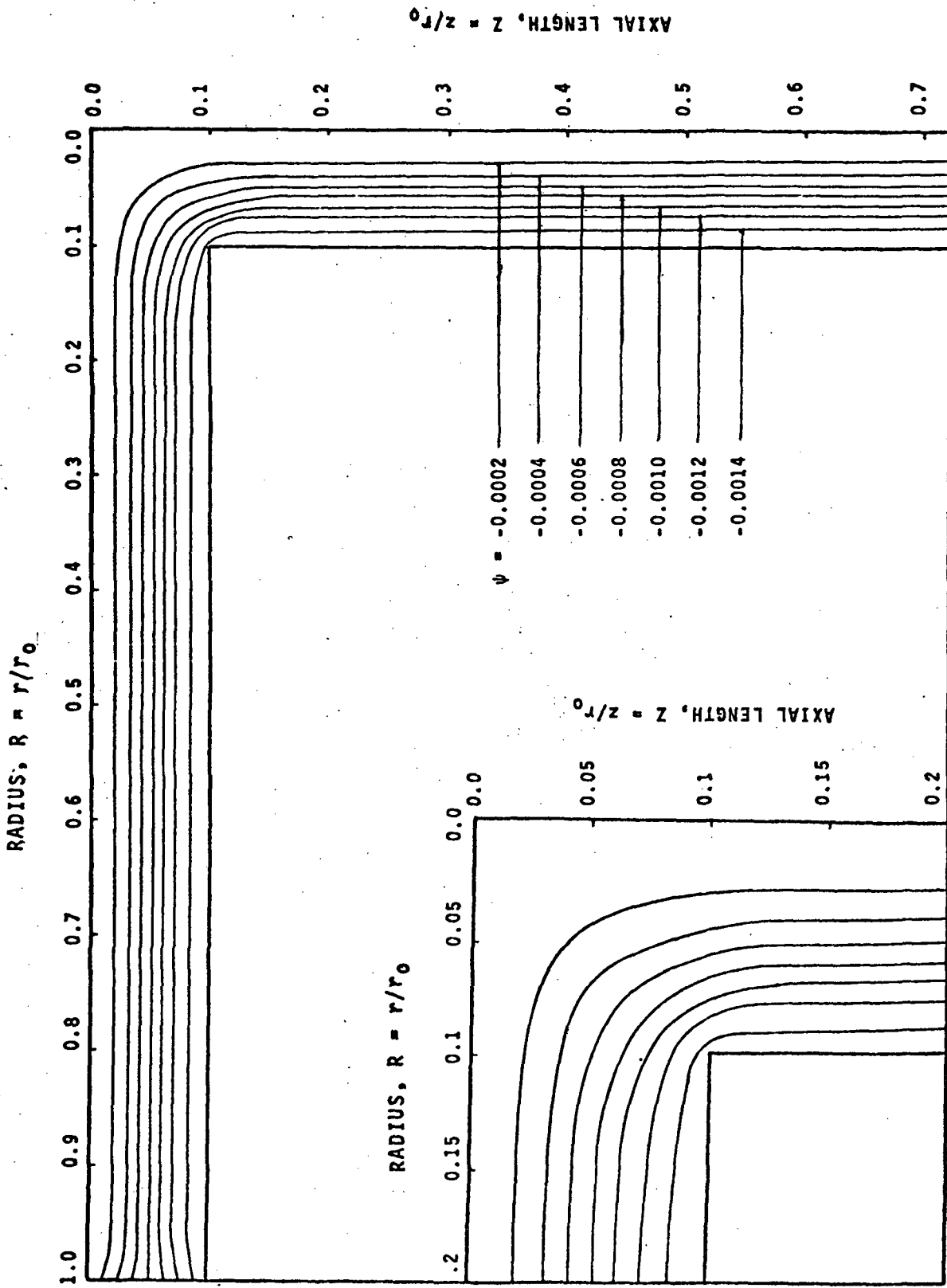
Figure 4.1   Constant Streamline Pattern (for $N_{Re-u} = 8$ and $N_{Re-\theta} = 512$)

AXIAL LENGTH, $Z = z/r_0$

RADIUS, $R = r/r_0$

$\psi = -0.024$

-0.021

-0.015

-0.012

-0.006

-0.003

Figure 4.2   Constant Streamline Pattern (for $N_{Re-u} = 4$ and $N_{Re-\theta} = 16$)

Figure 4.3 Variation of Stream Function, ψ, with Radius, R, at Different Z (for $N_{Re-u} = 8$ and $N_{Re-\theta} = 512$)
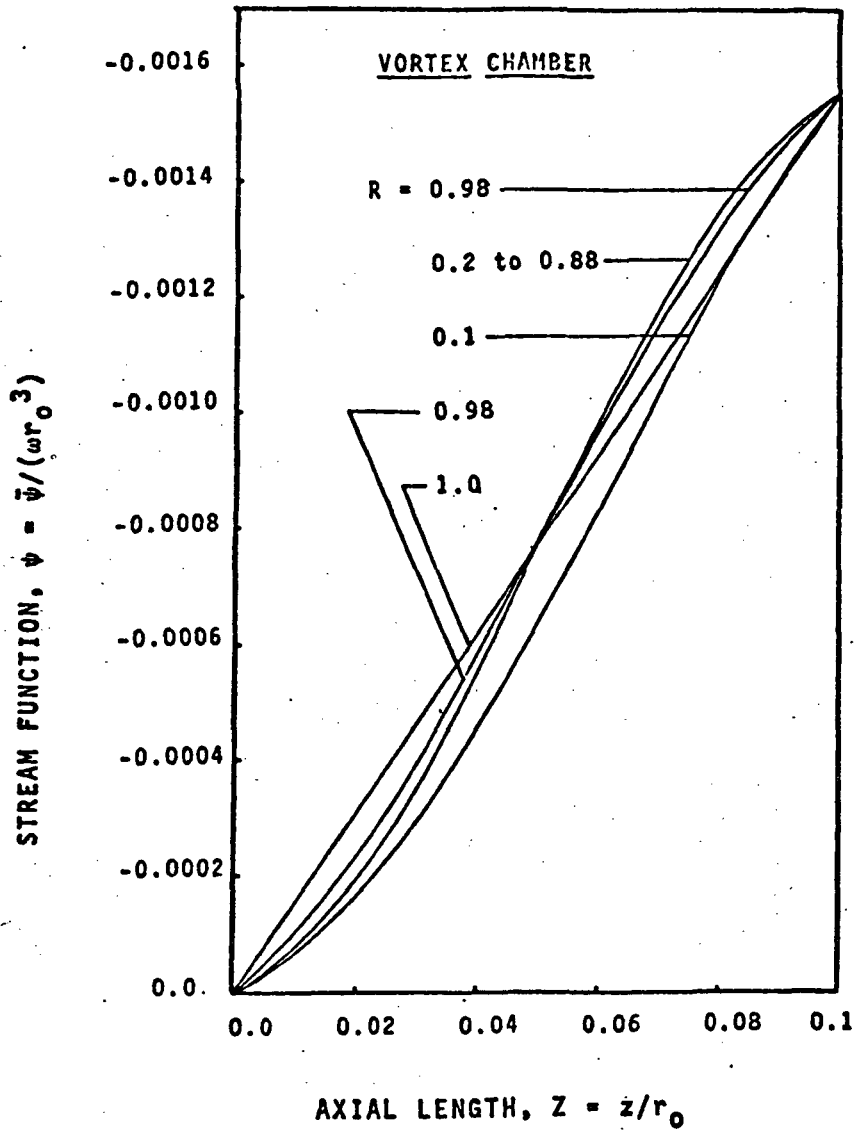
Figure 4.4   Variation of Stream Function, ψ, with Axial Length, Z, at Different R (for $N_{Re-u} = 8$ and $N_{Re-\theta} = 512$)

parallel to the plates. This indicates that in this region, the variation in the boundary layer thickness is negligible. The existence of the sink at the center of the bottom plate produces considerable streamline movement toward the sink for R values less than 0.2. In Fig. (4.4) the same results for stream function are plotted as a function of axial length with R being the parameter.

The effect of the rotational speeds on the flow pattern within the vortex chamber was investigated under various flow conditions. As the tangential Reynolds number, $N_{Re-\theta}$, was increased from 1 to 512, the numerical results revealed no appreciable effect on the flow pattern. The results further indicated that for $R \leq 0.2$ the streamlines moved toward the top plate, as the tangential Reynolds number was increased. However, this movement was so small, that it was very difficult to illustrate this effect on any figure. This slight effect could be due to the increase in centrifugal force resulting from the increase in rotation.

As the tangential Reynolds number is increased and reaches a value in excess of 2000, the streamline pattern within the vortex chamber changes from that observed at lower Reynolds numbers. This pattern is shown in Fig. (4.5). In the region $0.14 \leq R \leq 0.9$, the streamlines, above Z = 0.4H and below Z = 0.6H, move toward the plates. The boundary layer thickness at these Reynolds numbers is much thinner than at lower Reynolds numbers. This pattern indicates that the flow is no longer laminar but becomes turbulent. For values of $Z \geq 0.6H$, in the vicinity of the sink (i.e., at the geometrical axis),
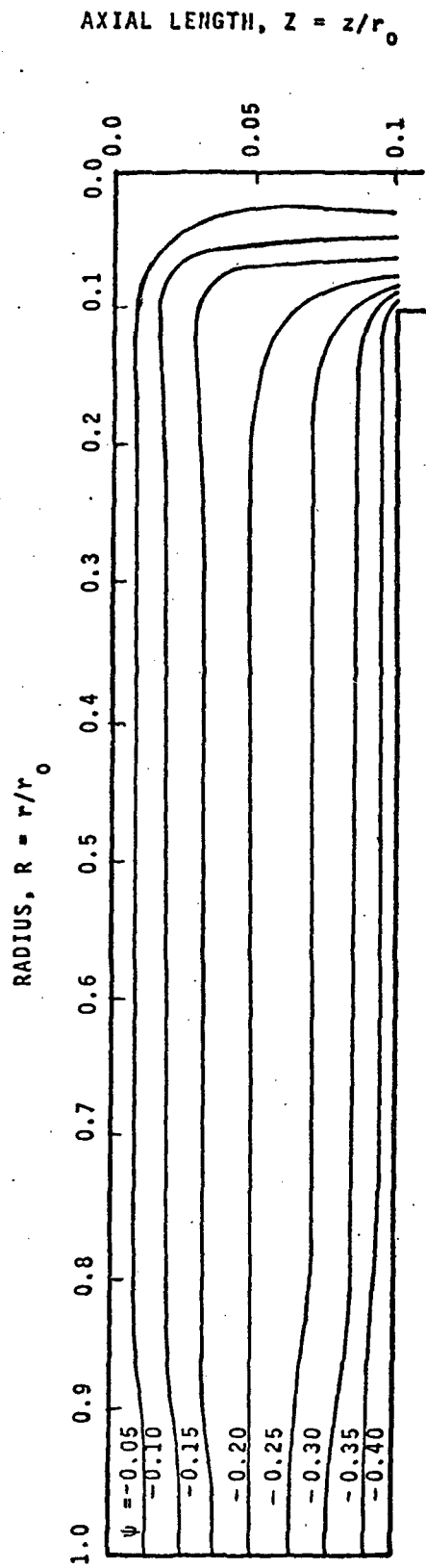
Figure 4.5   Constant Streamline Pattern, (for $N_{Re-u} = 8$ and $N_{Re-\theta} = 2048$)

the flow appears outward rather than inward.

The flow pattern within the sensor is indeed affected as the rate of flow is increased. The numerical results as shown in Figs. (4.6) and (4.2) indicate that the boundary layer thickness decreases as the flow increases. As a consequence of this condition the streamlines appear to move toward the plates as well as closer to the sink tube wall.

As shown in Figs. (4.7) and (4.8), the discharge from the vortex chamber into the sink tube results in smooth continuous streamlines of appreciable curvature. For a short distance into the sink tube the streamlines remain close to the geometric axis. This is due to the conservation of the radial momentum. However, farther into the sink tube, the streamlines are somewhat removed from the geometric axis. This shift is not appreciable. This effect is probably a result of stability conditions becoming evident in the flow. The streamlines ultimately become parallel to the geometric axis. In the immediate vicinity of the geometric axis, a core region (i.e., a region with no streamlines) is observed. The core region is a consequence of the centrifugal forces tending to move fluid away from the geometric axis.

4.2 Tangential Velocity

The dimensionless tangential velocity is defined as the ratio of actual tangential velocity to the tangential velocity at the entrance (i.e., at R = 1). Thus the dimensionless tangential velocity at the entrance to the vortex chamber is assigned the value one. On the top and bottom plates, where.

AXIAL LENGTH Z = z/r_0

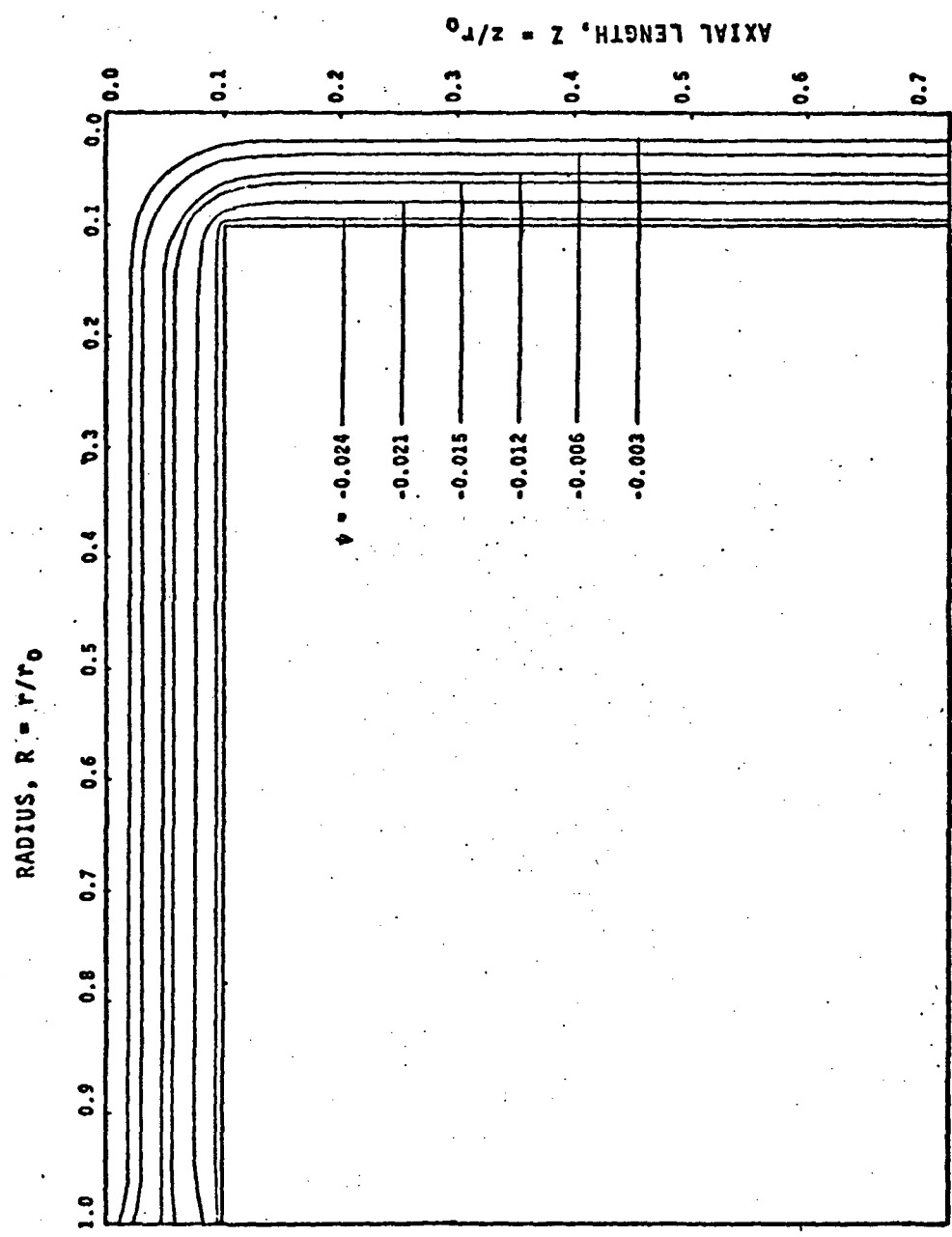RADIUS, R = r/r_0

ψ = -0.01
-0.02
-.0.04
-0.06
-0.08
-0.09
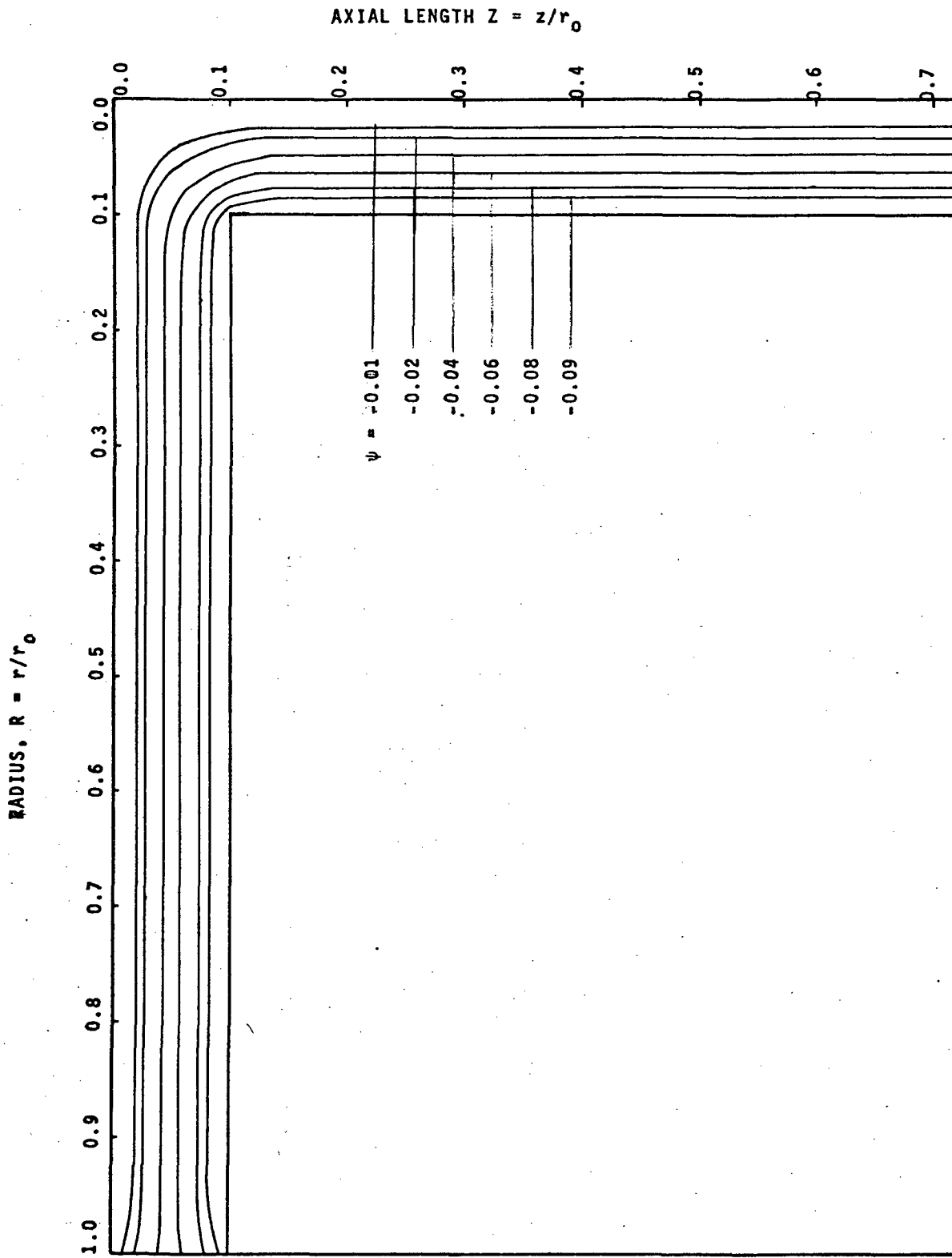
Figure 4.6 Constant Streamline Pattern (for $N_{Re-u} = 1$ and $N_{Re-\theta} = 1$)
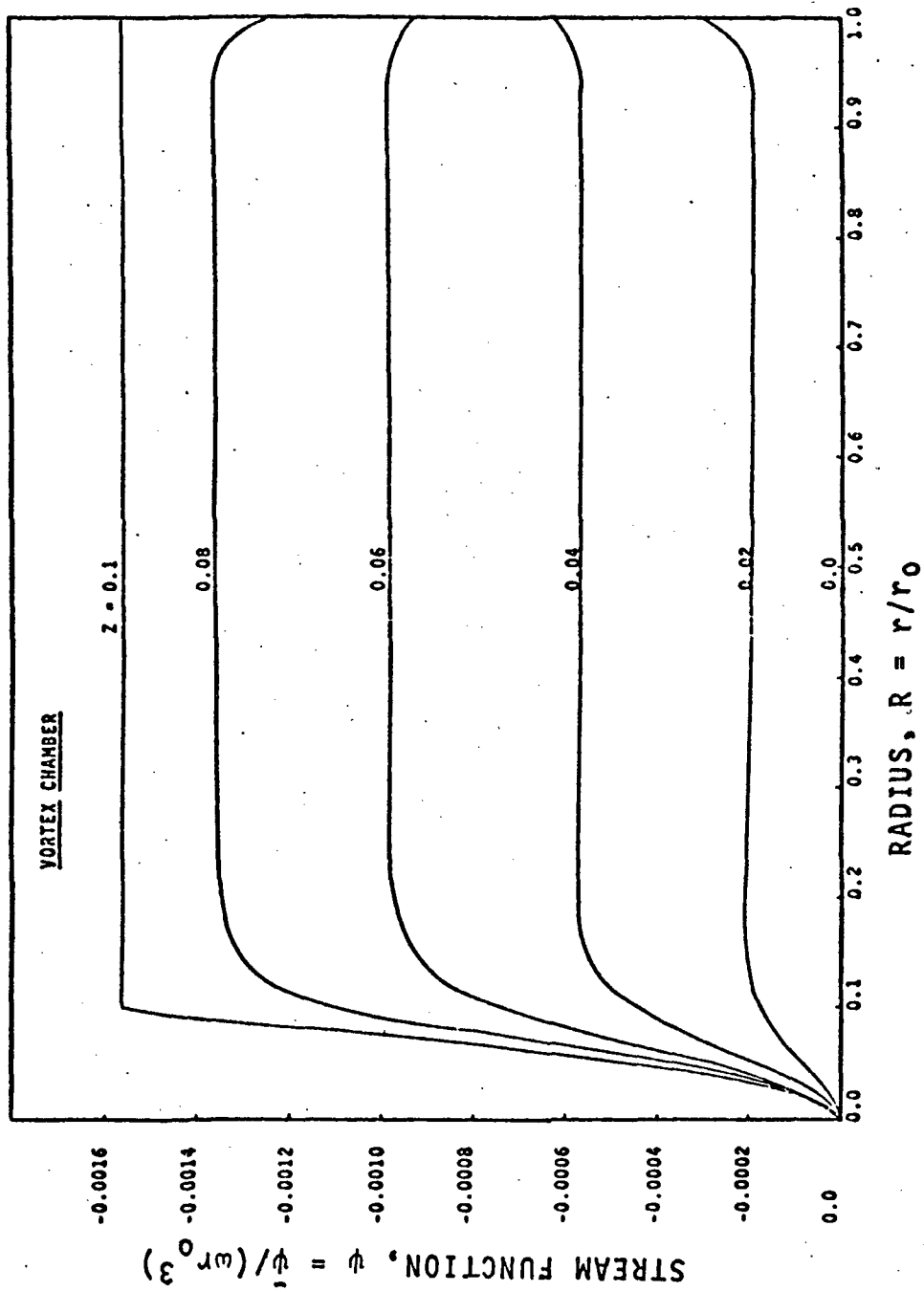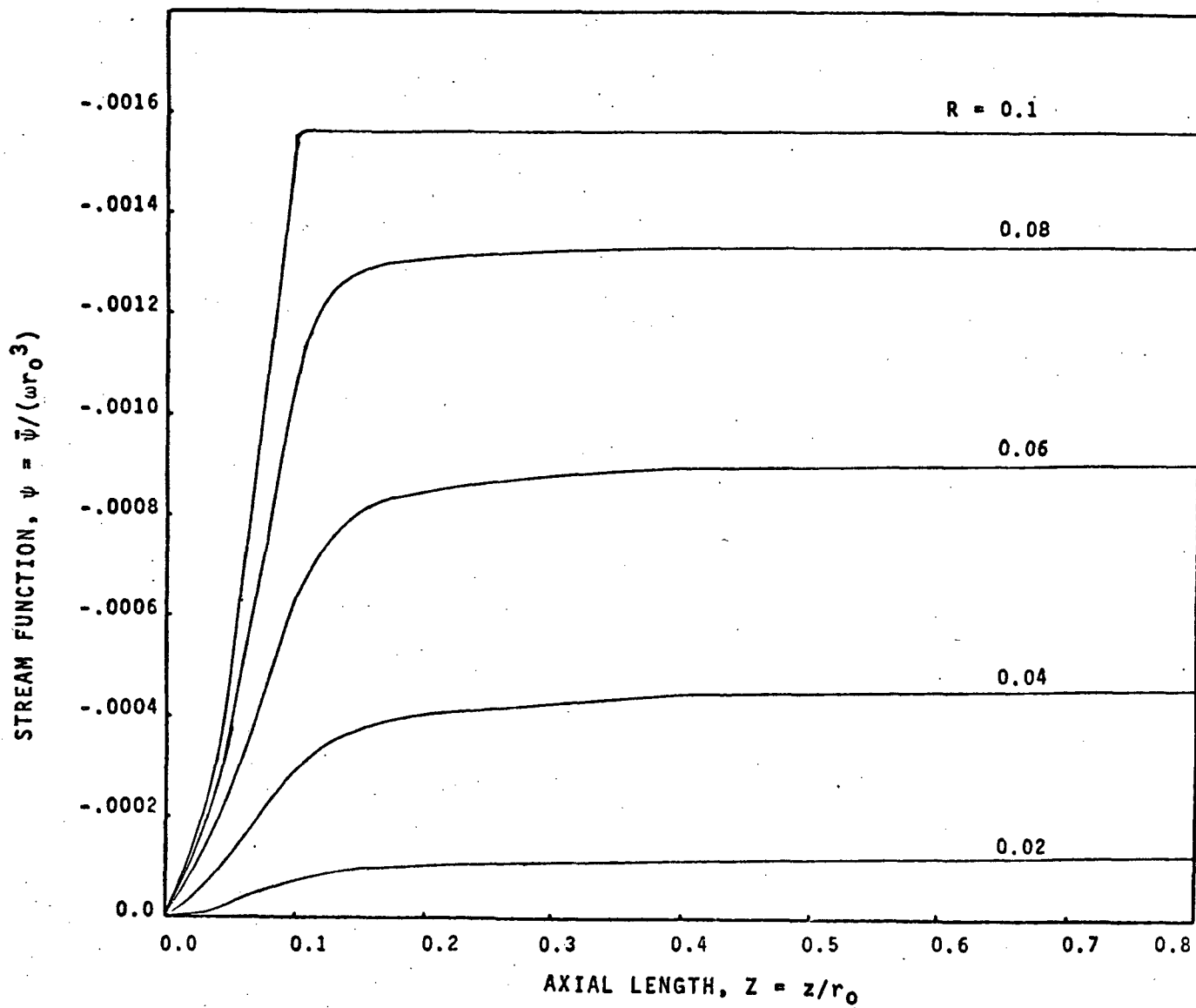
Figure 4.7   Variation of Stream Function, ψ, with Axial Length, Z, at Different R (for $N_{Re-u} = 8$ and $N_{Re-\theta} = 512$)
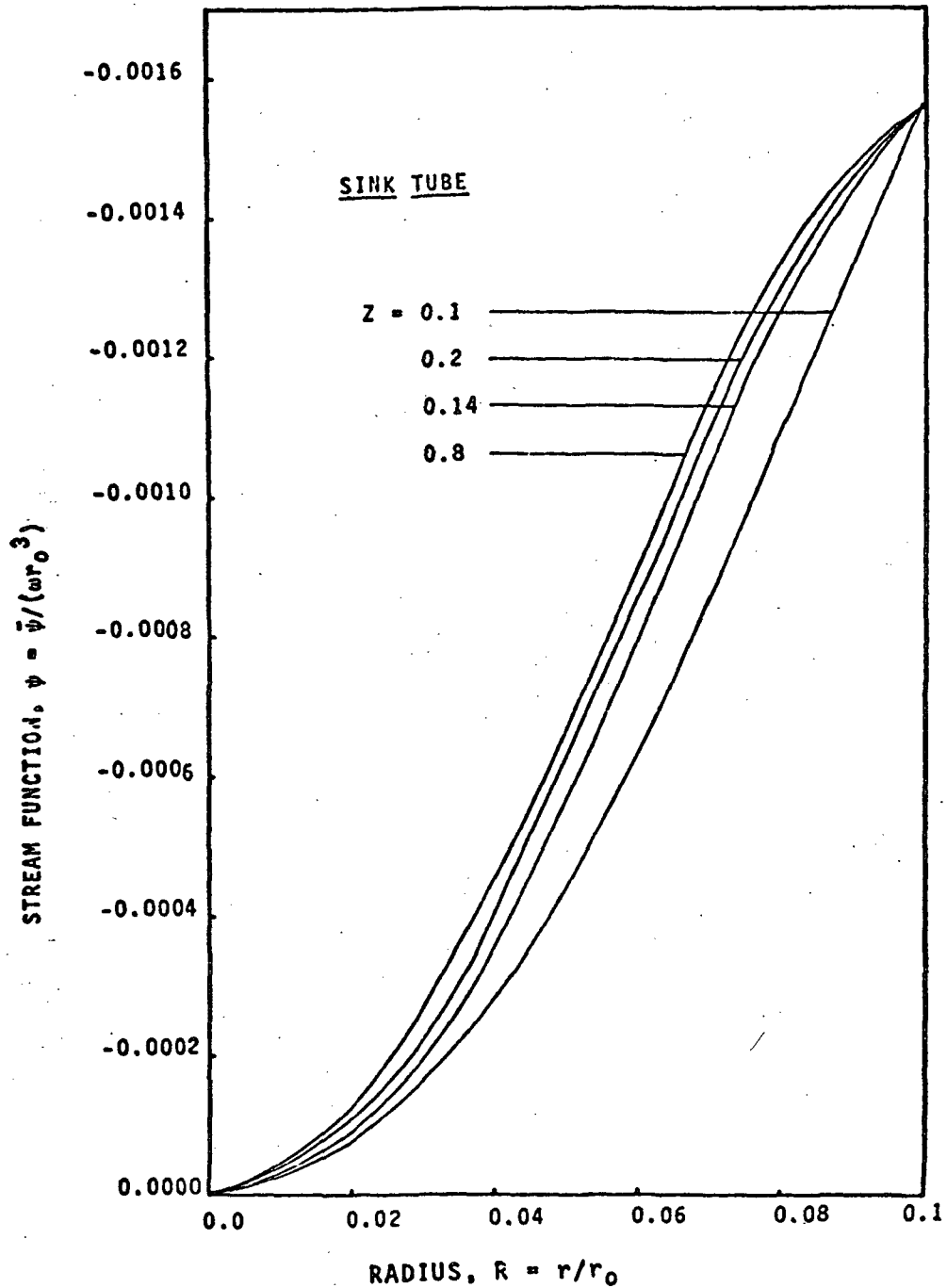
Figure 4.8   Variation of Stream Function, ψ, with Radius, R, at Different, Z, (for $N_{Re-u}=8$ and $N_{Re-\theta} = 512$)

solid body rotation exists, the velocity is assumed to have
a linear relation with the radius R, i.e., $V \propto R$. Along the
sink tube wall this velocity is assumed to be a constant.
With this as input data, the tangential velocity, at any
location in the sensor is obtained from Equation (3-20) by
following the procedure discussed in Section (3.4).

The variation in the tangential velocity in the vortex
chamber is shown in Figs. (4.9) and (4.10). It is noted that
for low radial Reynolds numbers, (N_{Re-u}) and for values of
R > 0.2, there is no appreciable change in the tangential
velocity. The velocity in the interior region however is
seen to be consistently higher than at the plates. As shown
in Fig. (4.10), the velocity profile, parallel to the Z-axis,
is found to be parabolic. It should also be noted that the
velocity reaches a maximum in the plane midway between the
plates. In general, the parabolic velocity profile is seen to
increase in size as the radius R decreases and is found to
reach a maximum value near R approximately equal to 0.1. This
is due to the conservation of an angular momentum combined with
the fluid viscosity effect near the plates. Along the geo-
metrical axis (i.e., at R = 0), the tangential velocity is zero
for all values of Z.

The effect of the tangential Reynolds numbers on the tan-
gential velocity is shown in Figs. (4.11), (4.12) and (4.13).
As $N_{Re-\theta}$ is increased from the value 1 to 16, the tangential
velocity in the vicinity of the sink tube entrance increases
in almost a linear manner, as noted in Fig. (4.11). This in-
dicates that the velocity V is approximately constant. This is

Figure 4.9   Variation of Tangential Velocity, V, with Radius, R, at Different Z (for N_{Re-u} = 8 and $N_{Re-\theta}$ = 512)
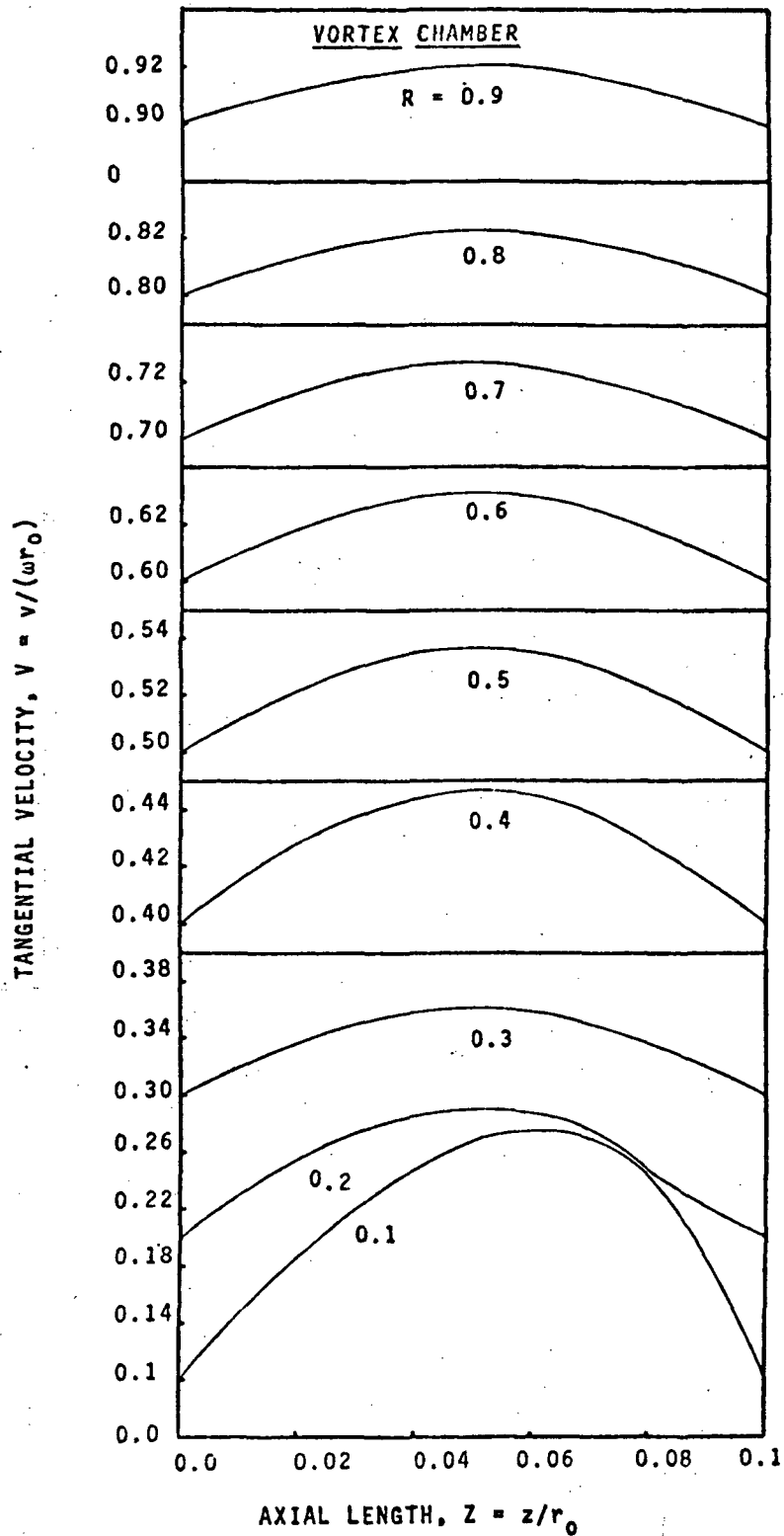
Figure 4.10 Variation of Tangential Velocity, V, with Axial Length, Z, at Different R (for N_{Re-u} = 8 and $N_{Re-\theta}$ = 512)

Figure 4.11   Variation of Tangential Velocity, V, with Axial Length
Z at Different R (for Different $N_{Re-\theta}$ and N_{Re-u} = 4)

Figure 4.12 Variation of Tangential Velocity, V, with Radius, R, at Entrance to the Sink Tube (for $N_{Re-u} = 8$)

Figure 4.13   Variation of Tangential Velocity,
                v, with Radius R, at Z = 0.06
                (for N_{Ra-u} = 8 and $N_{Re-\theta}$ = 16 to
                2048 N_{Ra-u} = 8 and $N_{Re-\theta}$ = 16 to

particularly true for low $N_{Re-\theta}$, as the flow behavior is linear. Also it is noted that the characteristic curve of R = 0.08 has very high tangential velocity near the sink region. But as the flow progresses into the sink tube, due to the sink tube wall, the velocity reduces rapidly and in the downstream section of the sink tube velocity profile is proportional to the radius. Thus such profile is obtained, (crossing two times of profiles of R = 0.06 and R = 0.04).

At a $N_{Re-\theta}$ = 16, the velocity reaches its peak value. As $N_{Re-\theta}$ is further increased to a value of 512, Fig. (4.12), the velocity decreases continuously. For the range of $N_{Re-\theta}$ values from 16 to 512, the maximum decrease in tangential velocity is only 3 percent. However, as $N_{Re-\theta}$ is further increased beyond the value of 512 this rate of decrement of maximum value increases. The decrease continues, and as $N_{Re-\theta}$ reaches a value of 2048, the decrease in the velocity is approximately 25 percent of that at $N_{Re-\theta}$ = 16. This pattern reflects the fact that the flow at the higher $N_{Re-\theta}$, is behaving much like that of a solid body rotation.

As shown in Fig. (4.14), the presence of the sink has an appreciable effect on the tangential velocity profile in the vortex chamber and becomes apparent for R < 0.2. Thus, in the presence of the sink, the rate of tangential velocity increase appears greater in the vicinity of the sink than at other regions. This results in a velocity profile distortion and bending towards the sink entrance.

The magnitude of tangential velocities in the sink region, on the discharge side of the vortex chamber, is higher than
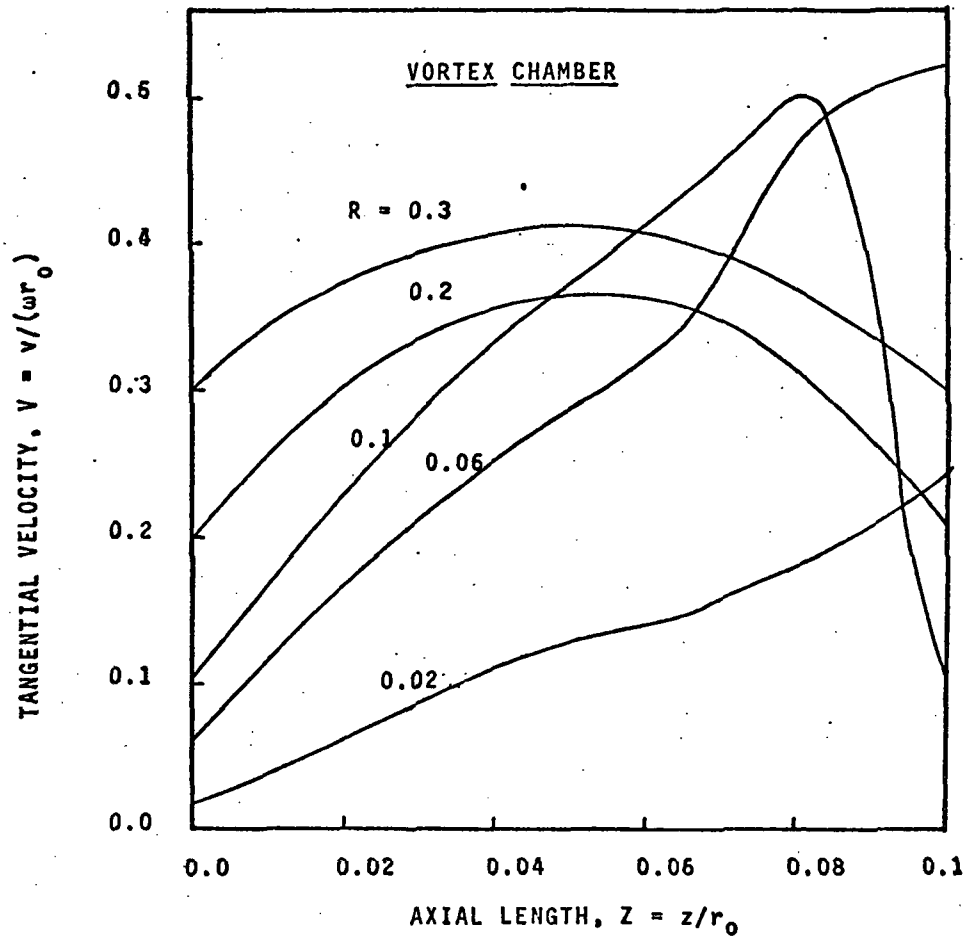
Figure 4.14 Variation of Tangential Velocity, V, with Axial Length, Z at Different R (for N_{Re-u}=32 and $N_{Re-\theta}$=32)

those near the other plate. The presence of the sink opening produces a greater momentum on the sink tube side and accounts for the above result.

The effect of the radial Reynolds numbers, N_{Re-u}, on the tangential velocity within the vortex chamber is illustrated in Figs. (4.15) and (4.16). In the vortex chamber, as the flow is increased (i.e., for higher value of N_{Re-u}), a rapid increase in tangential velocity is observed for $R \leq 0.2$. At low N_{Re-u} and for $R \geq 0.2$, however, the increase of this velocity is not appreciable. In this case, the tangential velocity is observed to be only slightly higher than the values at the wall (i.e., the flow is approximately that of the solid body rotation). As shown in Fig. (4.17) at higher value of N_{Re-u}, the circulation (or angular momentum) is conserved at the midplane of the vortex chamber. Everywhere, in the region, the tangential velocity is higher than its inlet value for $R \geq 0.1$. Also due to the higher radial and tangential Reynolds numbers, the instability in the flow is observed in the sink region, therefore a wavy profile of the tangential velocity is obtained.

As shown in Fig. (4.16), in the vicinity of the sink tube entrance, the tangential velocity shows a rapid increase as N_{Re-u} values are increased. Approximately a one hundred percent increase in tangential velocity is noted in the immediate vicinity of the sink tube, as N_{Re-u} is increased from 8 to 16 whereas approximately a fifty percent increase is observed for values of $R < 0.1$. This is so because as the N_{Re-u} increases the mass flow rate also increases and thus the momentum of mass
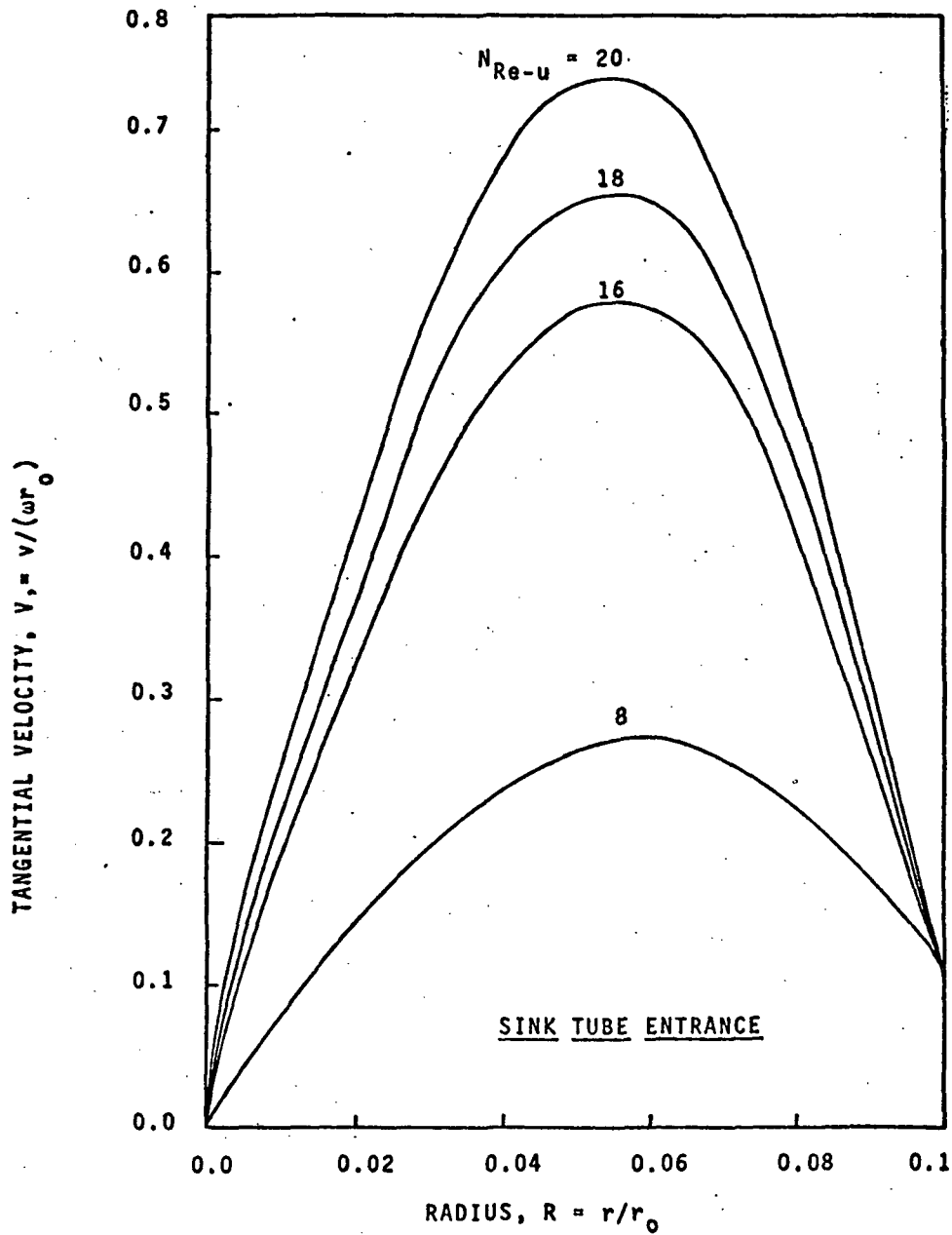
Figure 4.15 Variation of Tangential Velocity, V, with Radius, R, at the Entrance to Sink Tube for $N_{Re-\theta} = 8$
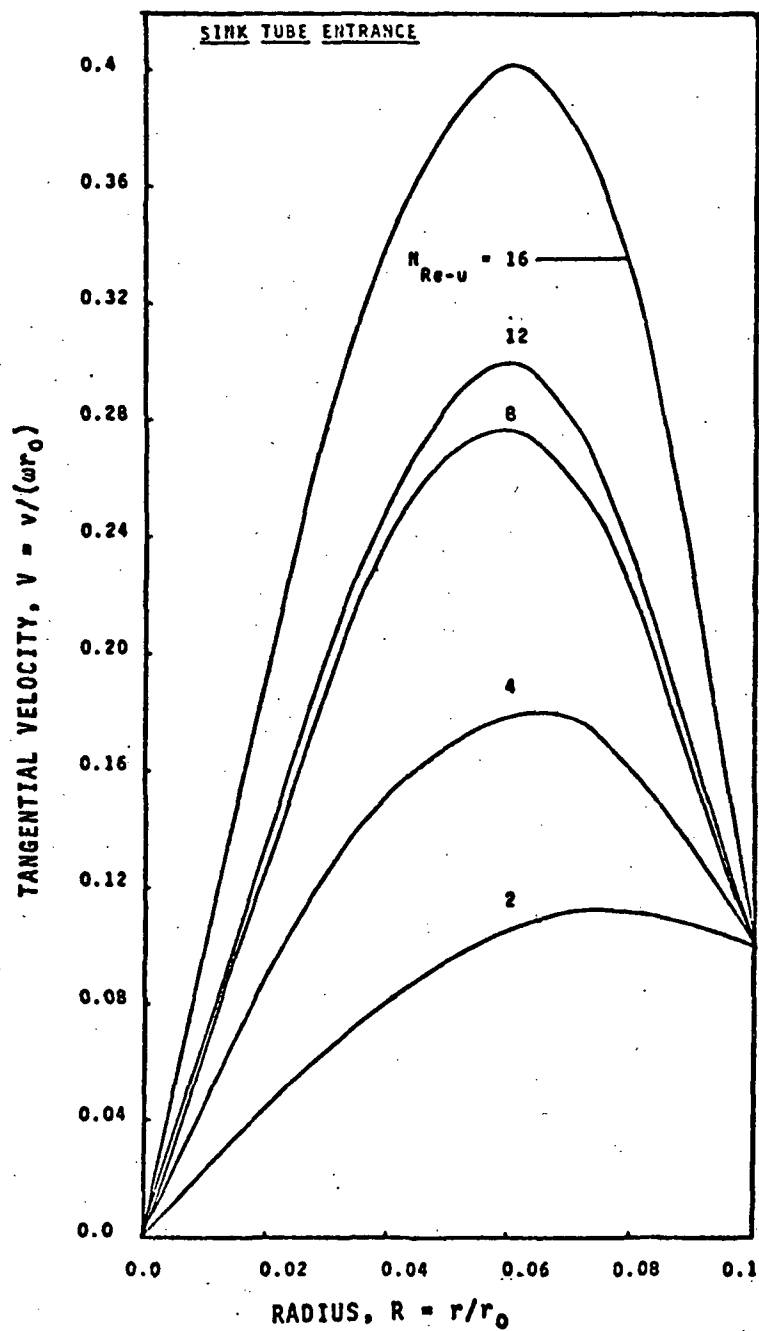
Figure 4.16   Variation of Tangential Velocity,
V, with Radius, R, at Entrance
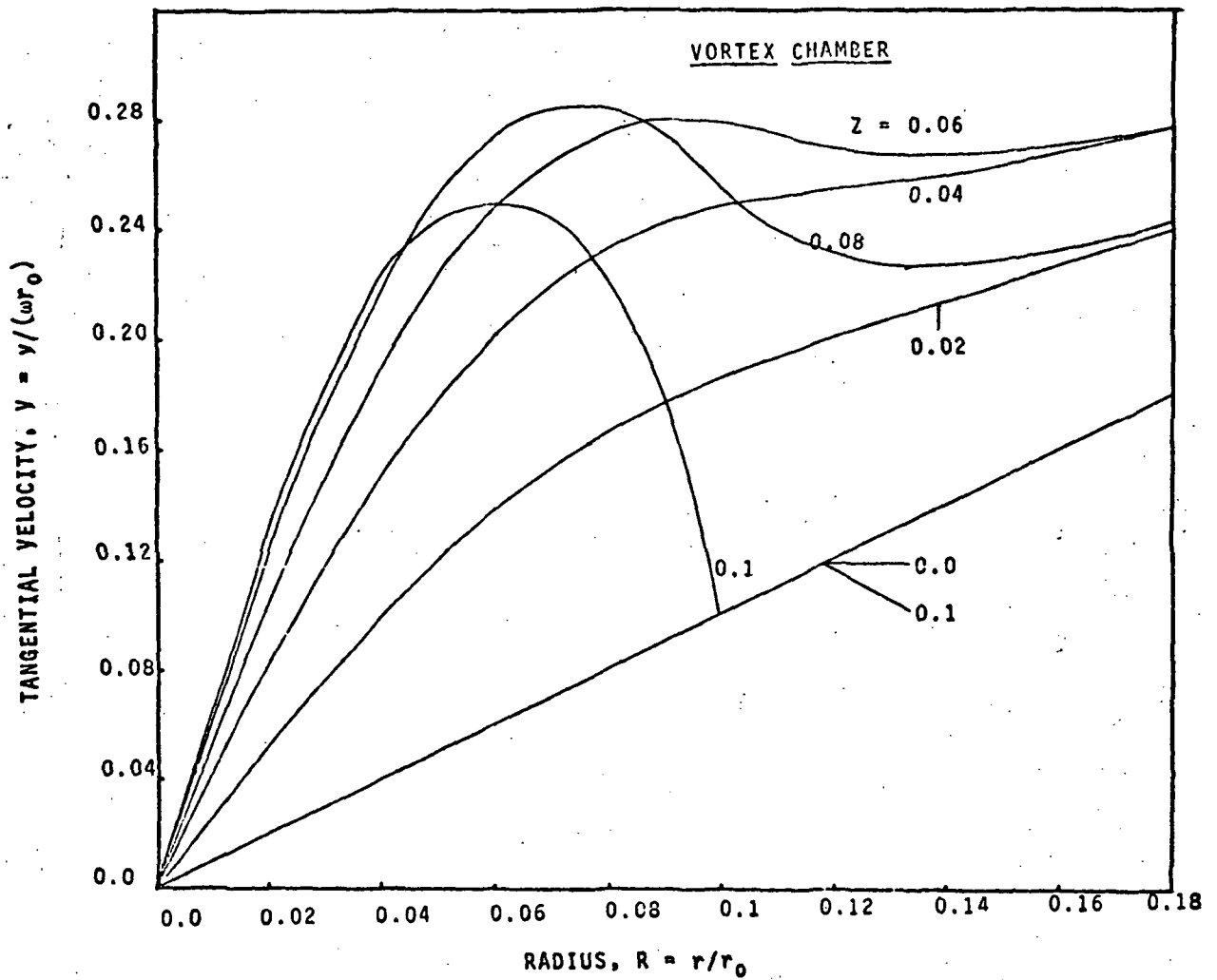to the Sink Tube (for $N_{Re-\theta} = 16$)

VORTEX CHAMBER
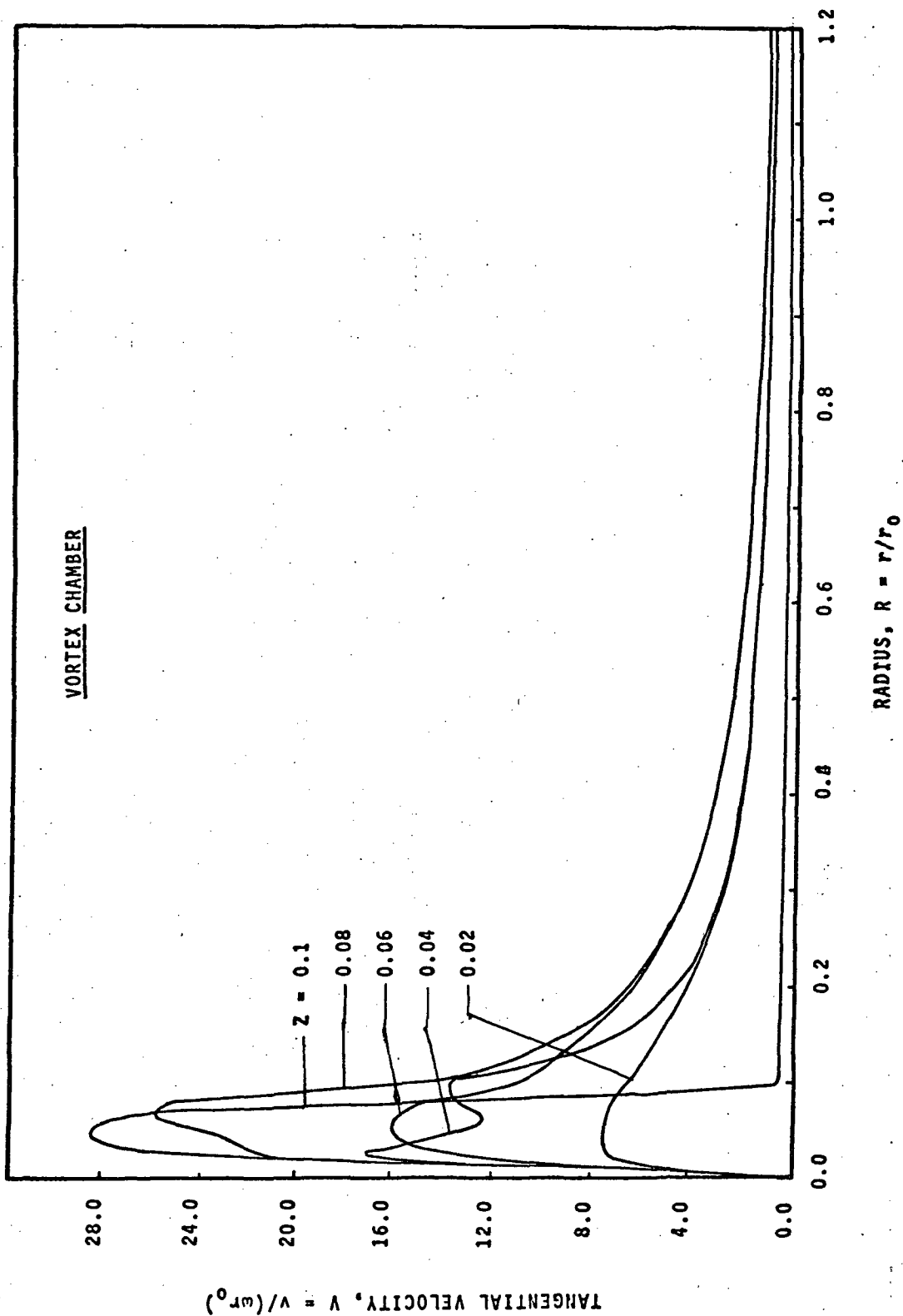
Figure 4.17   Variation of Tangential Velocity, V, with Radius, R, at Different
Z (for N_{Re-u} = 524.5 and $N_{Re-\theta}$ = 9090)

increases at a greater rate than the mass increment.

As shown in Figs. (4.18) and (4.10), the tangential velocity is considerably higher in the immediate vicinity of the sink tube entrance than anywhere else in the tube. For $Z > 0.2$, the velocity decreases rapidly with an increase in Z. At very low $N_{Re-\theta}$ and N_{Re-u} values, the tangential velocity becomes the equivalent of a solid body rotation. This occurs at a distance into the sink tube of approximately three times the height of the vortex chamber. This condition continues for all subsequent downstream sections. The equivalence of solid body, rotation is principally due to the fact that the viscous effect of the fluid predominates and therefore the fluid rotates at the same angular velocity as the tube. As $N_{Re-\theta}$ and N_{Re-u} are increased, the distance into the sink tube at which solid body rotation first becomes evident is also increased.

4.3 Axial Velocity

The axial velocity is calculated after determining the stream function values. Equation (3-28) is used to obtain the axial velocity at any location within the sensor. The axial velocity along geometric axis however is calculated by using Equation (3-20).

Figure (4.19) shows the variation of the axial velocity within the vortex chamber. As the entrance flow to the vortex chamber is uniform and purely radial, the axial velocity is assumed to be zero at that location. It however rises rapidly into the chamber for a short distance (from $R = 1$ to $R = 0.9$)
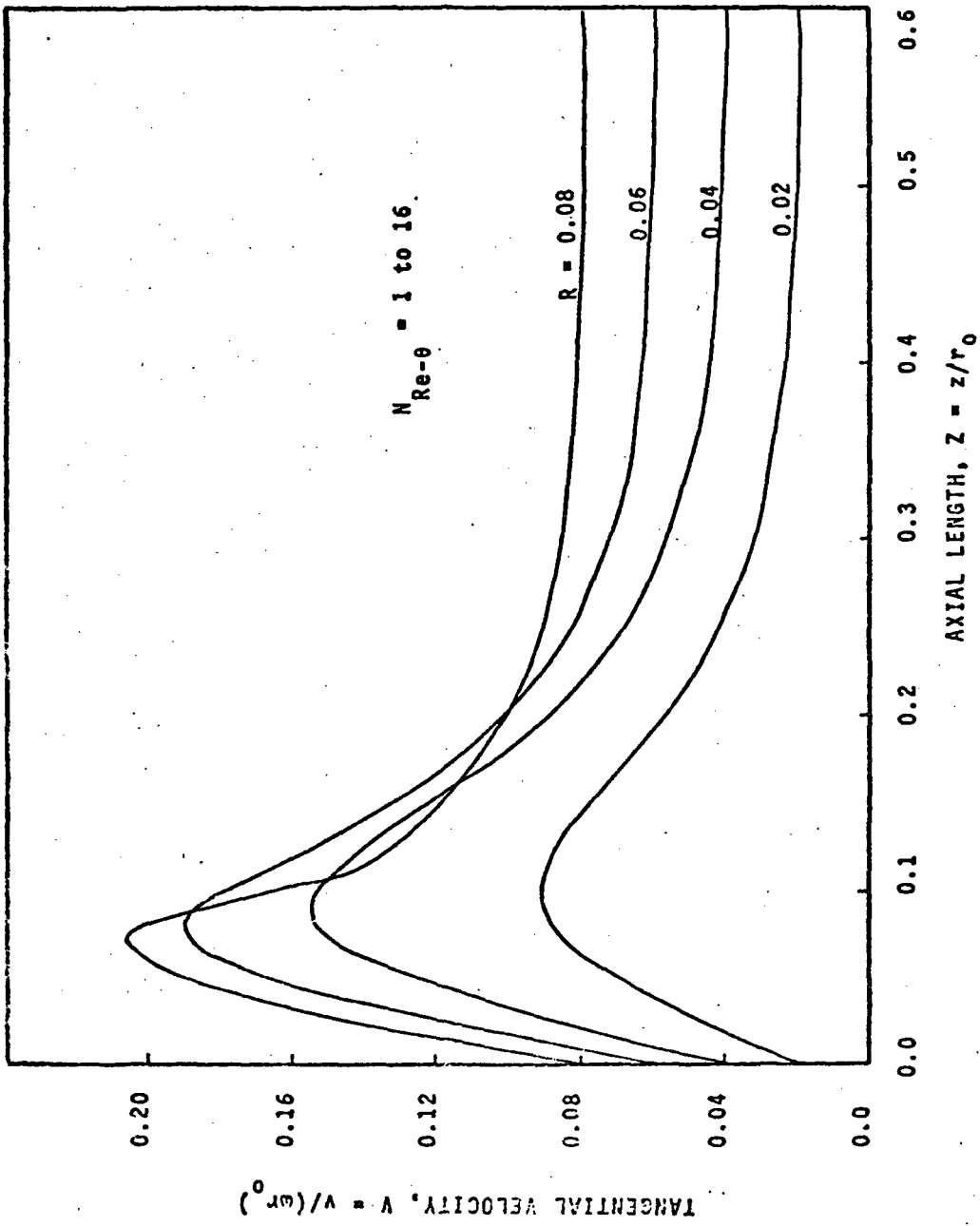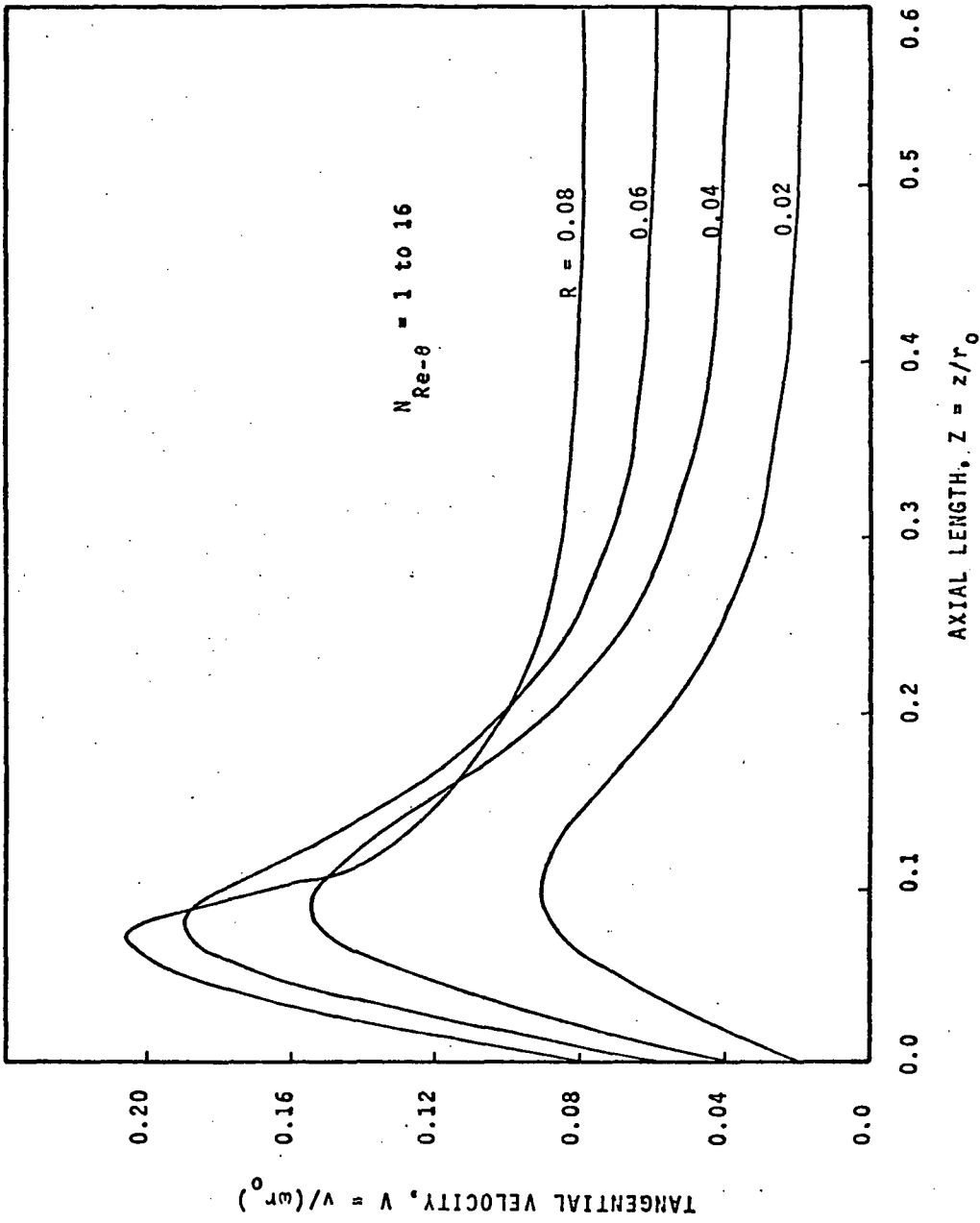
Figure 4.18   Variation of Tangential Velocity, V, with Axial Length
Z at Different R (for Different $N_{Re-\theta}$ and N_{Re-u} = 4)
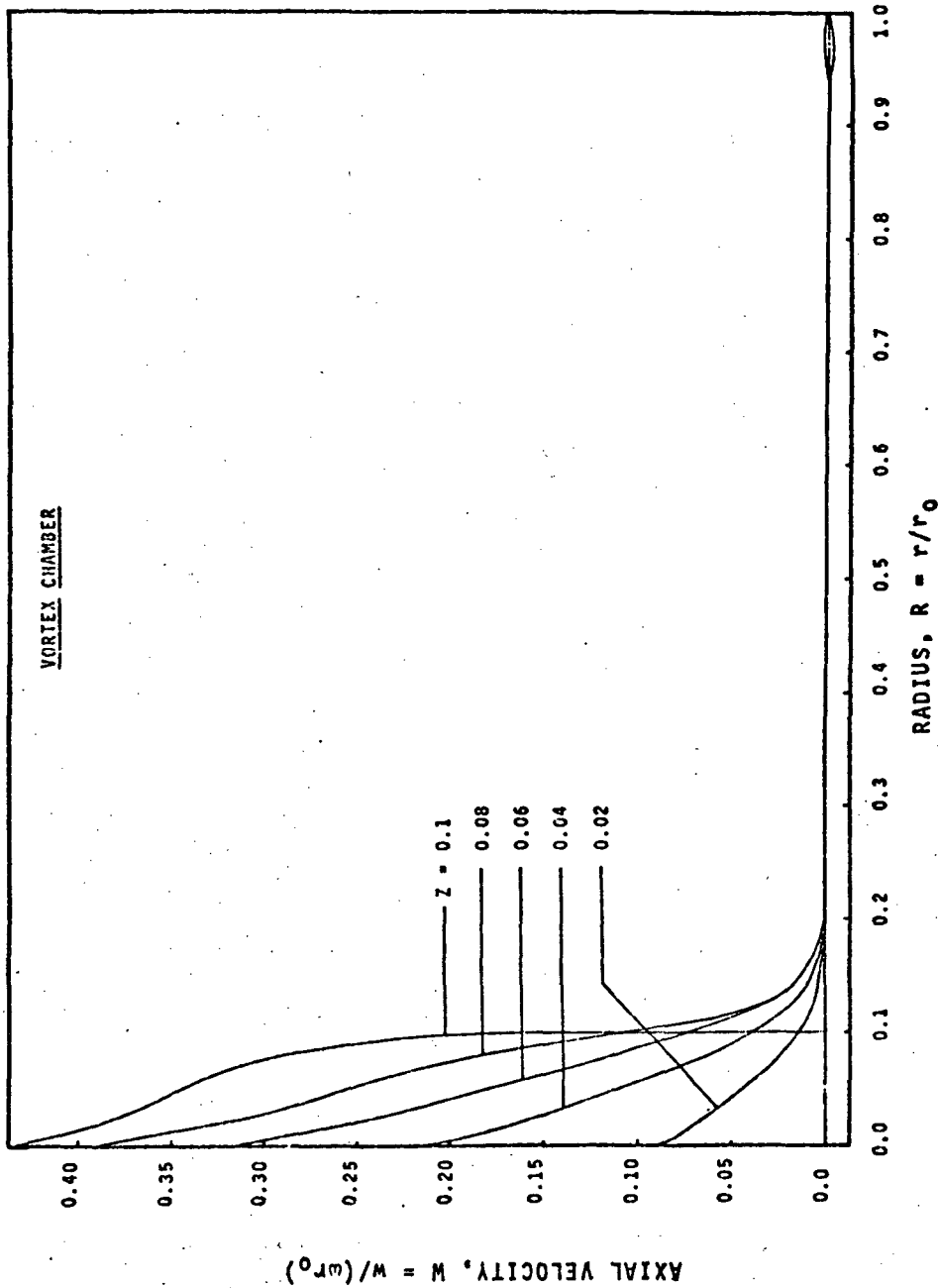
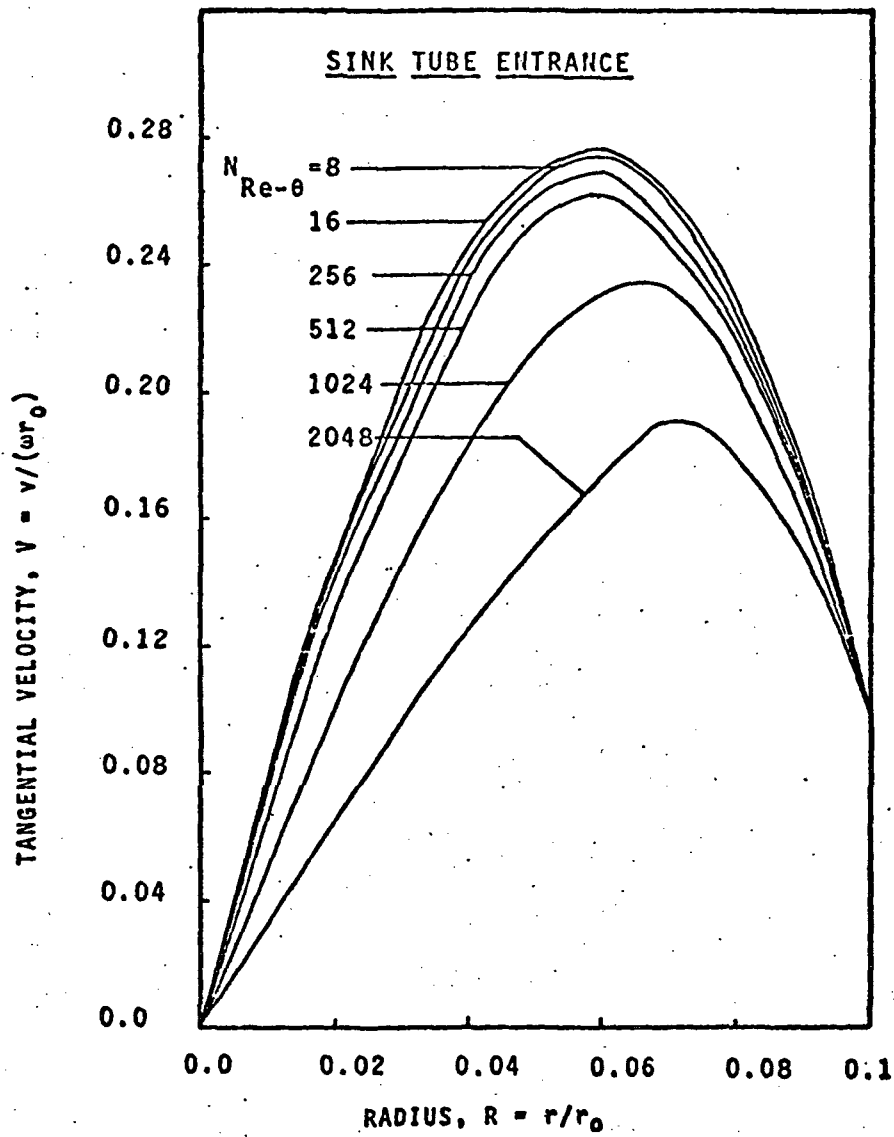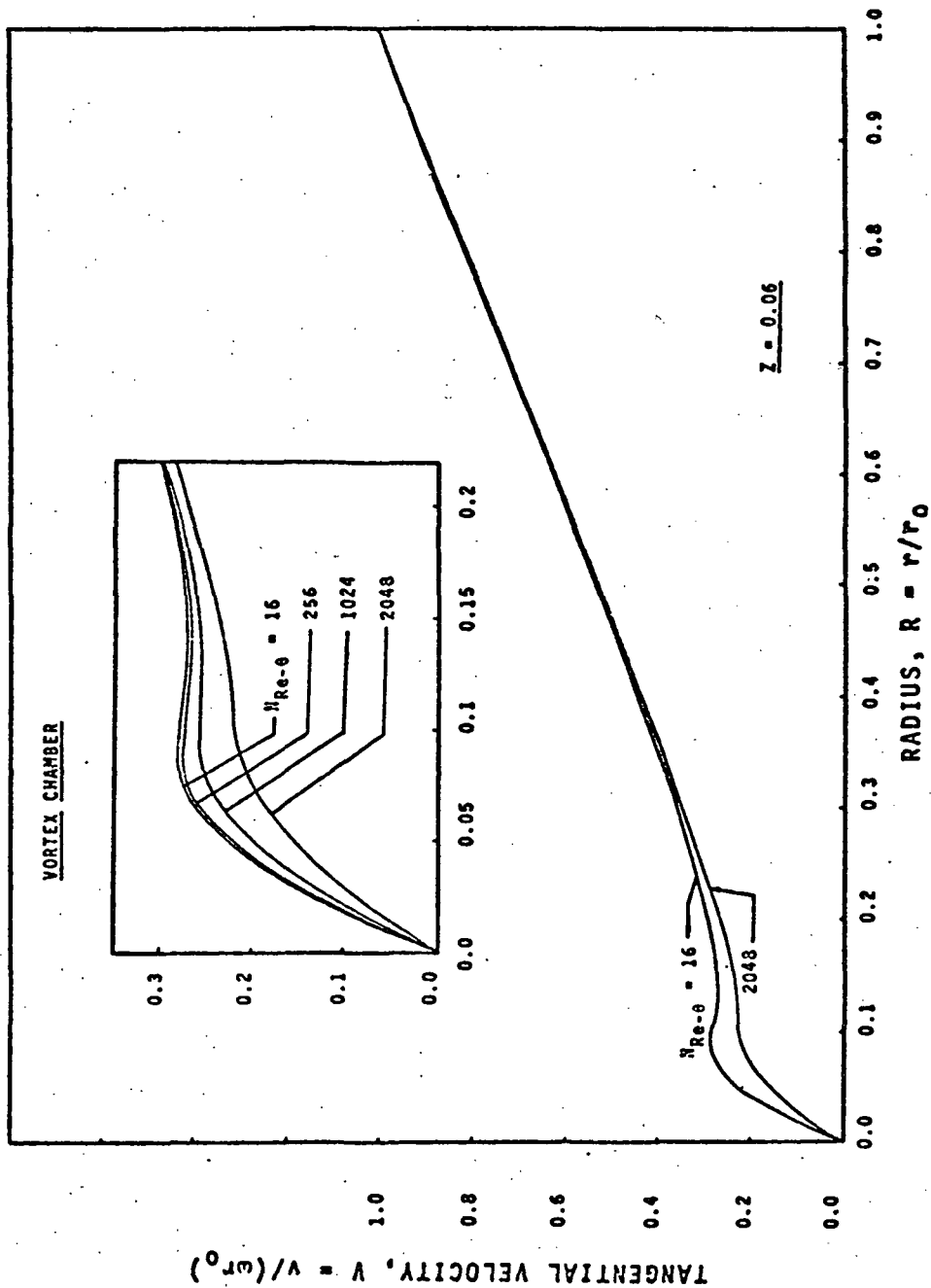Figure 4.19   Variation of Axial Velocity, W, with Radius, R, at
Different Z (for N_{Re-u}=8 and $N_{Re-\theta}$=512)

and then almost becomes zero at R = 0.94. For values of R > 0.94, the axial velocity is positive in the upper portion of the vortex chamber, while it is negative in the lower portion. This result is a direct consequence of the boundary layer growth, which occurs at the entrance section and then stabilizes in the region $0.2 \leq R \leq 0.94$. The axial velocity, for R < 0.2, increases rather rapidly, and becomes everywhere positive, as R decreases. This phenomena takes place as a result of the presence of the sink located on the bottom plate. Thus, in the vicinity of the sink, the flow tends toward the sink entrance and the axial velocity becomes positive everywhere. The axial velocity is observed to have a maximum value near the geometrical axis of the vortex chamber. This is a result of both the axial velocities on the plate and the sink tube wall being zero. The axial velocity near the wall is small because of the boundary layer growth, and it is a maximum near the geometrical axis.

Figures (4.20) and (4.21) reveal the variation of the axial velocity in moving from the top plate of the vortex chamber to the exit of the sink tube. It is noted that the axial velocity is positive everywhere within the sink tube, with the maximum value occurring along the geometrical axis. As shown in Fig. (4.20), the axial velocity in the vicinity of the geometric axis, from the sink tube entrance to a distance approximately 3H into the sink tube, continuously increases to a maximum, then decreases slightly, and subsequently becomes constant at the downstream section. A reverse flow pattern to the above is observed within the sink tube for

72

Figure 4.20   Variation of Axial Velocity, W,
with Axial Length, Z, at Different
R (for N_{Re-u} = 8 and $N_{Re-\theta}$ = 512)

AXIAL LENGTH, Z = z/r_0

AXIAL VELOCITY, W = $w/(\omega r_0)$

R = 0.0

0.02

0.04

0.06

0.08

Figure 4.21   Variation of Axial Velocity, W, with Radius, R, at Different Z (for N_{Re-u} = 8 and $N_{Re-\theta}$ = 512)

$R \geq 0.06$. This variation in pattern is possibly due to the radial momentum having a higher magnitude at a sink entrance and then decreasing to zero for the short distance (3H). Within this short distance the radial momentum is converted to axial momentum, and as seen the axial velocity rises for $R \leq 0.04$. However, beyond this (3H) length, due to stability of flow the value of axial velocity changes and becomes a constant along the axial length. At $R = 0.08$, however, the axial velocity rises continuously until a peak value is reached and this is accounted for, by the gain of axial momentum over radial momentum. At $R = 0.08$ and beyond (where the peak velocity occurs), the viscosity effect reduces the velocity at a greater rate near the wall, and ultimately produces a constant velocity in the downstream section.

In Fig. (4.21) the axial velocity results are plotted as a function of radius with Z as a parameter. Here, the axial velocity profile is not fully parabolic as encountered in the Poiseville flow. This is due to the sensor rotation which moves the fluid toward the wall and away from the geometrical axis.

As N_{Re-u} was increased, the axial velocity, within the sink tube, along the geometrical axis, increased at a faster rate than elsewhere. This was substantiated by the predominate effect that N_{Re-u} has over $N_{Re-\theta}$, at the higher values. Thus at the higher flow rates the flow was attempting to become similar to the Poiseville flow.

The effect of the tangential Reynolds number on the axial velocity, within the sink tube, was negligibly small. There-

fore it was difficult to show this effect in graphs. This effect, however, is mentioned here merely for discussion purposes. As $N_{Re-\theta}$ was increased to a value of 16, the axial velocity at a given station along the geometrical axis, increased continuously and reached a peak value at $N_{Re-\theta}$ = 16. However, as $N_{Re-\theta}$ was further increased to a value of 512, the axial velocity decreased continuously. This pattern was interpreted as being due to the predominate centrifugal effect at the higher $N_{Re-\theta}$ values.

4.4 Radial Velocity

The radial velocity is considered negative when it is directed towards the geometrical axis and considered positive in the reverse direction. The radial velocity is assumed constant at the entrance to the vortex chamber and zero on all remaining boundaries. After obtaining the stream function values, Equation (3-27) is solved numerically to obtain the radial velocity at any location in the vortex sink rate sensor.

The variation of radial velocity within the vortex chamber is illustrated in Figs. (4.22) and (4.23). As a consequence of the radial momentum conservation, the radial velocity continuously increases as R decreases to the value R $\simeq$ 0.1. At that location it reaches a peak value and then decreases to zero at the geometrical axis. This is due to symmetry about the geometrical axis. The figures also show that there is a slight decrement of radial velocity at the entrance region of the vortex chamber near the plates which is attributable to the growth of the boundary layer near the
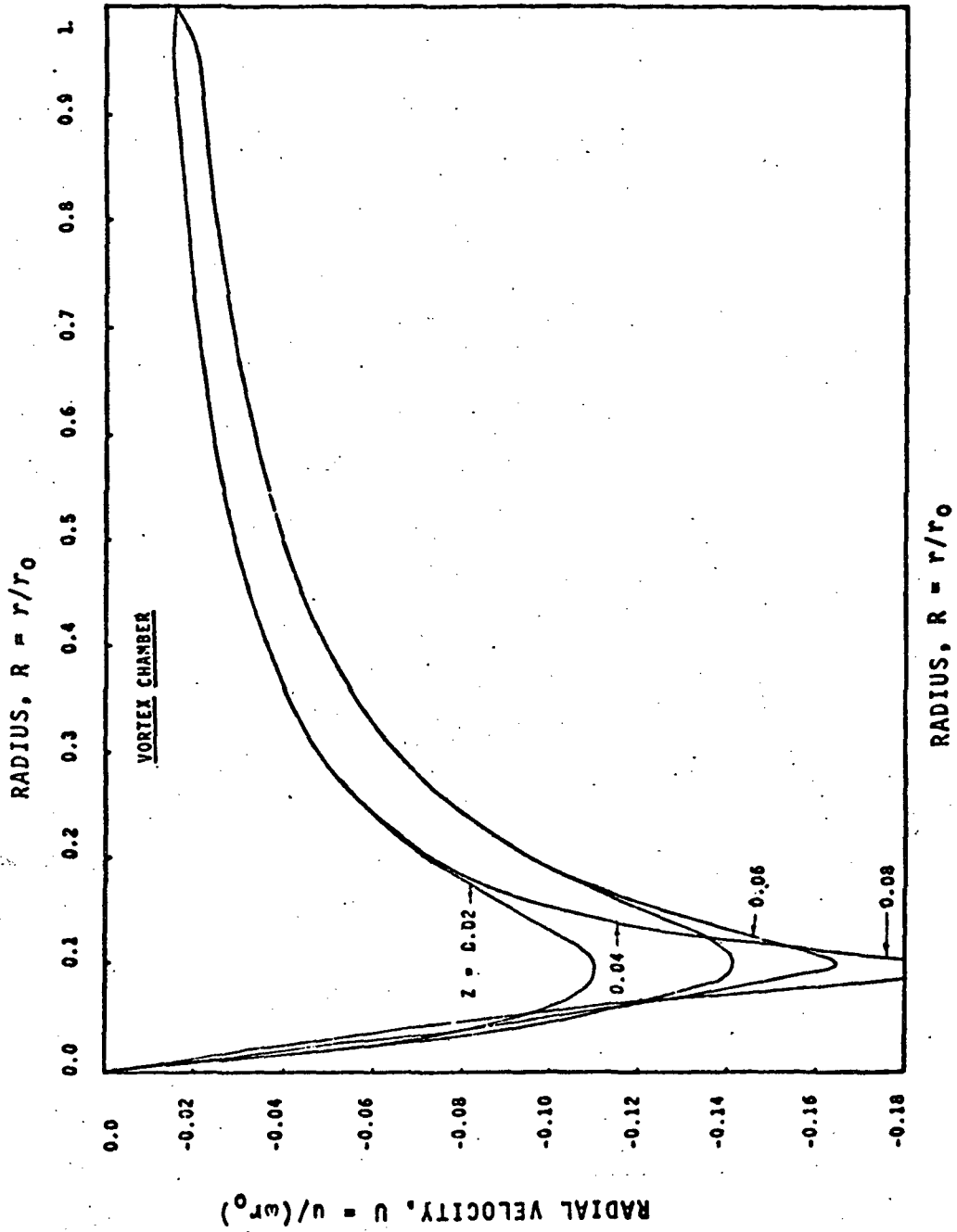
Figure 4.22   Variation of Radial Velocity, U, with Radius, R, at Different Z (for N_{Re-u} = 8 and $N_{Re-\theta}$ = 512)
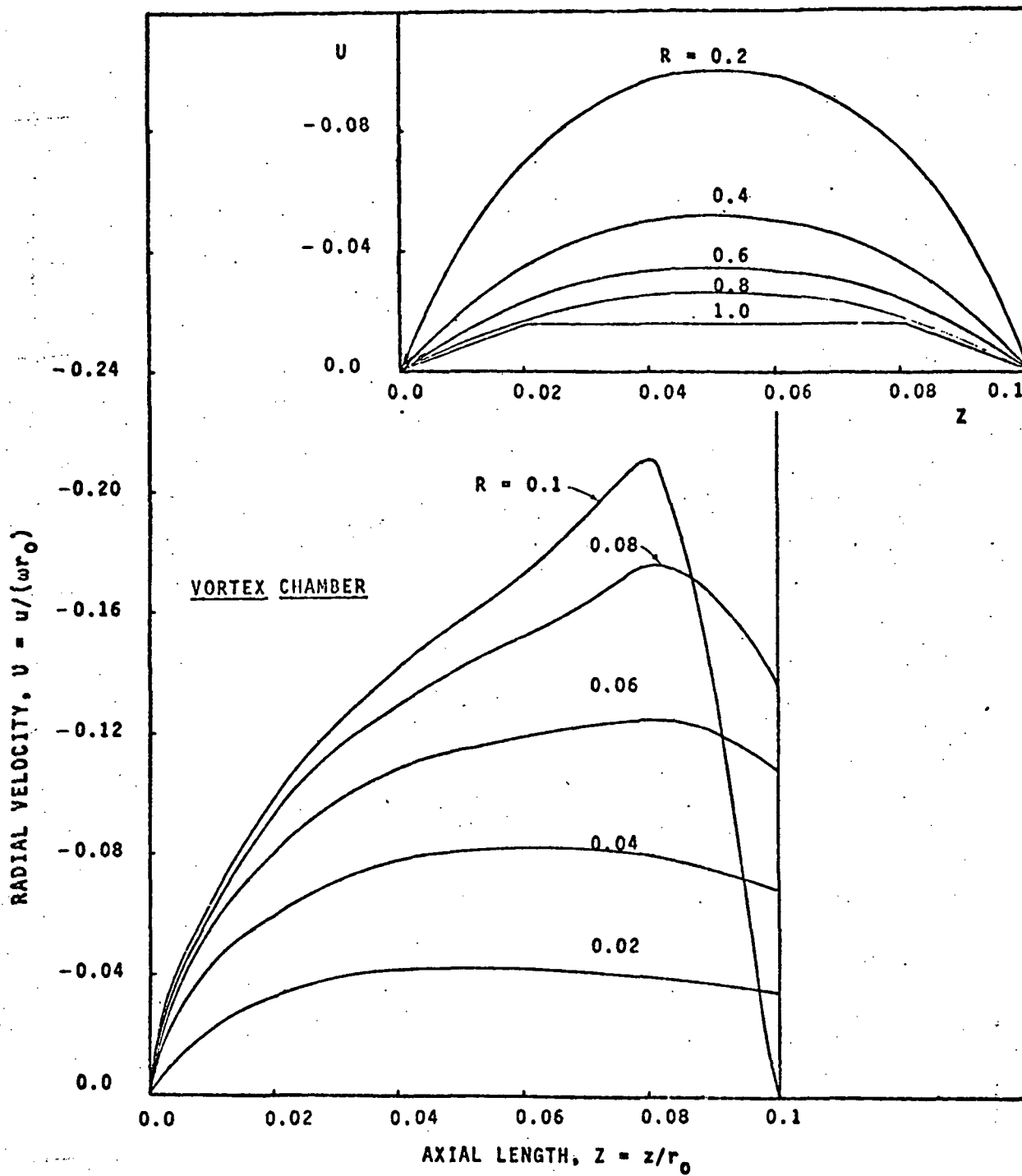
Figure 4.23   Variation of Radial Velocity, U, with Axial Length, Z, at Different R (for N_{Re-u} = 8 and $N_{Re-\theta}$ = 512)

plates. It is also observed that the radial velocity is approximately inversely proportional to the radius for R > 0.1. The radial velocity, overall, within the vortex chamber is negative everywhere.

The radial velocity profile is found to be of parabolic shape, symmetrical about Z = 0.5H. This profile remains as such up to a value R $\geq$ 0.3. As R is further decreased, the presence of the sink, distorts this profile. The sink tube tends to suck the fluid and thus the radial velocity, on the sink side, rises faster than near the top plate. The distorted parabolic profile therefore turns toward the sink entrance.

The results of the radial velocity in the sink tube are illustrated in Figs. (4.24) and (4.25). The radial velocity is highest at the entrance region. This is due to the conservation of radial momentum in the vortex chamber. As the flow progresses into the sink tube, the radial momentum rapidly converts to axial momentum and thus the radial velocity rpaidly decreases. At a distance of approximately 5H into the sink tube, the radial velocity changes direction, (the negative radial velocity becomes positive). The establishing of stability of flow causes this to occur. The radial velocity subsequently approaches a value of zero at the tube exit section. As observed, the positive magnitude of velocity is negligible for low radial Reynolds numbers. However, as will be shown in Chapter VII, this velocity is significant at the higher radial Reynolds numbers. The change from a negative to a positive value is a result, of the higher rates of flow, within the vortex chamber, at the higher N_{Re-u} values and thus
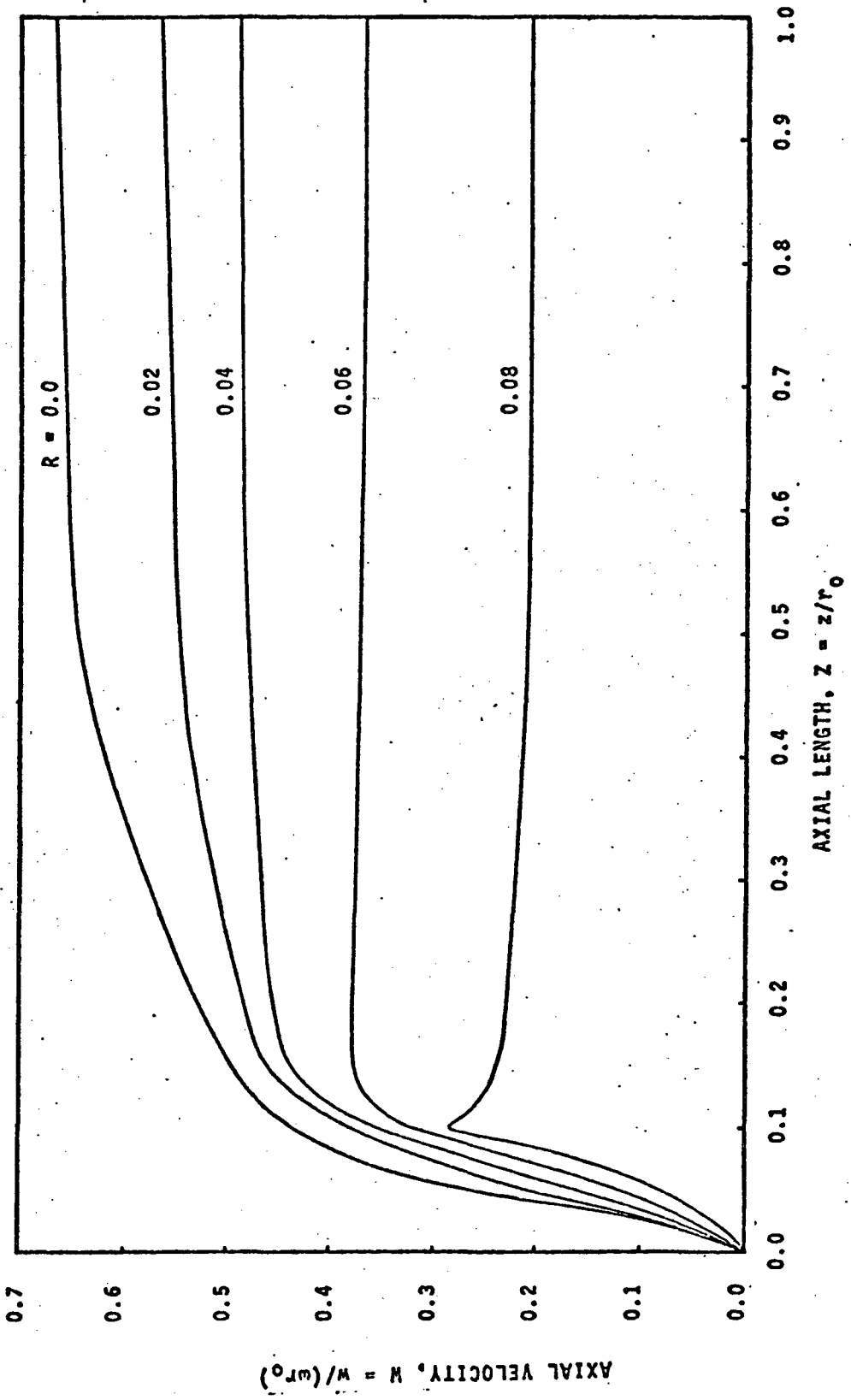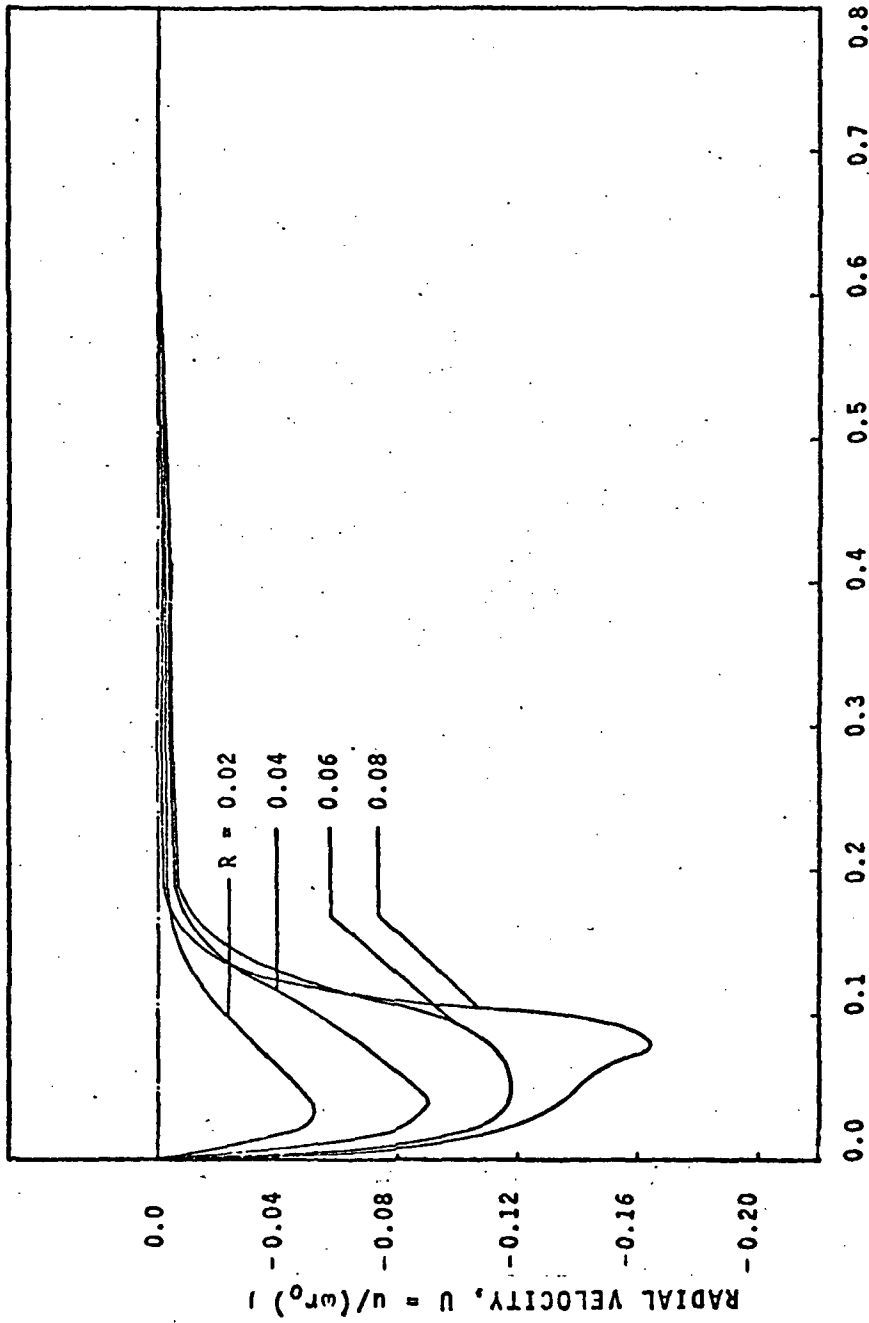
AXIAL LENGTH, Z = z/r₀

Figure 4.24 Variation of Radial Velocity, U,
with Axial Length, Z, at Different
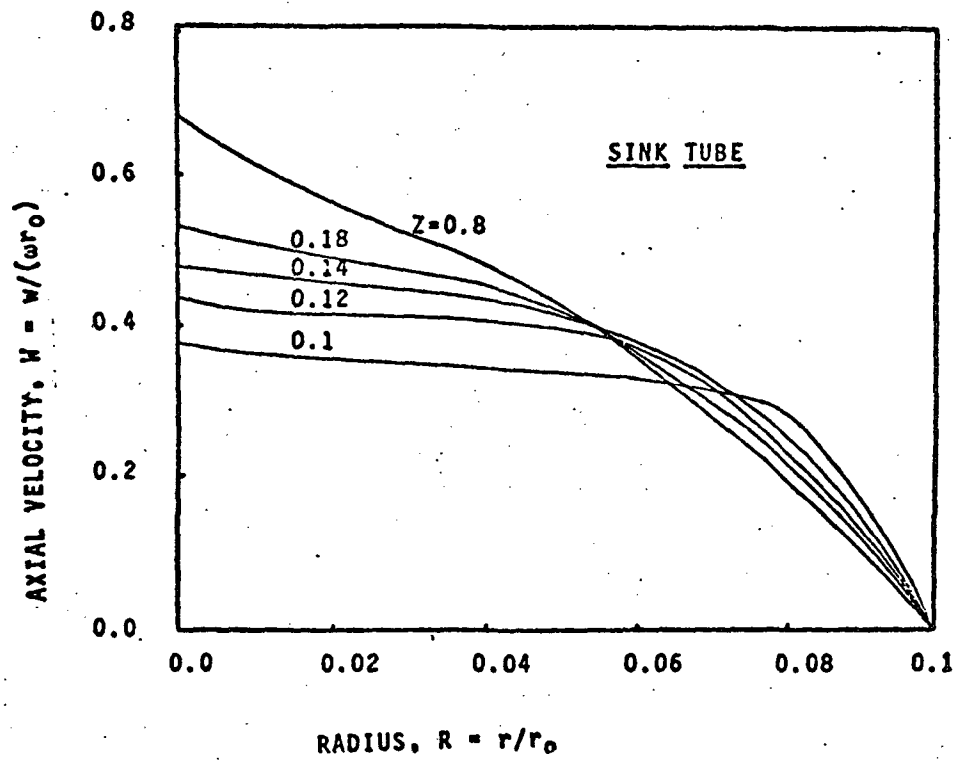R (for N_{Re-u} = 8 and $N_{Re-\theta}$ = 512)
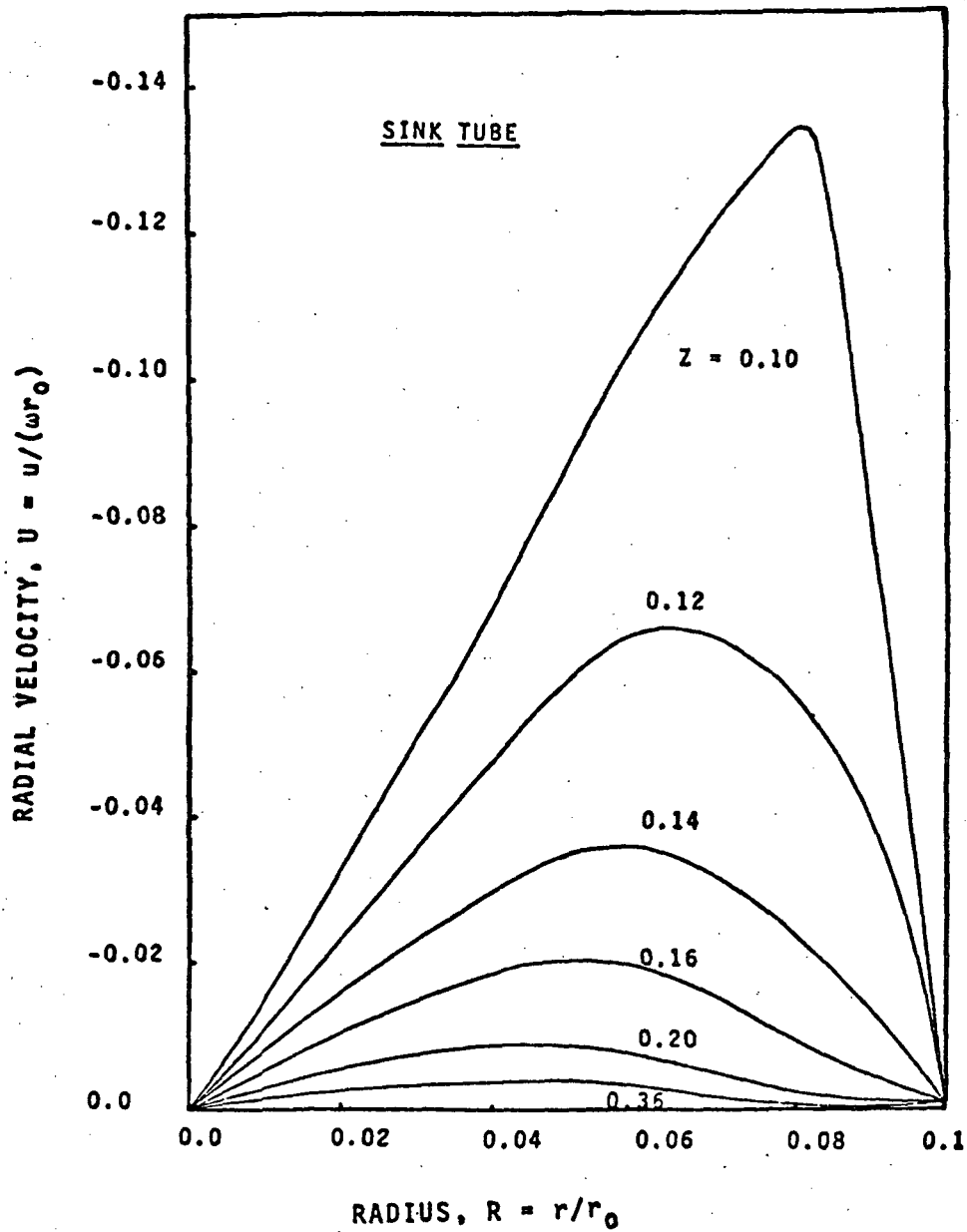
Figure 4.25 Variation of Radial Velocity, U, with Radius, R, at Different Z (for N_{Re-u} = 8 and $N_{Re-\theta}$ = 512)

the fluid experiences a greater force moving it away from the geometrical axis.

As noted in Fig. (4.25), throughout the sink tube region, the radial velocity profile at any given axial station is somewhat of a parabolic shape. The profile begins to develop at the tube entrance, continues its development into the sink tube and ultimately becomes a fully developed parabolic profile about $R = 0.5 R_i$ at $Z > 4H$. The development of the parabolic profile is in part due to the fact that the viscosity reduces the radial velocity both near the wall and near the core, with the velocities there ultimately becoming zero. The conversion of the radial momentum to axial momentum also contributes to the development of the profile.

4.5 Tangential Vorticity

The tangential vorticity is defined as the difference between the gradient of the radial velocity along the axial length and the gradient of the axial velocity along the radius.

As a result of uniform radial flow into the vortex chamber, the vorticity is considered zero at the entrance to the flow field region, (except of the corners). As discussed in Appendix A [Equation (A-12)], the vorticity along the geometrical axis is zero. The tangential vorticity on the vortex chamber plates and on the sink tube wall is calculated through use of the stream function results and Equations (3-14), (3-15) and (3-16). This information is used as the boundary conditions for Equation (3-6) which is then solved numerically, by following the procedure described in Section (3.1).

Figures (4-26) and (4-27) show the variation of vorticity within the vortex chamber, in moving from the periphery to its center. As a result of the large velocity gradients, a maximum absolute value of vorticity occurs in the boundary layer regions within the vortex chamber as well as at the entrance corner of the sink tube. Thus the vorticity on both plates is higher than the vorticity in the flow field. The vorticity η on the top plate is found to have a negative value while a positive value is observed on the bottom plate. A zero value of vorticity occurs, for $R > 0.3$ in the midplane of the vortex chamber plates. The vorticity pattern discussed above is a consequence of the axial velocity gradient along R being negligible in the entire vortex chamber except for $R < 0.2$, and also due to the radial velocity gradient along Z being negative near the top plate, zero at the midplane of the chamber plates and positive near the bottom plate.

As discussed earlier, the vorticity at $R = 1$ is zero and it is due to the uniform radial flow at this section. There is, however, some vorticity at the plate edges for this location and it is attributable to the boundary layer effect. The vorticity on the plates decreases approximately 20 percent from $R = 1$ to $R = 0.9$, at which location it reaches a minimum value. It then continuously increases to a maximum value as R decreases to $R \simeq 0.1$. This occurs because near the plates, the radial velocity also follows the same trend as discussed before in Section (4.4) and the vorticity is indeed an axial gradient of radial velocity, and there the radial gradient of axial velocity is negligible.
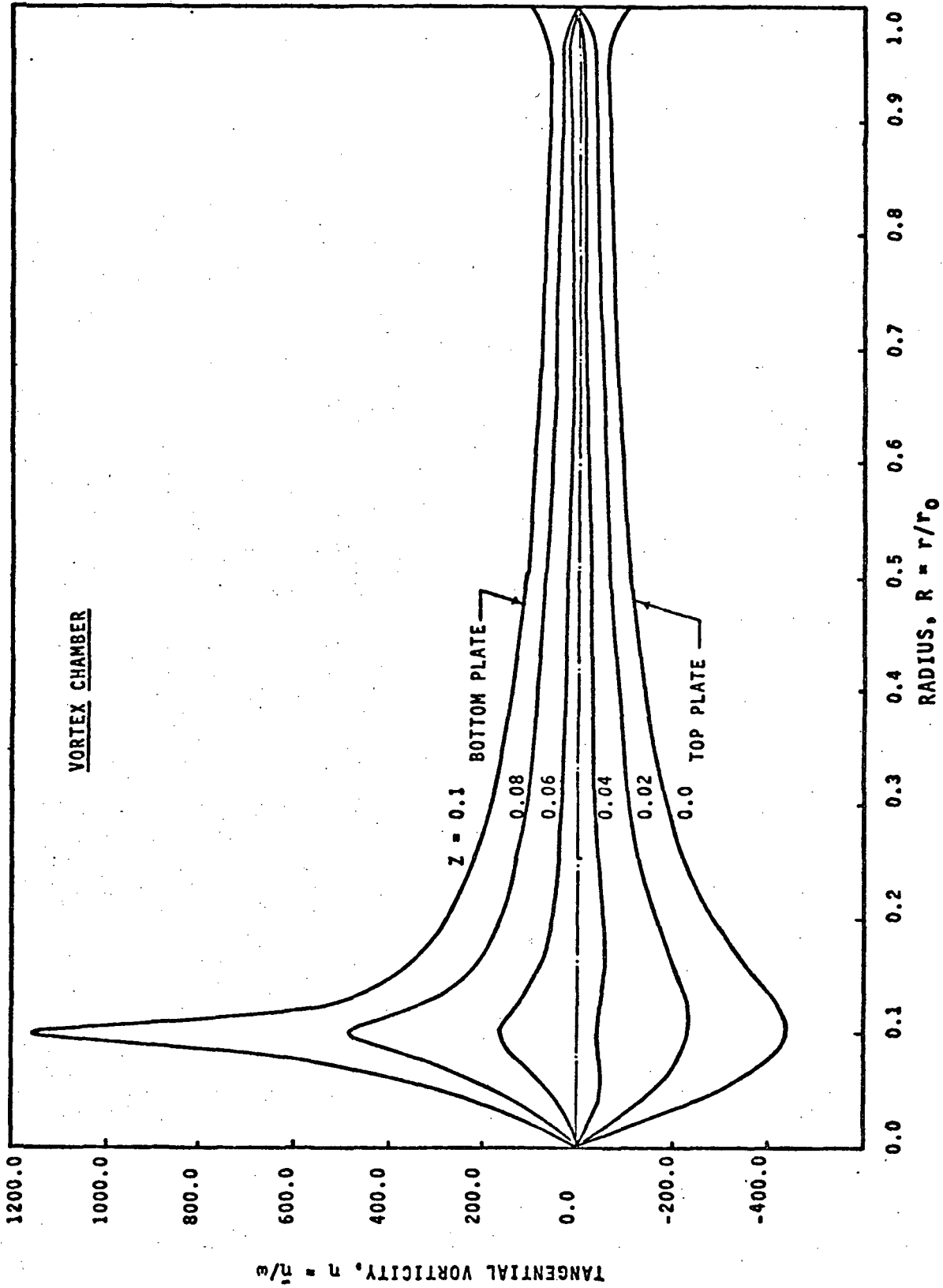
Figure 4.26   Variation of Tangential Vorticity, η, with Radius, R, at Different Z (for $N_{Re-u} = 1$ and $N_{Re-\theta} = 1$)
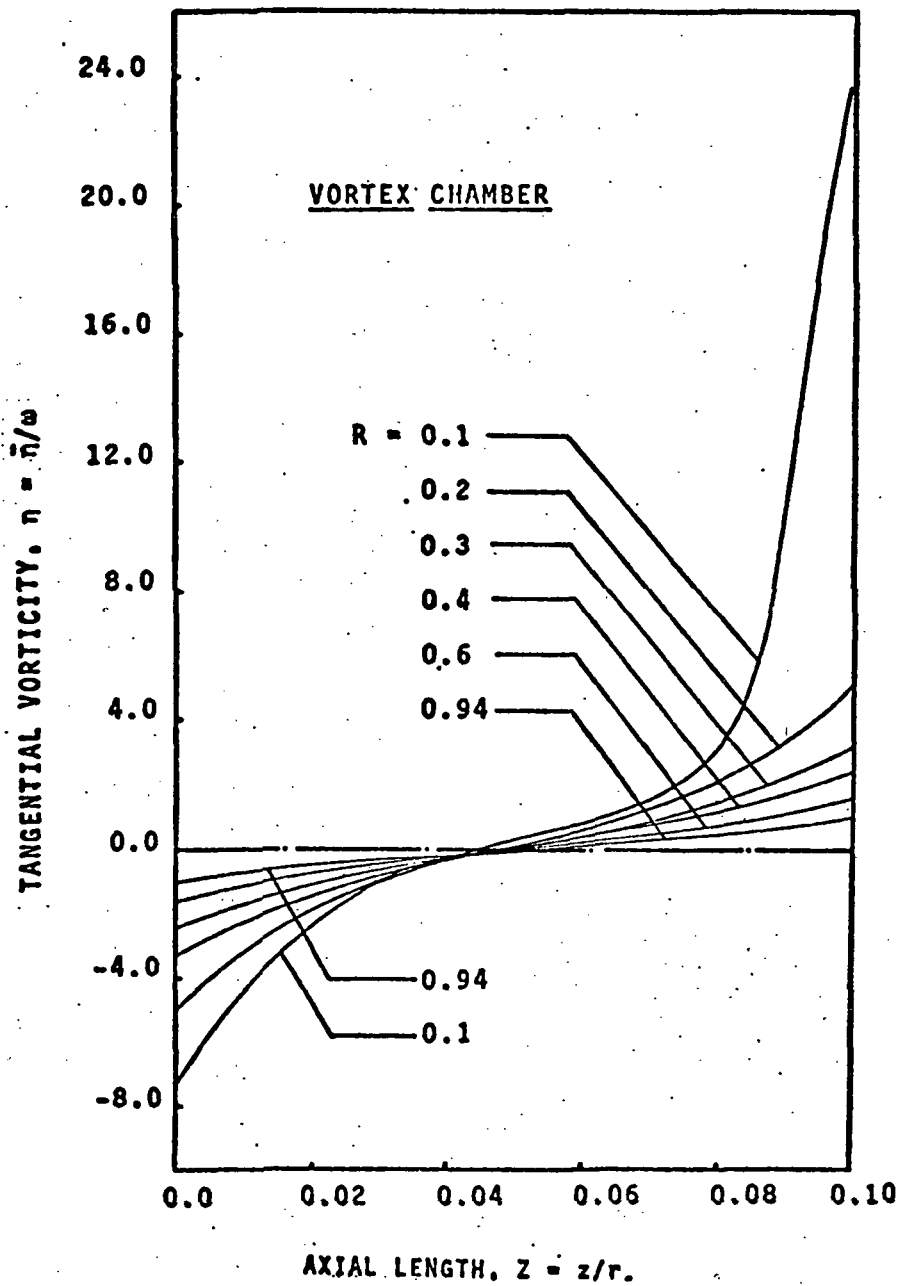
Figure 4.27   Variation of Tangential Vorticity, η, with Axial Length, Z, at Different R (for $N_{Re-u}=8$ and $N_{Re-\theta}=512$)

As shown in Fig. (4.27), the vorticity in the flow field continuously increases from the value zero, which occurs at the entrance section up to R = 0.1 Throughout the range 0.3 ≤ R < 1, it is observed to be approximately a linear function of Z, except within the boundary layer region. The above pattern is attributable to the fact that within the flow field, the radial velocity profile along Z is approximately parabolic.

The effect of the sharp corner at the entrance to the sink becomes evident at values of R < 0.3. This is particularly noticeable as the velocity on the bottom plate increases at a faster rate than on the top plate. At the corner, the vorticity reaches a maximum and is approximately 10 to 25 times greater than the maximum vorticity on the plate. In explaining this pattern it should be noted that the velocity gradients near the bottom plate are higher than those near the top plate. In addition, it is seen that the magnitude of the radial velocity, in the vicinity of the corner, is greatest and also that the magnitude of the axial velocity is significant. It is also observed that the axial gradient of the radial velocity is positive and of appreciable value while the radial gradient of axial velocity is negative. Thus, a high value of vorticity occurs at the corner due to the difference of both of these gradients.

Figure (4.27) also reveals that, within the vortex chamber, the radial velocity gradient is significant in the flow field at R ≃ 0.1. The vorticity then appears to decrease as R increases, ultimately reaching a value of zero at the

geometrical axis.

Figures (4.28) and (4.29) illustrate how the tangential vorticity varies within the sink tube. It is apparent that the vorticity within the sink tube flow field is greater than that existing within the chamber flow field. The radial gradient of the axial velocity within the sink tube is ostensibly much greater than the axial gradient of the radial velocity within the vortex chamber. This appears to be so as the average axial velocity within the sink tube is much higher than the inlet radial velocity, and also since both the radial velocity gradient in the axial direction within the sink tube as well as the axial velocity gradient along the radius in the vortex chamber are negligible. As a result of this the vorticity in the sink tube appears to be higher.than that within the vortex chamber. Since the axial velocity gradient is, in general, negative the vorticity is overall positive everywhere within the sink tube.

As discussed in Section (4.3) for R ≃ 0.08, the axial velocity decreases in the entrance section of the sink tube. After determining its radial gradient it becomes evident that along the sink tube wall and in its immediate vicinity, the vorticity continuously decreases. This decrease occurs from the sink tube entrance Z ≃ H to approximately a distance Z = 3H into the tube. From this point on the vorticity becomes virtually constant. For R < 0.04, no appreciably variation in vorticity is noticeable. However, within a sink tube entrance length, the vorticity decreases to a lower value and then increases to an equilibrium value. The vorticity for a given R within
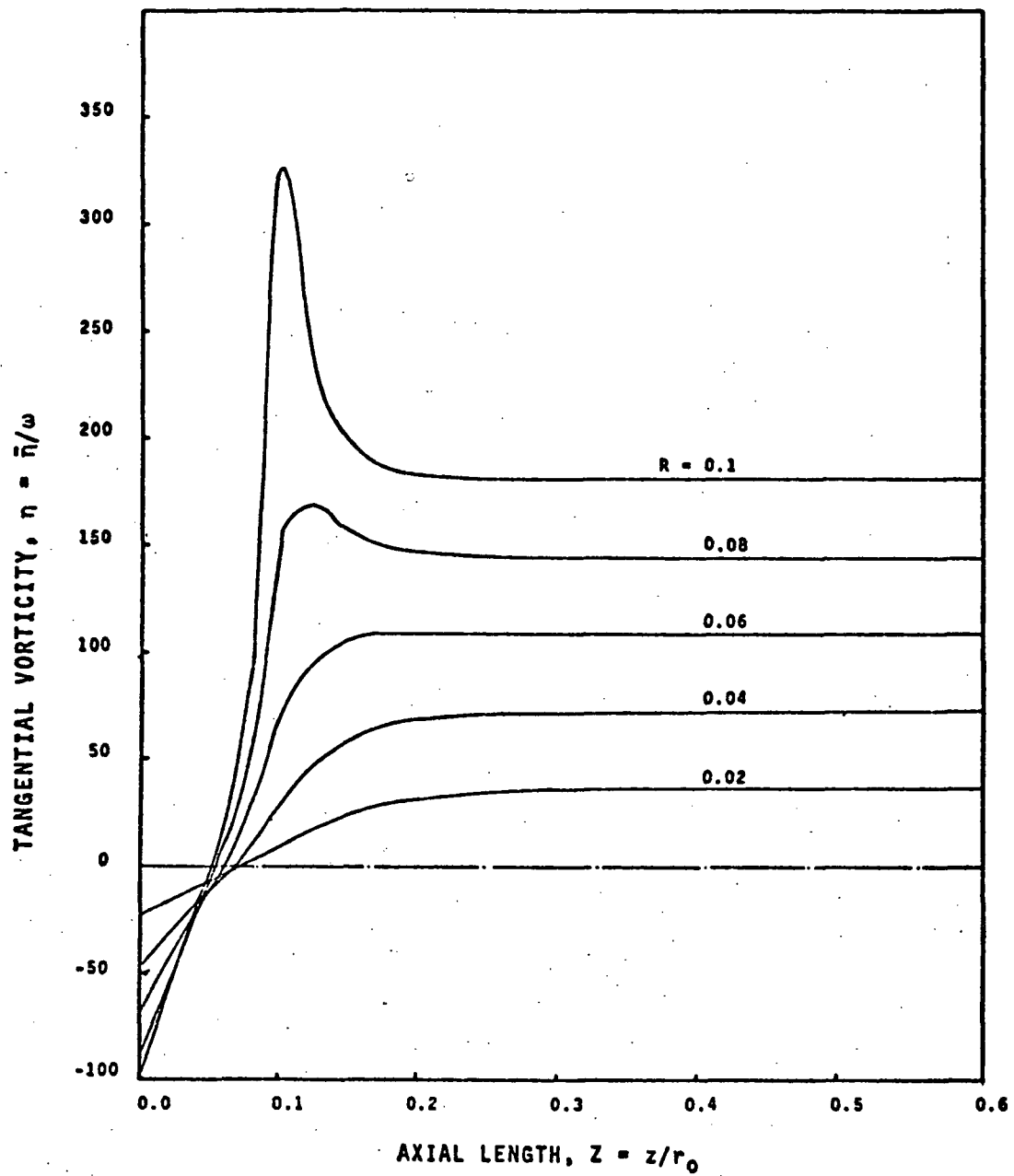
Figure 4.28   Variation of Tangential Vorticity,
n, with Axial Length, Z, at
Different R (for N_{Re-u} = 4 and

$N_{Re-\theta}$ = 16)
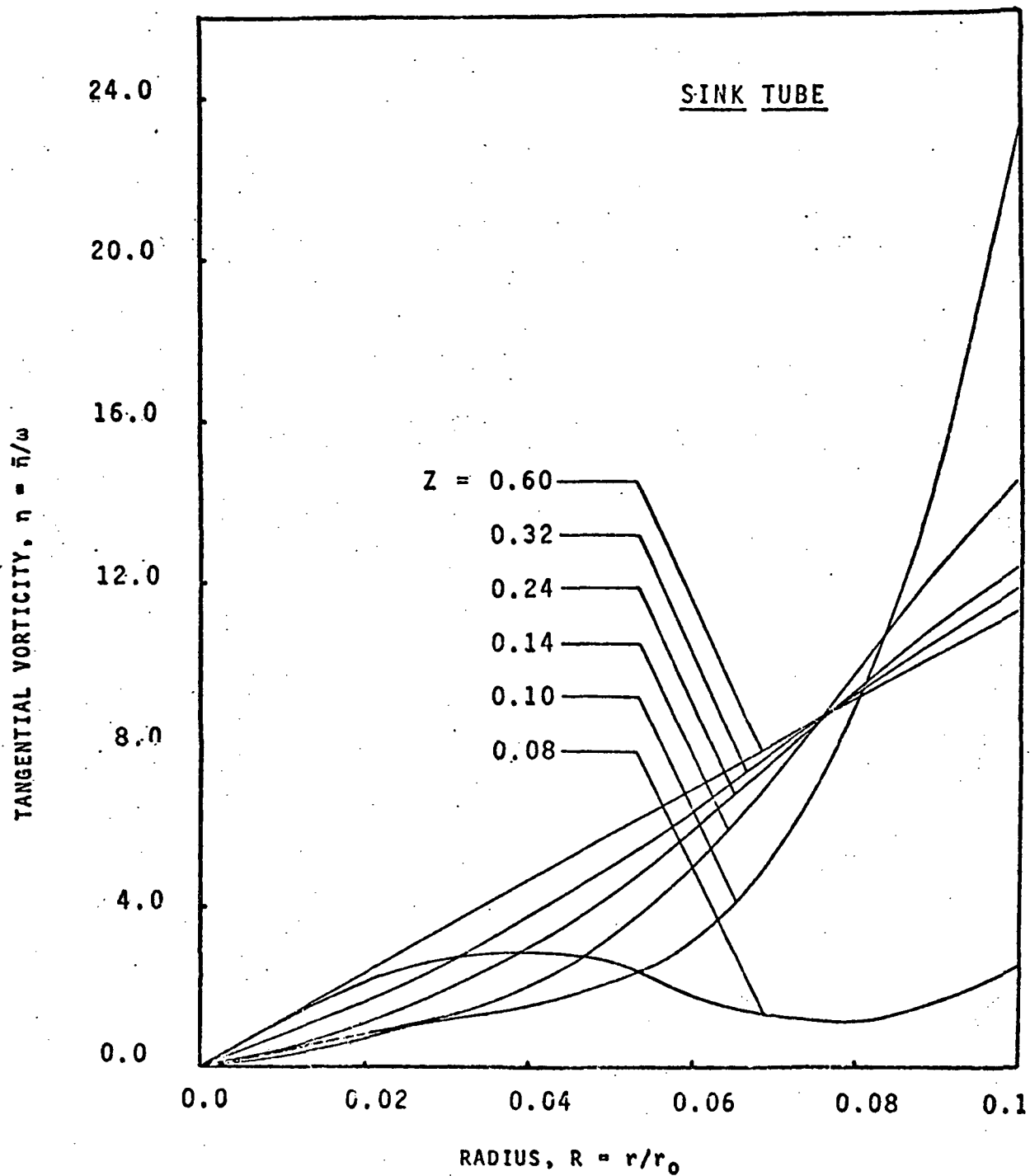
Figure 4.29   Variation of Tangential Vorticity, η, with Radius, R, at Different Z (for $N_{Re-u}=8$ and $N_{Re-\theta}=512$)

the downstream region, remains constant along Z.

The vorticity, in the downstream section of the sink tube, is observed to be approximately directly proportional to the radius for low radial and tangential Reynolds numbers. This is particularly true at low Reynolds numbers where the effect of rotation on axial velocity is negligible and the axial velocity profile is approximately parabolic as for poiseuille flow. Thus the radial gradient is a straight line. At the higher Reynolds numbers, however, due to the effect of higher rotational speeds nonlinearities become evident.

The effect that $N_{Re-\theta}$ has on vorticity along the bottom plate and along the sink tube wall is illustrated in Figs. (4.30) and (4.31). As the flow is maintained constant and the rotation is increased, the vorticity, $\eta(\eta = \frac{\bar{\eta}}{W})$ decreases in an inversely proportional manner with respect to $N_{Re-\theta}$. Since the rate of decrease in vorticity is greater than the rate of decrease in $N_{Re-\theta}$, the flow changes to a spiral form with a small helical angle in the sink tube. Thus the rate of production of the vortices reduces near the corner. This indicates that the flow becomes more stable at the higher $N_{Re-\theta}$ values.

The effect that N_{Re-u} has on vorticity along bottom plate and along the sink tube wall is shown in Figs. (4.32) and (4.33). As N_{Re-u} increases, the rate of increase in vorticity is greater in the region R < 0.2 elsewhere in the vortex chamber. At the corner of the sink tube the vorticity increases by a factor of 2-1/4 as N_{Re-u} increases from 8 to 16. Within the sink tube, the vorticity also increases as N_{Re-u} increases.
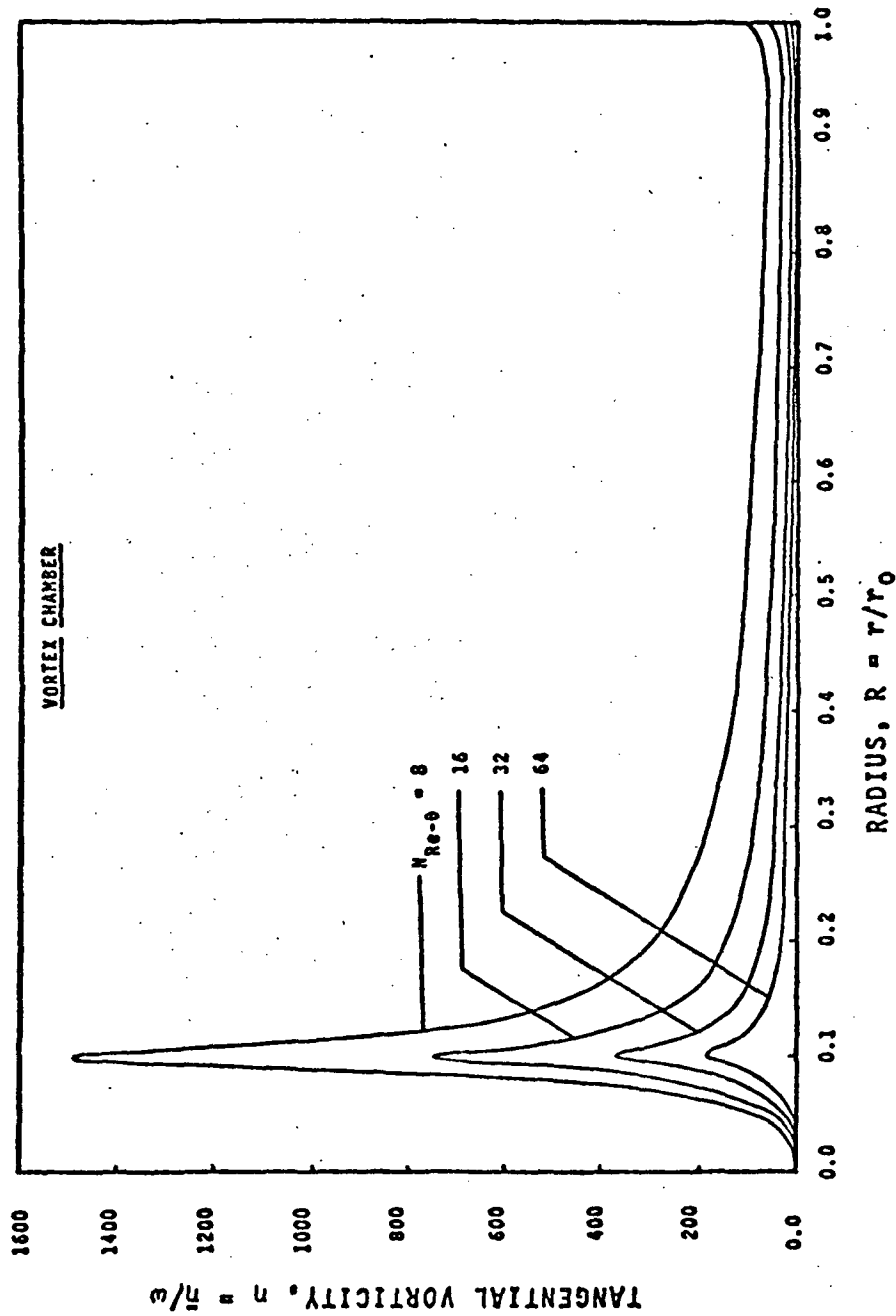
Figure 4.30 Variation of Tangential Vorticity,
η, with Radius, R, on Bottom Plate
(for Different $N_{Re-\theta}$ and N_{Re-u} = 8)
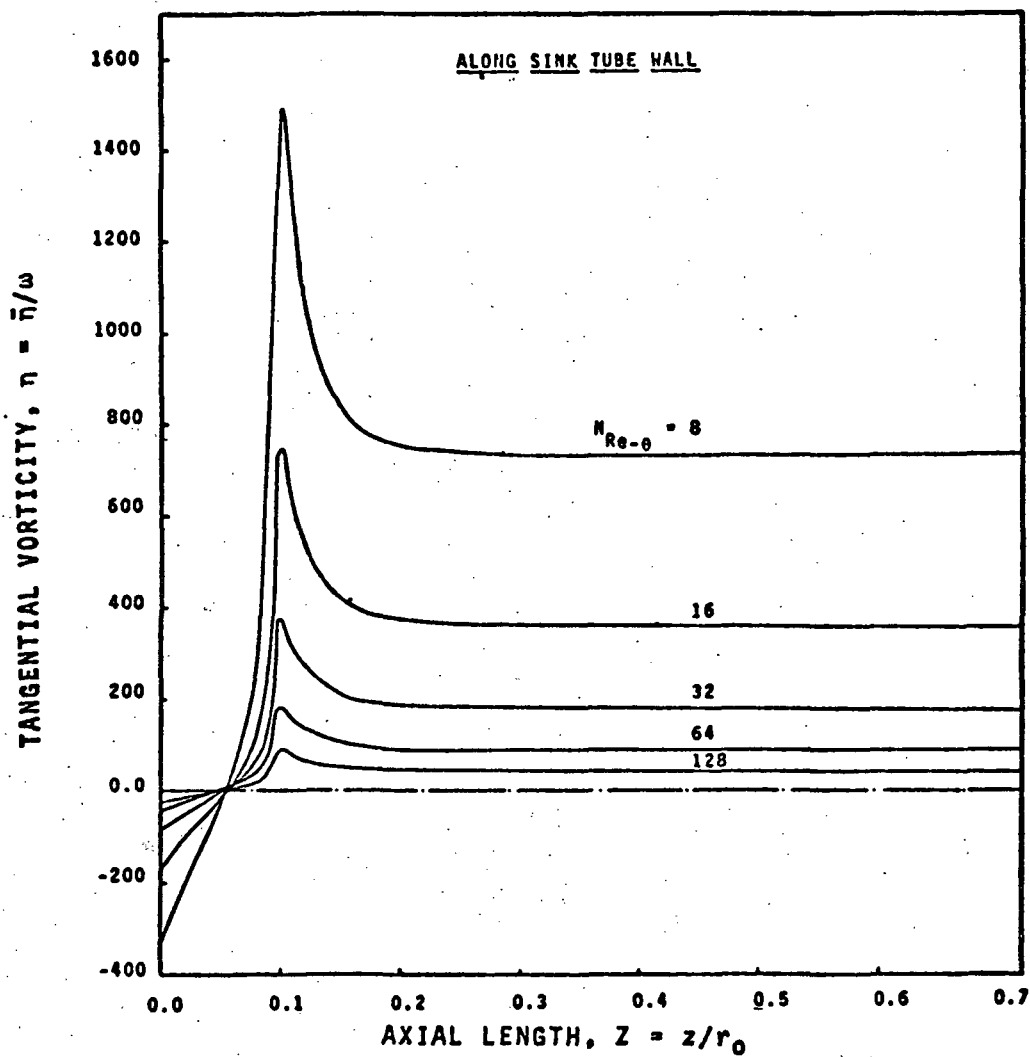
Figure 4.31   Variation of Tangential Vorticity,
n, with Axial Length, Z, on Sink
Tube Wall (for Different $N_{Re-\theta}$ and
$N_{Re-u} = 8$)
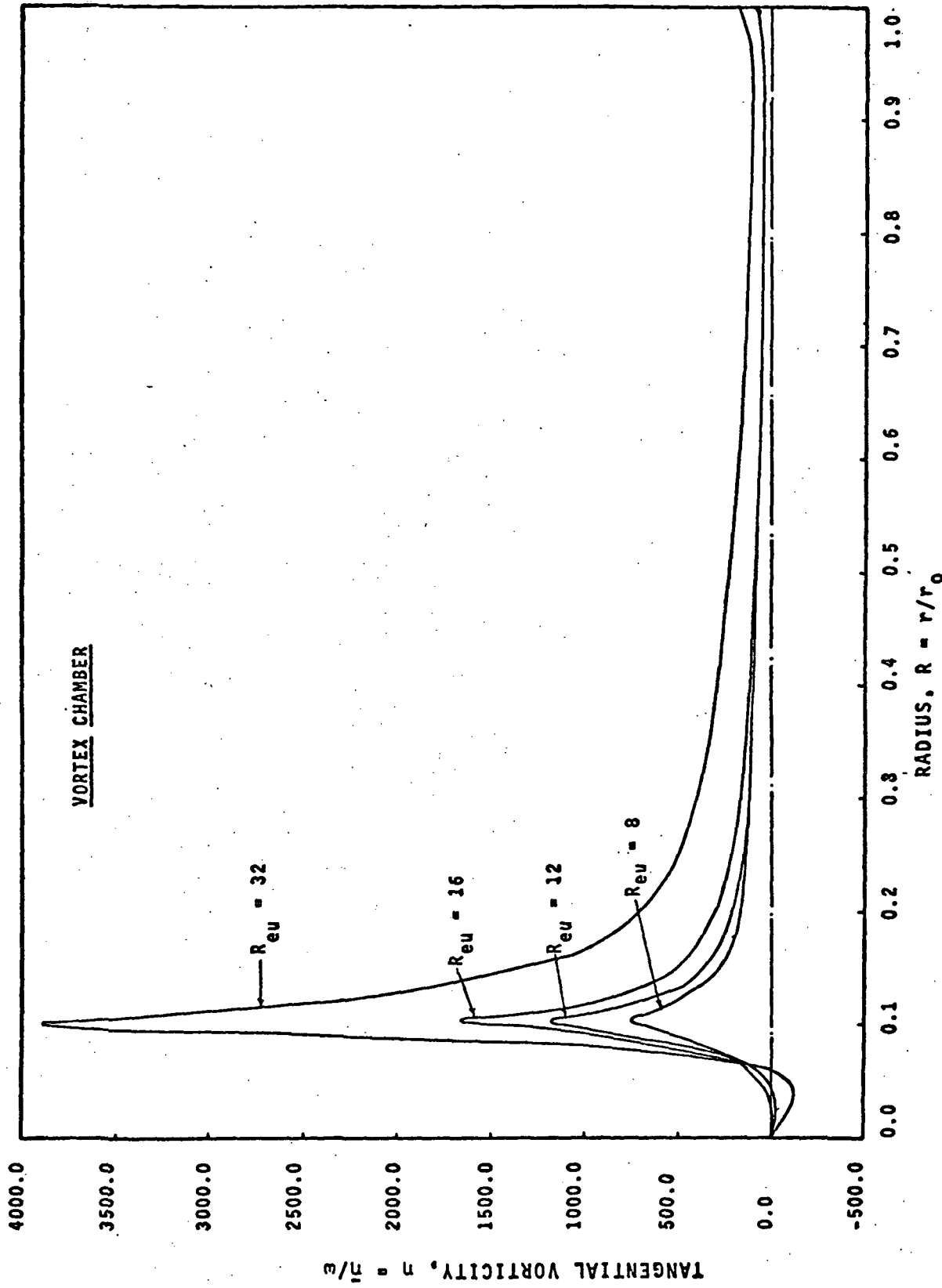
Figure 4.32 Variation of Tangential Vorticity, η, with Radius, R, on Bottom Plate (for Different N_{Re-u} and $N_{Re-\theta} = 16$)
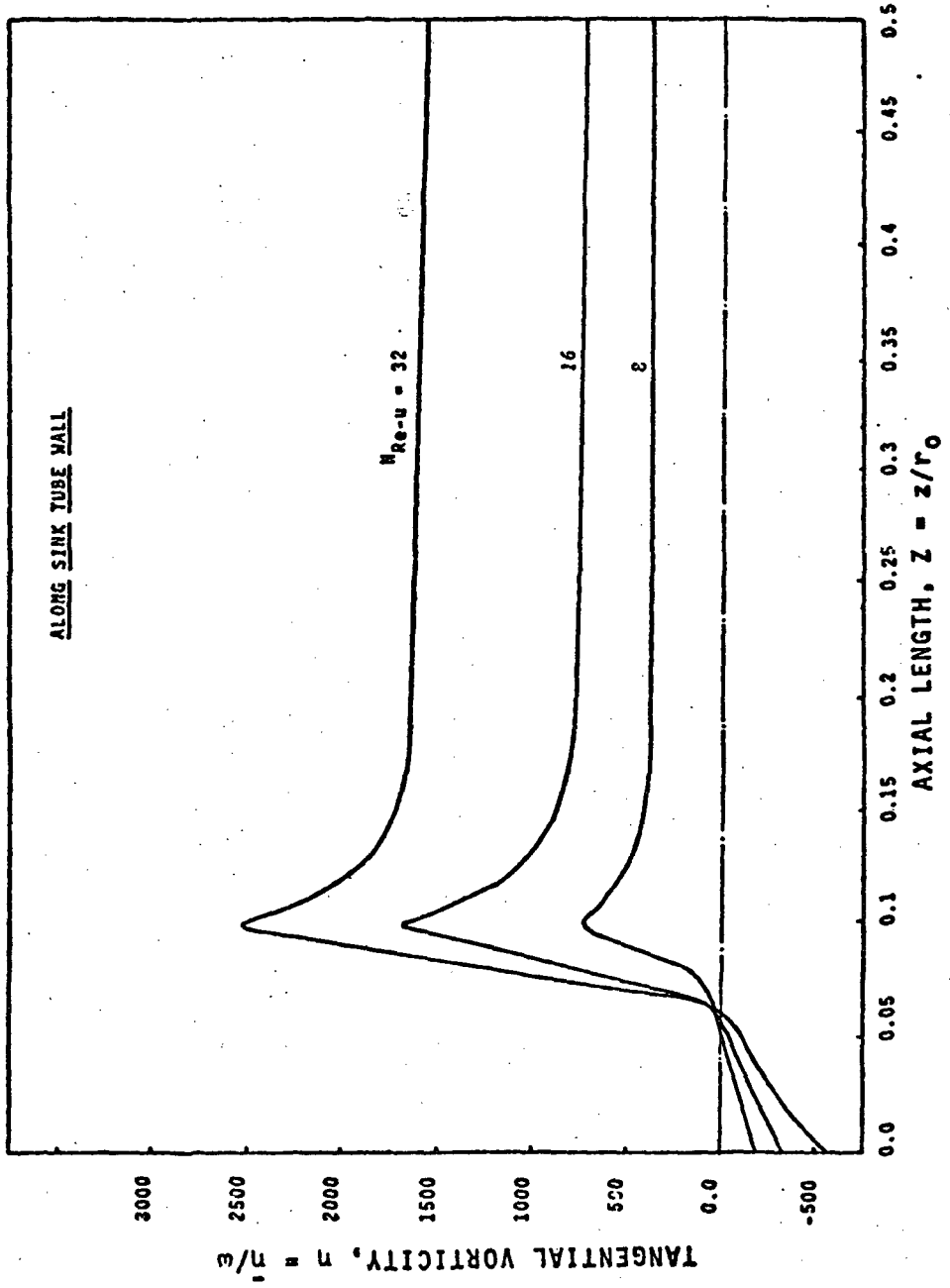
Figure 4.33 Variation of Tangential Vorticity, n, with Axial Length, Z, on Sink Tube Wall (for Different N_{Re-u} and $N_{Re-\theta} = 16$)

Thus at high flow rates, more vortices are created near the solid boundaries as well as near the corner.

Figures (4.34) and (4.35) illustrate the constant tangential vorticity lines for two different sets of values of radial and tangential Reynolds numbers. It is evident that the highest vorticity occurs at the sink tube corner. As discussed before this is the location at which instability in the flow begins. It is also observed from Fig. (4.35) that vortices are produced in the flow at the higher radial Reynolds numbers. The vorticity lines are found to be parallel to geometrical axis in the downstream section of the sink tube. A zero vorticity line exists in the midplane of the vortex chamber plates for $R > 0.3$. The curvature of the zero vorticity line, near the sink corner increases as the flow rate increases.
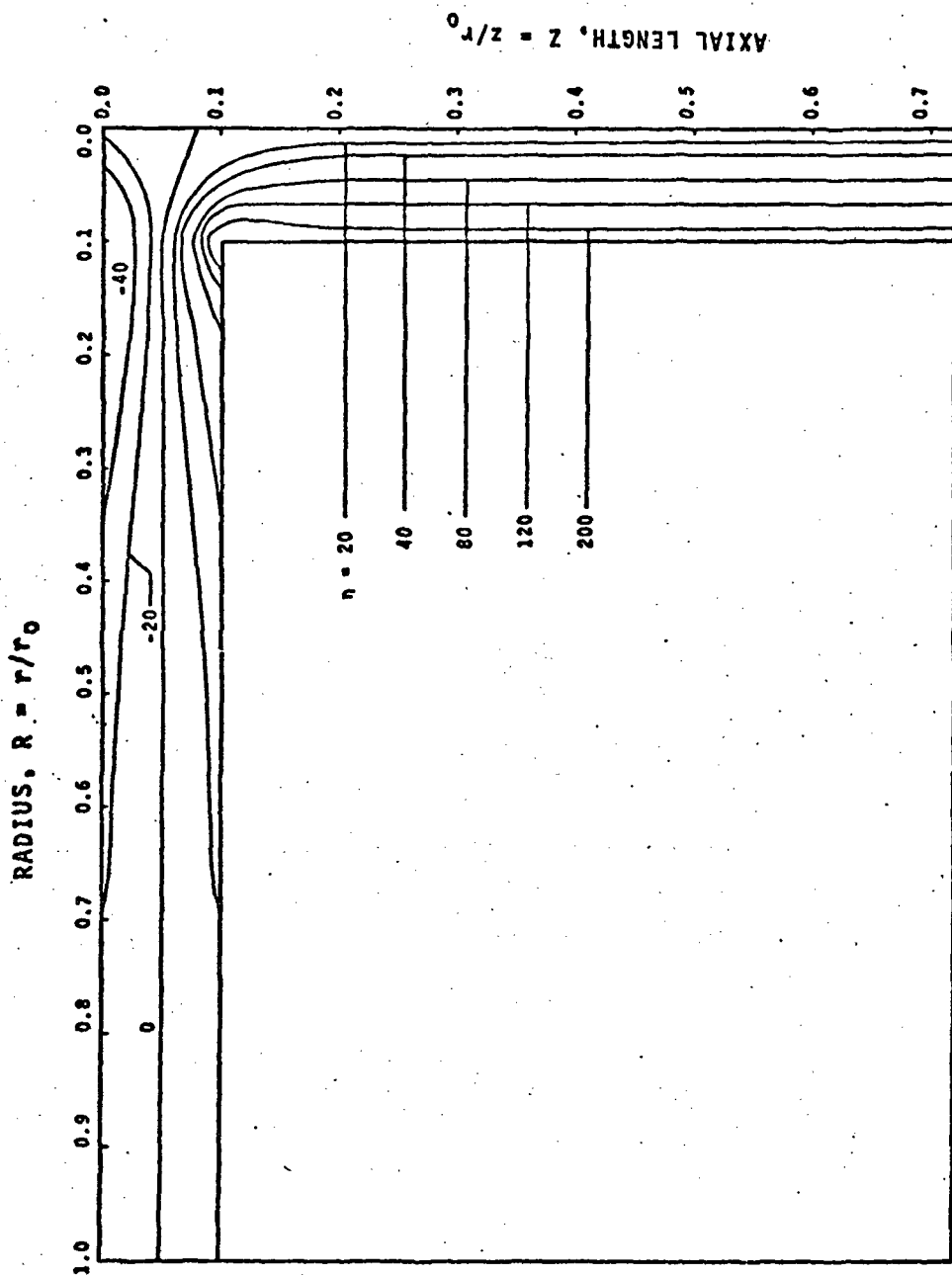
Figure 4.34   Constant Vorticity Line Pattern (for $N_{Re-u} = 4$ and $N_{Rp-\theta} = 16$)

AXIAL LENGTH, Z = z/r_0

RADIUS, R = r/r_0
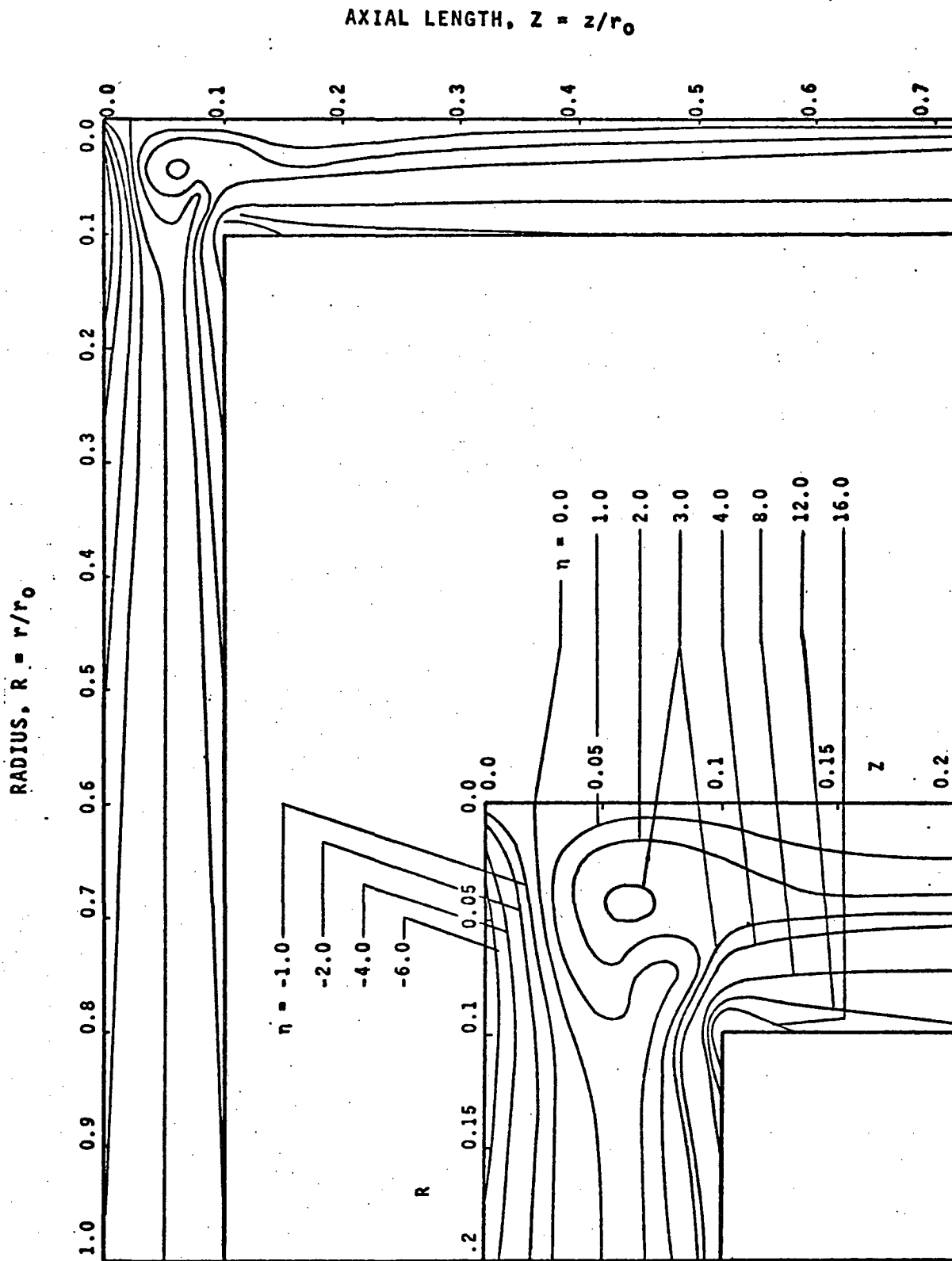
Figure 4.35   Constant Tangential Vorticity Line Pattern
(for $N_{Re-u}=8$ and $N_{Re-\theta}=512$)

V. EFFECT ON FLOW PATTERN WITHIN SENSOR DUE TO CONFIGURATION CHANGES

5.1 Effects Due To Variation of Vortex Chamber Radius, r_o

To determine the effect, if any, that the variation in vortex chamber radius had on the flow pattern within the sensor, a numerical computation was undertaken for assigned values of vortex chamber radii of 5, 10, 15 and 20 inches respectively. For each radius the vortex chamber height (h) as well as the sink tube radius (r_i) were held constant at 1 inch. In each case the flow rate and rotation were also assumed to be constant. The following conclusions were drawn from the numerical results.

1) The streamlines in both the vortex chamber and the sink tube moved closer to the wall surfaces as, the chamber radius was decreased.

2) As shown in Fig. (5.1), the tangential velocity, V, in the vortex chamber (at the same radial location, R) decreases as the vortex chamber radius increases. However, in the immediate vicinity of the sink region and also within the sink tube there is no noticeable effect on the velocity, V.

3) There was only a negligible effect on the tangential vorticity throughout the vortex chamber and the sink tube.

4) There was a negligible effect on the radial and axial velocities throughout the vortex chamber and the sink tube.
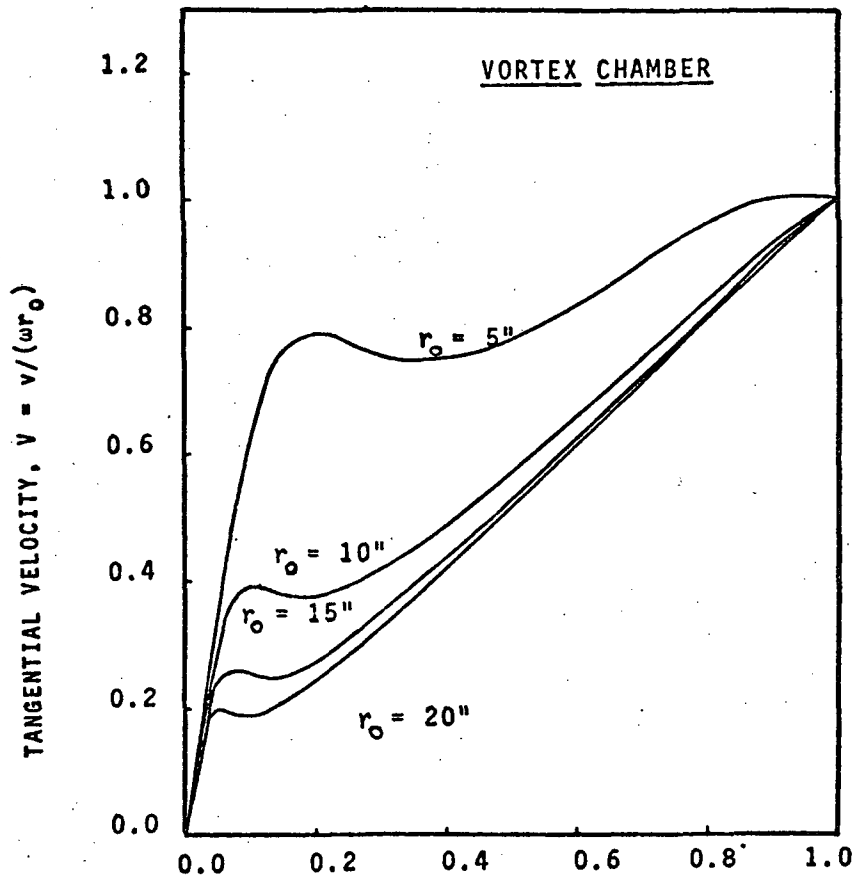
RADIUS, $R = r/r_0$

Figure 5.1   Variation of Tangential Velocity, V, with Radius, R, for Different Sizes of Vortex Chamber (for $N_{Re-u} = 16$ and $N_{Re-\theta} = 256$)

5.2 Effect Due to the Variation of the Sink Tube Radius r_i

To determine the effect of the variation in the sink
tube radius on the flow pattern within the sensor, a numerical
computation was undertaken for assigned values of sink tube
radii of 1/2, 5/8, 3/4, 7/8, 1 and 1-1/8 inches respectively.
For each sink tube radius both the vortex chamber height and
vortex chamber radius were held constant at 3/4 and 10 inches
respectively. For constant flow rate and rotation the
numerical results revealed the following conclusions.

1) As shown in Fig. (5.2), the tangential velocity in
the vortex chamber near the sink tube region in-
creases as the sink tube radius is decreased. An
increase in the peak value of the tangential
velocity is also noticed at the sink tube entrance.

2) The distance into the sink tube required to obtain
constant axial velocity in the downstream section
decreased as the sink tube radius was increased.

3) The radial velocity within the vortex chamber near
the sink tube region (i.e., for R < 0.1) increased
as the sink tube radius was decreased.

4) The tangential vorticity, near the sink region in
the vortex chamber (at the junction of the vortex
chamber and sink tube) and within the sink tube,
increased as the sink tube radius was decreased.

5) The slope of the zero vorticity line, at the
entrance section of the sink tube, decreased as the
sink tube radius was decreased. This resulted in
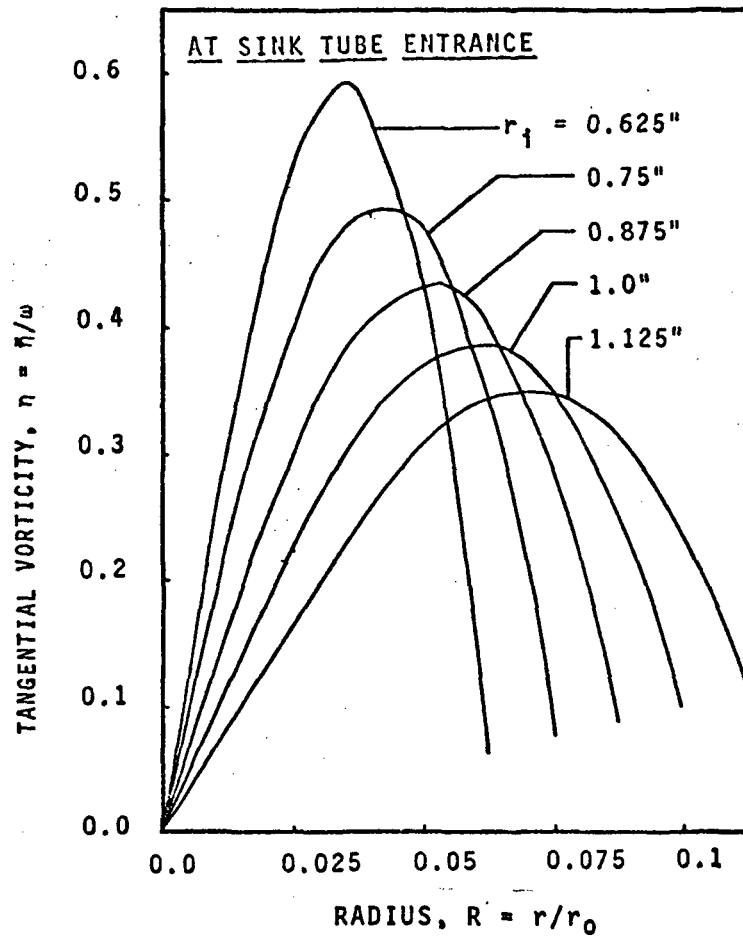
Figure 5.2   Variation of Tangential Velocity,
             V, with Radius, R, for Different
             Sizes of Sink Tube

the intersection of the zero vorticity line with the sensor's geometrical axis which is moved closer to the center plane of the vortex chamber.

5.3 Effect Due to the Variation of Vortex Chamber Spacing h

To determine the effect of the variation in vortex chamber spacing on the flow pattern within the sensor, a numerical computation was undertaken for assigned values of vortex chamber spacing of 1, 1.2, 1.4, 1.8 and 2 inches respectively. For each spacing the vortex chamber radius as well as the sink tube radius were held constant at 10 inches and 1 inch respectively. For constant flow rate and rotation, the numerical results revealed the following conclusions.

1) The tangential velocity decreases at the sink tube entrance, as the spacing increases [Fig. (5.3)]. The distance into the sink tube, where the flow becomes equivalent to a solid body rotation, also increases slightly. As the vortex chamber spacing decreases, a peak tangential velocity is observed midway between the geometrical axis and wall of the sink tube. As the spacing h was increased, the peak value of tangential velocity decreased and moved smoothly either toward the geometrical axis or sink tube wall. The same result was obtained experimentally by Lu [32]. For the higher values of spacing h, since the velocity profile was not affected by the boundary layer, the peak value of velocity moved closer to either the geometrical axis·
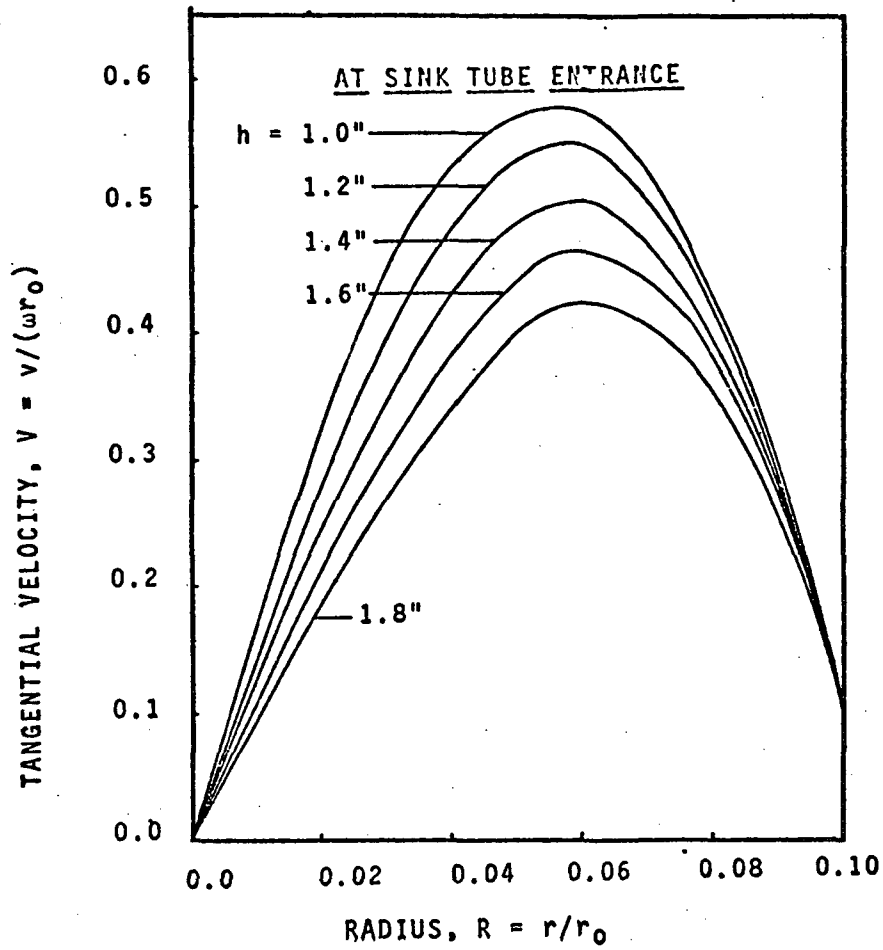
Figure 5.3   Variation of Tangential Velocity,
V, with Radius, R, for Different
Sizes of Vortex Chamber (for
N_{Re-u} = 16 and $N_{Re-\theta}$ = 256)

or the sink tube wall. From its peak value, the tangential velocity decreased rapidly but smoothly to both the geometrical axis and sink tube wall.

2) The uniform entrance radial velocity to the vortex chamber decreased as the spacing was increased. The radial velocity at the entrance section of the sink tube also decreased for increased spacing heights.

3) The streamlines, at the sink tube entrance, appeared to move closer to the geometric axis as the spacing height was increased. That is to say that the bulk of the flow was closer to the geometrical axis.

4) The distance into the sink tube where the axial velocity became a constant, increased as the spacing height was increased.

5) The tangential vorticity along the solid surfaces of the vortex chamber as well as at the sink tube entrance, decreased as the spacing h was increased. There was, however, no appreciable effect on the tangential vorticity along the sink tube wall.

6) The entrance length into the sink tube increased as the spacing height was increased. (The entrance length is defined as the depth into the sink tube where radial velocity changes direction from inward to outward).

VI. EXPERIMENTAL INVESTIGATION

6.1 Description of Apparatus

The apparatus which was constructed and assembled consists of a vortex chamber, three sink tubes, a high pressure as well as a low pressure regulator, an air filter, an air dehydrator, a flow meter, a manifold, a probe assembly, a positive drive assembly and the necessary gages, valves and piping. The vortex sink rate sensor, in which a sink tube is assembled to the vortex chamber, was so designed as to permit a number of possible combinations of physical dimensions. A constant temperature Hot Wire Anemometer was used in obtaining the velocity distributions.

A schematic of the vortex sink rate sensor is shown in Fig. (6.1). The vortex chamber is made of two circular plexiglass disks held apart by a porous coupling securely mounted at the periphery of the circular disks. One circular disk has a threaded opening at its center to permit the attachment of a sink tube. The second circular disk is attached, by means of a flanged coupling, to a drive shaft that is supported on two bearings. The drive shaft, through a speed reduction gear box and sprocket wheel and chain drive, is connected to a variable low speed motor to assure concentricity with the axis of symmetry of the circular disks. Both plexiglass disks have grooves on their surfaces for proper setting of the porous coupler. To provide rigidity and uniformity of spacing between the disks eight spacers,

104
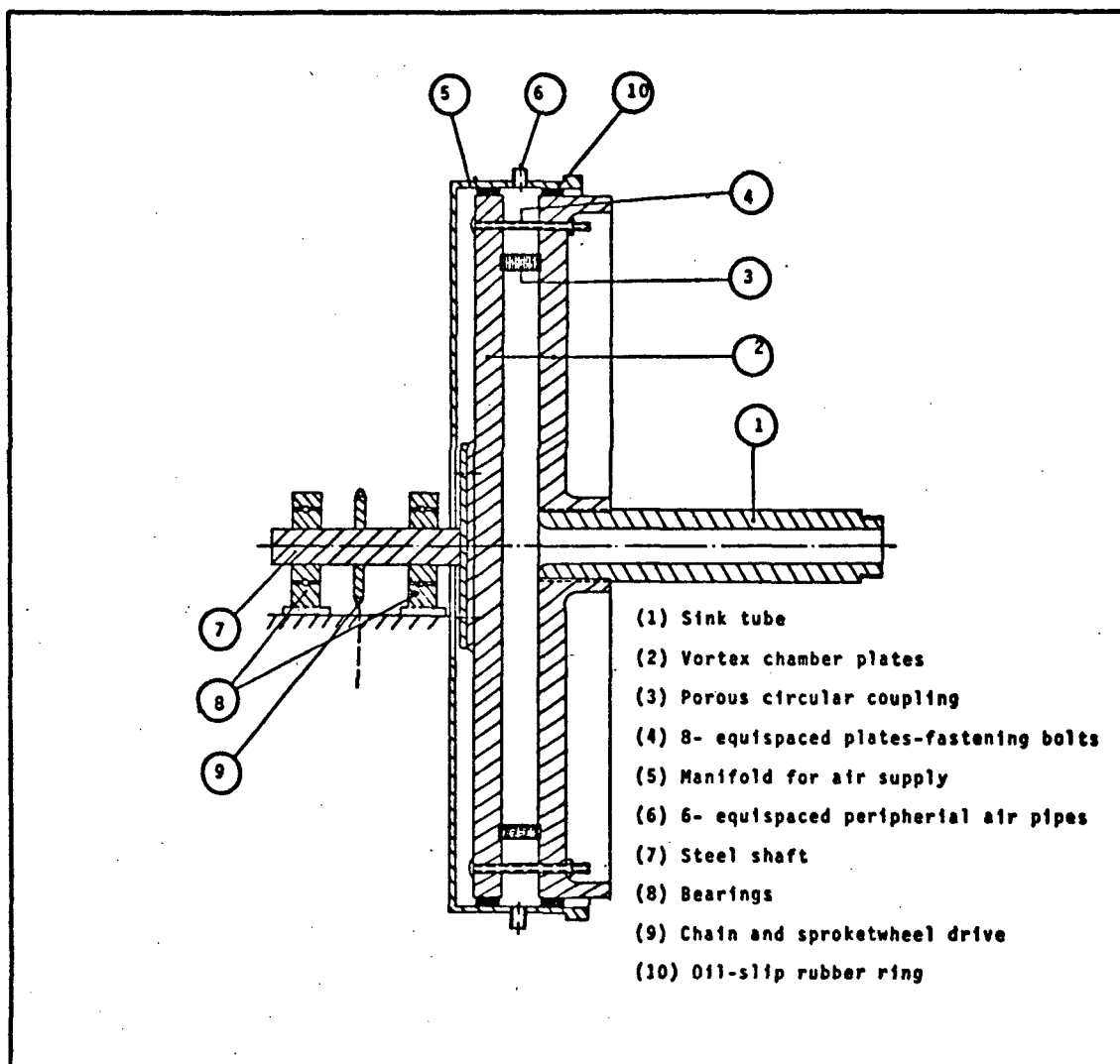
Figure 6.1   Vortex Sink Rate Sensor

(1) Sink tube

(2) Vortex chamber plates

(3) Porous circular coupling

(4) 8- equispaced plates-fastening bolts

(5) Manifold for air supply

(6) 6- equispaced peripherial air pipes

(7) Steel shaft

(8) Bearings

(9) Chain and sproketwheel drive

(10) Oil-slip rubber ring

symmetrically positioned around the circumference, are used.

The vortex sensor is mounted within a manifold assembly in such a manner that its axis of rotation is horizontal. The sensor rotates freely within the manifold assembly. As a result of a sealed ring pressfitted to the assembly the possibility of air leakage from the sensor is negligible. The manifold assembly is rigidly fastened to a steel frame platform to which the variable speed motor and speed reducer are also mounted. The design permits a vortex sensor speed range from 0 to 35 revolutions per minute.

Three interchangeable plexiglass sink tubes of 1, 1-1/4 and 1-1/2 inches inside diameters were used to vary the sink tube sizes. Two sets of such sink tubes, one of twelve and the other of twenty-four inches length were employed. The sink tubes were designed to enable pitot tube pressure measurements as well as hot wire velocity measurements at various stations along the length of the sink tube as well as along any given radius.

The porous coupler, used in the vortex chamber, was similar to the one used and discussed by Burke [6]. The coupler was made from stacked 0.0625 inch thick steel rings with an inside diameter of 20 inches. Triangular grooves of 0.0227 inches in width (approximately) and 0.03 inches in depth were cut radially towards the center of each of the rings. The grooves were cut, side by side, such that on the inside circumference of the ring, they were continuous, that was, without any flat tops between grooves. In all approximately 2700

such grooves were cut around the periphery of each ring. The rings were stacked with the grooved side of one ring against the smooth side of the next ring. The stacked rings were held under compression in the assembly of the sensor forming triangular nozzles of 0.375 inches in length. The aggregate jet area was about twenty-five percent of the inside area of the coupler. The coupler was practically uniform throughout its circumference. The rings, therefore, could be stacked to any desired height from a minimum of 1 inch to a maximum of 1-1/2 inches. This arrangement provided the means by which different coupler heights could be achieved.

The static pressure probe, as shown in Fig. (6.2), was fabricated from two stainless steel tubes of 0.06 and 0.03 inches outside diameter both having a thickness of 0.01 inches. The larger diameter tube was tapered to a conical shape at its closed end. In its periphery at distance of 0.1625 and 0.1937 inches from the closed end, are eighteen equispaced 0.005 inch drilled holes arranged in a manner resembling a pizometer tube. The smaller diameter tube at its closed end was chamfered and a 0.01 inch hole was drilled through the tube at 3/4 of an inch from its closed end. The tubes were assembled in such a manner, the smaller tube inside the larger tube was then soldered to the inner tube. Static pressure measurements are obtained by connecting one open end of the pressure transducer, to the static pressure probe, while the other is open to the atmosphere. The circuit diagram for the pressure transducer is shown in Fig. (6.3)
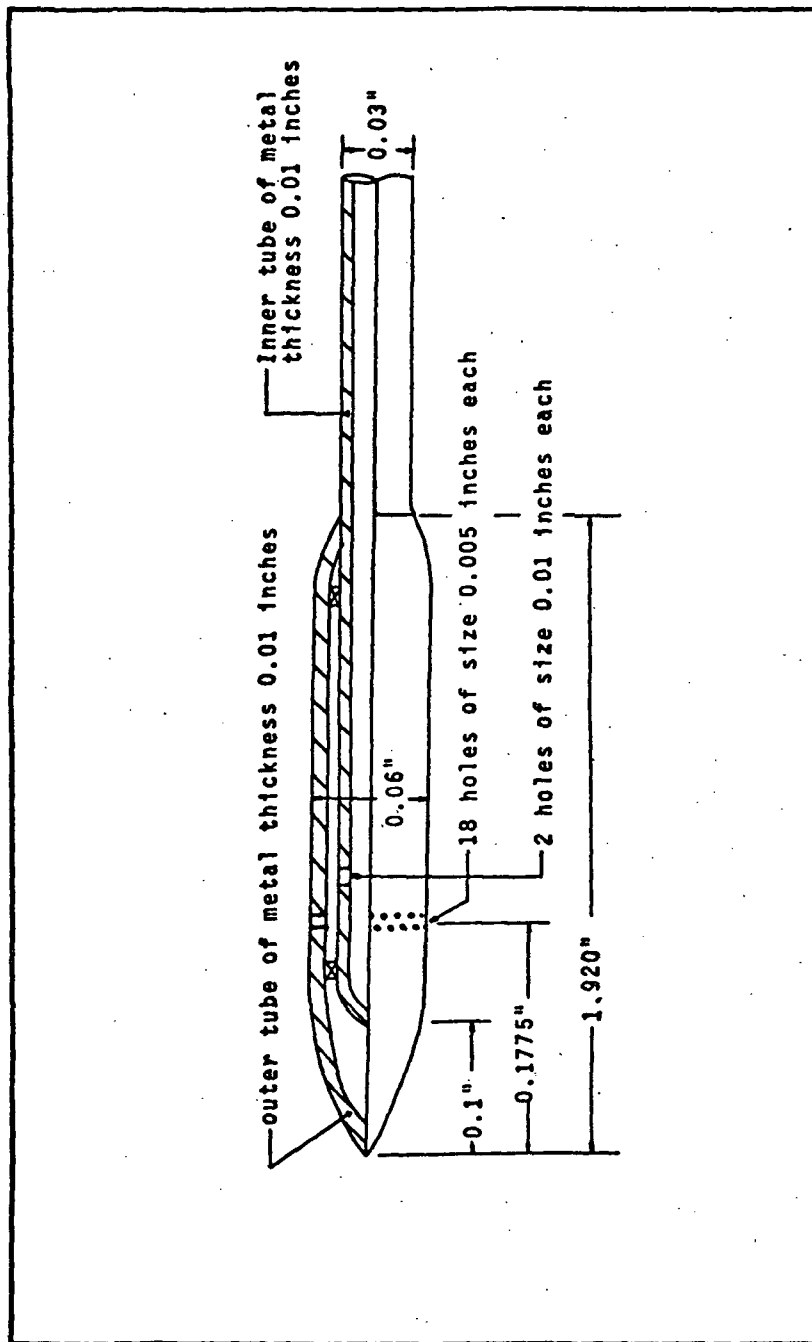
Figure 6.2   Static Pressure Probe
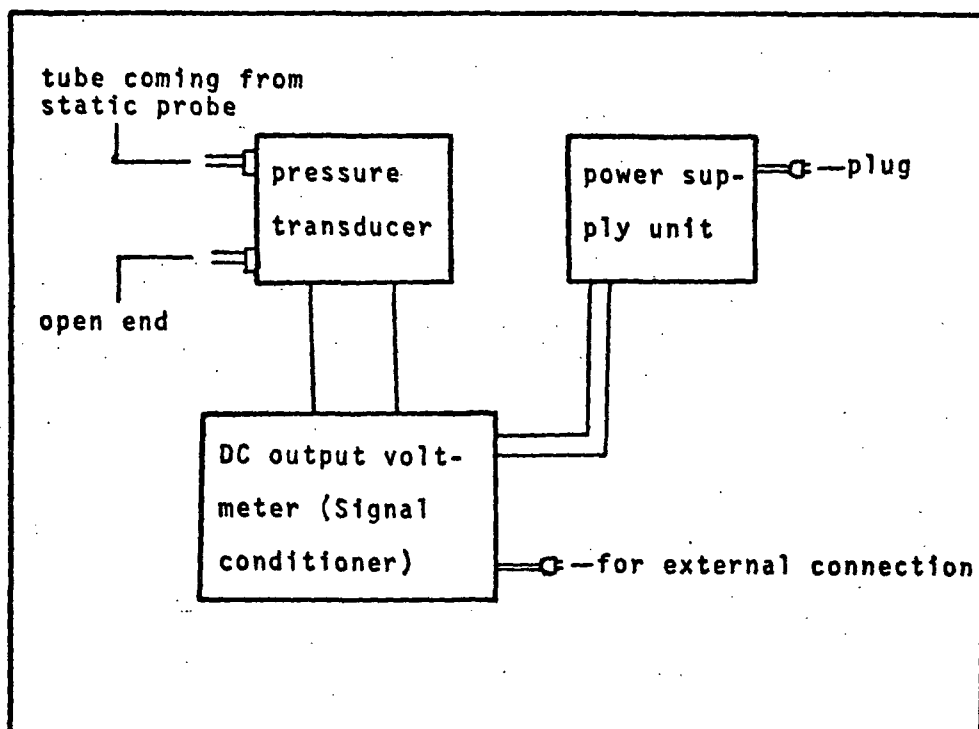
Figure 6.3   Pressure Transducer Unit

The schematic of the probe holder stand is shown in
Fig. (6.4). The probe support mechanism has been so designed
with a rack and pinion arrangement, to allow for a longitu-
dinal movement of the static pressure probe and probe holder
along the sink tube length. The probe support mechanism has
also been so designed to provide means by which the static
pressure probe and probe holder can be moved in a vertical
direction normal to and intersecting with the sink tube axis.
For all movements it is possible to maintain the static
pressure probe and hot wire probe holder axis parallel to the
sink tube axis, at all times.

The velocity distribution throughout the sink tube is
obtained by use of a constant temperature hot wire probe as
shown in Fig. (6.5). The hot wire probe used in conjunction
with the anemometer is supported by a pin-joint on its own
support as shown in Fig. (6.6). The hot wire probe can easily
be positioned anywhere within the sink tube. The probe is
also capable of being rotated spherically, so as to position
the probe, to be perpendicular to the resultant velocity.
A disc worm wheel and worm screw arrangement provides the
mechanism by which an azimuth angle of rotation can be obtained.
A string and roller arrangement provides the means by which
a longitudinal angle can be obtained. Thus the hot wire probe
can easily be positioned to measure the resultant velocity.
From the measurement of the resultant velocity, and the longi-
tudinal and azimuth angles, the axial, radial and tangential
velocity components can be calculated.

(1) Rack and pinion for horizontal drive
(2) Probe support rod
(3) Circular rotary plate
(4) Handle (with worm for circular plate rotation)
(5) Holding C-clamp with vertical movement
(6) Stand for probe support
(7) Bottom plate with groved slot
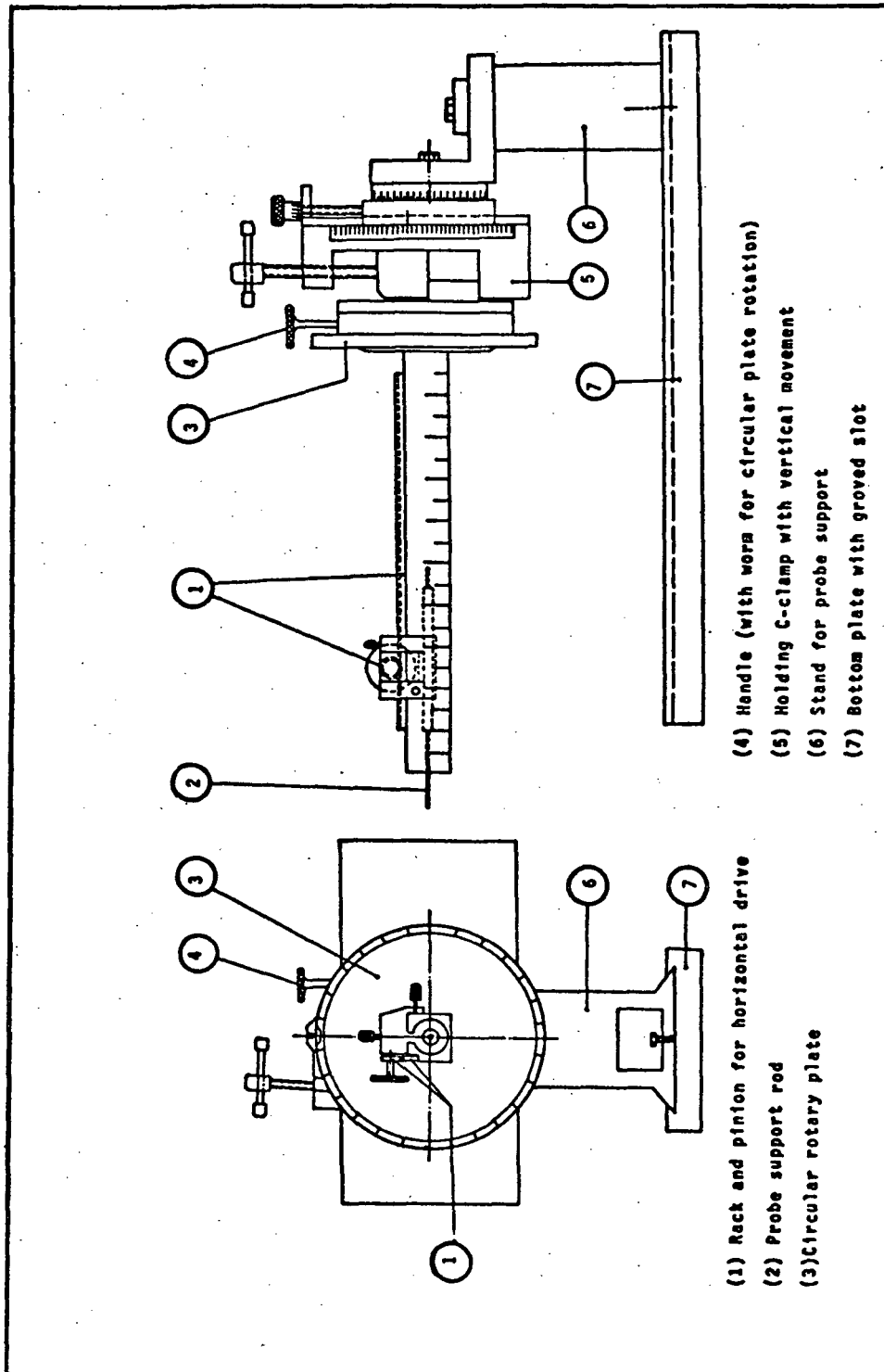
Figure 6.4   Probe Support Stand

terminal

probe body
hot-wire supported rod
hot-wire element

DISA TYPE.- 55F21
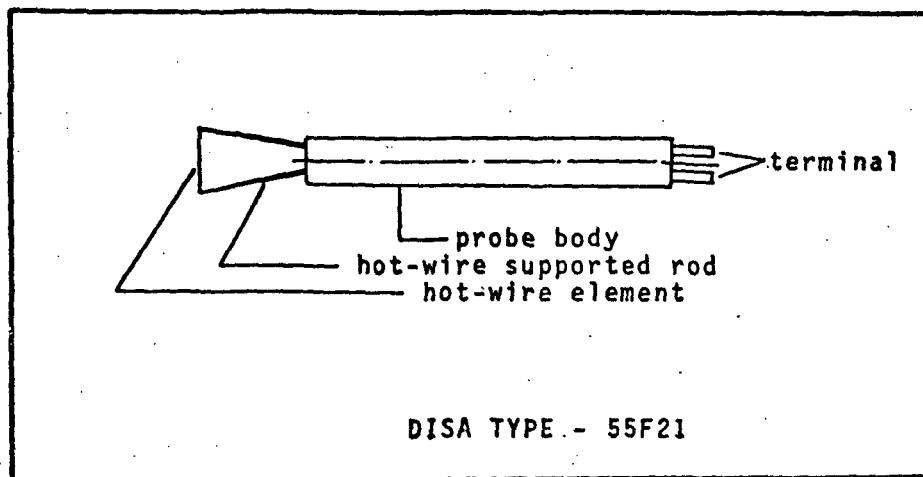
Figure 6.5   Hot wire probe
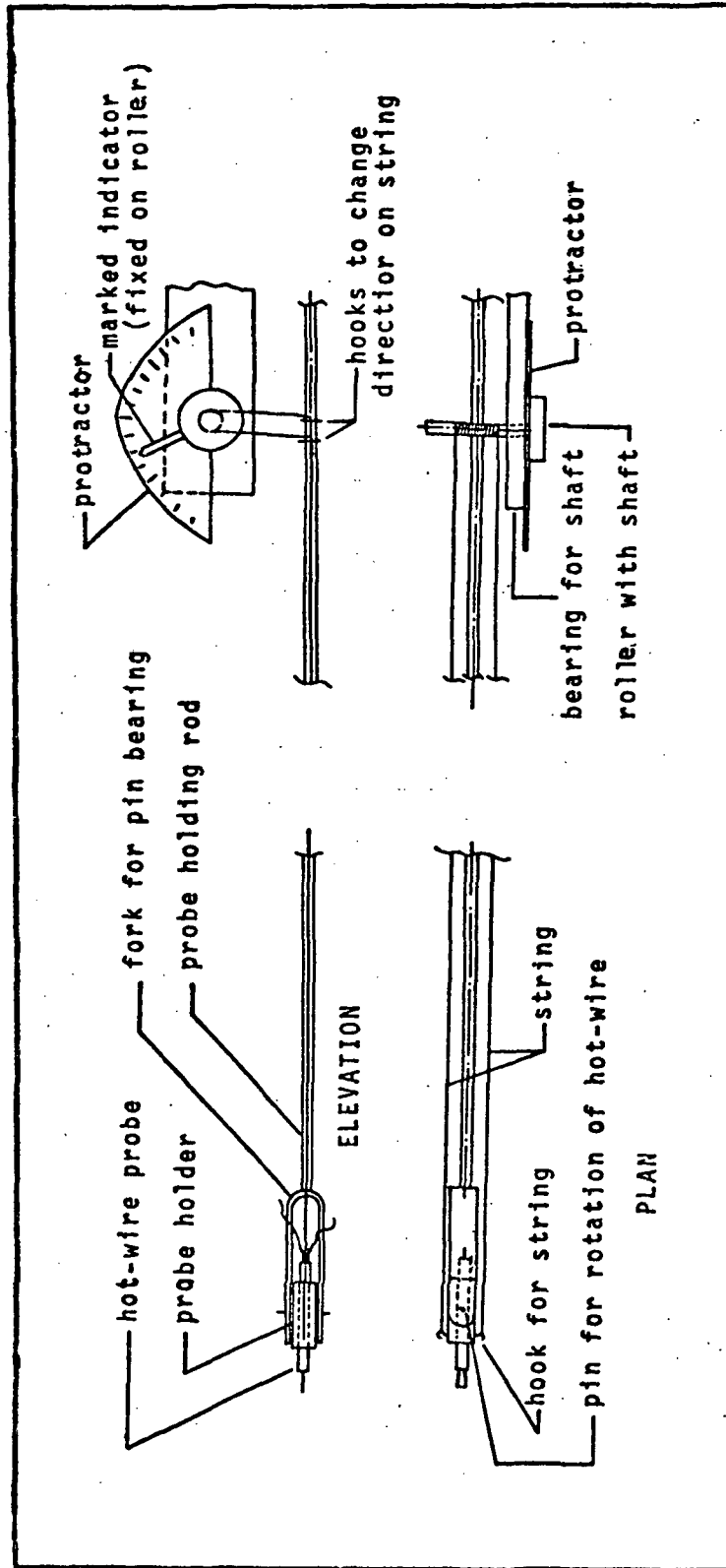
Figure. 6.6   Longitudinal Rotation Mechanism for the Hot Wire Probe

A block diagram of the DISA constant temperature hot
wire anemometer (No: 55A01) used in this investigation is
shown in Fig. (6.7). The anemometer, in essence consists of
a fine electrically heated wire which is convectively cooled
when placed in an air stream. The resistance of the wire,
which increases linearly with temperature, is uniquely related
to the mean speed of the air stream and the current. The
equation for calculating the velocity with this anemometer is

$$\frac{V'^2}{\Omega} = A + B \sqrt{\bar{W}} \qquad (6-1)$$

where V' is the bridge voltage, $\bar{W}$ is the mean flow velocity,
Ω is the probe operating resistance, and A and B are con-
stants which depend only on the physical properties of the
wire and fluid.

This relationship which governs the equilibrium behavior
of the wire is in reality a heat balance. The left hand
side of the equation is proportional to the heat input of the
wire, while the first-term on the right hand side is proportional
to the forced convection cooling. With the constant temperature
hot wire anemometer, a feedback amplifer system is employed
to keep the probe resistance and hence also the probe tempera-
ture constant. Fundamentally, the measured quantity is the
power required to keep the temperature constant.

The hot wire probes that were referred to earlier and used
in this investigation are the DISA type No: 55F21 and are
shown in Fig. (6.4). The wire itself is a platinum-plated
tungsten, 5μm in diameter, and is stretched across two needle
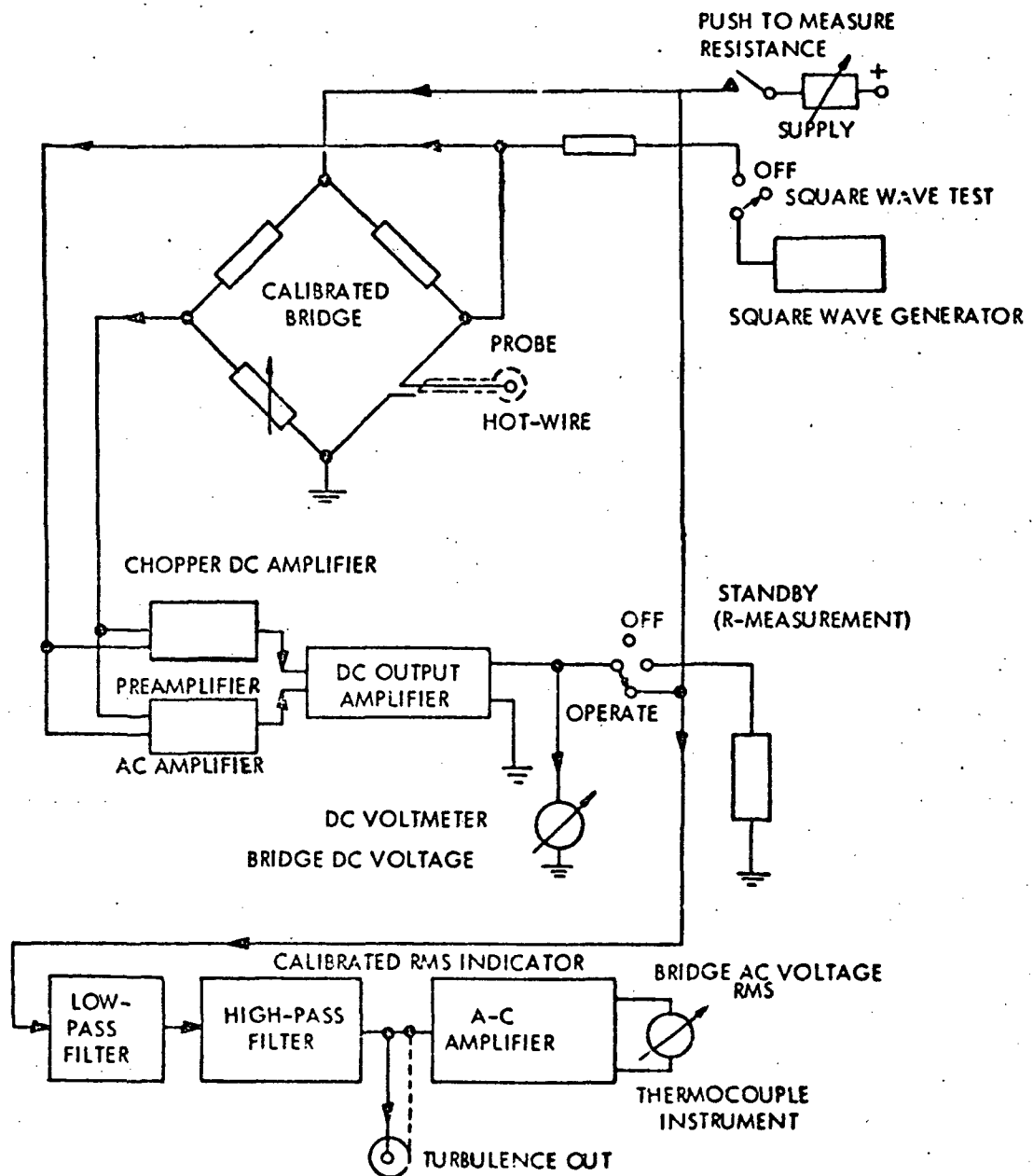
Figure 6.7   BLOCK DIAGRAM OF DISA CONSTANT-
TEMPERATURE HOT-WIRE ANEMOMETER

supports. The probe resistance is 4.0Ω. The average flow velocity is indicated by a multirange D.C. bridge voltmeter which has an accuracy of ± one percent. This accuracy was improved by use of zero shift D.C. voltages of 1, 2, 5 and 10 volts. This also permitted the meter operation in the lowest full scale range. A square wave generator is incorporated into the instrument to allow checking actual dynamic responses under operating conditions.

A DISA type No: 55D10 linearizer is connected to the anemometer to determine the linear relationship between the velocity and the bridge voltage.

The air flow system is shown in Fig. (6.8). Filtered and metered low pressure air is supplied to the vortex sensor through six symmetrically spaced inlets which are on a manifold attached to the vortex chamber. Compressed air is first passed through a dehydrator and then reduced to approximately 5 psig. pressure as it passes through a high pressure regulator. The air is then filtered and its flow regulated as it passes through a low pressure regulator. The air flow rate is measured by means of a flowmeter and finally the air is supplied radially to the vortex chamber of the sensor.
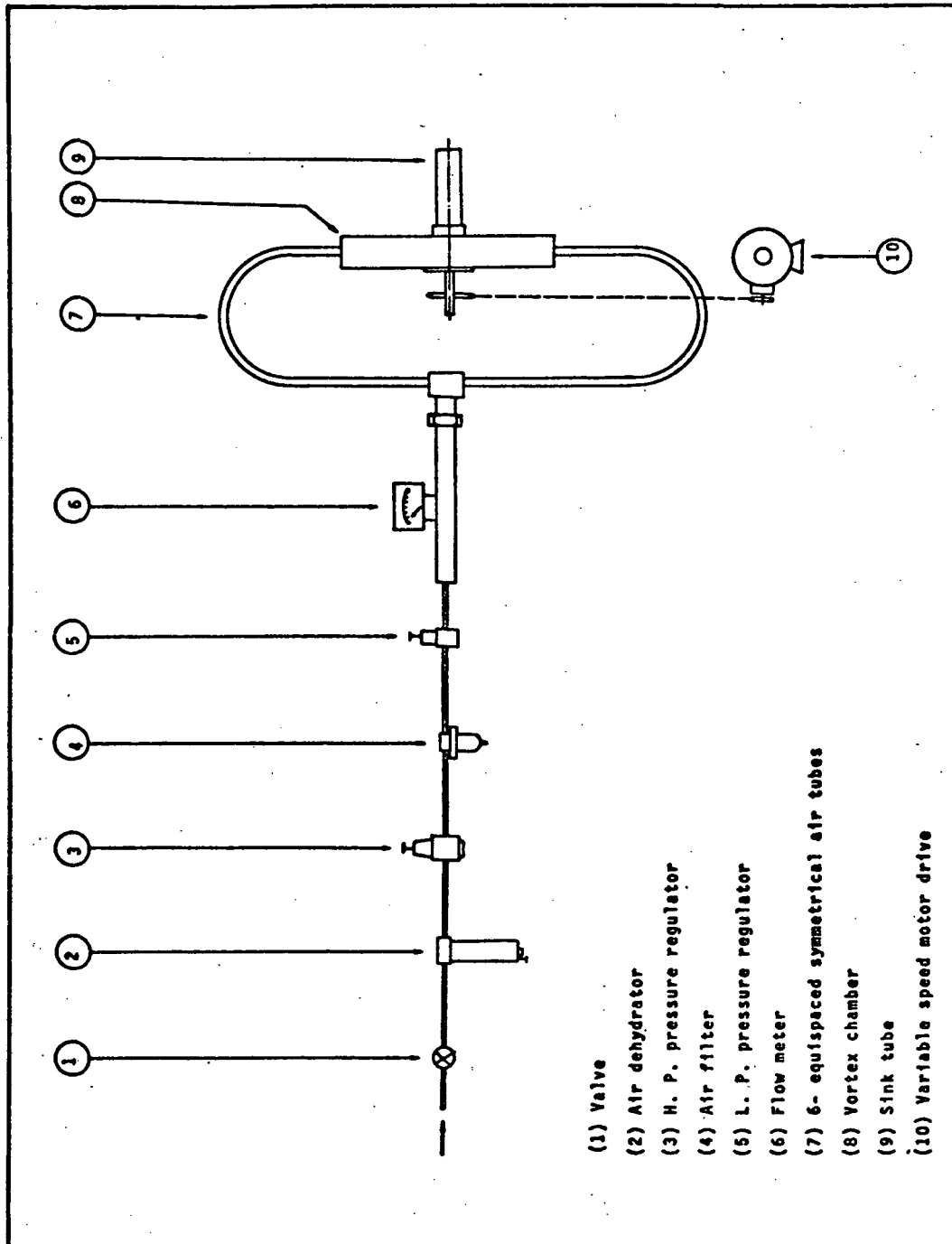
Figure 6.8   Air Flow Circuit and Components

(1) Valve
(2) Air dehydrator
(3) H. P. pressure regulator
(4) Air filter
(5) L. P. pressure regulator
(6) Flow meter
(7) 6- equispaced symmetrical air tubes
(8) Vortex chamber
(9) Sink tube
(10) Variable speed motor drive

6.2 Test Procedures

As mentioned under the description of apparatus, the vortex sink rate sensor was designed to allow a number of possible combinations of its physical dimensions. The vortex chamber has a radius of 10 inches. Its design, however is such that through use of spacers the distance between disks can be changed. This arrangement makes possible a number of slenderness ratios (r_i/h) for experimental purposes. Three interchangable sink tubes of 1, 1-1/4 and 1-1/2 inches in diameter make possible a number of different chamber to sink tube radii ratios. A variable speed motor further provided the means of obtaining a sensor speed of rotation range from 0 to 35 revolution per minute.

For each test run velocity profiles as well as static pressure distributions were obtained at a number of different axial locations within the sink tube. The axial locations, along the sink tube, selected for recording measurements were Z equal to 0.0, 0.25, 0.5, 0.75, 1.0, 1.25, 1.5, 1.75, 2.0, 2.5, 3.0, 3.5, 4.0, 5.0, 6.0, 9.0, 12.0, 15.0, 18.0, and 21.0 inches respectively. At each axial location the radius was traversed, with measurements in general taken at r values of 0.0, $0.1r_i$, $0.2r_i$, $0.3r_i$, $0.4r_i$, $0.5r_i$ inches respectively where r_i was the inside radius of the sink tube. Three sink tubes were used with respective inside radii of 0.5, 0.625 and 0.75 inches.

Prior to conducting any of the experiments, all instruments were calibrated according to the standard procedure.

However, it is considered desirable to include here a brief discussion of the calibration and technique of using the hot wire probe. The hot wire probe was calibrated with the use a special pitot tube shown in Fig. (6.9) in conjunction with a transducer. The pitot tube and the hot wire probe both were positioned at the immediate exit of the sink tube in such a manner as to have symmetry with respect to the sink tube axis. The longitudinal angle of the hot wire probe was set at zero. Then as the air flow rate, for zero rotation, was varied both the pitot tube and the hot wire probe readings were recorded through use of the exponential and gain adjustments on the linearizer, the linear relation between the anemometer voltage and air velocity was obtained. This therefore resulted in a hot wire probe calibration curve shown in Fig. (6.10).

The calibration curve,relating to the probe longitudinal angle and the protractor angle,is given in Fig. (6.11).

A calibration curve was also plotted to correct for any lag existing within the roller-string mechanism. One straight line curve was for the clockwise rotation of the roller (pointer and protractor) and the second curve was for the counterclockwise rotation of the roller. The protractor was graduated in degrees and as a reading was recorded, then with the appropriate calibration curve for roller rotation, the probe longitudinal angles θ and ϕ were obtained. These longitudinal angles θ and ϕ were then used to calculate the velocity components u, v and w.

CONNECTIONS FOR
PRESSURE TRANSDUCER
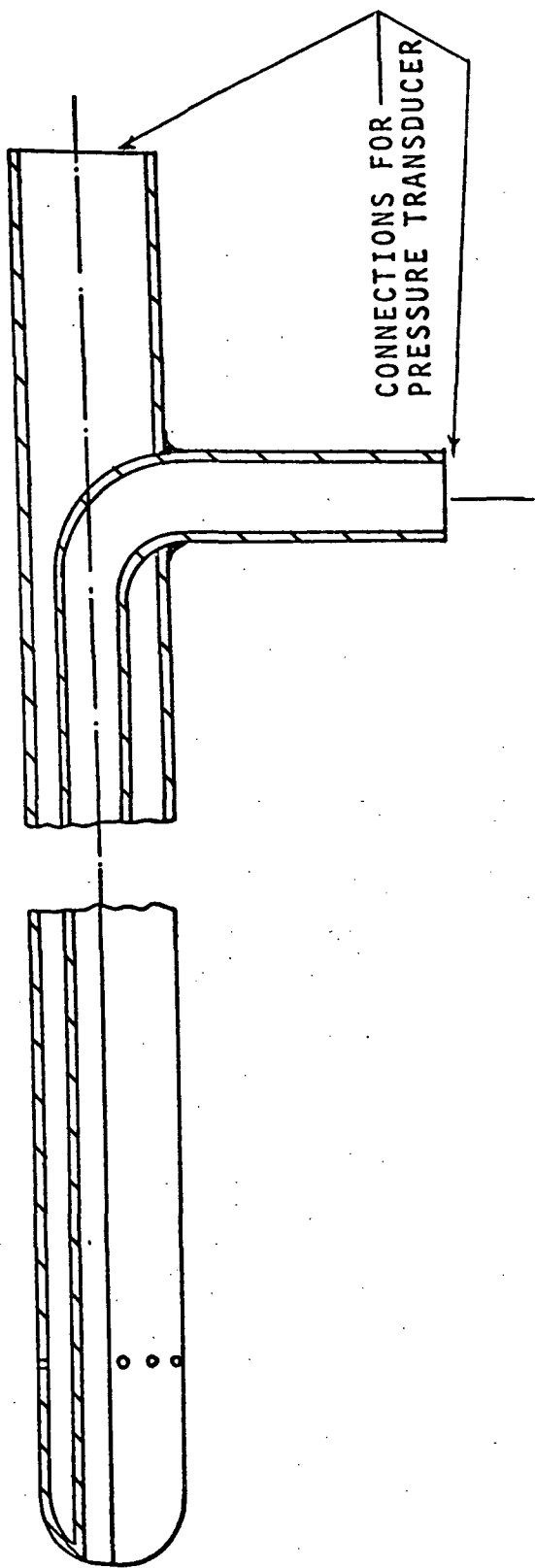
Figure 6.9 Pitot Tube for Velocity Calibration
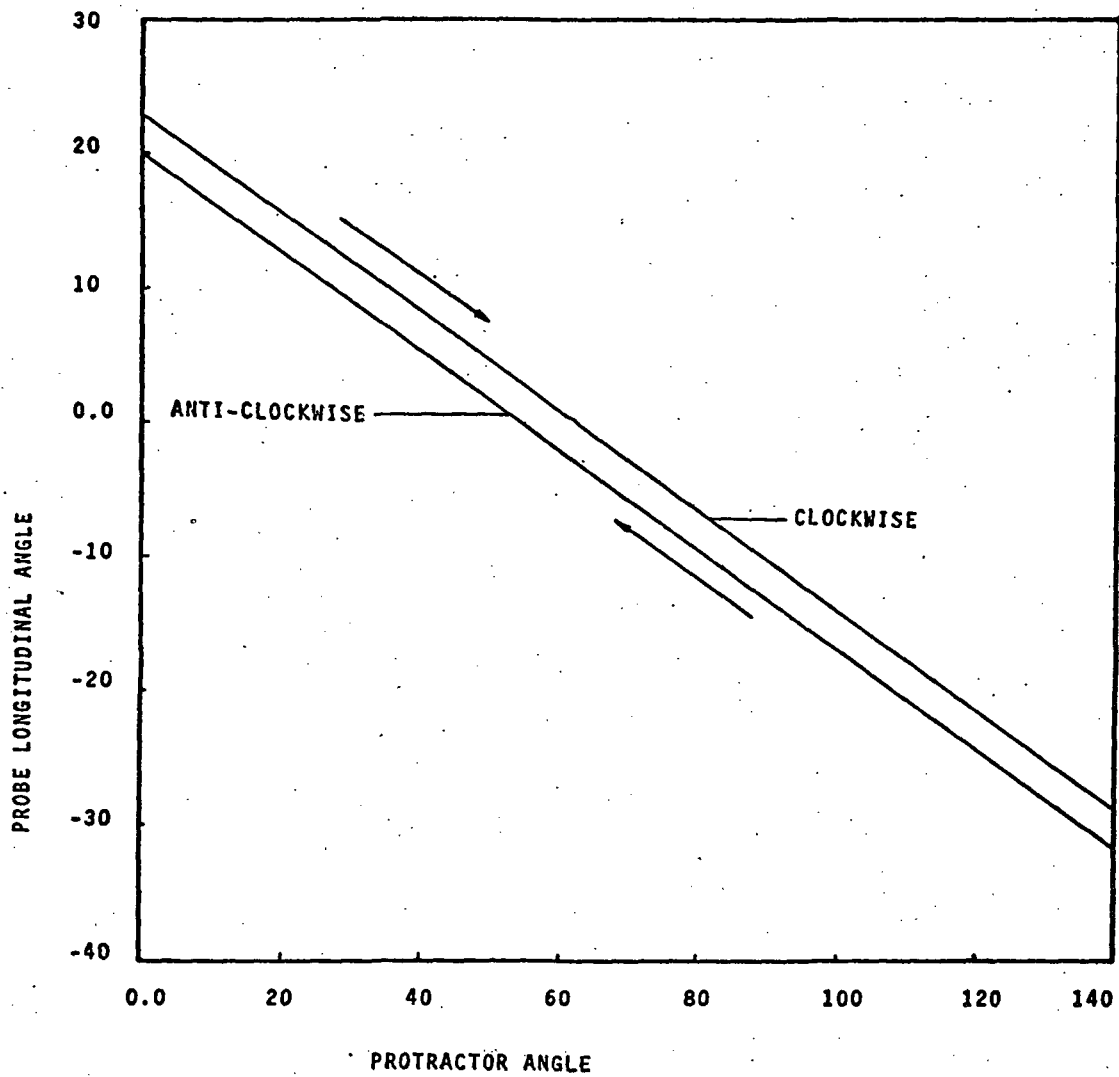
Figure 6.10   Calibration Curve for Probe Angle Measurements
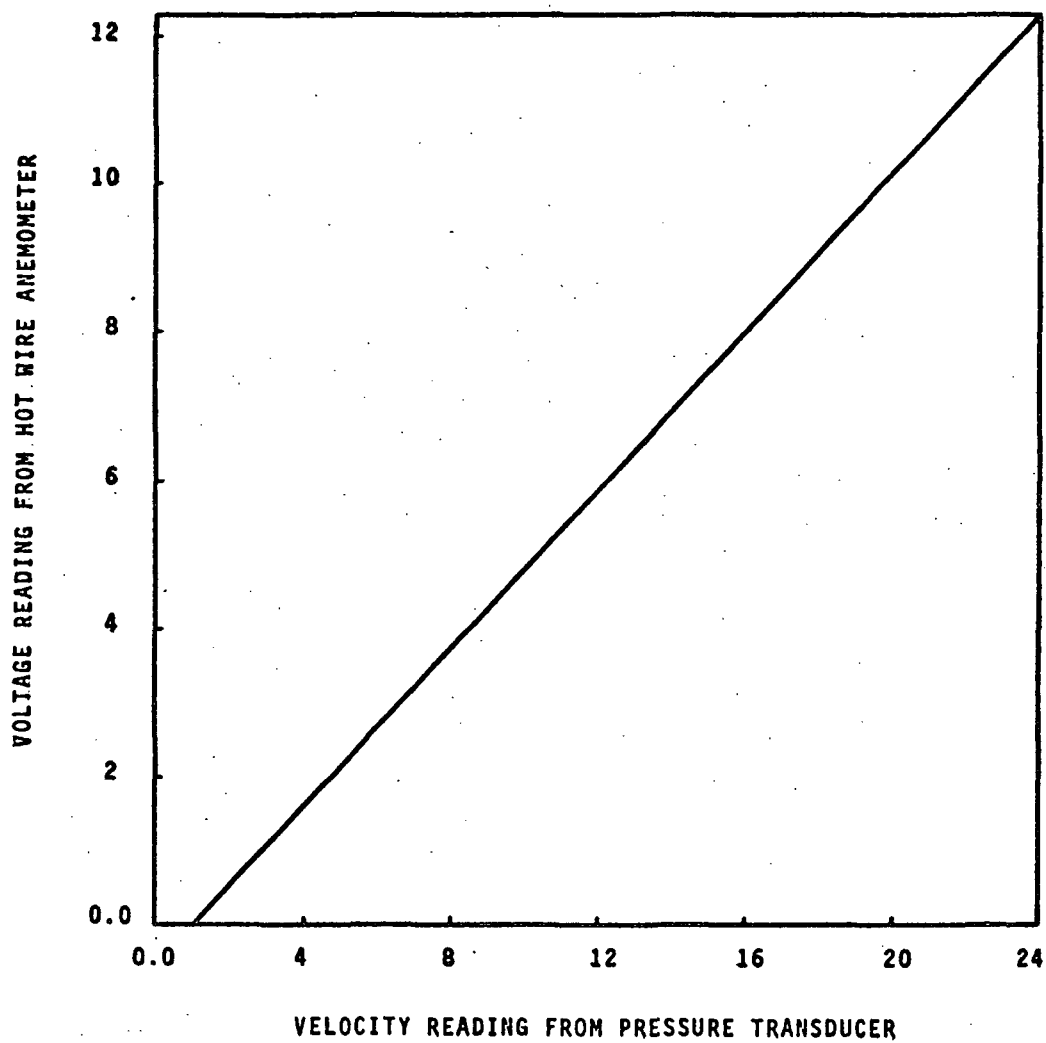
Figure 6.11   Calibration Curve for Hot Wire Probe.

The technique of how the hot wire probe was used to measure the resultant air velocity also merits a brief discussion. A more elaborate explanation is given in Appendicies C and D. The hot wire probe was introduced into the air stream within the sink tube in such a manner that the wire itself was in a horizontal position. Simultaneously the probe support was secured in a position to only permit the hot wire probe movement in a longitudinal direction in the horizontal plane. The hot wire was then rotated such that a point on the wire would sweep out a spherical curve. The hot wire probe, thus positioned, only sensed a velocity due to the axial and radial components. The effect of tangential velocity component on the probe, for the probe so positioned, was negligible. Rotation of the probe in an longitudinal direction then accounted for the tangential velocity component. As the hot wire probe was rotated in the longitudinal direction a maximum reading on the anemometer was ultimately observed. This reading is the resultant air velocity at that particular location. The hot wire probe holder mechanism was designed to enable the measurement of the longitudinal angle (θ).

In a manner similar to the above the hot wire probe was introduced into the air stream, within the sink tube, such that the wire itself was in a vertical position. Simultaneously the probe support was secured in position to only permit the hot wire movement in a longitudinal direction within the vertical plane. The hot wire probe thus positioned,

only sensed a velocity due to the axial and tangential components. The effect of the radial velocity component on the probe, for the probe so positioned, was negligible. Rotation of the probe in a longitudinal direction then accounted for the radial component. As the hot wire probe was rotated in the longitudinal direction, a maximum reading was ultimately observed. This reading is the resultant air velocity at that particular location. The hot wire probe holder mechanism had been so designed that the longitudinal angle ϕ was also measurable. In all measurements using the hot wire probe, the probe holder axis was, at all times, parallel to the sink tube axis. This technique made certain that the air velocity was perpendicular to the hot wire and also that the air velocity measured was the resultant velocity. Having, at a particular location, measured the resultant velocity and the angles ϕ and θ the radial, axial and tangential velocity components could then be calculated as indicated in Appendix C.

The experimental investigation began with the case of constant air flow of 3.93 cubic feet per minute, sensor rotations of 0, 5, 10 and 20 revolutions per minute respectively, and maintaining throughout a unity slenderness ratio. In the sink tube, the experimental data were taken at 6 to 10 prescribed axial stations, depending on the length of each sink tube.

At each station along the sink tube from 5 to 7 static pressure readings were taken as the radius was traversed.

The static pressures were measured by a static pressure probe used in conjunction with a transducer. The static pressure probe was first located at the innermost station in a manner such that the static pressure probe and probe holder axis coincided with the sink tube axis. Once the static pressure at this location was recorded, the probe was then successively positioned and the pressures were recorded at the other prescribed sink tube stations along the sink tube axis. Thus at each sink tube station 5 to 7 static pressure readings were recorded as the probe was traversed along the radius.

In addition to measuring the static pressure at each sink tube station the resultant velocity as well as the longitudinal angles ϕ and θ were also measured. The manner in which these readings were taken is similar to that discussed previously.

In view of the fact that the radial velocity u, within the sink tube (except at its entrance section) is everywhere approximately zero, a simplified technique was also used to measure the axial and tangential velocities. This measurement technique was also used to check the results of previous experimentators and has been found to be most satisfactory.

A previous technique used for the velocity measurements was found to be far too time consuming and on occasions difficulties were encountered due to the fluctuations in the meter readings. The time required particularly to measure the longitudinal angles θ and ϕ, was considerable and therefore a simplified but accurate method was desirable.

Therefore, another technique which was reliable as well as

accurate was employed and is briefly described here. A constant temperature hot wire anemometer was used for the velocity measurements. The same apparatus used for making the velocity measurements is described under the description of apparatus. In making the velocity measurements at any location two hot wire readings were taken. The first reading was taken with the hot wire maintained in a horizontal position, while the hot wire probe axis was maintained parallel to the sink tube axis as well as in the central vertical plane of the sink tube. It was then possible by this arrangement to have the hot wire, at a given station, traverse along the radius. With the hot wire located at a given radius, by means of the rack and pinion device the hot wire could then be moved along the axial length of the sink tube. Thus with the hot wire maintained in the horizontal position, as described, one reading V_H was recorded for each position.

The second reading, at a given position, was taken with the hot wire maintained in a vertical position, while the hot wire probe axis was maintained parallel to the sink tube. The hot wire was changed to its vertical position by means of a rotary disk that was turned 90^0 degrees. As discussed above a second reading V_V was then recorded for each position.

The V_H and V_V values were then used to calculate the tangential and axial velocity components. This was accomplished in the following manner:

The equations obtained from Fig. (6.12) are

$$\text{Tan } \alpha_1 = \sqrt{\frac{v}{u^2 + w^2}} \quad , \text{ and} \tag{6-2}$$

$$\text{Tan } \alpha_2 = \sqrt{\frac{u}{v^2 + w^2}} \tag{6-3}$$

where α_1 is the angle made by resultant velocity with the plane perpendicular to the hot wire, when the hot wire was horizontal and α_2 is the angle made by resultant velocity with the plane perpendicular to the hot wire, when the hot wire was vertical.

Since the radial velocity u is considered negligible, the above two equations reduce to

$$\text{Tan } \alpha_1 = \frac{v}{w} \quad , \quad \text{and} \tag{6-4}$$

$$\text{Tan } \alpha_2 = 0 \quad \text{or } \alpha_2 = 0 \quad . \tag{6-5}$$

Now by invoking the hot wire theory [62], the relation between the resultant velocity V^*, V_H and V_V can be written as

$$V^* = \frac{V_H}{(\cos^2\alpha_1 + K_0^2 \sin^2\alpha_1)^{1/2}}$$

$$= \frac{V_V}{(\cos^2\alpha_2 + K_0^2 \sin^2\alpha_2)^{1/2}} \tag{6-6}$$

where K_0 is a constant and equal to 0.2 for low velocity flow. In view of the fact that α_2 is zero, V^* then becomes V_V and

$$(V^*)^2 = \frac{(V_H)^2}{\cos^2\alpha_1 + K_0^2 \sin^2\alpha_1} \quad . \tag{6-7}$$
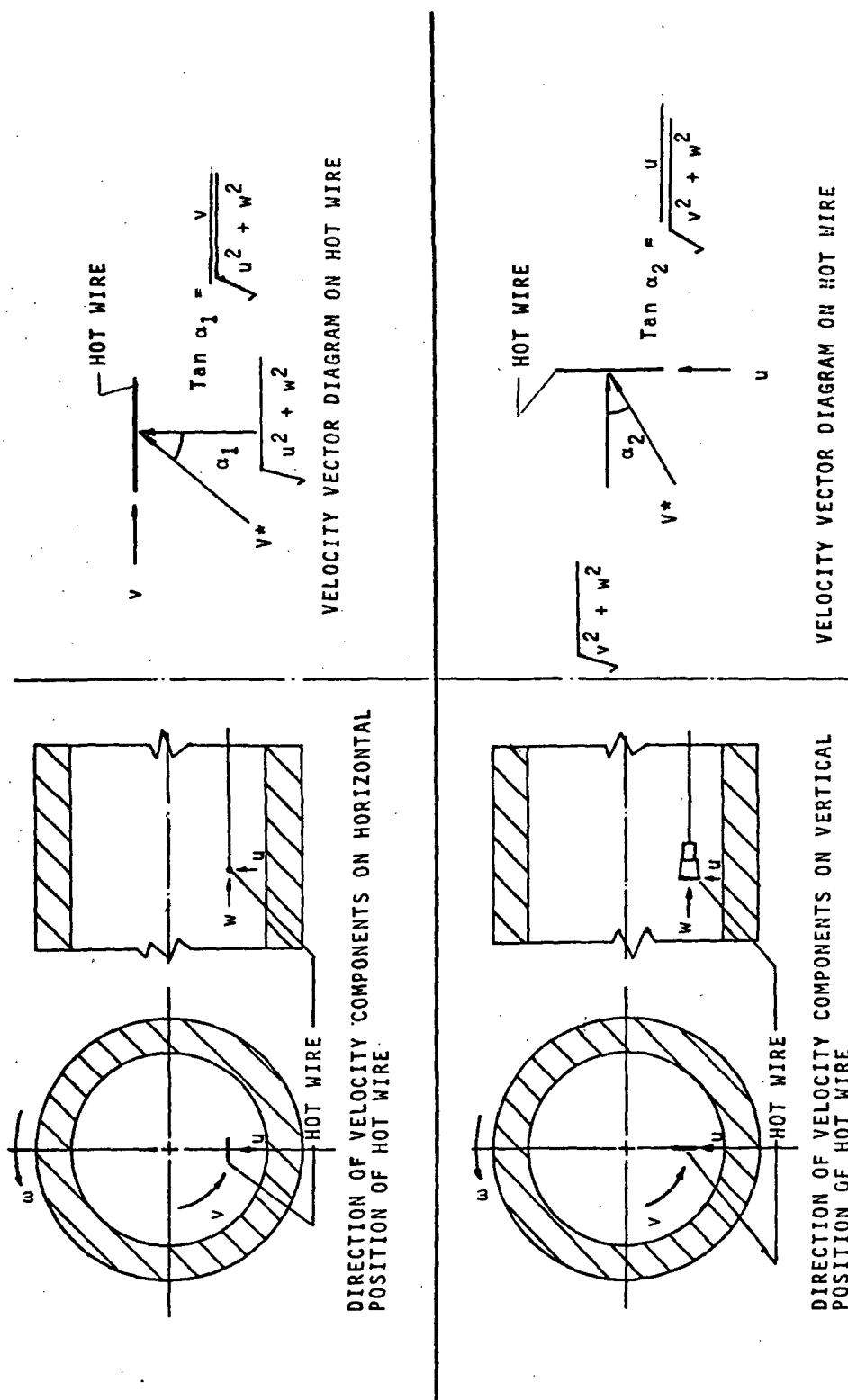
Figure 6.12. Velocity Measurement Technique By Hot Wire Probe

With $\text{Tan}^2\alpha_1 = \dfrac{v^2}{w^2}$, one can write

$$(V*)^2 = \frac{(V_H)^2}{\dfrac{1}{1 + \text{Tan}^2\alpha_1} + \dfrac{K_0^2 \, \text{Tan}^2\alpha_1}{1 + \text{Tan}^2\alpha_1}} \qquad (6\text{-}8)$$

Thus,

$$(V*)^2 = \frac{(V_H)^2}{\dfrac{1}{1 + \dfrac{v^2}{w^2}} + \dfrac{K_0^2 \, \dfrac{v^2}{w^2}}{1 + \dfrac{v^2}{w^2}}} \qquad (6\text{-}9)$$

or

$$(V*)^2 = \frac{(V_H)^2 \, (v^2 + w^2)}{w^2 + K_0^2 \, v^2} \qquad (6\text{-}10)$$

Since $v^2 + w^2 = (v*)^2$, then the above equation reduces to

$$V_H^2 = w^2 + K_0 \, v^2 \qquad (6\text{-}11)$$

and

$$V_V^2 = V*^2 = w^2 + v^2 \qquad (6\text{-}12)$$

The above equations were are solved for the velocity components and there is obtained

$$v = \sqrt{\frac{V_V^2 - V_H^2}{1 - K_o^2}}$$ (6-13)

and

$$w = \sqrt{\frac{V_H^2 - K_o^2 V_V^2}{1 - K_o^2}} .$$ (6-14)

Thus the tangential velocity v, and the axial velocity w are calculated from the measured values of V_H and V_V.

6.3 Experimental Results

An experimental investigation was undertaken to determine the flow pattern existing in a steady state weak vortex.

The vortex sink rate sensor is shown in Fig. (6.1). The measurements were only taken within the sink tube and air was the only working fluid used. A constant temperature hot wire anemometer was used for the velocity measurements while a pressure transducer was used in conjunction with a pitot tube for the pressure measurements. The radial Reynolds numbers were approximately maintained at values of 524.5, 629 and 767 for a flow rate of 3.93 cubic feet per minute while the characteristic vortex chamber spacing height h was fixed at 1-1/2", 1-1/4" and 1" respectively. The tangential Reynolds numbers were successively maintained at valued of 0.0, 2272.5, 4545 and 9090 based on the vortex chamber radius of 10 inches and the respective speeds of 0, 5, 10 and 20 rpm.

The fact that the radial velocity within the sink tube was approximately zero everywhere, with the exception of the sink tube entrance section, revealed that the flow was helical. The flow helical angle within the sink tube decreased as the rate of rotation increased. This was supported by the fact that the tangential velocity was found to be approximately proportional to the rate of rotation.

No appreciable variation of the axial velocity within the sink tube was observed. The axial velocity in the vicinity of the sink tube geometric axis, however, was found to be slightly lower than neighboring points. Throughout the remaining

portion of the sink tube (with the exception of the region near the sink tube wall) and for a given radius, the axial velocity was approximately constant. In the immediate vicinity of the sink tube wall the axial velocity decreased rapidly.

The external effect on static pressure measurements became observable at a distance 9 inches into the sink tube for the short tube whereas the same observation was noted at a distance of 21 inches for the longer tube. When a comparison was made for the two tubes at a given r value, a step increase in static pressure was observed in going from the longer tube to the shorter tube.

The result of static pressure measurements within the sink tube are shown in Figs. (6.13) and (6.14). They reveal that a minimum value below atmospheric occurs in the immediate vicinity of the sink tube geometrical axis. Slightly higher values of static pressure are observed along the geometrical axis. The variation of static pressure along axial length, with R as a parameter, is shown in Fig. (6.15) for a flow rate of 3.93 cubic feet per minute and a speed of 20 revolutions per minute.

Along a given axial location and beyond the radius mentioned above, the static pressure increases continuously as the static pressure probe is moved toward the sink tube wall. At a given radius and along the axial length the static pressure increases continuously from the sink tube entrance and ultimately becomes atmospheric near the sink tube exit. An exception to the above is noted in the vicinity of the sink tube wall. Every-
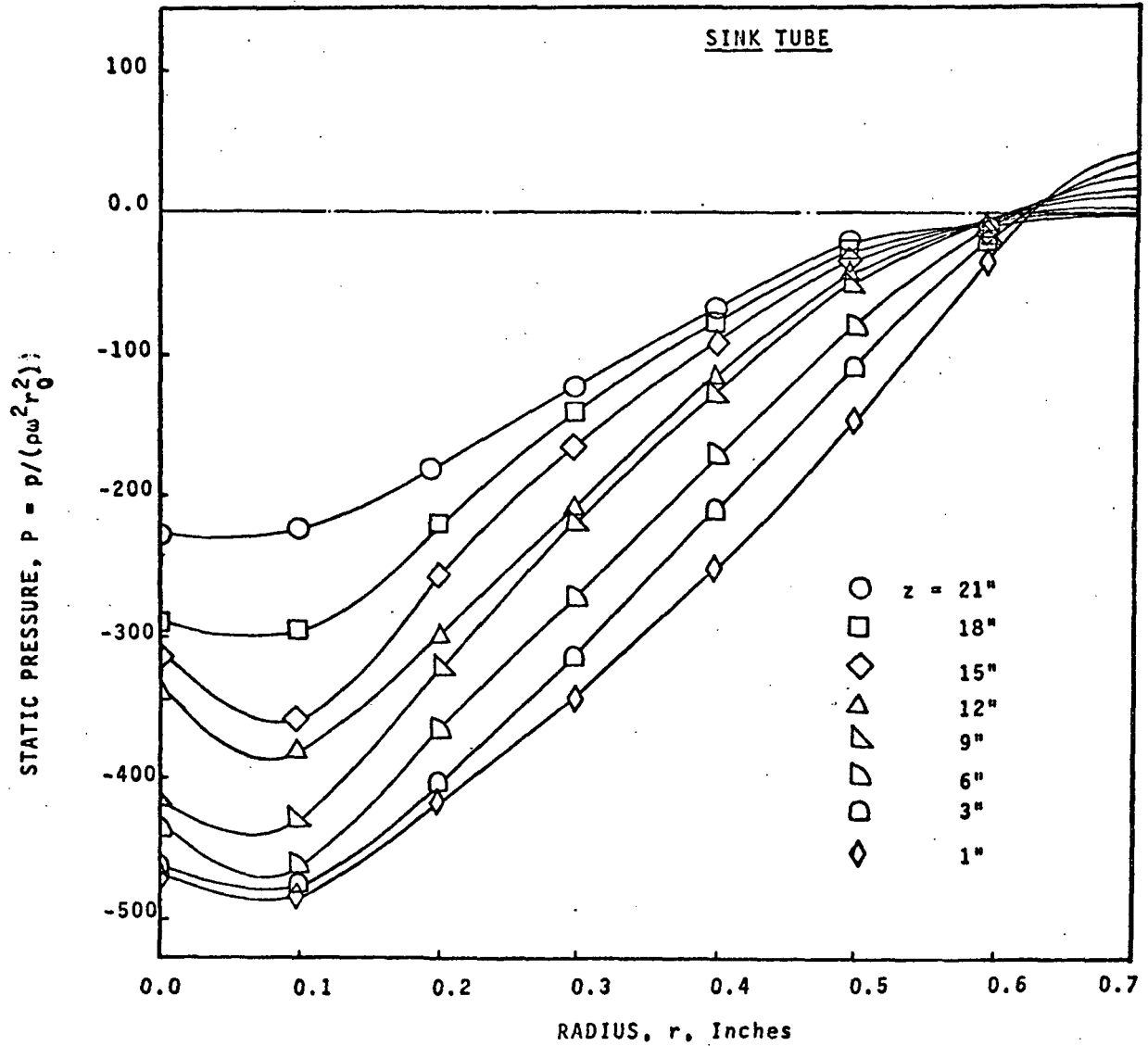
Figure 6.13 Variation of Static Pressure, P, with Radius, r, at Different Z (for $N_{Re-\theta}$=9090 and N_{Re-u}=524.5)
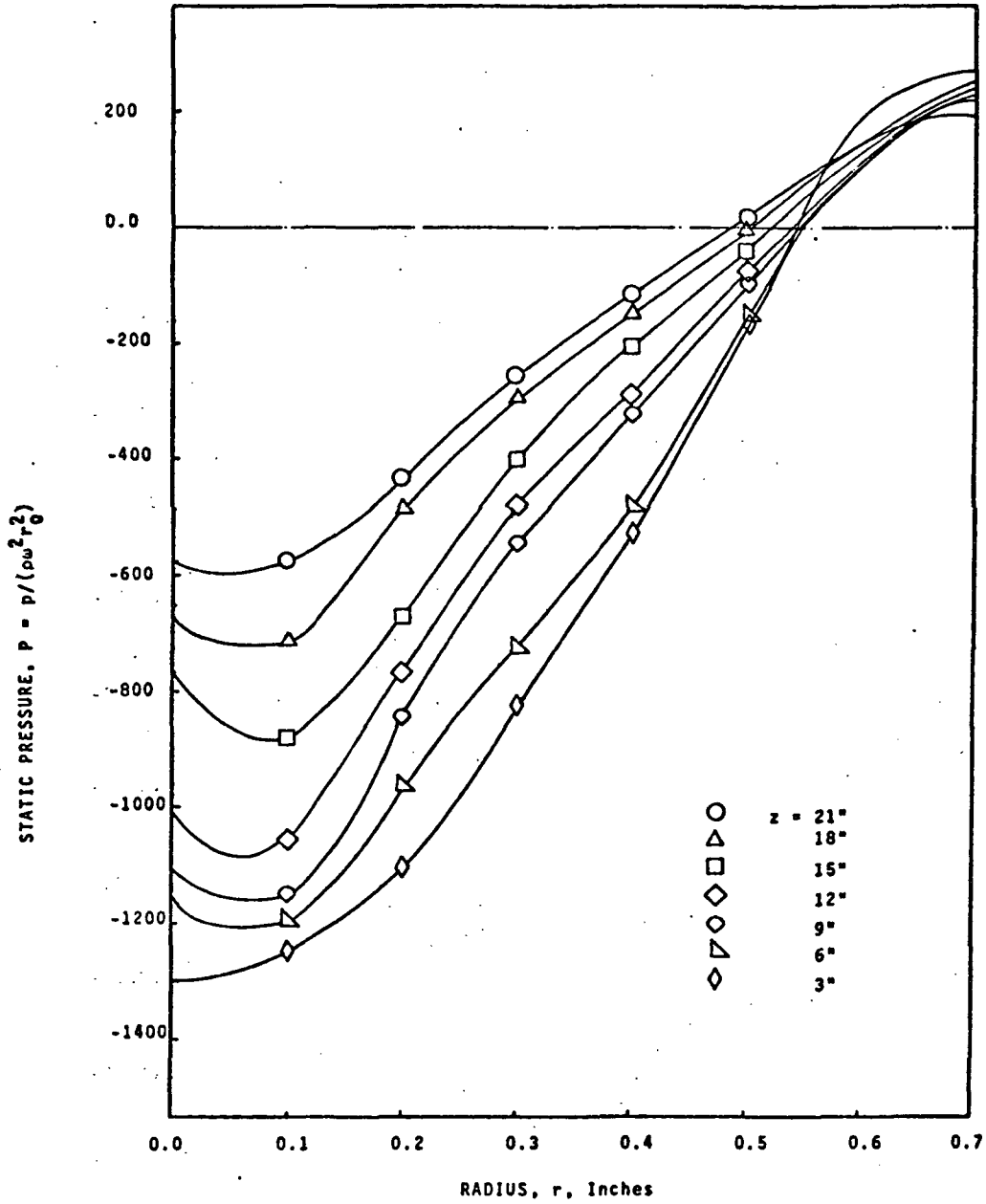
Figure 6.14   Variation of Static Pressure, P, with Radius, r, at Different Z (for $N_{Re-\theta}$=4545 and N_{Re-u}=524.5)
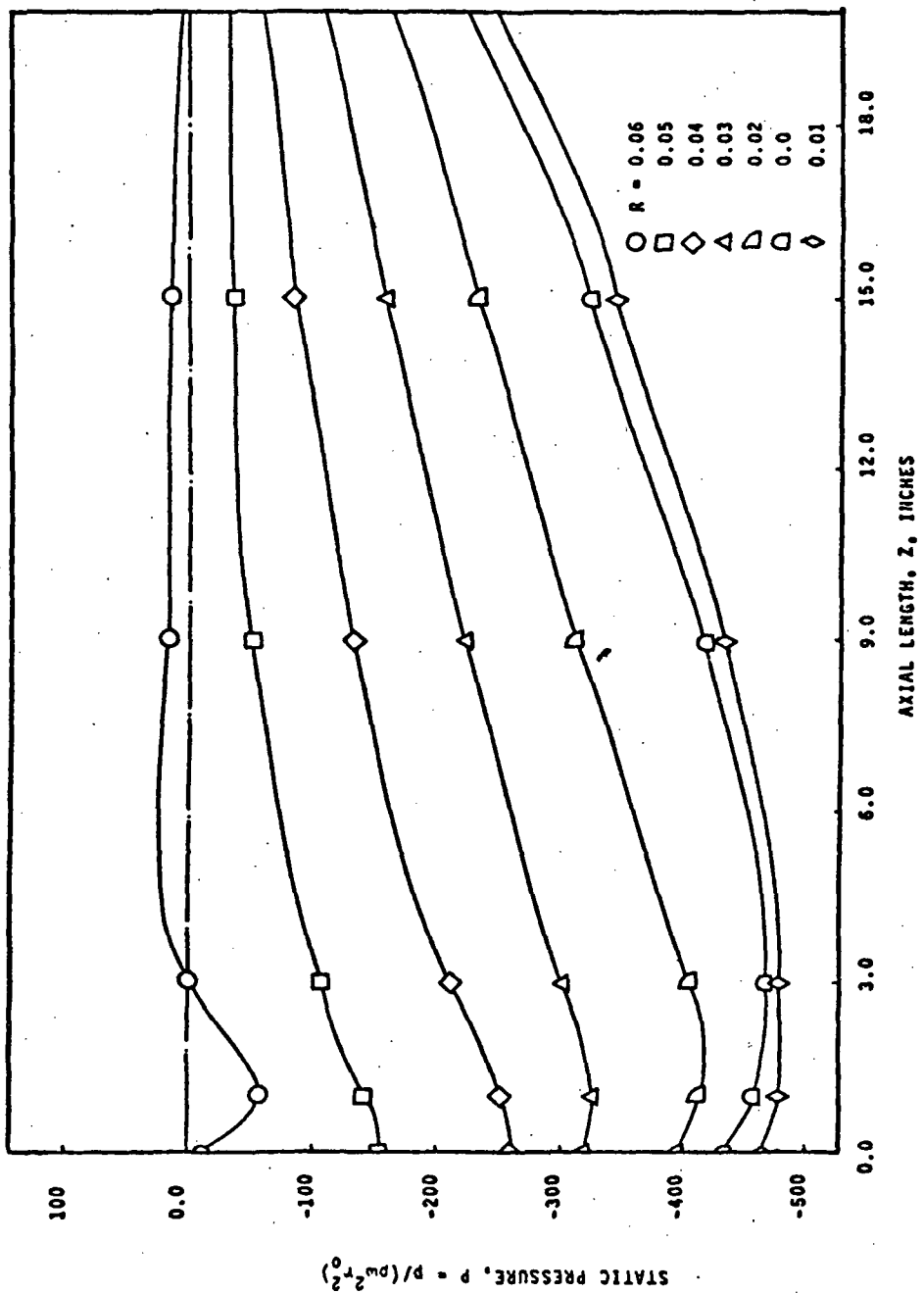
Figure 6.15   Variation of Static Pressure, P, with Axial Length, Z, at Different R (for $N_{Re-\theta} = 9090$ and $N_{Re-u} = 524.5$)

where along the sink tube wall the static pressure values are above atmospheric. As the static pressure probe is moved toward the sink tube exit the static pressure values decrease continuously and ultimately become atmospheric at the exit section. This characteristic of static pressure is obtained as a result of a vortex imposed on the fluid due to the rotation of the sensor.

VII. CORRELATION OF RESULTS

Air is supplied to the vortex chamber through a porous coupling by means of six circumferentially placed equispaced tubes. Therefore, analytically it is difficult to conclude whether the flow in the vortex chamber is axisymmetric or not. This remains to be proven. The symmetry assumed in this case, however, merely refers to the symmetries with respect to the sink tube axis. This assumption is particularly valid for the sink tube, is not also for the vortex chamber.

Numerical and experimental results, for the radial velocity variation in the sink tube, are illustrated in Fig. (7.1). The radial velocity measurements for the entrance length of four inches into the sink tube are not only accurately and easily measurable but they also seem to correlate well with the numerical results. However, farther into the sink tube the radial velocity values are negligible and are difficult to measure.

As shown in Fig. (7.2), for the case of zero rotation of the sensor, the axial velocity profile at the downstream section of the sink tube is not parabolic in shape. For r values less than 0.6 r_i, the axial velocity appears approximately constant. This indicates that either the flow is not fully developed or that it has indeed become purely turbulent. As the speed of rotation is increased, the fluctuations, evident at the lower speeds, virtually disappeared. Thus at the higher speeds the experimental results should be considered more reliable than at the lower speeds. At a speed of

137
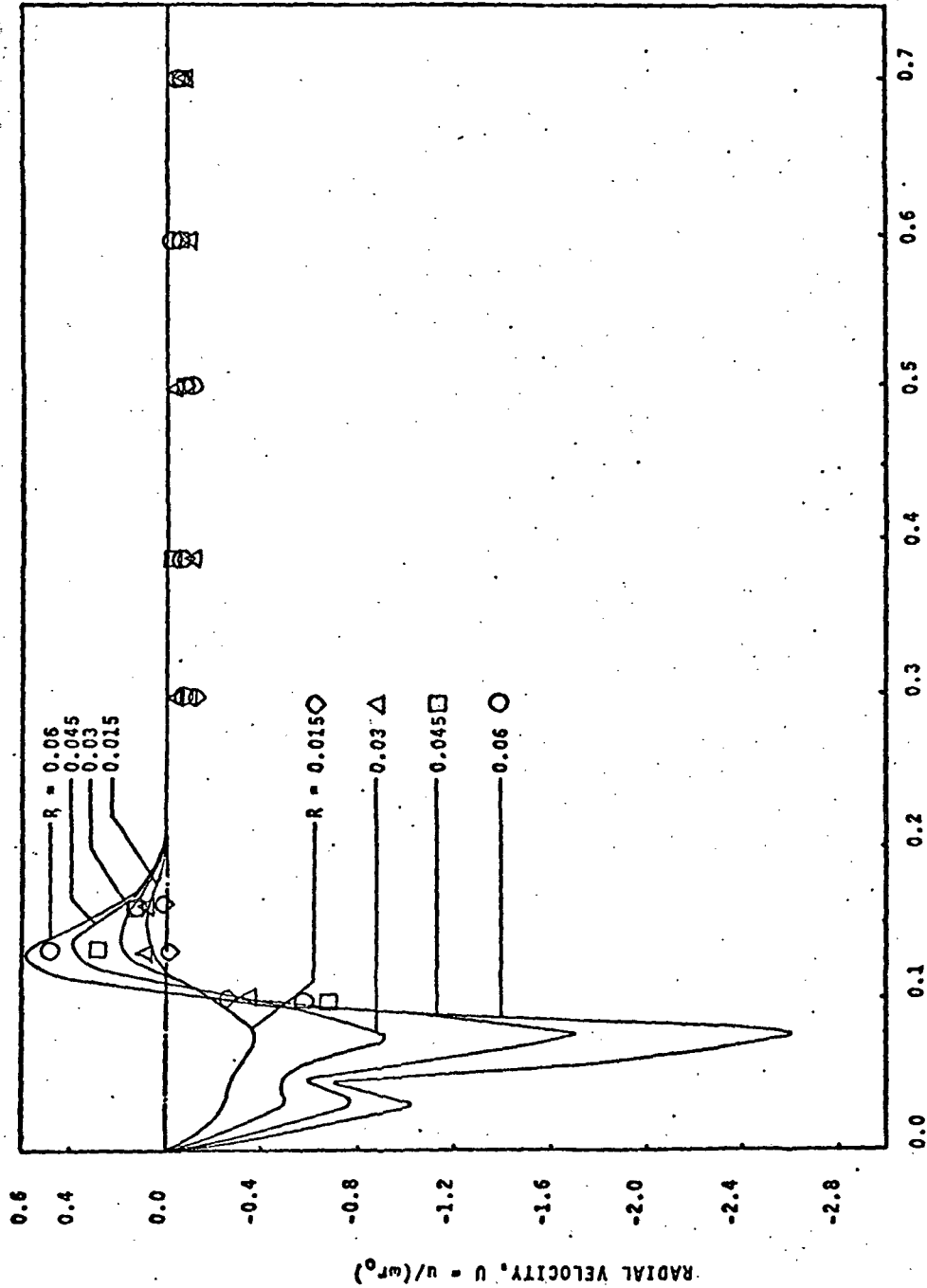
Figure 7.1 Variation of Radial Velocity,
U, with Axial Length, Z, at
Different R, (for $N_{Re-u} = 524.5$
and $N_{Re-\theta} = 9090$)
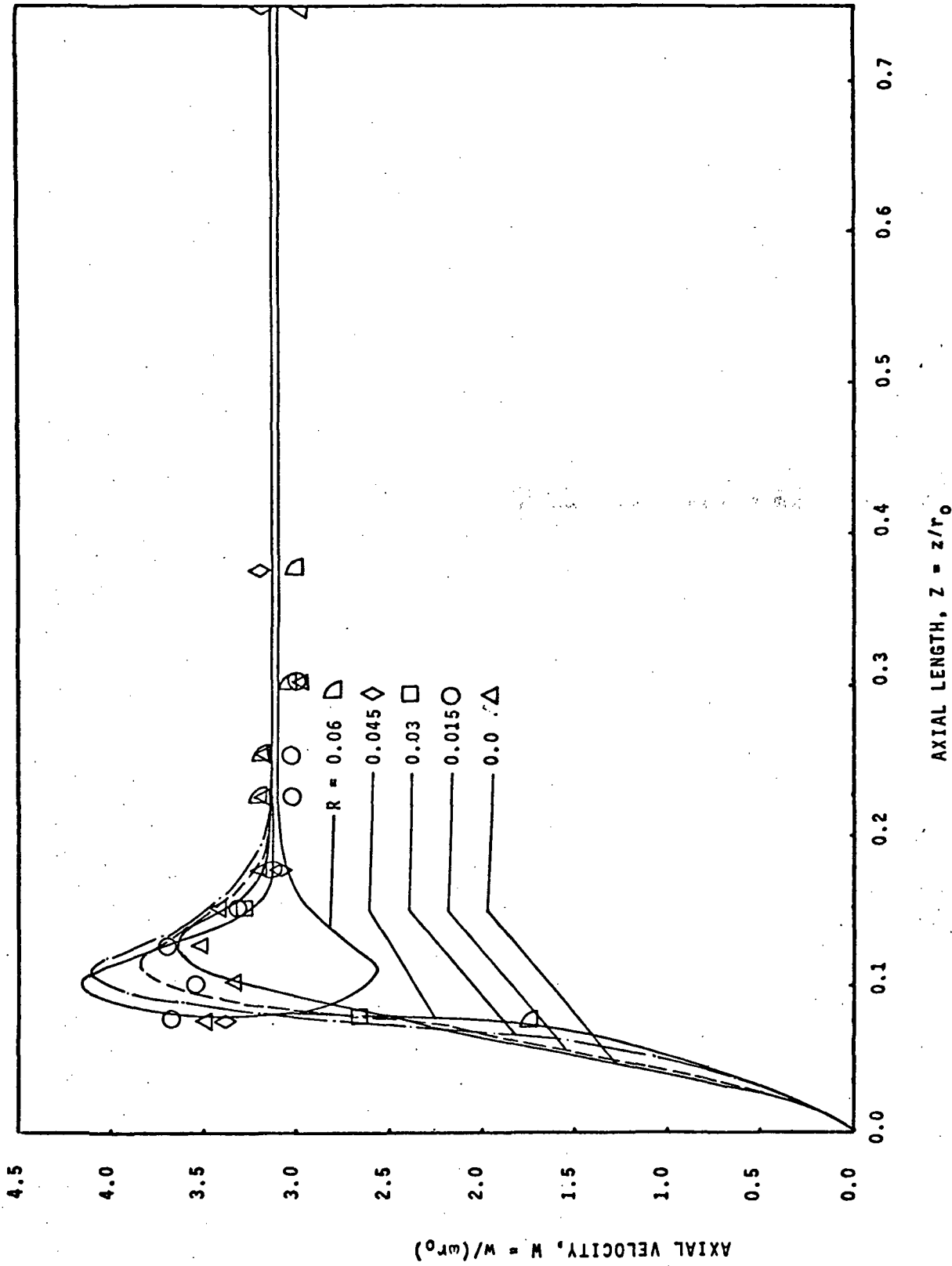
Figure 7.2   Variation of Axial Velocity, W, with Axial Length, Z, at Different R, (for $N_{Re-u} = 524.5$ and $N_{Re-\theta} = 9090$)

rotation of 20 revolutions per minute, for example, the correlation of the experimental results with the numerical results proves to be most satisfactory. It is also observed that the experimental axial velocity values correlate very well with the numerical results for the larger r values. Closer to the sink tube geometrical axis, however, the axial velocity values do not correlate that well with the numerical results. This is attributed to the existence of a core region.

Experimental and numerical results for the tangential velocities, in the sink tube, are illustrated in Fig. (7.3) and (7.4). These results reveal that the tangential velocity is consistently higher near the sink tube entrance and it decreases continuously as the flow progresses into the sink tube. Throughout the sink tube, and within the region between the sink tube wall and the sink tube geometric axis (i.e., $0 \leq r \leq r_i$), the tangential velocity is observed to be positive everywhere and its magnitude is found to be greater there than at the wall. Within the sink tube, the tangential velocity profile, which may be characterized by a parabolic profile, has two peaks, one at $r = 0.2r_i$ and the other at approximately $r = 0.75r_i$. For the location $Z = 0.2$, a depression in the velocity profile is noticed, in Fig. (7.4), around midway between the axis and the wall. The data collected further reveals that the maximum tangential component of velocity over the entire range of r/r_i approximately occurs between 0.25 and 0.55.

As discussed previously nonlinearity effects are taken into account in the theoretical analysis and the nonlinear
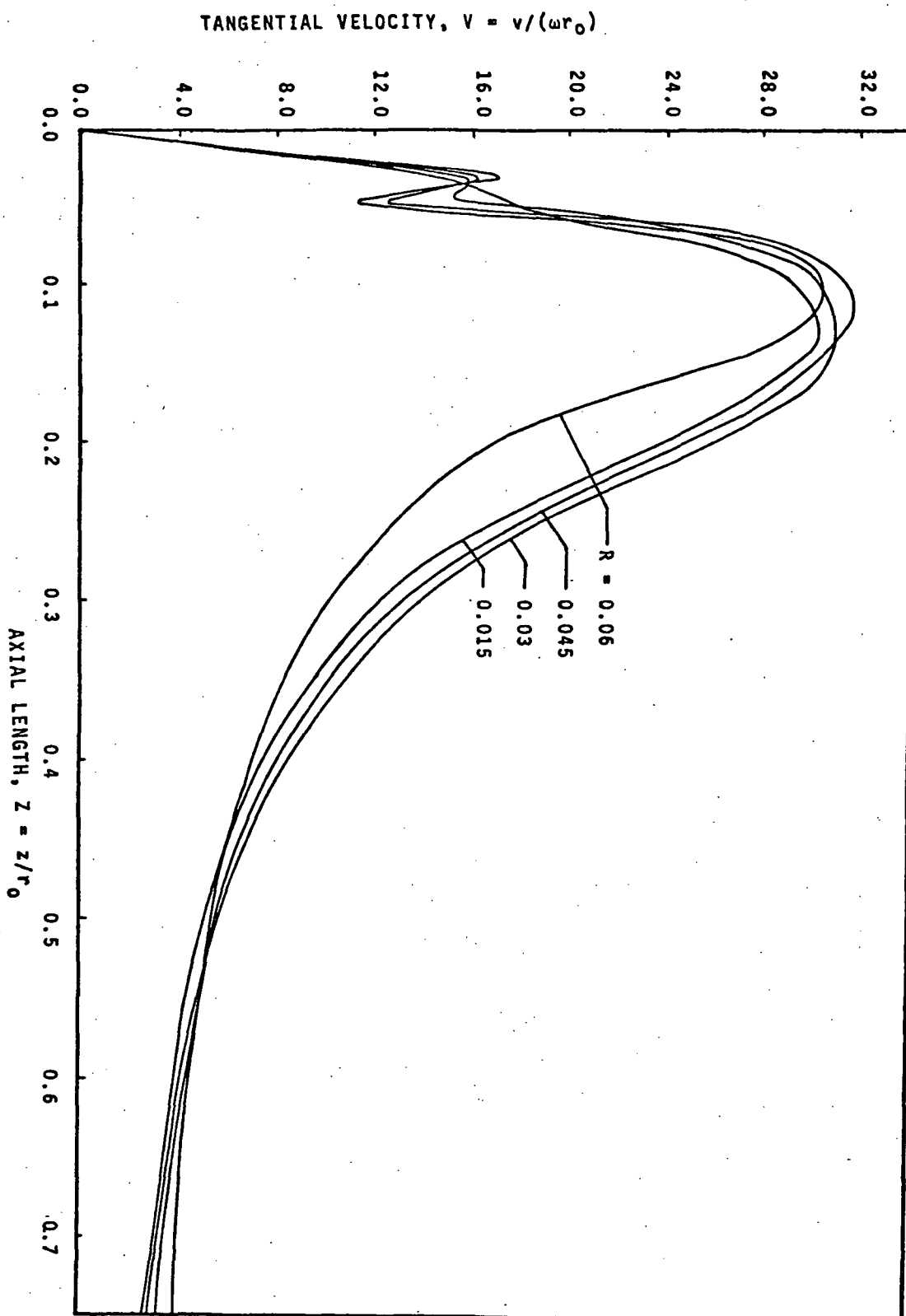
Figure 7.3   Variation of Tangential Velocity, V, Axial Length, Z,
at Different R, (for N_{Re-u}=524.5 and $N_{Re-\theta}$=9090)
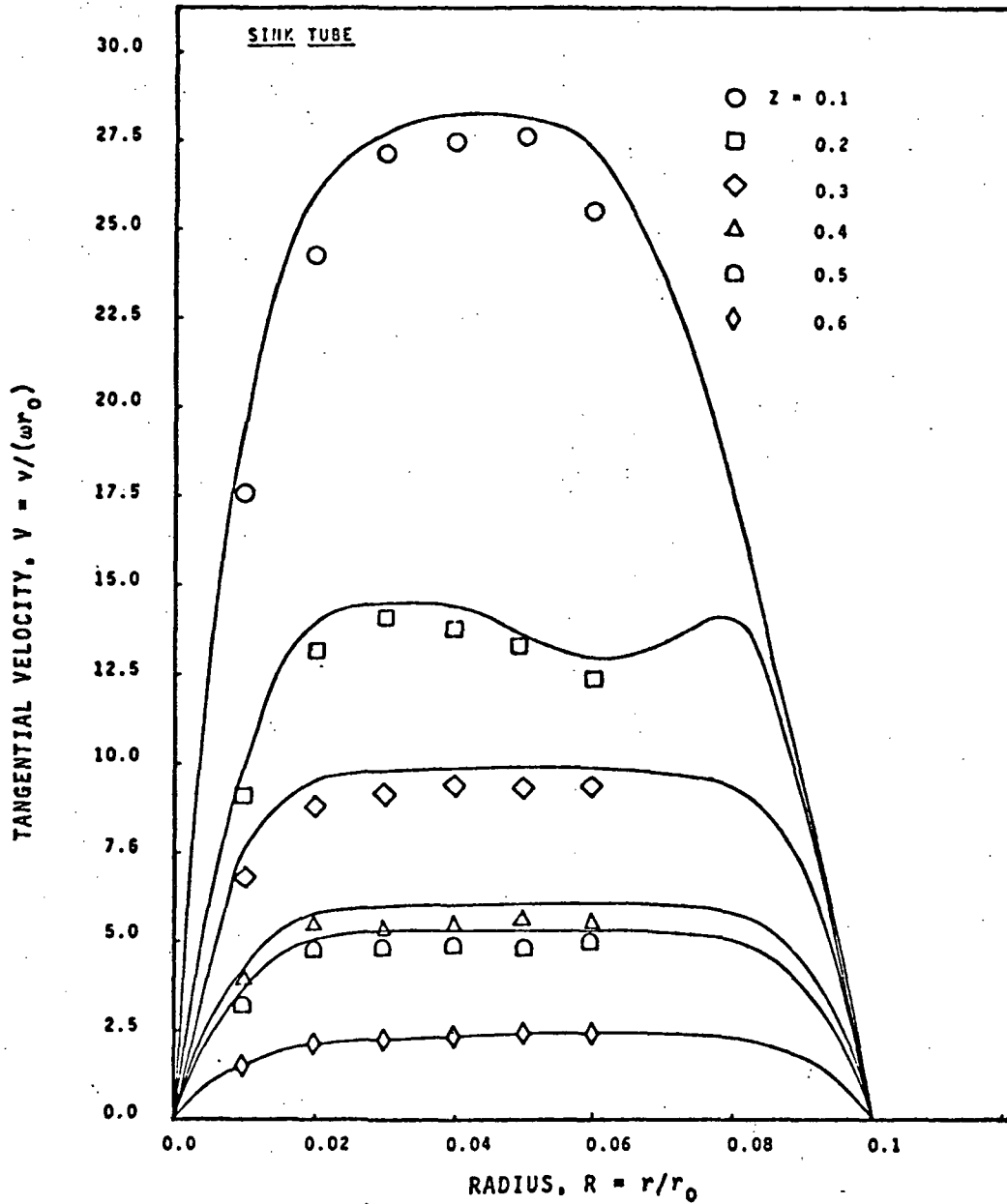
Figure 7.4   Variation of Tangential Velocity,
              V, with Radius, R, at Different
              Z (for N_{Re-u} = 524.5 and $N_{Re-\theta}$=9090)

equations are solved by numerical techniques. The experimental results as shown in Fig. (7.4) also reveal the presence of nonlinear effects and these nonlinearities were similar to those in the theoretical analysis.

In the process of comparing the experimental results with those in the theoretical analysis, it is necessary to recall that the axial length differed by the vortex chamber spacing height h. This is because the axial length in the theoretical analysis is measured from the outer plate of the vortex chamber, whereas for the experimental investigation it is measured from the sink tube entrance. A similar characteristic is noted from the experimental results reported by Lu [32].

As shown in Appendix E, an error analysis has been undertaken for both the numerical and experimental aspects of the investigation. The curves of Figs. (7.1), (7.2) and (7.3) show the comparison of experimental and numerical results of velocity components. The numerical results are seen to be in good agreement with the experimental results.

The scatter of data in the experimental results in slightly greater than the limits of error estimated in Appendix E.

VIII. CONCLUSIONS AND RECOMMENDATIONS

The objective of this study was to investigate the flow phenomenon numerically as well as experimentally within a vortex sink rate sensor. The conclusions deduced from both the theoretical and experimental results are as follows.

The theoretical and experimental results are in good agreement particularly for the 20 revolutions per minute rotational speed of the sensor, flow rate of 3.93 cubic feet per minute and for a sink tube diameter of 1-1/2 inches.

The results reveal that the tangential velocity near the sink tube entrance is higher for the higher flow rates.

An unstable situation is noted within the numerical as well as experimental results for the rotational speeds of 5 and 10 revolutions per minute, with a flow rate of 3.93 cubic feet per minute. However, stability is indeed observed at 20 revolutions per minute speed for the sensor.

At the higher radial Reynolds numbers, the angular and radial momentum within the vortex chamber are approximately conserved.

Due to the exclusion of the entrance energy losses occurring in the sink tube and also partly due to interference introduced by the presence of the probes within the sink tube, the experimental values of the tangential velocity are slightly lower than the theoretical values.

As $N_{Re-\theta}$ is increased, the tangential vorticity η decreases, thus it appears that an increase in speed of rotation brings about a more stable flow.

As a consequence of these observations for a vortex sink rate sensor to have maximum signal amplifications, it is suggested that the sensor be operated at the high flow rate condition.

As a direct consequence of this investigation, a number of recommendations are suggested here for future studies. In general, these recommendations suggest a correlation of existing data, conducting additional tests and/or analyses as well as summarizing the information in a form suitable for design purposes.

Specific recommendations for future investigations are as follows:

1) study of the viscous core area.

2) study the noise generation.

3) investigate the non-conventional boundary conditions for the sensor.

4) theoretical and experimental flow phenomena studies within a sensor with symmetric sink tube, and consideration of proper location for pick off points.

5) study the temperature, density and viscosity variation.

6) investigate the unresolved problem of rapid fluctuations and wondering of the stagnation point within the core region of the sink tube.

IX. REFERENCES

1) Anderson, O. L., "Theoretical Solutions for the Secondary Flow on the End Wall of a Vortex Tube," Report No. R-2492-1, United Air-craft Corp. (1961)

2) Armilli, R. V., "An Experimental Study of a Type of Vortex Sink Rate Sensors," M.S. Thesis, Old Dominion University, Norfolk, Va., (1969)

3) Batchelor, G. K., "Note of a Class of Solutions of the Navier-Stokes Equations Representing Steady Rotationally Symmetric Flow," Quarterly Journal of Mech. & Applied Maths, Vol. 4, pp. 29-41 (1951)

4) Bödewadt, U. T., "Die Derehströmung Uber festem Gerund," ZAMM, Vol. 20, pp. 241-253 (1940)

5) Burgers, J. M., "A Mathematical Model Illustrating the Theory of Turbulence," Advances in Applied Mech., Vol. 1, pp. 197-199, Academic Press, Edited by Mises and Kármán, New York (1948)

6) Burke, J. F., "Evaluation of a Flueric Angular Rate Sensor with High Sensitivity," ASME Transactions, Paper No. 67-WA/FE-36 (1967)

7) Burke, J. and Roffman, G. L., "A Pickoff Element for an Angular Rate Sensor," Fluid Amplification Symposium, Vol. 5, Harry Diamond Lab., Washington, D. C. (1964) (Confidential Report)

8) Chorin, A. J., "A Numerical Method for Solving Incompressible Viscous Flow Problems," Journal of Computational Physics, Vol. 2, pp. 12-26 (1967)

9) Cochran, W. G., "The Flow Due to a Rotating Disc," Proc. of Cambridge Phil. Society, Vol. 30, pp. 365-375 (1934)

10) DeSantis, M. J. and Rakowsky, E. L., "An Experimental Investigation of the Viscous Flow Field in a Pneumatic Vortex Rate Sensor," ASME Transactions, Paper No. 70-Flec-16 (1970)

11) DeSantis, M. J. and Rakowsky, E. L., "An Experimental Investigation of a High Pressure Hydraulic Fluidic Vortex Rate Sensor," Society of Automotive Engineers, Paper No. 700-788 (1970)

12) Donaldson, C. D., "The Magnetohydrodynamic Vortex Power Generator, Basic Principles and Practical Problems," Report No. 30, Aeronautical Research Association of Princeton, Inc., (ARAP) (1961)

13) Donaldson, C. D. and Sullivan, R. D., "Examination of the Solutions of the Navier-Stokes Equations for a Class of Three-Dimensional Vortices, Part I, Velocity Distribution for Steady Motion," Aeronautical Research Association of Princeton, Inc., N.J., Report No. AFOSR TN 60-1227 (1960)

14) Egli, W. H., Kizilos, A. P. and Reilly, R. J., "Study of Vortex Gyro (U)," Honeywell, Inc., Tech. Doc. No. ac - TKA-64-50, Washington, D. C. (1964) (Confidential Report)

15) Fiebig, M., "On the Motion Within Fluid Gyroscopes," AIAA Journal, Vol. 4, pp. 667-674 (1966)

16) Fromm, J. E. and Harlow, F. H., "Numerical Solution of the Problem of Vortex Street Development," Physics of Fluids, Vol. 6, pp. 975-982 (1963)

17) Gala, K. K., "An Experimental Study of Velocity and Pressure Distribution in a Type of Vortex Sink Rate Sensor," M.S. Thesis, Old Dominion University, Norfolk, Va. (1970)

18) Granger, R., "Study of Three-Dimensional Vortex Flow," Journal of Fluid Mech., Vol. 25, pp. 557-576 (1966)

19) Hall, M. G., "A Theory for the Core of a Leading Edge Vortex," Journal of Fluid Mech., Vol. 11, pp. 209-228 (1961)

20) Hall, M. G., "A Numerical Method for Solving the Equations for a Vortex Core," Royal Aircraft Establishment, R.A.E. Technical Report No. 65106 (1965)

21) Harlow, F. H. and Ansden, A. A., "A Numerical Fluid Dynamics Calculation Method for All Flow Speeds," Journal of Computational Physics, Vol. 8, pp. 197-213 (1971)

22) Hellbaum, R. E., "Flow Studies in a Vortex Rate Sensor," Presented at the Third Fluid Amplification Symposium, NASA Langley Research Center, Hampton, Va. (1965)

23) Hung, T. K., "Laminary Flow in Conduit Expansion," Ph.D. Dissertation, The University of Iowa, Iowa City, Iowa (1966)

24) Jones, B. M., "Flight Experiments on the Boundary Layer," Journal of Aero/Space Science, Vol. 5, pp. 81-101 (1938)

25) Kármán, T. V., "Laminare und Turbulente Reibung," ZAMM, Vol. 1, pp. 233-252 (1921)

26) Kelsall, D. F., "A Study of the Motion of Solid Particles in Hydraulic Cyclone," Trans. Inst. Chem. Engrs., Vol. 30, pp. 87-108 (1952)

27) Kendall, J. M., Jr., "Experimental Study of a Compressible Viscous Vortex," Tech. Report No. 32-290, Jet Prop. Lab, C.I.T. (1962)

28) Kerrebrock, J. L. and Meghreblian, R. V., "Vortex Containment for the Gaseous Fission Rocket," Journal of Aero/Space Science, Vol. 28, pp. 710-724 (1961)

29) Kidd, G. J. and Farris, G. J., "Potential Vortex Flow Adjacent to a Stationary Surface," Journal of Applied Mech., Vol. 35, pp. 209-215 (1968)

30) Lewellen, W. S., "Three-Dimensional Viscous Vortices in Incompressible Flow," Ph.D. Thesis, University of California, Los Angeles (1964)

31) Long, R. R., "A Vortex in an Infinite Viscous Fluid," Journal of Fluid Mech., Vol. 11, pp. 611-623 (1961)

32) Lu, N., "An Experimental Investigation of the Vortex Sink Rate Sensor," M.S. Thesis, Old Dominion University, Norfolk, Va. (1971)

33) Ludwieg, H., "Die Ausgebildete Kanalströmung in einem rotierenden System," Ingenieur Archiv, Vol. 19, pp. 296-308 (1951)

34) Macagno, E. O., and Hung, Tin-kan, "Computational and Experimental Study of a Captive Annular Eddy," Journal of Fluid Mech., Vol. 28, pp. 43-64 (1967)

35) Mack, L. M., "The Laminar Boundary Layer on a Disk of Finite Radius in a Rotating Flow, Part I," Tech. Report No. 32-224, Jet Prop. Lab, C.I.T. (1962)

36) Matsch, L. and Rice, W., "Potential Flow Between Two Parallel Circular Disks with Partial Admission," Journal of Applied Mech., Vol. 43, pp. 239-240 (1967)

37) Matsch, L. and Rice, W., "Flow at Low Reynolds Number with Partial Admission Between Rotating Disks," Journal of Applied Mech., Vol. 34, pp. 768-770 (1967)

38) Matsch, L. and Rice, W., "An Asymptotic Solution for Laminar Flow of an Incompressible Fluid Between Rotating Disks," Journal of Applied Mech., Vol. 35, pp. 155-159 (1968)

39) Milne, W. E., Numerical Calculus, Chapter V, Princeton University Press, Princeton, N.J. (1949)

40) Ostdiek, A. J., "Viscous Vortex Rate Sensor," Harry Diamond Laboratories, Tech. Report No. HDL-TR-1555, Washington, D. C. (1971)

41) Ostrach, S. and Loper, D. E., "An Analysis of Confined Vortex Flow," *AIAA* Paper No. 66-68 (1966)

42) Pao, H. P., "A Numerical Computation of a Confined Rotating Flow," *Journal of Applied Mech.*, Vol. 37, pp. 480-487 (1970)

43) Pao, H. P., "Numerical Solution of the Navier-Stokes Equations for the Flows in the Disk-Cylinder System," *Physics of Fluids*, Vol. 15, pp. 4-11 (1972)

44) Pearson, C. E., "Numerical Solution for the Time Dependent Viscous Flow Between Two Rotating Coaxial Disks," *Journal of Fluid Mech.*, Vol. 21, pp. 623-633 (1965)

45) Pearson, C. E., "A Computational Method for Time Dependent Two Dimensional Incompressible Viscous Flow Problems," Sperry Rand Research Center Report, S.R.R.C., No. 64-17 (1964)

46) Ragsdale, R. G., "Applicability of Mixing Length Theory to a Turbulent Vortex System," NASA TN D-1051 (1961)

47) Rakowosky, E. L. and Schmidlin, A. A., "Fluid Vortex Phenomena in Fluidic Applications," *Design Technology* (1967)

48) Richards, C. G., "A Numerical Study of the Flow in the Vortex Angular Rate Sensor," *ASME Transactions*, Paper No. 70-WA/FE-5 (1970)

49) Richards, C. G.; Crarmer, H. D.; Hellbaum, R. F. and Ostdiek, A. J., "A Numerical Study of the Flow in a Vortex Rate Sensor," Report prepared for NASA under Grant No. NGR 32-004-026, Langley Research Center, Hampton, Va. (1972)

50) Roache, P., *Computational Fluid Dynamics*, Hermosa Publishers, Albuquerque, New Mexico (1972)

51) Roache, P. J. and Mueller, T. J., "Numerical Solutions of Laminar Separated Flows," *AIAA Journal*, Vol. 8, pp. 530-538 (1970)

52) Rosenzweig, M. L.; Lewellen, W. S.; Ross, D. H., "Confined Vortex Flows with Boundary Layer Interaction," *AIAA Journal*, Vol. 2, pp. 2127-2134 (1964)

53) Rott, N., "On the Viscous Core of a Line Vortex," ZAMP, Vol. 9B, pp. 543-553 (1958)

54) Sarpkaya, T., "A Theoretical and Experimental Invest-
igation of the Vortex-Sink Angular Rate Sensor," Paper
presented at Third Fluid Amplification Symposium,
Harry Diamond Lab., Washington, D. C. (1965)

55) Savino, J. M. and Keshock, E. G., "Experimental Profiles
of Velocity Components and Radial Pressure Distribution
in a Vortex Contained in a Short Cylindrical Chamber,"
paper presented at the Third Fluid Amplification
Symposium, Lewis Research Center, NASA (1965)

56) Schlichting, H., Boundary Layer Theory, 6th Edition,
McGraw-Hill Publications, pp. 213-222 (1968)

57) Stewartson, K., "On the Flow Between Two Rotating Co-
axial Disks," Proc. of Cambridge Phil. Society, Vol. 49,
pp. 333-341 (1953)

58) Stewartson, K. and Hall, M. G., "The Inner Viscous
Solution for Core of Leading Edge Vortex," Journal of
Fluid Mech., Vol. 15, pp. 306-318 (1963)

59) Stewartson, K., "On Rotating Laminar Boundary Layers,"
Proc. of I.U.T.A.M. Symposium Boundary Layer Research,
Freiburg, i, Br., Springer (1957)

60) Thwaites, B., "Note on the Circulatory Flow about a
Circular Cylinder Through Which the Normal Velocity is
Large," Quarterly Journal of Mech. & Applied Maths.,
Vol. 3, pp. 74-79 (1950)

61) Vogelpohl, G., "Die Strömung der Wirbelquette zwischen
ebenen Wanden mit Berucksichtigung der Wandrubung,"
ZAMM, Vol. 24, pp. 289-294 (1944)

62) Webster, C. A. G., "A Note on the Sensitivity to Yaw
of a Hot-wire Anemometer," Journal of Fluid Mech.,
Vol. 13, pp. 307-312 (1962)

63) Welch, J. W.; Marlow, F. M.; Shannon, J. P. and Daly,
B. J., "The Mac Method, A Computing Technique for Solving
Viscous Incompressible Transient Fluid Problem Involving
Free Surface," USABC Report LA-3425, Los Alamos
Scientific Lab, Los Alamos, New Mexico (1966)

64) Williamson, G. G. and McCune, J. E., "A Preliminary
Study of the Structure of Turbulent Vortices," Report
No. 32, Aeronautical Research Association of Princeton,
Inc. (1961)

65) Yih, C. S., "Two Solutions for Inviscid Rotational Flow
with Corner Eddies," Journal of Fluid Mech., Vol. 5,
pp. 36-40 (1959)

66) Young, H. D., _Statistical Treatment of Experimental Data_, McGraw-Hill Book Company, New York (1962)

APPENDIX A

BOUNDARY CONDITIONS

The boundary conditions for the systems shown in Fig. (24) are as follows:

On the top and bottom plates of the vortex chamber and along the sink tube wall, the no slip condition must be satisfied (i.e. the fluid must move with these surfaces). Thus, for the sensor rotating with an angular velocity, ω, this requirement mandates that

a) at z = 0
$$\left. \begin{array}{l} u(r,0) = 0 \\ v(r,0) = r\omega \\ \bar{\Gamma}(v,0) = r^2\omega \end{array} \right\} \quad 0 \le r \le r_o \qquad \text{(A-1)}$$

b) at z = h
$$\left. \begin{array}{l} u(v,h) = 0 \\ v(r,h) = r\omega \\ \bar{\Gamma}(v,h) = r^2\omega \end{array} \right\} \quad r_i \le r \le r_o \qquad \text{(A-2)}$$

c) at $r = r_i$
$$\left. \begin{array}{l} w(r_i,z) = 0 \\ v(r_i,z) = r_i\omega \\ \bar{\Gamma}(r_i,z) = r_i{}^2\omega \end{array} \right\} \quad h \le z \le \ell \qquad \text{(A-3)}$$

d) at $r = r_o$
$$\left. \begin{array}{l} v(r_o,z) = r_o\omega \\ \bar{\Gamma}(r_o,z) = r_o{}^2\omega \end{array} \right\} \quad 0 \le z \le h \qquad \text{(A-4)}$$

where h is the vortex chamber height and r_i is the sink tube radius.

In view of the fact that both plates of the vortex chamber as well as the sink tube wall are non porous, they are considered as stream surfaces. The bottom plate of the vortex chamber and the sink tube wall are considered the same stream surface. Thus the boundary conditions for these surfaces are

e) at $z = 0$ $\left. \begin{array}{l} w(r,0) = 0, \\ \bar{\psi}(r,0) = C_1, \end{array} \right\}$ $0 \leq r \leq r_0$ (A-5)

f) at $z = h$ $\left. \begin{array}{l} w(r,h) = 0, \\ \bar{\psi}(r,h) = C_2, \end{array} \right\}$ $r_i \leq r \leq r_0$ (A-6)

g) at $r = r_i$ $\left. \begin{array}{l} u(r_i,z) = 0, \\ \bar{\psi}(r_i,z) = C_2, \end{array} \right\}$ $h \leq z \leq \ell$ (A-7)

where C_1 and C_2 are constants.

At the periphery of the vortex chamber ($r = r_0$), the fluid enters in a uniformly radial manner (relative to sensor). Hence the boundary condition is

h) at $r = r_0$ $w(r_0,z) = 0$

$u(r_0,z) = u_0 = \dfrac{Q_0}{2\pi r_0 h}$. $0 < z < h$ (A-8)

The axis of symmetry for the sensor is considered a streamline which is the same streamline as for the top plate of the vortex chamber. This is so because, along the axis of symmetry, both the radial and tangential velocity components vanish. Thus at $r = 0$,

$$\left. \begin{array}{l} \bar{\psi}(0,z) = C_1, \\ u(0,z) = 0, \\ v(0,z) = 0, \\ \bar{\Gamma}(0,z) = 0. \end{array} \right\} \quad 0 \leq z \leq \ell \qquad \text{(A-9)}$$

Along the axis of symmetry, a minor difficulty is encountered with respect to the definition of the radial velocity which is expressed in the terms of the stream function. For instant, at $r = 0$, the velocity $w(0,z)$ is expressed as

$$w(0,z) = \lim_{r \to 0} \left[-\frac{1}{r} \frac{\partial \bar{\psi}}{\partial r} \right] .$$

By applying the L'Hospital rule, this can be written as

$$\text{at } r = 0 \qquad w(0,z) = -\left.\frac{\partial^2\bar\psi}{\partial r^2}\right|_{r=0} \qquad 0 \leq z \leq \ell , \qquad \text{(A-10)}$$

and since the limit does exist, it indicates that

$$\text{at } r = 0 \qquad \left.\frac{\partial\bar\psi}{\partial r}\right|_{r=0} = 0 \qquad\qquad \text{(A-11)}$$

Also, on the axis of symmetry, the boundary condition for the tangential vorticity component is written as

$$\text{at } r = 0 \qquad \bar\eta(0,z) = \lim_{r\to 0}\left[-\frac{\partial w}{\partial r}\right] \quad 0 \leq z \leq \ell \qquad \text{(A-12)}$$

since the radial velocity at the location is zero. Thus at r = 0, the axial gradient of radial velocity is zero. If $\frac{\partial w}{\partial r}$ is not zero at r = 0, then the velocity profile would have a cusp at the axis of symmetry resulting in a discontinuity in the value of the derivative as one crossed the axis of symmetry. This would result in a shear stress, which is proportional to the first derivative of the velocity, being discontinuous. This condition can not occur in a physical system. Thus, an additional necessary requirement is that

$$\text{at } r = 0 \qquad \frac{\partial w}{\partial r} = 0 . \qquad\qquad \text{(A-13)}$$

This, therefore, results in the tangential vorticity being zero on the axis of symmetry, i.e.

$$\text{at } r = 0 \qquad \bar\eta(0,z) = 0 \qquad 0 \leq z \leq \ell . \qquad \text{(A-14)}$$

At the periphery of the vortex chamber, the entering fluid is assumed uniform as well as purely radial, hence

$$\text{at } r = r_0 \qquad \frac{\partial u}{\partial z} = 0 , \qquad \frac{\partial w}{\partial r} = 0 \qquad \text{(A-15)}$$

Thus, the tangential vorticity is considered zero at $r = r_0$, i.e.

at $r = r_0$ $\qquad \bar{\eta}(r_0, z) = 0$ $\qquad 0 < z < h$. $\qquad$ (A-16)

The difference between the value of the stream function on the top plate of the vortex chamber (or the sensor geometrical axis) and the stream function value on the bottom plate of vortex chamber (or the sink tube wall) is proportional to the flow discharge rate Q_0. This is shown to be so in the following manner. The continuity equation requires that at $r = r_0$

$$-Q_0 = 2\pi r_0 \int_0^h u\,dz \quad . \qquad (A-17)$$

By using the definition of u, this is written as

$$-Q_0 = 2\pi r_0 \int_0^h \frac{1}{r_0} \frac{\partial \bar{\psi}}{\partial z}\,dz \quad . \qquad (A-18)$$

This equation is then used to show that at r_0, $\bar{\psi}$ is a function of z only. Since at $r = r_0$, $u = u_0 = $ constant, then $\frac{\partial \bar{\psi}}{\partial z} = $ constant. Thus, at $r = r_0$, $\bar{\psi}$ is a linear function of z and the integral is an exact differential. Thus, Q_0 can be expressed as

$$-Q_0 = 2\pi \left[\bar{\psi}(h) - \bar{\psi}(0) \right] , \qquad (A-19)$$

where $\bar{\psi}(0)$ is a constant and is assigned the stream function value for the top plate, i.e., $\bar{\psi}(0) = C_1 = 0$. Consequently, the stream function for the bottom plate, $\bar{\psi}(h)$, is given by the relation

$$\bar{\psi}(h) = -\frac{Q_0}{2\pi} = \text{const.} = C_2 \qquad (A-20)$$

The tangential vorticity values on the top and bottom plates of the vortex chamber as well as on the sink tube wall are calculated from the stream function by use of the Taylor Series. The general value of tangential vorticity $\bar{\eta}$, as expressed in terms of the stream function $\bar{\psi}$, is

$$\bar{\eta} = \frac{\partial u}{\partial z} - \frac{\partial w}{\partial r} = \frac{1}{r} \frac{\partial^2 \bar{\psi}}{\partial r^2} - \frac{1}{r^2} \frac{\partial \bar{\psi}}{\partial r} + \frac{\partial^2 \bar{\psi}}{\partial z^2} \qquad \text{(A-21)}$$

Specifically then along top and bottom plates of the vortex chamber, one can state that, at $z = 0$ and $z = h$

$$\left. \begin{array}{l} u(r,0) = u(r,h) = 0 \\ w(r,0) = w(r,h) = 0 \end{array} \right\} \qquad \text{(A-22)}$$

and with

$$\frac{\partial w}{\partial r} (r,0) = \frac{\partial w}{\partial r} (r,h) = 0 , \qquad \text{(A-23)}$$

the tangential vorticity $\bar{\eta}$ is reduced to

$$\bar{\eta} = \frac{\partial u}{\partial z} = \frac{1}{r} \frac{\partial^2 \bar{\psi}}{\partial z^2} , \qquad \text{(A-24)}$$

i.e.,

$$\text{at } z = 0 \qquad \bar{\eta}(r,0) = \frac{1}{r} \frac{\partial^2 \bar{\psi}}{\partial z^2} \bigg|_{z = 0} \quad 0 \le r \le r_0 \qquad \text{(A-25)}$$

$$\text{at } z = h \qquad \bar{\eta}(r,h) = \frac{1}{r} \frac{\partial^2 \bar{\psi}}{\partial z^2} \bigg|_{z = h} \quad r_i \le r \le r_0 \qquad \text{(A-26)}$$

Along the sink tube wall at $r = r_i$ with

$$u(r_i,z) = w(r_i,z) = 0 \qquad \text{(A-27)}$$

and

$$\frac{\partial u}{\partial z} \bigg|_{r_i} = 0 , \qquad h \le z \le \ell \qquad \text{(A-28)}$$

the tangential vorticity is reduced to

$$\bar{\eta}(r_i,z) = \frac{1}{r} \frac{\partial^2 \bar{\psi}}{\partial r^2} \bigg|_{r = r_i} \quad h \le z \le \ell \qquad \text{(A-29)}$$

In the downstream section of the sink tube the characteristics of stream function, circulation and tangential vorticity are assumed such that the slope of streamline, circulation line and tangential vorticity lines are zero along the z-direction. In addition to the above, the radial velocity is also assumed to be zero at the downstream section of the sink tube. Thus, the boundary conditions at downstream section of the sink tube are given by

at $z = \ell$
$$\frac{\partial \bar{\psi}}{\partial z} = 0 , \qquad \frac{\partial v}{\partial z} = 0$$
$$\frac{\partial \bar{\Gamma}}{\partial z} = 0 , \qquad \frac{\partial w}{\partial z} = 0 \left. \right\} \quad 0 \leq r \leq r_i \quad \text{(A-30)}$$
$$\frac{\partial \bar{n}}{\partial z} = 0 , \qquad u = 0 .$$

APPENDIX B

159

DETAILS OF THE
NUMERICAL FORMULATION

In view of the axial symmetry of the sensor, only the flow in the region D = {(R,Z)}, as shown in Fig. (2.2) has to be considered. Within a region D, a network of uniformly spaced grid lines is constructed. At each interior mesh point (the intersection of two grid lines), the derivatives that appear in Eqs. (2-28) through Eqs. (2-30) are approximated by the central difference technique.

For example, if Λ be any dependent variable and R and Z be independent variables in the i and j direction respectively then $\frac{\partial \Lambda}{\partial R}$, $\frac{\partial \Lambda}{\partial Z}$, $\frac{\partial^2 \Lambda}{\partial R^2}$, and $\frac{\partial^2 \Lambda}{\partial Z^2}$ can be written as

$$\frac{\partial \Lambda}{\partial R} = \frac{\Lambda_{i+1,j} - \Lambda_{i-1,j}}{2\Delta R} + 0(\Delta R)^2 , \qquad \text{(B-1)}$$

$$\frac{\partial \Lambda}{\partial Z} = \frac{\Lambda_{i,j+1} - \Lambda_{i,j-1}}{2\Delta Z} + 0(\Delta Z)^2 , \qquad \text{(B-2)}$$

$$\frac{\partial^2 \Lambda}{\partial R^2} = \frac{\Lambda_{i+1,j} - 2\Lambda_{i,j} + \Lambda_{i-1,j}}{(\Delta R)^2} + 0(\Delta R^2) , \qquad \text{(B-3)}$$

$$\frac{\partial^2 \Lambda}{\partial Z^2} = \frac{\Lambda_{i,j+1} - 2\Lambda_{i,j} + \Lambda_{i,j-1}}{(\Delta Z)^2} + 0(\Delta Z)^2 , \qquad \text{(B-4)}$$

where ΔR represents the grid size along R (or i) direction and ΔZ along Z (or j) direction. Furthermore, higher orders

than the second order of grid size are neglected, and U and W can be eliminated from the governing equations, by employing the definition of the stream function as

$$U_{i,j} = \frac{1}{R} \frac{\partial \psi}{\partial Z}\bigg|_{i,j} = \frac{\psi_{i,j+1} - \psi_{i,j-1}}{2(i-1)\,\Delta R \Delta Z} \quad , \qquad (B-5)$$

$$W_{i,j} = -\frac{1}{R} \frac{\partial \psi}{\partial R}\bigg|_{i,j} = \frac{\psi_{i-1,j} - \psi_{i+1,j}}{2(i-1)\,(\Delta R)^2} \qquad (B-6)$$

The following formulation illustrates how the various equations are approximated by the central difference technique.

1. Stream Function Equation.

The equation for the stream function is written as

$$\frac{\partial^2 \psi}{\partial R^2} - \frac{1}{R} \frac{\partial \psi}{\partial R} + \frac{\partial^2 \psi}{\partial Z^2} = R\eta \quad . \qquad (B-7)$$

By employing the central difference technique and by choosing equal grid size along R and Z (i.e., $\Delta R = \Delta Z = a$), the above equation is written as

$$\frac{\psi_{i+1,j} - 2\psi_{i,j} + \psi_{i-1,j}}{a^2} - \frac{\psi_{i+1,j} - \psi_{i-1,j}}{2aR}$$

$$+ \frac{\psi_{i,j+1} - 2\psi_{i,j} + \psi_{i,j-1}}{a^2} = R\eta_{i,j} \quad . \qquad (B-8)$$

In the above equation the subscripts i and j correspond to the R and Z coordinates respectively, since R is the instantaneous

radius, thus $R = (i-1)a$. Equation (B-8) is then solved for $\psi_{i,j}$, which results in

$$\psi_{i,j} = \frac{1}{4} (\psi_{i+1,j} + \psi_{i-1,j} + \psi_{i,j+1} + \psi_{i,j-1})$$

$$- \frac{a}{8R} (2R^2 a n_{i,j} + \psi_{i+1,j} - \psi_{i-1,j}) \qquad (B-9)$$

where $R = (i-1)a$.

2. Steady State Equations

2.1 Circulation Equation

The circulation equation is written as

$$U\frac{\partial \Gamma}{\partial R} + W\frac{\partial \Gamma}{\partial Z} = \frac{1}{N_{Re-\theta}} \left[\frac{\partial^2 \Gamma}{\partial R^2} - \frac{1}{R} \frac{\partial \Gamma}{\partial R} + \frac{\partial^2 \Gamma}{\partial Z^2} \right] . \qquad (B-10)$$

By expressing the velocities in terms of the stream function, the above equation is written as

$$\frac{1}{R} \frac{\partial \psi}{\partial Z} \frac{\partial \Gamma}{\partial R} - \frac{1}{R} \frac{\partial \psi}{\partial R} \frac{\partial \Gamma}{\partial Z} = \frac{1}{N_{Re-\theta}} \left[\frac{\partial^2 \Gamma}{\partial R^2} - \frac{1}{R} \frac{\partial \Gamma}{\partial R} + \frac{\partial^2 \Gamma}{\partial Z^2} \right] . \qquad (B-11)$$

In the difference form, this is expressed as

$$\frac{1}{R} \left[\frac{\psi_{i,j+1} - \psi_{i,j-1}}{2a} \right] \left[\frac{\Gamma_{i+1,j} - \Gamma_{i-1,j}}{2a} \right]$$

$$- \frac{1}{R} \left[\frac{\psi_{i+1,j} - \psi_{i-1,j}}{2a} \right] \left[\frac{\Gamma_{i,j+1} - \Gamma_{i,j-1}}{2a} \right] = \frac{1}{N_{Re-\theta}} \text{ x}$$

$$\left[\frac{\Gamma_{i+1,j} - 2\Gamma_{i,j} + \Gamma_{i-1,j}}{a^2} - \frac{1}{R} \frac{\Gamma_{i+1,j} - \Gamma_{i-1,j}}{2a} \right.$$

$$\left. + \frac{\Gamma_{i,j+1} - 2\Gamma_{i,j} + \Gamma_{i,j-1}}{a^2} \right] \qquad (B-12)$$

Equation (B-12) is then solved for $\Gamma_{i,j}$, which results in

$$
\begin{aligned}
\Gamma_{i,j} = \frac{1}{4}\Big[&\Gamma_{i+1,j} + \Gamma_{i-1,j} + \Gamma_{i,j+1} + \Gamma_{i,j-1}\Big] \\
- \frac{N_{Re-\theta}}{16R}\Big[&\Big\{\psi_{i,j+1} - \psi_{i,j-1} + \frac{2a}{N_{Re-\theta}}\Big\}\Big\{\Gamma_{i+1,j} - \Gamma_{i-1,j}\Big\} \\
- &\Big\{\psi_{i+1,j} - \psi_{i-1,j}\Big\}\Big\{\Gamma_{i,j+1} - \Gamma_{i,j-1}\Big\}\Big] .
\end{aligned} \tag{B-13}
$$

2.2 Tangential Vorticity Equation

The equation for the tangential vorticity is written as

$$
U\frac{\partial \eta}{\partial R} + W\frac{\partial \eta}{\partial Z} - \frac{U\eta}{R} - \frac{2\Gamma}{R^3}\frac{\partial \Gamma}{\partial Z} = \frac{1}{N_{Re-\theta}} \; \times
$$

$$
\Bigg[\frac{\partial^2 \eta}{\partial R^2} + \frac{1}{R}\frac{\partial \eta}{\partial R} - \frac{\eta}{R^2} + \frac{\partial^2 \eta}{\partial Z^2} \Bigg] . \tag{B-14}
$$

Upon eliminating U and W by use of the stream function ψ, this is expressed as

$$
\frac{1}{R}\frac{\partial \psi}{\partial Z}\frac{\partial \eta}{\partial R} - \frac{1}{R}\frac{\partial \psi}{\partial R}\frac{\partial \eta}{\partial Z} - \frac{\eta}{R^2}\frac{\partial \psi}{\partial Z} - \frac{2\Gamma}{R^3}\frac{\partial \Gamma}{\partial Z}
$$

$$
= \frac{1}{N_{Re-\theta}}\Bigg[\frac{\partial^2 \eta}{\partial R^2} + \frac{1}{R}\frac{\partial \eta}{\partial R} - \frac{\eta}{R^2} + \frac{\partial^2 \eta}{\partial Z^2} \Bigg] . \tag{B-15}
$$

The above equation is now written in the difference form as

$$
\frac{1}{R}\Big\{ \frac{\psi_{i,j+1} - \psi_{i,j-1}}{2a} \Big\}\Big\{ \frac{\eta_{i+1,j} - \eta_{i-1,j}}{2a} \Big\}
$$

$$
- \frac{1}{R}\Big\{ \frac{\psi_{i+1,j} - \psi_{i-1,j}}{2a} \Big\}\Big\{ \frac{\eta_{i,j+1} - \eta_{i,j-1}}{2a} \Big\} - \frac{\eta_{i,j}}{R^2} \; \times
$$

$$
\Big\{ \frac{\psi_{i,j+1} - \psi_{i,j-1}}{2a} \Big\} - \frac{2\Gamma_{i,j}}{R^3}\Big\{ \frac{\Gamma_{i,j+1} - \Gamma_{i,j-1}}{2a} \Big\}
$$

$$= \frac{1}{N_{Re-\theta}} \left[\left\{ n_{i+1,j} + n_{i-1,j} + n_{i,j+1} \right. \right.$$

$$\left. + n_{i,j-1} - 4n_{i,j} \right\} / a^2 + \left\{ n_{i+1,j} - n_{i-1,j} \right\} \Big/ (2aR)$$

$$\left. - \frac{n_{i,j}}{R^2} \right] . \qquad \text{(B-16)}$$

Equation (B-16) is then solved for $n_{i,j}$ which results in

$$n_{i,j} = \left[\frac{1}{4} \left\{ n_{i+1,j} + n_{i-1,j} + n_{i,j+1} + n_{i,j-1} \right\} \right.$$

$$- \frac{N_{Re-\theta}}{16R} \left\{ (\psi_{i,j+1} - \psi_{i,j-1} - \frac{2a}{N_{Re-\theta}}) \times \right.$$

$$(n_{i+1,j} - n_{i-1,j}) - (\psi_{i+1,j} - \psi_{i-1,j}) \times$$

$$\left. \left. (n_{i,j+1} - n_{i,j-1}) - \frac{4a}{R^2} \Gamma_{i,j} (\Gamma_{i,j+1} - \Gamma_{i,j-1}) \right\} \right]$$

$$\Big/ \left[1 + \frac{a^2}{4R^2} + \frac{aN_{Re-\theta}}{8R^2} (\psi_{i,j-1} - \psi_{i,j+1}) \right] , \quad \text{(B-17)}$$

where R = (i-1)a, with subscripts i and j are along R and Z direction respectively.

3. Transient Case

3.1 Circulation Equation

In the circulation equation,

$$\frac{\partial \Gamma}{\partial T} + U\frac{\partial \Gamma}{\partial R} + W\frac{\partial \Gamma}{\partial Z} = \frac{1}{N_{Re-\theta}} \left[\frac{\partial^2 \Gamma}{\partial R^2} - \frac{1}{R} \frac{\partial \Gamma}{\partial R} + \frac{\partial^2 \Gamma}{\partial Z^2} \right] , \quad \text{(B-18)}$$

U and W are eliminated by the stream function ψ and one obtains

$$\frac{\partial \Gamma}{\partial T} + \frac{1}{R} \frac{\partial \psi}{\partial Z} \frac{\partial \Gamma}{\partial R} - \frac{1}{R} \frac{\partial \psi}{\partial R} \frac{\partial \Gamma}{\partial Z} = \frac{1}{N_{Re-\theta}} \quad \times$$

$$\left[\frac{\partial^2 \Gamma}{\partial R^2} - \frac{1}{R} \frac{\partial \Gamma}{\partial R} + \frac{\partial^2 \Gamma}{\partial Z^2} \right] \qquad (B-19)$$

The difference equation is then rewritten by use of the central time and central space technique. Consequently, Eq. (B-19) becomes

$$\left[\Gamma_{i,j}^{k+1} - \Gamma_{i,j}^{k-1} \right] \Big/ (2\Delta T) + \left\{ \psi_{i,j+1}^{k} - \psi_{i,j-1}^{k} \right\} \times$$

$$\left\{ \Gamma_{i+1,j}^{k} - \Gamma_{i-1,j}^{k} \right\} \Big/ (4Ra^2)$$

$$- \left\{ \psi_{i+1,j}^{k} - \psi_{i-1,j}^{k} \right\} \left\{ \Gamma_{i,j+1}^{k} - \Gamma_{i,j-1}^{k} \right\} (4Ra^2)$$

$$= \frac{1}{N_{Re-\theta}} \left[\left\{ \Gamma_{i+1,j}^{k} + \Gamma_{i-1,j}^{k} + \Gamma_{i,j+1}^{k} + \Gamma_{i,j-1}^{k} \right. \right.$$

$$\left. - 4\Gamma_{i,j}^{k} \right\} \Big/ a^2 \left. - \left\{ \Gamma_{i+1,j}^{k} - \Gamma_{i-1,j}^{k} \right\} \Big/ (2aR) \right] \quad .$$

$$(B-20)$$

In the first term of right hand side, $4\Gamma_{i,j}^{k}$ is written as

$$4\Gamma_{i,j}^{k} = 2\Gamma_{i,j}^{k+1} + 2\Gamma_{i,j}^{k-1} \quad , \qquad (B-21)$$

and then the equation is solved for $\Gamma_{i,j}^{k+1}$ to give

$$\Gamma_{i,j}^{k+1} = \left[\Gamma_{i,j}^{k-1} + \frac{\Delta T}{2a^2 R} \left\{ (\psi_{i+1,j}^{k} - \psi_{i-1,j}^{k}) \times \right. \right.$$

$$(\Gamma_{i,j+1}^{k} - \Gamma_{i,j-1}^{k}) - (\psi_{i,j+1}^{k} - \psi_{i,j-1}^{k}) \times$$

$$(\Gamma_{i+1,j}^{k} - \Gamma_{i-1,j}^{k}) - 2a (\Gamma_{i+1,j}^{k} - \Gamma_{i-1,j}^{k}) \Big/ N_{Re-\theta}$$

$$+ 4R (\Gamma_{i+1,j}^{k} + \Gamma_{i-1,j}^{k} + \Gamma_{i,j+1}^{k} + \Gamma_{i,j-1}^{k} - 2\Gamma_{i,j}^{k-1})$$

$$\Big/ N_{Re-\theta} \Big\} \Big] \Big/ \left[1 + 4\Delta T \Big/ \left\{ N_{Re-\theta} \cdot a^2 \right\} \right] \quad , \quad \text{(B-22)}$$

where $R = (i-1)a$.

3.2 Tangential Vorticity

The equation for the tangential vorticity is written as

$$\frac{\partial \eta}{\partial T} + \frac{1}{R} \frac{\partial \psi}{\partial Z} \frac{\partial \eta}{\partial R} - \frac{1}{R} \frac{\partial \psi}{\partial R} \frac{\partial \eta}{\partial Z} - \frac{\eta}{R^2} \frac{\partial \psi}{\partial Z} - \frac{2\Gamma}{R^3} \frac{\partial \Gamma}{\partial Z}$$

$$= \frac{1}{N_{Re-\theta}} \left[\frac{\partial^2 \eta}{\partial R^2} + \frac{1}{R} \frac{\partial \eta}{\partial R} - \frac{\eta}{R^2} + \frac{\partial^2 \eta}{\partial Z^2} \right] \quad . \quad \text{(B-24)}$$

Through the use of the central time and central space technique, the above equation is written in the difference form and there results

$$\left\{ \eta_{i,j}^{k+1} - \eta_{i,j}^{k-1} \right\} \Big/ (2\Delta T) + \left\{ \psi_{i,j+1}^{k} - \psi_{i,j-1}^{k} \right\} \times$$

$$\left\{ \eta_{i+1,j}^{k} - \eta_{i-1,j}^{k} \right\} \Big/ (4Ra^2)$$

$$- \left\{ \psi_{i+1,j}^{k} - \psi_{i-1,j}^{k} \right\} \left\{ \eta_{i,j+1}^{k} - \eta_{i,j-1}^{k} \right\} \Big/ (4Ra^2)$$

$$- n_{i,j}^{k} \left\{ \psi_{i,j+1}^{k} - \psi_{i,j-1}^{k} \right\} / (2aR^2)$$

$$-\Gamma_{i,j}^{k} \left\{ \Gamma_{i,j+1}^{k} - \Gamma_{i,j-1}^{k} \right\} / (aR^3) = \frac{1}{N_{Re-\theta}} \quad x$$

$$\left[\left\{ n_{i+1,j}^{k} + n_{i-1,j}^{k} + n_{i,j+1}^{k} + n_{i,j-1}^{k} - 4n_{i,j}^{k} \right\} / a^2 \right.$$

$$\left. + \left\{ n_{i+1,j}^{k} - n_{i-1,j}^{k} \right\} / (2aR) - n_{i,j}^{k} / R^2 \right]. \quad \text{(B-25)}$$

In the first term of right hand side $4n_{i,j}^{k}$ is rewritten as

$$4n_{i,j}^{k} = 2n_{i,j}^{k+1} + 2n_{i,j}^{k-1} \quad \text{(B-26)}$$

and then the equation is solved for $n_{i,j}^{k+1}$ to obtain

$$n_{i,j}^{k+1} = \left[n_{i,j}^{k-1} + \frac{\Delta T}{2a^2 R} \left\{ (\psi_{i+1,j}^{k} - \psi_{i-1,j}^{k}) \quad x \right. \right.$$

$$(n_{i,j+1}^{k} - n_{i,j-1}^{k}) - (\psi_{i,j+1}^{k} - \psi_{i,j-1}^{k}) \quad x$$

$$(n_{i+1,j}^{k} - n_{i-1,j}^{k}) + 2an_{i,j}^{k} (\psi_{i,j+1}^{k} - \psi_{i,j-1}^{k}$$

$$- 2a/N_{Re-\theta}) / R + 4a\Gamma_{i,j}^{k} (\Gamma_{i,j+1}^{k} - \Gamma_{i,j-1}^{k}) / R^2$$

$$+ 2a (n_{i+1,j}^{k} - n_{i-1,j}^{k}) / N_{Re-\theta} + 4R (n_{i+1,j}^{k}$$

$$\left. \left. + n_{i-1,j}^{k} + n_{i,j+1}^{k} + n_{i,j-1}^{k} - 2n_{i,j}^{k-1}) / N_{Re-\theta} \right\} \right]$$

$$/ \left[1 + 4\Delta T / (N_{Re-\theta} \cdot a^2) \right]. \quad \text{(B-27)}$$

Equations (B-5), (B-9) and (B-13) constitute the governing difference equations for the steady state case and Eqs. (B-5), (B-20) and (B-27) for the transient case.

APPENDIX C

VELOCITY COMPONENT
CALCULATION PROCEDURE

As discussed under the test procedure,(Section (6.2)) the resultant velocity V* as well as the longitudinal angles θ and ϕ are measured at a particular location in the sink tube by a constant temperature hot wire anemometer. The angle θ is the longitudinal angle made by the probe with the sink tube axis in a horizontal plane, whereas ϕ is the longitudinal angle made by the probe with the sink tube axis in a vertical plane.

The measured values of V*, θ and ϕ are used to calculate the radial (u), axial (w) and tangential (v) velocity components. The resultant velocity is defined as

$$V^* = \sqrt{u^2 + v^2 + w^2} \quad . \tag{C-1}$$

Since θ is measured in a tangential direction then

$$v = w \tan \theta \quad . \tag{C-2}$$

Similarly since ϕ is measured in a radial direction then

$$u = w \tan \phi \quad . \tag{C-3}$$

Thus the square of the resultant velocity becomes

$$V^{*2} = w^2 [1 + \tan^2 \theta + \tan^2 \phi]$$

or

$$w = \frac{V^*}{\sqrt{1 + \tan^2 \theta + \tan^2 \phi}} \quad . \tag{C-4}$$

The axial velocity component w is calculated first by use of Eq. (C-4), and then the tangential and radial velocity components are calculated by use of Eqs. (C-2) and (C-3) respectively.

APPENDIX D

PROBE MECHANISM FOR RESULTANT
VELOCITY MEASUREMENT

The probe holder and mechanism used, for measurement of the resultant velocity within the sink tube is shown in Fig. (6.6). This Appendix is devoted to a discussion as to how the probe is positioned to measure the resultant velocity.

The distance between the center of the probe wire and the probe rotating axis (probe longitudinal rotating axis) is denoted by r_1. The instantaneous vertical movement (radius) of the probe support axis from the sink tube axis is denoted by S_1 when probe wire is horizontal, and S_2 when the probe wire is vertical. Thus the instantaneous radius made by the probe wire in its movement, for the case when the probe wire is horizontal, is given by

$$r = \sqrt{S_1{}^2 + (r_1 \sin \theta)^2} \quad . \tag{D-1}$$

Similarly the instantaneous radius made by the probe wire in its movement, for the case when the probe wire is vertical, is given by

$$r = S_2 + r_1 \sin \phi \quad . \tag{D-2}$$

As the probe wire is positioned at a particular location for measurement of the resultant velocity both radii, as given by Eqs.(D-1) and (D-2), have to be equal. This results in

$$r = \sqrt{(S_1)^2 + (r_1 \sin \theta)^2} = S_2 + r_1 \sin \phi \quad . \tag{D-3}$$

within the sink tube the radial velocity u is negligible and the measured value of ϕ is rather small, therefore, the value of $r_1 \sin \phi$ is also very small. However, the tangential velocity v is of appreciable value, so the measured value of θ, and thus $r_1 \sin \theta$ is of an appreciable magnitude. Hence from Eq. (D-3), it is concluded that S_2 is greater than S_1 and that the difference between r and S_2 is negligible.

In the process of measurement of the resultant velocity, the probe and probe support are first positioned at a particular z location. The probe support is then moved vertically making a radius S_1 with respect to the sink tube axis. By use of the roller-string arrangement the horizontally mounted probe wire is then rotated about its axis to obtain the location at which the anemometer voltmeter reading is maximum. This procedure determines the distance r_1, between the center of the probe wire and the probe rotating axis. At that particular location, the longitudinal angle θ is then measured. Thus with the values of S_1, r_1 and θ, the instantaneous radius r is calculated through use of Eq. (D-1). The maximum anemometer voltmeter reading is the resultant velocity at that location.

In a similar manner and with the vertically mounted hot wire probe, S_2 is adjusted equal to r, and then the probe wire is rotated to obtain the longitudinal angle ϕ. The resultant velocity is then checked and corrected for S_2, since u << v in the sink tube, and ϕ << θ. Also, since ϕ is small, and r > S_2, then r-S_2 is very small. Thus r can be approximated by S_2.

In a similar manner to the method used in calculating the radial distance, the correction for z is accounted for and results in the expression

$$z = z_1 - r_1 \cos \theta = z_2 - r_1 \cos \phi \qquad \text{(D-4)}$$

where z is the instantaneous location of probe wire. In this equation, z_1 and z_2 are the axial distances of the longitudinal rotation of the probe axii measured from the sink tube entrance, when hot wire is in a horizontal and a vertical position respectively.

APPENDIX E

ERROR ANALYSIS

The possible sources of error throughout this study may be due to either experimental or numerical errors. The experimental error may be subdivided into the static pressure measurement error and the velocity measurement error resulting from use of both velocity calculation methods.

Experimental Error Analysis

In an experiment requiring measurements of several quantities, each of which has an error associated with it, the total error that propagates into the final result may be estimated by the expression [66]

$$e_E^2 = \sum_{n=1}^{i} (\frac{\partial F}{\partial n})^2 \; e_n^2 \qquad\qquad (E-1)$$

where F is a function of n independent variables having errors e_n. For repeated measurements of the variables, it is assumed that errors are normally distributed about the true value.

The possibilities of errors in velocity measurements may be attributed to several factors; (i) exact positioning of probe holder in sink tube for either a radial or axial position, (ii) longitudinal rotation of the probe in either a horizontal or vertical direction through use of the roller-string arrangement, (iii) calibration of hot wire anemometer (specifically the linearizer for gain and exponent adjustment), and (iv) human error in reading the scales.

The error in positioning the probe holder is fixed and is considered as e_{r_1}, for the radial location and e_{z_1} for the

axial location.

The error due to the longitudinal rotation of the probe in a horizontal plane is obtained as follows. The quantity r is defined in Equation (D-1), and by applying Equation (E-1), the expression for error becomes

$$e_{r_2}^2 = (\frac{\partial r}{\partial s_1})^2 e_{s_1}^2 + (\frac{\partial r}{\partial \theta})^2 e_\theta^2 \quad . \tag{E-2}$$

The partial derivatives in this equation are obtained from Equation (D-1) and are found to be

$$\frac{\partial r}{\partial s_1} = \frac{s_1}{\sqrt{s_1^2 + r_1^2 \sin^2\theta}} \tag{E-3}$$

$$\frac{\partial r}{\partial \theta} = \frac{r_1^2 \sin\theta \cos\theta}{\sqrt{s_1^2 + r_1^2 \sin^2\theta}} \tag{E-4}$$

By substituting Equation (E-3) and (E-4) into Equation (E-2), the expression for error is obtained as

$$e_{r_2}^2 = \frac{s_1^2 e_{s_1}^2 + r_1^4 \sin^2\theta \cos^2\theta \, e_\theta^2}{s_1^2 + r_1^2 \sin^2\theta} \quad . \tag{E-5}$$

In a similar manner the error equation for location of axial length, due to the longitudinal rotation of the probe in a horizontal plane, is determined by using Equation (D-4)

$$e_z^2 = e_{z_1}^2 + r_1^2 \sin^2\theta \, e_\theta^2 \quad . \tag{E-6}$$

The error equation due to the longitudinal rotation of the probe in a vertical plane is obtained in a similar manner.

As the radial velocity in the sink tube is negligible, the longitudinal rotation of the probe in the vertical plane is also negligible. Thus, no additional discussion is necessary in arriving at the error equations given below

$$e_{r_2}^2 = e_{s_2}^2 + r_1^2 \cos^2\phi \; e_\phi^2 \qquad\qquad (E-7)$$

and

$$e_{z_2}^2 = e_{z_2}'^2 + r_1^2 \sin^2\phi \; e_\phi^2 \qquad . \qquad (E-8)$$

The calibration errors are fixed and are denoted by e_{c_1} and e_{c_2}. The quantity e_{c_1} denotes the error for probe longitudinal rotation calibration and e_{c_2} denotes the error of calibration of the hot wire anemometer combined with linearizer.

The error in velocity measurement is obtained by deriving an error equation for each component of velocity. The error equations are obtained through use of Equation (E-1) and the fundamental definition of the velocity components, (C-2), (C-3) and (C-4), and are found to be

$$e_w^2 = e_{V*}^2 + \frac{V*^2(\tan^2\theta \; \sec^4\theta \cdot e_\theta^2 + \tan^2\phi \; \sec^4\phi \cdot e_\phi^2)}{(1 + \tan^2\theta + \tan^2\phi)} \Bigg/ (1 + \tan^2\theta + \tan^2\phi) \qquad (E-9)$$

$$e_u^2 = \tan^2\phi \; e_w^2 + w^2 \sec^4\phi \; e_\phi^2 \qquad (E-10)$$

$$e_v^2 = \tan^2\theta \; e_\theta^2 + w^2 \sec^4\theta \; e_\theta^2 \qquad . \qquad (E-11)$$

To estimate the relative magnitudes of errors associated with the uncertainties in the measurements, numerical values from a typical test condition are substituted in the above equations.

The following values are taken from a typical test run from which the velocity components are determined

Radial location of pin bearing
from the sink tube axis $\qquad$ s_1 = 0.5 inch,

Length of rotating arm of probe
(hot wire) $\qquad$ r_1 = 0.546 inch,

Axial location of pin bearing
from sink tube entrance $\qquad$ z_1 = 6 inches,

Horizontal longitudinal angle $\qquad$ θ = 38.7 degrees,

Vertical longitudinal angle $\qquad$ ϕ = 0.0 degree,

Resultant velocity $\qquad$ V^* = 6.95 ft/sec.,

Speed of sensor $\qquad$ N = 20 rpm.,

and Radius of vortex chamber $\qquad$ r_0 = 10 inches.

By using V^*, θ and ϕ, the axial, tangential and radial velocity components are calculated and found to be 5.45, 4.36 and 0.0 feet per sec. respectively.

The following errors or uncertainties are assumed, taking into account instrumentation accuracy errors due to lack of resolution, human errors in reading instruments and general velocity losses, etc.

Name of Error	Errors in Percentage	Error Symbols	Magnitude of Errors
Resultant velocity horizontal	± 1%	e_V*	0.0695 ft/sec
Longitudinal angle vertical	± 1%	e_θ	0.387 degrees
Longitudinal angle	± 1%	e_ϕ	0.0 degrees
Calibration of longitudinal angle	± 1%	e_{c_1}	-
Calibration of anemometer	± 0.5%	e_{c_2}	0.03475 ft/sec
Radial distance	± 1%	e_{s_1}	0.005 inch
Axial location	± 0.2%	e_{z_1}	0.012 inch

The error in measuring the radius r in the horizontal plane position is calculated by using Equation (E-5). By using the values given in the Table above, the error is found to be

$$e_{r_2} = 0.006438 \text{ inch.} \tag{E-12}$$

The error in measuring the radius r in the vertical plane position is calculated by using Equation (E-7). By using the values given in the Table above, the error e_{r_2} is calculated and found to be

$$e_{r_2} = 0.005 \text{ inch.} \tag{E-13}$$

Comparing (E-12) and (E-13), the larger value is chosen for the total error calculation. The magnitude of error in measuring the radial distance s_1 (given in Table) is $e_{s_1} = 0.005$ inch. Thus the total error in measuring the radius is given by

$$er = (e_{s_1}^2 + e_{r_2}^2)^{0.5}$$

$$= (0.005^2 + 0.006438^2)^{0.5}$$

$$= 0.008152 \text{ inch.} \tag{E-14}$$

The magnitude of error in measuring the axial length z_1, is (from Table) e_{z_1} = 0.012 inch. This error in axial length is calculated from Equation (E-6) and is found to be very small (i.e., e_{z_1} = 0.00003), and therefore is neglected. Similarly the error e_{z_2} obtained from Equation (E-8) is also neglected.

The error in axial velocity is calculated as follows. The error in measuring the axial velocity is a result of human error, error due to positioning of the probe in either the axial or radial location and the error arising from calibration of the anemometer.

The value of the human error in reading of the meter is used in Equation (E-9) to determine its portion of the error occurring in the measuring of the axial velocity. This value is found to be $e_{w,h}$ = 0.1459 feet per second.

The value of the error resulting from positioning the probe in either the radial or axial location is obtained through use of numerical data. The magnitude of error for positioning the probe in the radial location is taken from Equation (E-14). This value is e_r = 0.008152 inches. The portion of the error occurring in measuring the axial velocity due to this positioning error is then calculated and found to be $e_{w,r}$ = 0.0043 feet per second. In a similar manner the calculated error in axial velocity due to positioning of the

probe in the axial location is found to be $e_{w,z}$ = 0.0036 feet per second.

The portion of the error in measuring the axial velocity that is due to the calibration of the hot wire anemometer must also be accounted for. This value is found to be e_{c_2} = 0.03475 feet per second.

The total error in measuring the axial velocity is then determined by use of the equation

$$e_w = [e_{w,h}^2 + e_{w,r}^2 + e_{w,z}^2 + e_{c_2}^2]^{1/2} \qquad \text{(E-15)}$$

and is found to be 0.15 feet per second. The percent error therefore is 2.75.

In a procedure similar to the above, the error in measuring the tangential velocity is also obtained. The estimate of the human error $e_{v,h}$ found from Equation (E-11) is 0.1316 feet per second. The magnitude of the error for probe positioning in the radial direction is e_r = 0.008152 inch which results in a value of $e_{v,r}$ = 0.0124 feet per second. Then from the value of e_z = 0.012 inches the value of $e_{v,z}$ becomes 0.014 feet per second. These component values then result in a total error of 0.1374 feet per second and a percentage error or 3.15.

In a manner similar to the above, the error in measuring the radial velocity is shown to be zero since the radial velocity is zero for this location.

The same procedure is adopted for obtaining the error analysis in the second method of velocity measurement.

In this method the radial velocity is assumed to be zero.

The tangential and axial velocities are given by Equations (6-13) and (6-14) respectively. By using the same technique as before, these equations are transformed to the error equations.

$$e_V^2 = \frac{V_V^2 \, e_{V_V}^2 + V_H^2 \, e_{V_H}^2}{(1 - K_o^2)(V_V^2 - V_H^2)} \tag{E-16}$$

and

$$e_w^2 = \frac{V_H^2 \, e_{V_H}^2 + K_o^4 \, V_V^2 \, e_{V_V}^2}{(1 - K_o^2)(V_H^2 - K_o^2 V_V^2)} \tag{E-17}$$

After combining all errors as discussed previously the resultant total error in tangential and axial velocities are found to be respectively 0.1455 and 0.157 feet per second, while on a percentage basis these values are 3.34 and 2.88 respectively.

In addition to accounting for the errors in measuring the component velocities it is also necessary to account for the error in measuring the static pressure.

The static pressure is measured by a specially designed static pressure probe. The probe consists of two concentric tubes. Very small holes were drilled through the outer tube so as to eliminate the dynamic pressure head. The static pressure then is directly measured by means of the inner tube which is connected to a pressure transducer. Since the transducer directly measures the pressure, the possibilities of error are minimal. Nevertheless, a discussion pertaining to any error, thus resulting, follows.

An error could result from not properly positioning the static pressure probe in either the radial or axial directions. The probe is located at a given radial position through means of a precision mechanism having a measuring scale whose smallest graduation is 0.001 inches. Thus any error arising is indeed negligible. Similarly the rack and pinion mechanism used to position the probe at a given axial location has a measuring scale with its smallest graduation being 0.05 inches. Again, any error occurring would indeed be minimal. The error arising due to the boundary layer growth effects are minimized due to the tapered tip of the probe. Another possible error could result from the flow being at an angle to the sink tube geometric axis and thus to the probe. This effect experimentally is observed to be negligible up to angles of forty degrees. Beyond this angle a deviation of 3 to 4 percent is noted in the readings. As observed from the experimental data the axial velocity is higher than the tangential velocity. Also it is noted that the radial velocities are negligible. Therefore, the flow angle encountered throughout the experiment never exceeded 35 degrees and hence the error is negligible.

Any error resulting from use of the transducer is also minimal as it is calibrated and checked by means of a standard resistance.

The probable human error arising from reading of the transducer scale is estimated to be less than one percent. The smallest division on the transducer scale has a 0.0005 mm of mercury head and this is sufficiently small for the pressure range encountered within the sink tube.

Error Analysis Pertinent to the Numerical Results

The steady state and transient governing equations consist of first and second order derivatives in R and Z. When these differential equations are written in the difference form a truncation error results. The evaluation of this error is determined for any dependent variable as here described.

Let Λ be any dependent variable, x be any independent variable and a be assigned the grid size, then Λ can be expressed as function of x and a, $\Lambda = \Lambda(x,a)$. By use of the Taylor series expansion $\Lambda(x+a)$ and $\Lambda(x-a)$ become respectively

$$\Lambda(x+a) = \Lambda(x) + a\Lambda'(x) + \frac{a^2}{2!} \Lambda''(x) + \frac{a^3}{3!} \Lambda'''(x)$$
$$+ \frac{a^4}{4!} \Lambda^{iv}(x) + \ldots \qquad (E-18)$$

$$\Lambda(x-a) = \Lambda(x) - a\Lambda'(x) + \frac{a^2}{2!} \Lambda''(x) + \frac{a^3}{3!} \Lambda'''(x)$$
$$+ \frac{a^4}{4!} \Lambda^{iv}(x) + \ldots \qquad (E-19)$$

The subtraction of these equations gives the first order derivative of Λ with respect to x, and is shown in Equation (E-20). The addition of these equations, however, gives the second order derivative of Λ with respect of x, and is shown in Equation (E-21)

$$\frac{\partial \Lambda}{\partial x} = \frac{\Lambda(x+a) - \Lambda(x-a)}{2a} + 0(a^2) \qquad (E-20)$$

and

$$\frac{\partial^2 \Lambda}{\partial x^2} = \frac{\Lambda(x+a) - 2\Lambda(x) + \Lambda(x-a)}{a^2} + 0 \ (a^2) \quad . \qquad \text{(E-21)}$$

It becomes evident that the central difference technique contains the truncation error of order a^2 for both the first and second order derivatives. In this analysis a is chosen to be ≤ 0.02 and, therefore, the truncation error is of order $(0.02)^2$ or 0.0004.

APPENDIX F

187

APPENDIX F

COMPUTER PROGRAM - TRANSIENT CASE

```
READ (2,500) N,M,NN,MM
READ (2,550) QO, OMEGA, RO, H, TOL
READ (2,600) XLL, LL1, LL2, LL3, LLX
XNEU = 0.00016
RE = OMEGA * RO * RO/ XNEU
ROSB = QO / (2.*3.14159*OMEGA * RO **3 )
VO = RO * OMEGA
GEMAO = OMEGA * RO ** 2
UO = QO / (2. * 3.141593 * RO8H )
REU = UO * RO / XNEU
R = 1.0
N1 = N - 1
XN1 = N1
M1 = M - 1
MP = M + 1
XM1 = M1
NN1 = NN - 1
NNP = NN + 1
XNN = NN
XNN1 = NN1
MM1 = MM - 1
MM3 = MM - 3
MM4 = MM - 4
A = R / XN1
DELR = A
DELZ = A
DT = XLL
RI = A * XNN1
REI = 1. / RE
R3 = 1. / ( A * A )
CA = 4. * DT * REI * R3
CB = 2.0 * A * REI
DENO = 1. + CA
WRITE (3,700) QO, OMEGA, H, RO, RE, GEMAO, ROSB
WRITE (3,710) UO, REU, VO
WRITE (3,720) N, M, NN, MM
T = 0.
MMT = MM
DO 3 I = 1, N
X1 = I - 1
RA = X1 * A
DO 1 J = 1, MMT
PA (I,J) = 0.
GA (I,J) = RA * RA
GB (I,J) = GA (I,J)
SA (I,J) = 0.0
SB (I,J) = 0.
1       CONTINUE
```

```
        IF ( I - NN) 3,2,2
2       MMT = M
3       CONTINUE
        DO 4 J = 1, M
        X2 = J - 1
        PA (N,J) = - ROSB * X2 / XM1
4       CONTINUE
        DO 5 I = NN, N
        PA (I,M) = - ROSB
5       CONTINUE
        DO 6 J = M, MM
        PA (NN,J) = - ROSB
6       CONTINUE
C       **********************************************************
C
C
C       STREAM FUNCTION CALCULATION WITH ZERO VORTICITY TERM
C
C       **********************************************************
C
        K2 = 0
        DO 15 I5 = 1, LL1
        K2 = K2 + 1
        MMT = MM
        DO 9 I = 1, N
        DO 7 J = 1, MMT
        PB (I,J) = PA (I,J)
7       CONTINUE
        IF ( I - NN) 9,8,8
8       MMT = M
9       CONTINUE
        DEVMP = 0.0
        MMT1 = MM1
        DO 13 I = 2, N1
        X1 = I - 1
        RA = X1 * A
        DO 11 J = 2, MMT1
        TEMP = PB (I,J)
        PA (I,J) = 0.25*(PB(I+1,J) + PB(I-1,J) + PB(I,J+1)
       1+ PB(I,J-1) - PA*(A-*)RA **SA (I,J) + (PB (I+1,J)
       2-PB*(I-1,J)) *0.5)/+RA*))(I-1,J) - PB (I-1,J))*0.5
        DEV = ABS( PA(I,J) - TEMP)
        IF (DEV - DEVMP) 11,11,10
10      DEVMP = DEV
11      CONTINUE
        IF (I - NN1) 13,12,12
12      MMT1 = M1
13      CONTINUE
        DO 14 I = 2 NN1
14      PA(I,MM) = PA(I,MM4) - 2.* PA(I,MM3) + 2.* PA(I,MM1)
15      CONTINUE
        WRITE (3,730)
        WRITE (3,740) K2
        WRITE (3,750) DEVMP, TOL
        WRITE (3,760) (J, J = 1, M)
```

```
        DO 16 I = 1, N
        WRITE (3,770) I, (PA(I,J), J = 1, M )
 16     CONTINUE
        WRITE (3,780) (I, I = 1, NN )
        DO 17 J = M, MM
        WRITE (3, 770) J, (PA(I,J), I = 1, NN )
 17     CONTINUE
        MX = LL3
        DO 53 KX = 1, LLX
        T = T + DT
C       *********************************************************
C
C
C       STREAM FUNCTION CALCULATION WITH NEW VORTICITY TERM
C
C
C       *********************************************************
        DO 26 I6 = 1, LL2
        MMT = MM
        DO 20 I = 1, N
        DO 18 J = 1, MMT
        PB (I,J) = PA (I,J)
 18     CONTINUE
        IF ( I - NN) 20,19,19
 19     MMT = M
 20     CONTINUE
        DEVMP = 0.0
        MMT1 = MM1
        DO 24 I = 2, N1
        X1 = I - 1
        RA = X1 * A
        DO 22 J = 2, MMT1
        TEMP = PB (I,J)
        PA(I,J) = 0.25*(PB(I+1,J) + PB(I-1,J) + PB(I,J+1)
    1+PB(I,J-1) - A* (A * RA * SA (I,J) + (PB (I+1,J)
    2- PB (I-1,J)) * 0.5 / RA ))
        DEV = ABS( PA(I,J) - TEMP)
        IF (DEV - DEVMP) 22,21,21
 21     DEVMP = DEV
 22     CONTINUE
        IF ( I - NN1) 24,23,23
 23     MMT1 = M1
 24     CONTINUE
        DO 25 I = 2, NN1
 25     PA(I,MM) = PA(I,MM4) - 2.* PA(I,MM3) + 2.* PA(I,MM1)
 26     CONTINUE
C       *********************************************************
C
C
C       CIRCULATION CALCULATION BY ITERATION TECHNIC  'PB' IS
C       USED FOR STORING THE PREVIOUS VALUE OF 'GB'
C
C
C       *********************************************************
        MMT = MM
        DO 29 I = 1, N
        DO 27 J = 1, MMT
        PB (I,J) = GB (I,J)
```

```
         GB (I,J) = GA (I,J)
27       CONTINUE
         IF (I - NN) 29,28,28
28       MMT = M
29       CONTINUE
         DEVMG = 0.0
         MMT1 = MM1
         DO 33 I = 2, N1
         X1 = I - 1
         RA = X1 * A
         DO 31 J = 2, MMT1
         TEMP = GB (I,J)
         VA = 0.5 * DT * R3 / RA
         VB = 4.0 * REI * RA
         VC = 2.0 * A / RA
         GA (I,J) = (PB (I,J) + VA * (  (PA(I+1,J) - PA(I-1,J))
        1*(GB(I,J+1) - GB(I,J)) - (PA(I,J+1) - PA(I,J-1))*
        2(GB(I+1,J) - GB(I-1,J)) + VB* (GB(I+1,J) + GB(I-1,J)
        3+GB(I+1,J) + GB(I,J-1) - 2.* PB(I,J)) - CB * ( GB(I=1,J)
        4-GB(I-1,J)))) / DENO
         GA (I,J) = ( GA (I,J) + GB (I,J)) / 2.0
         DEV = ABS( GA(I,J) - TEMP)
         IF (DEV - DEVMG) 31,31,30
30       DEVMG = DEV
31       CONTINUE
         IF (I - NN1) 33,32,32
32       MMT1 = M1
33       CONTINUE
         DO 34 I = 2, NN1
         GA (I,MM) = GA (I,MM4) - 2.* GA(I,MM3) + 2.* GA(I,MM1)
34       CONTINUE
C        ********************************************************
C
C
C        BOUNDARY CONDITIONS FOR TANGENTIAL VORTICITY CALCULATION
C
C
C        ********************************************************
         DO 35 J = MP, MM
         SA (NN,J) = 3.* (PA(NN1,J) - PA(NN,J)) / (A*A*RI)
        1-SA (NN1,J)/2.
35       CONTINUE
         J = 1
         DO 36 I = 2, N
         XI = I
         RN = (XI - 1.) * A
         SA (I,J) = 3. * PA (I,J+1) - PA (I,J)) / (A*A*RN)
        1- SA (I,J+1)/2.
36       CONTINUE
         J = M
         DO 37 I = NN, N
         XI = I
         RN = (XI - 1.) * A
         SA (I,J) = 3. * (PA (I,J-1) - PA (I,J)) / (A*A*RN)
        1- SA (I,J-1)/2.
37       CONTINUE
```

```
      SA (NN,M) = 1.5 *( PA(NN1,M) + PA(NN,M1) - 2. * PA(NN,M))
     1/ (A*A*RI) - ( SA(NN1,M) + SA(NN,M1)) / 4.0
C     **********************************************************
C
C     TANGENTIAL VORTICITY CALCULATION BY ITERATION TECHNIC
C     'PB' IS USED FOR STORING THE PREVIOUS VALUE OF 'SB'
C
C     **********************************************************
      MMT = MM
      DO 40 I = 1, N
      DO 38 J = 1, MMT
      PB (I,J) = SB (I,J)
      SB (I,J) = SA (I,J)
38    CONTINUE
      IF (I - NN) 40,39,39
39    MMT = M
40    CONTINUE
      DEVME = 0.0
      MMT1 = MM1
      DO 44 I = 2, N1
      X1 = I - 1
      RA = X1 * A
      DO 42 J = 2, MMT1
      TEMP = SB (I,J)
      VA = 0.5 * DT * R3 / RA
      VB = 4.0 * REI * RA
      VC = 2.0 * A / RA
      VD = 2.0 * VC / RA
      SA (I,J) = (PB (I,J) + VA * ((PA(I+1,J) - PA(I-1,J))*
     1(SB(I,J+1) - SB(I,J-1)) - (PA(I,J+1) - PA(I,J-1))*
     2( SB(I+1,J) - SB(I-1,J)) + VC * SB(I,J)*(PA(I,J+1)
     3- PA(I,J-1) - CB) + VD * GB(I,J)*( GB (I,J+1) - GB(I,J-1))
     4+ CB *(2.0 * XI * ( SB(I+1,J) + SB(I-1,J) + SB(I,J+1)
     5+ SB(I,J-1) - 2.0 * PB(I,J) + (SB(I+1,J) - SB(I-1,J)))))
     6)) / DENO
      SA(I,J) = ( SA (I,J) + SB (I,J)) / 2.0
      DEV = ABS( SA(I,J) - TEMP)
      IF (DEV - DEVME) 42,42,41
41    DEVME = DEV
42    CONTINUE
      IF (I - NN1) 44,43,43
43    MMT1 = M1
44    CONTINUE
      DO 45 I = 2, NN
      SA (I,MM) = SA (I,MM4) - 2.* SA(I,MM3) + 2. * SA(I,MM1)
45    CONTINUE
      IF (KX - MX)53,46,46
46    WRITE (3,790) MX
      MX = MX + LL3
      WRITE (3,810) T
      WRITE (3,800)
```

```
C          *********************************************************
C
C
C          PRINTOUT OF STREAM FUNCTION, CIRCULATION AND TANGENTIAL
C          VORTICITY
C
C
C          *********************************************************
           WRITE (3,730)
           WRITE (3,750) DEVMP, TOL
           WRITE (3,760) (J, J = 1, M )
           DO 47 I = 1, N
           WRITE (3,770) I, ( PA (I,J), J = 1,MN)
    47     CONTINUE
           WRITE (3,780) (I, I = 1, NN)
           DO 48 J = M,MM
           WRITE (3,770) J, ( PA (I,J), I = 1, NN )
    48     CONTINUE
           WRITE (3,820)
           WRITE (3,273) DEVMG, TOL
           WRITE (3,760) (J, J = 1, M )
           DO 49 I = 1, N
           WRITE (3,770) I, ( GA (I,J), J = 1, MN)
    49     CONTINUE
           WRITE (3,780) ( I, I = 1, NN )
           DO 50 J = M, MM
           WRITE (3,770) J, ( GA (I,J), I = 1, NN)
    50     CONTINUE
           WRITE (3,830)
           WRITE (3,750)  ) DEVME, TOL
           WRITE (3,760) ( J, J = 1, M )
           DO 51 I = 1, N
           WRITE (3,770) I, ( SA (I,J), J = 1, M )
    51     CONTINUE
           WRITE (3,780) (I, I = 1, NN )
           DO 52 J = M, MM
           WRITE (3,770) J, ( SA (I,J), I = 1, NN )
    52     CONTINUE
    53     CONTINUE
C          *********************************************************
C
C
C          RADIAL VELOCITY IS CALCULATED FROM STREAM FUNCTION
C          DEFINITION,'SA' IS USED FOR 'U' CALCULATION FOR SAVING
C          STORAGE CAPACITY.
C
C          *********************************************************
           MMT = MM
           DO 56 I = 1, N
           DO 54 J = 1, MMT
           SA (I,J) = 0.0
           SB (I,J) = 0.0
    54     CONTINUE
           IF ( I - NN) 56,55,55
    55     MMT = M
    56     CONTINUE
           MMT1 = MM1
```

```
          DO 59 I = 1, N
          X1 = I - 1
          RA = X1 * A
          DO 57 J = 2, MMT1
          SA(I,J) = ( PA(I,J+1) - PA(I,J-1)) / (2.* RA * A)
   57     CONTINUE
          IF (I - NN1) 59,58,58
   58     MMT1 = M1
   59     CONTINUE
          WRITE (3,840)
          WRITE (3,760) ( J, J = 1, M )
          DO 60 I = 1, N
          WRITE (3,770) I,( SA (I,J), J = 1, M)
   60     CONTINUE
          WRITE (3,780) ( I, I = 1, NN )
          DO 61 J = M, MM
          WRITE (3,770) J,( SA (I,J), I = 1, NN )
   61     CONTINUE
   C      *******************************************************
   C
   C
   C      AXIAL VELOCITY IS CALCULATED FROM STREAM FUNCTION
   C      DEFINITION 'SB' IS USED FOR 'W' CALCULATION FOR SAVING
   C      STORAGE CAPACITY
   C
   C      *******************************************************
          MMT1 = MM1
          DO 64 I = 2, N1
          X1 = I - 1
          RA = X1 * A
          DO 62 J = 2, MMT1
          SB(I,J) = ( PA(I-1,J) - PA(I+1,J)) / (2. * RA * A)
   62     CONTINUE
          IF (I - NN1) 64,63,63
   63     MMT1 = M1
   64     CONTINUE
          DO 65 J = 2, MM
          SB(1,J) = (PA(4,J) - 2.*PA(3,J) - 11.*PA(2,J)) / (5.*
         1A ** 2)
   65     CONTINUE
          DO 65 I = 2, NN1
          SB(I,MM) = SB(I,MM4) - 2.0* SB(I,MM3) + 2.0* SB(I,MM1)
   66     CONTINUE
          WRITE (3,850)
          WRITE (3,760) ( J, J = 1, M )
          DO 67 I = 1, N
          WRITE (3,770) I, ( SB (I,J), J=1,M)
   67     CONTINUE
          WRITE (3,780) (I, I = 1, NN )
          DO 68 J = M, MM
          WRITE (3,770) J,(SB (I,J), I = 1, NN )
   68     CONTINUE
```

```
C        ************************************************
C        TANGENTIAL VELOCITY IS CALCULATED FROM CIRCULATION
C        'PB' IS USED FOR 'V' CALCULATION FOR SAVING STORAGE
C        CAPACITY
C
C        ************************************************
         DO 69 J = 1, MM
         PB(1,J) 0.0
69       CONTINUE
         MMT = MM
         DO 72 I = 2, N
         X1 = I - 1
         RA = X1 * A
         DO 70 J = 1, MMT
         PB(I,J) = GA (I,J) / RA
70       CONTINUE
         IF (I - NN ) 72,71,71
71       MMT = M
72       CONTINUE
         WRITE (3,860)
         WRITE (3,760) ( J, J = 1, M )
         DO 73 I = 1, N
         WRITE (3,770) I,(PB (I,J), J=1,M)
73       CONTINUE
         WRITE (3,780) ( I, I = 1, NN )
         DO 74 J = M, MM
         WRITE (3,770) J, ( PB (I,J), I = 1, NN)
74       CONTINUE

500      FORMAT (416)
550      FORMAT (5F12.7  )
600      FORMAT (F10.5, 4I10)
700      FORMAT (//' QO = ' E16.7 '/ OMEGA =', E16.7/ ' H =  ',
        1E16.7 /' RO = ', E16.7/ 10X, 'TANGENTIAL REYNOLDS NUMBER
        2= ',E16.7 / 10X, ' INLET CIRCULATION = ', E16.7 / 10X, '
        3ROSSBY NUMBER = ', E17.7 )
710      FORMAT (/ 10X,' RADIAL INLET VELOCITY = ', E18.7 / 10X, '
        1RADIAL REYNOLDS NUMBER = ', E18.7 / 10X,' TANGENTIAL
        2INLET VELOCITY = ', E18.7/ )
720      FORMAT ( /5X,'N = ',I3,5X,'M = ', I3,5X, 'NN =', I3,5X,
        1'MM = ', I3 )
730      FORMAT (/' STREAM FUNCTION TABLE  ' // )
740      FORMAT (// I7, '   ITERATIONS WERE USED  ' / )
750      FORMAT ( '  MAXIMUM DEVIATION = ', E18.7 / ' ASSUMED
        1TOLERANCE  = ', E18.7    )
760      FORMAT (/ 8X, ' I / J = ' 7( I2, 15X ) / )
770      FORMAT (  I10, 6E17.7 )
780      FORMAT (  / 8X, ' J / I = ',7( I2, 15X ) / )
790      FORMAT (/8X, ' NUMBER OF ITERATIONS ARE ' , I5 / )
800      FORMAT (8X, ' ***************************** ' / )
810      FORMAT ( / 5X, 7H TIME = F10.5 )
820      FORMAT (// '  CIRCULATION DISTRIBUTION ' / )
830      FORMAT ( // ' TANGENTIAL VORTICITY DISTRIBUTION ' / )
840      FORMAT ( / 10X, '  RADIAL VELOCITY DISTRIBUTION ' / )
```

```
850    FORMAT ( / 10X, '  AXIAL VELOCITY DISTRIBUTION ' / )
860    FORMAT ( / 10X, '  TANGENTIAL VELOCITY DISTRIBUTION ' / )
       STOP
       END
```

APPENDIX F

COMPUTER PROGRAM - STEADY STATE CASE

```
      PROGRAM PATEL
      IMPLICIT REAL *8(A-H,O-Z)
      DIMENSION PSY (51,51), GEMA(51,51), ETA(51,51), U (51,51)
      READ(2,82) N, M, NN, MM
      READ (2,90)LA,LB,LC,LX
      XNEU = 160.E-6
      R = 1.
      N1 = N-1
      XN = N
      M1 = M-1
      MP = M + 1
      XM = M
      NN1 =NN-1
      NNP = NN + 1
      XNN = NN
      MM1 = MM - 1
      MM3 = MM - 3
      MM4 = MM - 4
      DELR = R / (XN - 1. )
      DELZ = DELR
      A = DELR
      RI = R *(XNN - 1. ) / ( XN - 1. )
      MMT = MM
      DO 3 I = 1,N
      RN = (XI - 1. ) *A
      DO 1 J = 1, MMT
      PSY (I,J) = 0.
      ETA (I,J) = 0.
      GEMA (I,J) = RN**2
      U(I,J) = 0
1     CONTINUE
      IF(I - NN ) 3,2,2
2     MMT = M
3     CONTINUE
      READ (2,81) QO, OMEGA, RO, H, TOL
      VO = RO * OMEGA
      UO = QO / ( 2. * 3.14159 * RO * H )
      REU = UO * RO / XNEU
      ROSB = QO / ( 2. * 3.14159 * OMEGA * RO ** 3 )
      RE = OMEGA * RO ** 2 / XNEU
      GEMAO = OMEGA * RO ** 2
      RX = 2. * DELR / RE
      DO 4 I = NNP,N
4     PSY(I,M) = - ROSB
      DO 5 J = M, MM
      PSY (NN,J) = - ROSB
5     CONTINUE
      DO 6 J = 2,M1
      XJ = J
```

```
6        PSY(N,J) = -ROSB * (XJ - 1,) / (XM - 1.)
         WRITE (3,85) QO OMEGA, H, RO, RE, GEMAO, ROSB
         WRITE (3,89) N, M, NN, MM
         DO 14 I5 = 1, LA
C        *****************************************************
C
C
C        STREAM FUNCTION CALCULATION WITH ZERO VORTICITY TERM
C        'U' IS USED FOR TEMPORARY STORAGE OF STREAM FUNCTION
C
C        *****************************************************
         MMT1 = MM1
         DO 9 I = 2, N1
         XI = I
         RN = (XI-1.) * A
         DO 7 J = 2, MMT1
         P1 = 0.25 * ( PSY (I+1,J) + PSY (I-1,J) + PSY (I,J+1)
     1       + (PSY(I,J-1))
         P2 = 2. * ETA(I,J) * RN **2 * DELR + PSY(I+1,J)
     1       - PSY(I-1,J)
         U  (I,J) = P1 - P2 *A/(8.*RN)
7        CONTINUE
         IF (  I - NN1 ) 9,8,8
8        MMT1 = MM1
9        CONTINUE
         MMT1 = MM1
         DO 12 I = 2, N1
         DO 10 J = 2, MMT1
         PSY (I,J) = 0.2 * PSY(I,J) + 0.8 * U(I,J)
10       CONTINUE
         IF (I - NN1) 12,11,11
11       MMT1 = M1
12       CONTINUE
         DO 13 I = 2, NN1
         PSY(I,MM) = PSY(I,MM4) - 2.*PSY(I,MM3) + 2.* PSY(I,MM1)
13       CONTINUE
14       CONTINUE
         MX = LB
         DO 52 KX = 1, LX
C        *****************************************************
C
C
C        STREAM FUNCTION CALCULATION WITH NEW TANGENTIAL VORTICITY
C        TERM 'U' IS USED FOR TEMPORARY STORAGE OF STREAM FUNCTION
C
C        *****************************************************
         DO 23 I4 = 1, LC
         DEVMP = 0.
         MMT1 = MM1
         DO 18 I = 2, N1
         XI = I
         RN = A * (XI - 1.)
         DO 16 J = 2,MMT1
         TEMP = PSY(I,J)
         P1 = 0.25 * ( PSY (I+1,J) + PSY (I-1,J) + PSY (I,J+1)
     1       + PSY(I,J-1))
```

```
          P2 = 2. * ETA(I,J) * RN **2 * DELR + PSY(I+1,J)
        1        - PSY (I-1,J)
          U  (I,J) = P1 - P2 *A/8.*RN)
          DEV = ABS(  U (I,J) - TEMP)
          IF (DEV - DEVMP) 16,16,15
   15     DEVMP = DEV
   16     CONTINUE
          IF (  I - NN1 ) 18,17,17
   17     MMT1 = M1
   18     CONTINUE
          MMT1 = MM1
          DO 21 I = 2, N1
          DO 19 J = 2, MMT1
          PSY (I,J) = ( PSY (I,J) + U (I,J) ) / 2.0
   19     CONTINUE
          IF (I - NN1) 21, 20,20
   20     MMT1 = M1
   21     CONTINUE
          DO 22 I = 2, NN1
          PSY(I,MM) = PSY(I,MM4) - 2.* PSY(I,MM3) + 2.* PSY(I,MM1)
   22     CONTINUE
   23     CONTINUE
C         ****************************************************
C
C
C         CIRCULATION CALCULATION BY ITERATION TECHNIQUE
C         'U' IS USED FOR TEMPORARY STORAGE OF CIRCULATION
C
C         ****************************************************
          DEVMG = 0.
          MMT1 = MM1
          DO 27 I = 2,N1
          XI = I
          RN = A * (XI - 1.)
          RRX = RE / (16.0 * RN)
          DO 25 J = 2, MMT1
          TEMP = GEMA (I,J) gema 91-1,J)
          G4 = GEMA(I+1,J) + GEMA(I-1,J) + GEMA(I,J+1) + GEMA(I,J-1)
          G5 = ( PSY(I,J+1) - PSY(I,J-1) + RX )*( GEMA(I+1,J)
        1        - GEMA(I-1,J))
          G6 = ( PSY(I+1,J) - PSY(I-1,J))*( GEMA(I,J+1) - GEMA(I,J-1))
          G7 = RRX * ( G5 - G6 )
          U (I,J) = 0.25 * G4 - G7
          DEV = ABS( U (I,J) - TEMP)
          IF (DEV - DEVMG) 25,25,24
   24     DEVMG = DEV
   25     CONTINUE
          IF (  I - NN1) 27,26,26
   26     MMT1 = M1
   27     CONTINUE
          MMT1 = MM1
          DO 30 I = 2, N1
          DO 28 J = 2, MMT1
          GEMA(I,J) = 0.7*U (I,J) + 0.3 * GEMA(I,J)
   28     CONTINUE
```

```
         IF (I - NN1) 30,29,29
  29     MMT1 = M1
  30     CONTINUE
         DO 31 I = 2, NN1
         GEMA(I,MM)=GEMA(I,MM4) - 2.*GEMA(I,MM3) + 2.*GEMA(I,MM1)
  31CCN  CONTINUE
C        **********************************************************
C
C        TANGENTIAL VORTICITY CALCULATIONS BY ITERATION TECHNIQUE
C        'U' IS USED FOR TEMPORARY STORAGE OF TANGENTIAL VORTICITY
C
C        **********************************************************
         DEVME = 0.
         MMT1 = MM1
         DO 35 I = 2,N1
         XI = I
         RN = A * (XI - 1.)
         RRX = RE / (16.0 * RN)
         VX = 1.0 / (4.0 * (XI-1.)**2)
         VY = 1.0 / (( XI-1. ) ) * RN )
         VZ = RE / ( 8.0 * RN * (XI-1.))
         DO 111 J = 2, MMT1
         TEMP = ETA (I,J)
         ET4 = ETA(I+1,J) + ETA(I-1,J) + ETA(I,J+1) + ETA(I,J-1)
         ET5 = ( PSY(I,J+1) - PSY(I,J-1) - RX ) * (ETA(I+1,J)
        1      - ETA(I-1,J))
         ET6 = ( PSY(I+1,J) - PSY(I-1,J))*(ETA(I,J+1) - ETA(I,J-1))
         ET7 = 4.*GEMA(I,J)* (GEMA(I,J+1) - GEMA(I,J-1))*VY
         DENO = 1.0 + VX + (PSY(I,J-1) - PSY(I,J+1)) * VZ
         U (I,J) = (0.25*ET4 - (ET5 - ET6 - ET7) * RRX ) / DENO
         DEV = ABS (U (I,J) - TEMP)
         IF (DEV - DEVME) 33,33,32
  32     DEVME = DEV
  33     CONTINUE
         IF ( I - NN1 ) 35,34,34
  34     MMT1 - M1
  35     CONTINUE
         MMT1 = MM1
         DO 39 I = 2, N1
         DO 37 J = 2, MMT1
  36     ETA (I,J) = 0.2 * U (I,J) + 0.8 * ETA (I,J)
  37     CONTINUE
         IF (I - NN1) 39,38,38
  38     MMT1 = M1
  39     CONTINUE
C        **********************************************************
C
C        BOUNDARY CONDITIONS FOR TANGENTIAL VORTICITY
C
C        **********************************************************
         DO 40 I = 2, NN
         ETA(I,MM) = ETA(I,MM4) - 2.*ETA(I,MM3) + 2.*ETA(I,MM1)
  40     CONTINUE
```

```
      DO 41 J = 2, M1
      ETA (N,J) = 0.
   41 CONTINUE
      DO 42 I = 2, N
      XI = I
      RN = A * (XI - 1.)
      ETA (I,1) = 2. * (PSY(I,2) - PSY(I,1)) / (RN * DELZ ** 2 )
   42 CONTINUE
      DO 43 I = NNP, N
      XI = 1
      RN = A * (XI - 1.)
      ETA (I,M) = 2. * (PSY(I,M1) - PSY(I,M)) / ( RN * DELZ ** 2 )
   43 CONTINUE
      DO 44 J = MP, MM
      ETA (NN,J) = 2. * (PSY(NN1,J) - PSY(NN,J)) / (RI * DELR ** 2 )
   44 CONTINUE
      ETA (NN,M) = (PSY(NN,M1) - PSY(NN,M)) / (RI * DELZ ** 2 )
     1             + (PSY(NN1,M) - PSY(NN,M)) / (RI * DELR ** 2)
      IF (KX - MX ) 52,45,45
   45 WRITE (3,93) MX
      WRITE (3,91)
      MX = MX + LB
C     *************************************************************
C
C
C     PRINTOUT OF STREAM FUNCTION, CIRCULATION AND TANGENTIAL
C     VORTICITY
C
C     *************************************************************
      WRITE (3,95)
      WRITE (2,94) DEVMP, TOL
      WRITE (3,84) (J, J = 1, M)
      DO 46 I = 1,N
      WRITE (3,88) I, (PSY(I,J), J = 1, M )
   46 CONTINUE
      WRITE (3,93) ( I,I = 1, NN )
      DO 47 J = M,MM
      WRITE (3,88) J, (PSY(I,J), I = 1,NN )
   47 CONTINUE
      WRITE (3,86)
      WRITE (3, 94) DEVMG, TOL
      WRITE (3,84) ( J, J = 1, M )
      DO 48 I = 1, N
      WRITE (3,88) I, (GEMA(I,J), J=1,M)
   48 CONTINUE
      WRITE (3,93) (I,I = 1, NN )
      DO 49 J = M,MM
      WRITE (3,88) J, ( GEMA(I,J), I = 1, NN )
   49 CONTINUE
      WRITE (3,87)
      WRITE (3,94) DEVME, TOL
      WRITE (3,84) (J, J = 1, M )
      DO 50 I = 1, N
      WRITE (3,88) I, ( ETA(I,J), J=1,M)
```

```
   50      CONTINUE
           WRITE (3,93) ( I,I = 1,MN )
           DO 51 J = M, MM
           WRITE (3,88) J, ( ETA (I,J), I = 1, NN )
   51      CONTINUE
   52      CONTINUE
C          *********************************************************
C
C
C          RADIAL VELOCITY - U CALCULATION FROM STREAM FUNCTION
C
C          *********************************************************
           DO 53 J = 2, M1
           U (N,J) = -UO / ( RO * OMEGA)
   53      CONTINUE
           MMT1 = MM1
           DO 56 I = 2, N
           I = I
           RN = (XI - 1.) * A
           DO 54 J = 2, MMT1
           U (I,J) = (PSY(I,J+1) - PSY(I,J-1)) / (2. * RN * DELZ )
   54      CONTINUE
           IF ( I - NN1 ) 56,55,55
   56      CONTINUE
           WRITE (3,96)
           WRITE (3,84) (J,J = 1,M)
           DO I = 1, N
           WRITE (3,88) I, ( U (I,J), J=1,M)
   57      CONTINUE
           WRITE (3,93) (I, I = 1, NN )
           DO 58 J = M,MM
           WRITE (3,88) J, ( U(I,J), I = 1, NN )
   58      CONTINUE
C          *********************************************************
C
C
C          AXIAL VELOCITY CALCULATION FROM STREAM FUNCTION 'U' IS
C          USED FOR AXIAL VELOCITY CALCULATION FOR SAVING STORAGE
C          CAPACITY
C
C          *********************************************************
           DO 59 J = 1, M
           U (N,J) = 0.
   59      CONTINUE
           DO 60 J = 2, MM
           U (I,J) = -(-PSY(4,J) + 2. * PSY(3,J) + 11.*PSY(2,J)) /
          1          (5.*DELR 1 ** 2 )
   60      CONTINUE
           MMT1 = MM1
           DO 63 I = 2, N1
           XI = I
           RN = A * (XI - 1.)
           DO 61 J = 2, MMT1
           U (I,J) = ( PSY(I-1,J) - PSY(I+1,J) ) / (2. * RN * DELR )
   61      CONTINUE
           IF ( I - NN1 ) 63,62,62
```

```
62      MMT1 = M1
63      CONTINUE
        DO 64 I = 2, NN1
        U (I,MM) = U(I,MM4) - 2.* U (I,MM3) + 2.*U (I,MM1)
64      CONTINUE
        WRITE (3,97)
        WRITE (3,84) (J,J = 1, M)
        DO 65 I = 1, N
        WRITE (3,88) I, ( U(I,J), J=1,M)
65      CONTINUE
        WRITE (3,93) (I, I = 1, NN )
        DO 66 J = M, MM
        WRITE (3,88) J, ( U (I,J), I = 1, NN )
66      CONTINUE
C       ************************************************************
C
C
C       TANGENTIAL VELOCITY CALCULATION FROM CIRCULATION 'U'
C       IS USED FOR TANGENTIAL VELOCITY CALCULATION FRO SAVING
C       STORAGE CAPACITY
C
C       ************************************************************
        DO 67 J = 1, MM
        U (I,J) = 0.0
67      CONTINUE
        MMT = MM
        DO 70 I = 2, N
        XI = I
        RN = (XI-1.) * A
        DO 68 J = 1, MMT
        U (I,J) = GEMA (I,J) / RN
68      CONTINUE
        IF (I - NN) 70,69,69
69      MMT = M
70      CONTINUE
        WRITE (3,98)
        WRITE (3,84) (J,J = 1, M )
        DO 71 I = 1, N
        WRITE (3,88) I, ( U (I,J), J=1,M) NN )
71      CONTINUE
        WRITE (3,93) ( I,I = 1, NN )
        DO 72 (J = M, MM
        WRITE (3,88) J, ( U (I,J), I = 1, NN )
72      CONTINUE

81      FORMAT (5F12.7 )
82      FORMAT ( 416 )
83      FORMAT (/ 10X,' RADIAL INLET VELOCITY = ', E18.7 / 10X,
       1' RADIAL REYNOLDS NUMBER =', E18.7 / 10X,' TANGENTIAL
       2INLET VELOCITY =', E18.7 )
84      FORMAT ( /7X, ' J = ', 5X, 7( I2, 14X) / )
85      FORMAT (// ' QO = ', E16.7 / 'OMEGA ',E16.7/ ' H = ',
       1E16.7 /' RO =',E16.7 / 10X, ' TANGENTIALREYNOLDS NUMBER
       2= ',E16.7 / 10X, ' INLET CIRCULATION = ', E16.7 / 10X, '
       3ROSSBY NUMBER = ',E17.7 )
```

```
86    FORMAT (// ' CIRCULATION DISTRIBUTION ' / )
87    FORMAT ( // ' TANGENTIAL VORTICITY DISTRIBUTION / )
88    FORMAT ( 110,6E16.7 )
89    FORMAT (  /5X,'N =',I3,5X, 'M =2, I3,5X, )NN =', I3,5X,
     1          'MM = ',I3 )
90    FORMAT (4I6)
91    FORMAT   ( 8X, '  *************************** ' / )
92    FORMAT   (/8X   ' NUMBER OF ITERATIONS ARE  ', 15 / )
93    FORMAT   ( /7X, ' I = ', 5X, 7( 12, 14X ) / )
94    FORMAT   ( ' MAXIMUM DEVIATION = ' , E18.7 / ' ASSUMED
     1TOLERANCE  = ', E18.7     )
95    FORMAT (/'      STREAM FUNCTION TABLE    '      //   )
96    FORMAT (/ 5X, ' RADIAL VELOCITY DISTRIBUTION ' / )
97    FORMAT (/ 5X, ' AXIAL VELOCITY DISTRIBUTION  ' / )
98    FORMAT ( / 10X, ' TANGENTIAL VELOCITY DISTRIBUTION ' / )
      STOP
      END
```